# Polycrystalline Silicon Solar Cells on Glass – Toward an Industry Compatible Process

vorgelegt von
ir., M.Sc.
Tim Robin Frijnts,
geb. in Enschede

von der Fakultät IV - Elektrotechnik und Informatik
der Technischen Universität Berlin
zur Erlangung des akademischen Grades

Doktor der Ingenieurswissenschaften
- Dr.-Ing. –

genehmigte Dissertation

Promotionsausschuss:

| | |
|---|---|
| Vorsitzender: | Prof. Dr. Bernd Szyszka |
| Gutachter: | Prof. Dr. Bernd Rech |
| | Prof. Dr. Rutger Schlatmann |
| | Prof. Dr. Arno Smets |

Tag der wissenschaftlichen Aussprache: 13. Juni 2017

Berlin 2018

To my family

# Contents

# 1 Introduction

## 1.1 Motivation

For the past years, global temperature records have been broken almost every month [1], clearly indicating the ongoing impact of climate change. Climate change has been linked to drought, extreme weather, sea level rise and loss of biodiversity. In order to limit the global temperature increase to the 2° C, or even 1.5° C, as discussed in the Paris climate agreement, a very rapid reduction of $CO_2$ emissions will be needed in the coming decades [2].

To achieve this goal, photovoltaics (PV) deployment targets have been set to 2-10 TWp by 2030 [3]. In 2015, 18.1% of the global final energy consumption consisted of electricity [4]. At the end of 2014, 1 % of this global electricity consumption was produced by PV, corresponding to 177 GWp cumulative installed capacity [5]. Since then, approximately another 130 GWp has been added, indicating the rapid growth of the PV market, but also showing that PV is still very far from dominating the energy market. In ref. [3] economical modelling is used to determine if the PV industry will be able to scale up rapidly enough to meet climate change targets of 2-10 TWp installed PV capacity in 2030. It is concluded that, even in the demand unconstrained scenario, this will be very challenging and the authors stress the importance of reducing capital expenditure (capex), as this would allow PV manufacturers to expand more rapidly. Over 30 % of PV capex is due to poly-silicon production and it is therefore argued Si thickness should be reduced from 180 µm to 10-50 µm. However, doing so for Si wafers will be extremely challenging, as thin wafers break very easily.

The commercial development of thin film silicon solar cells in the years 2000-2010 was mainly motivated by the costs of poly-silicon, which was very high at that time. However, when poly-Si costs plummeted, after supply finally caught up with demand, it turned out that the thin film silicon technologies had too low efficiencies (8-10 % [6]) to compete. Low Si consumption was not the only advantage of thin film silicon over silicon wafers: beside their homogeneous appearance (better aesthetics), the thin film silicon process is much more integrated (i.e. glass in, module out), resulting in very lower costs [7, p. 192].

According to the Fraunhofer ISE Photovoltaics report, the annual PV production for 2015 was 43.9 GWp for multi-crystalline silicon (mc-Si), 15.1 GWp for mono-crystalline silicon, 2.5 GWp for CdTe, 1.1 GWp for CIGS and 0.6 GWp for a-Si [8]. The dominance of mc-Si (69 % in 2015) indicates that the largest market is still for moderate efficiency (15-16 %), low cost, mc-Si PV modules and not for higher cost, higher efficiency, mono-Si modules. In 2016, overcapacity has resulted in a drop of mc-Si module prices from 0.45-0.5 to 0.35-0.4 €/Wp, which might further increase the dominance of mc-Si in the coming years.

Another development of the past years is that difference in material quality between so called high performance (hp) mc-Si wafers and mono-Si wafers has strongly decreased. This was mainly achieved by changing the mc-Si growth process to obtain a small grained material, thereby reducing intra-grain dislocations, as grain boundaries have the ability to reduce stress [9]. Removing impurities by phosphorus gettering and passivating defects by hydrogen passivation have resulted in n-type mc-Si lifetimes >1 ms [10], making the material quality comparable to that of mono-Si wafers. Together with the commercial break-through of the Passivated Emitter Rear Cell (PERC) technology this has resulted in record mc-Si cell and module efficiencies of 21.25 % [11] and 19.86 % respectively. These results clearly indicate the efficiency potential of mc-Si.

The goal for the multi-crystalline silicon on glass technology used in this thesis, is to combine the low cost advantages of thin film silicon with the high efficiency of multi-crystalline silicon wafer cells.

## 1.2 Solar Cells Based on Crystallized Silicon on Glass

Figure 1-1 shows a schematic cross-section of a basic crystallized silicon on glass solar cell. An interlayer stack between the glass substrate and the crystallized silicon absorber, generally consisting of $SiO_x$, $SiN_x$ and $SiC_x$ layers, is needed as diffusion barrier, anti-reflection coating and defect passivation layer. The absorber thickness is typically between 2 and 20 µm. Crystallized silicon on glass can only be contacted from one side. Therefore, it requires a backside-contacting (BC) scheme with both contacts (absorber- and emitter contact) on the same side and some insulator or air in between to prevent shunting. Illumination is generally through the glass (superstrate configuration), but some devices are bifacial, i.e. can be illuminated from both sides. The generated minority carriers can only diffuse a relatively short distance before recombining and therefore the emitter, which collects the minority carriers, has to cover most of the cell area.

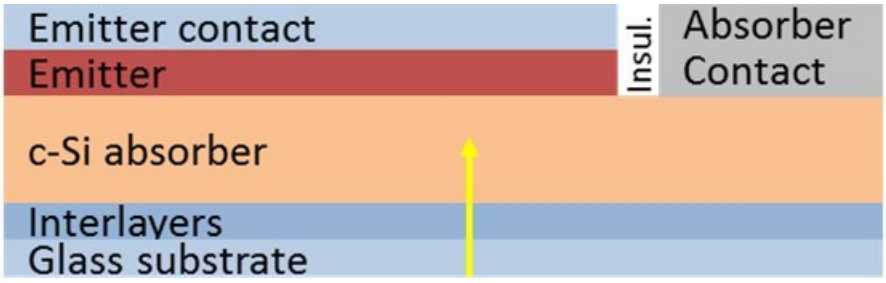


**Figure 1-1.** Schematic cross-section of a basic crystallized silicon on glass solar cell.

Development of crystallized silicon on glass solar cells started at the UNSW in the late 80's [12], resulting in the founding of the company Pacific Solar (1995-2004)[13]. The silicon on glass was crystallized by annealing of a 2-2.5 µm thick amorphous silicon (a-Si) precursor at 600 °C for 20-30 hours, in a process

called solid phase crystallization (SPC) [14]. At the same time, this technology was developed at Sanyo Electric Co. in Japan, resulting in an n-type cell with an open-circuit voltage ($V_{OC}$) of 553 mV and an efficiency ($\eta$) of 9.2 % in 1996 [15]. Pacific Solar was followed by the commercialization of the technology by the German company CSG Solar in 2004. Pacific Solar and CSG Solar developed a contacting scheme with point contacts for both contact polarities, resulting in the industrial production of 1.4 $m^2$ modules and a 94 $cm^2$ mini-module with a record efficiency of 10.4 % [16] in 2007. However, the high $V_{OC}$ of Sanyo could not be reproduced by others and the $V_{OC}$ values obtained since were limited to about 500 mV, indicating the need for a higher material quality.

Laser crystallization and annealing of silicon have been developed since the late 70's and are widely applied in the LCD industry to create fast switching transistors for high quality displays. In 1999 Pacific Solar applied for a patent on the recrystallization of a 0.1-10 µm thick silicon layer over a liquid phase for making a photovoltaic device [17]. Initially, most efforts in this field were focussed on seed-layer crystallization and subsequent epitaxial thickening [18]. It wasn't until 2011 that the first solar cell results were published that showed the liquid phase crystallization (LPC) of an approximately 10 µm thick Si precursor layer, resulting in a $V_{OC}$ of 545 mV [19], indicating a higher material quality than SPC-Si. Mainly by changing the interlayer stack between the glass and the c-Si from $SiC_x$ to a $SiO_2/SiN_x/SiO_2$ stack, the $V_{OC}$ was increased to 585 mV and an initial efficiency of 11.7 % [20] was obtained at UNSW, using an adapted version of the aforementioned CSG Solar point contact device. In parallel, the LPC-Si development and specifically the use of n-type doping at HZB resulted in $V_{OC}$ values above 600 mV and a stable efficiency of 11.8 % [21], [22], using a bifacial device concept with stacked contact fingers ("FrontERA").

Both at UNSW and HZB the interlayers were deposited by RF magnetron sputtering and the silicon precursor was deposited by electron-beam (e-beam) evaporation. At UNSW these layers were deposited on 3.3 mm Schott BOROFLOAT33 substrates and crystallized with a line shaped laser beam, while at HZB the layers were deposited on 1.1 Corning Eagle XG substrates and crystallized with a line-shaped e-beam.

The most visible material improvement of LPC-Si over SPC-Si is the increase in grain size from 1-3 µm for SPC-Si, to elongated grains in the $mm^2$ range for LPC-Si [14]. However, in ref. [23] it is argued that the increase in $V_{OC}$ for LPC vs SPC, is due to a decrease of intra-grain dislocation, rather than the increase of the grain size. The effective diffusion length ($L_{eff}$) in LPC-Si is estimated in the 10-30 µm range [24], [25]

LPC-Si cells have to be contacted on the backside, which has the potential advantage of avoiding optical shading by metal contact fingers and parasitic absorption by contact layers at the front. This is the reason why the three highest efficiency crystalline silicon wafer solar cells are all back-side contacted [26], [27].

However, in order to utilize this advantage of no optical shading, it is important to minimize losses due to "electrical shading" at the back side. Electrical shading occurs when most of the minority carriers generated above the absorber contact recombine before being collected at the emitter. This increased recombination can be due to the longer distance they have to traverse to the emitter and the (usually) high recombination at the absorber contact. One strategy to avoid electrical shading losses is to use passivated (low recombination) contacts, which are also narrow compared to the effective diffusion length. This strategy is followed for LPC-Si in ref. [28]. An alternative strategy to minimize electrical shading losses (used in the second part of this thesis) is to use point contacts. Point contacts cover only a very small fraction of the cell area (2-4 %) and therefore the electrical shading loss is limited to this small fraction.

Contrary to SPC, LPC results in a uniformly doped c-Si layer, requiring a separate, subsequent emitter formation. The UNSW group used high temperature (furnace) diffusion to create an n-type homo-emitter on a p-type c-Si absorber, resulting in the aforementioned 11.7 % LPC-Si point contact cell [20]. At HZB this point contact cell concept was adapted by laser firing of the absorber point contacts in order to stabilize the efficiency [29] and by using both an a-Si/c-Si heterojunction (SHJ) emitter and n-type absorber doping, resulting in an 11.5 % point contact cell with a $V_{OC}$ of 619 mV [30]. The efficiency of this cell was mainly limited by the low *FF* of 65.5 % and it was speculated that the high cell resistance was caused by the contact between the a-Si emitter and the transparent conductive oxide (TCO).

An important factor in the 10.4 % SPC-Si efficiency record was the high short circuit current density ($J_{SC}$) of 29.5 mA/cm$^2$, despite an absorber thickness of only 2.2 µm. The main reasons for this high $J_{SC}$ were the very low reflection loss and excellent light trapping provided by the homogeneous, high angle texturing of both the air/glass and glass/Si interfaces. Also, the texturing of the latter interface was (automatically) transferred to the Si backside, further improving the optical properties. For LPC-Si, such (high angle) glass/Si texturing is incompatible with the crystallization process [31], leading to the need for different anti-reflection and light trapping techniques.

## 1.3 Goals and Outline

In a cooperation with the thin film silicon company Masdar PV GmbH, the goal for the first part of this thesis (chapters 3 and 4) was the development of the precursor and interlayer deposition by plasma enhanced chemical vapour (PECVD) deposition, using the bifacial FrontERA contacting scheme. The main reason for this material development was because PECVD deposition was available on an industry scale, contrary to e-beam evaporation. After Masdar PV withdrew from PV production at the end of 2014, the goal of the thesis shifted to the understanding and reduction of the fill factor (*FF)* and $J_{SC}$ losses in textured

LPC-Si cells, using the (industry compatible) point contacting scheme (chapters 5 and 6).

In chapter 2 the characterisation methods are introduced. The fabrication methods are mostly specific to the first part (PECVD material, using FrontERA) or second part (point contact cells) of the thesis and are therefore introduced at the beginning of chapter 3 and chapter 5 respectively. Chapters 3 describes the development of PECVD interlayers and precursors, comparing them to sputtered interlayers and e-beam evaporated precursors, using bifacial FrontERA cells. In chapter 4 the photocurrent losses and potentials of these cells are analysed in more detail, e.g. investigating the effect of absorber texturing and a textured anti-reflection foil. This chapter also introduces several concepts and methods that will be used for the $J_{SC}$ analysis of the point contact cells in the subsequent chapter. Chapter 5 describes the further development of the point contacting scheme, focussing on reducing shunting, increasing the absorber doping, implementing absorber texturing and new emitter/TCO combinations. Analysis of the resistance and photocurrent losses results in the identification of several other potential efficiency improvements. Chapter 6 describes the first LPC-Si (point contact) mini-modules. This is followed by a comparison of the p- and n-type, FrontERA and point contacting schemes in chapter 7 and a summary in chapter 8.

# 2 Characterization Methods

In this chapter an overview is given of the characterization methods used in this thesis. This includes both the measurements setups and the methods that were used for analysing the measured data. Section 2.1 introduces the solar simulator measurement and derivation of the *J-V* parameters and section 2.2 describes the Suns-$V_{OC}$ measurement and derivation of the pseudo *J-V* parameters by. Section 2.3 introduces the reflectance (*R*) and transmittance (*T*) measurements, which is followed by a description of the external quantum efficiency (*EQE*) measurements in section 2.4. Section 2.5 describes the light beam induced current (LBIC) measurement and the derivation of the the dead area fraction. Section 2.6 introduces the dark lock-in thermography measurement and discusses how it can be used to determine the location of shunts and locally increased recombination. Section 2.7 describes the derivation of the recombination loss and effective diffusion length from the *EQE*, *R* and *T* measurements using the collection efficiency model.

## 2.1 *J-V* Curves and Parameters – Solar Simulator

The *J-V* curves were measured using a dual-source (tungsten and xenon lamp) sun simulator with class AAA characteristics (WXS-155 S-L2 by Wacom Electric Co, Japan). The lamp intensity was calibrated before starting the measurements using calibrated c-Si cells. A rotatable chuck (flip-flop-chuck) was used with which cells can be measured both in substrate and superstrate configuration. The solar simulator with flip-flop-chuck is shown in Figure 2-2a-c. The *J-V* measurements were made with a 4-point probe.

Figure 2-1a shows an examples of the *J-V* and *P-V* curves (for a point contact cell), as well as the derivation of all the *J-V* parameters. The $V_{OC}$ is the voltage for $J = 0$ and the $J_{SC}$ is the current density for $V = 0$. The power density (*P*) is obtained by multiplying *J* and *V,* and the efficiency ($\eta$) equals the maximum power density ($P_{max}$) divided by the solar irradiance ($I_0$ = 100 mW/cm$^2$). The $V_{MPP}$ and $J_{MPP}$ are the voltage and current density at the maximum power point. The *FF* is obtained by dividing $P_{max}$ by the $V_{OC}{\cdot}J_{SC}$ product.

The inverse of the slope of the *J-V* curve at $J_{SC}$ is generally presented as the parallel or shunt resistance ($R_{parallel}$). If the slope at $J_{SC}$ continues linearly for negative voltages, this indicates an Ohmic shunt. Non-linear slopes at or near $J_{SC}$ can have various causes as will be discussed in sections 4.1 (distributed resistance) section 5.3 (non-Ohmic shunts) and section 5.6 (locally increased recombination).

The slope of the *J-V* curve at $V_{OC}$ usually equals the sum of the series resistance ($R_s$) and the "apparent resistance" ($R_{diode}$). The apparent resistance is not a resistance, but the slope of the diode curve, which is usually about 1 Ωcm$^2$ at $V_{OC}$, but approaching 0 for higher voltages ($>>V_{OC}$). Figure 2-1b shows how the

slope of the *J-V* curve ("local $R_s$") approaches a limiting value for high voltage because $R_{diode}$ becomes negligible. Based on the figure, the cell resistance will be determined from the slope of the *J-V* curve at ~0.9 V.

For the *J-V* measurement of a module with series connected cells, the $V_{OC}$ (or $V_{MPP}$) per cell is obtained by dividing the measured $V_{OC}$ (or $V_{MPP}$) by the number of cells. The $J_{SC}$ (or $J_{MPP}$) per cell is obtained by dividing the measured current by the area of one of the series connected cells (not the entire module).

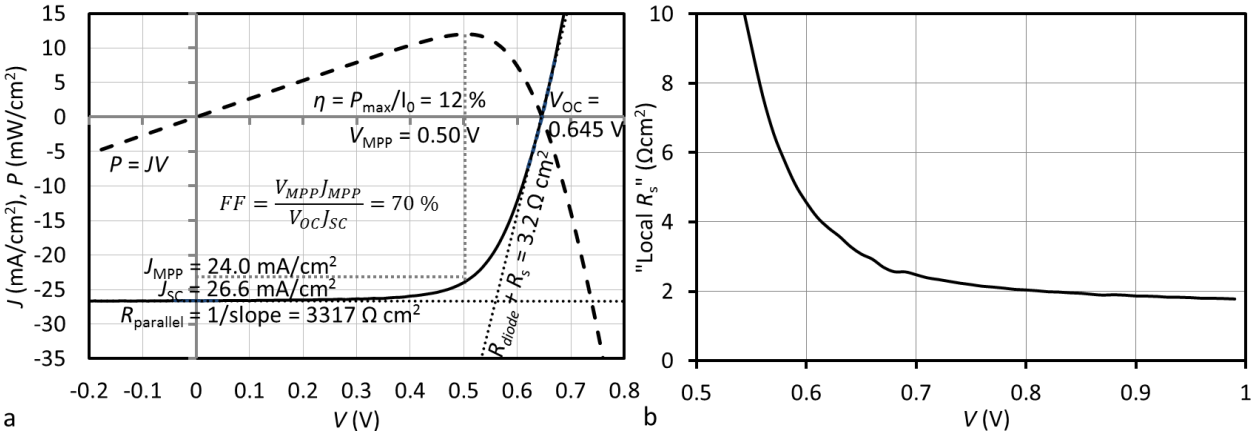


**Figure 2-1.** Fig. a shows example *J-V* (solid) and *P-V* (dashed) curves. All *J-V* parameters and their derivation are shown in the graph. $R_{diode}$ is the apparent (diode) resistance. Fig. b shows how the local $R_s$ (slope of the *J-V* curve) approaches a limiting value for high *V*.

In order to prevent overestimation of the $J_{SC}$, Tipp-Ex was applied at the edge of the best samples to prevent inscattering. This can be a significant factor because the sides of the 3.3 mm thick boro33 substrate are often broken under large angles.

As the point contact cells are optically uniform and their cell area is defined by a laser isolation scribe, they were measured with large area illumination (without mask). For FrontERA cells (and test cells [25]), there is the possibility of significant collection of carriers from outside the cell area (discussed in section 4.2). In order to obtain the correct $J_{SC}$ it is necessary to either use a mask or to determine the collection outside the cell area and correct for it.

Cells with light trapping/scattering in the glass substrate can also be affected by a measurement problem which causes an underestimation of the $J_{SC}$: if the measurement spot (or mask opening) is too small, then light is scattered out of the cell area, which is not (fully) compensated by light scattered into the cell area through the same mechanism. It is possible to prevent this outscattering problem by cutting the cell out of the sample and making the sides reflective, while still being able to measure with a mask. However, this would be very difficult and therefore the only practical solution to prevent the outscattering error is to increase the measurement spot (assuming optical uniformity over the illuminated area).

The *J-V* curves of the best cells were measured with a textured anti-reflection foil (ARF) by DSM advanced surfaces, featuring mm-sized pyramids [32], which is applied on the glass with a thin water adhesion layer in between. For measurements with the ARF, it is especially important to account for the in/outscattering effect described above, as the light is scattered through the (up to 3.3 mm thick) glass substrate before even entering the absorber.

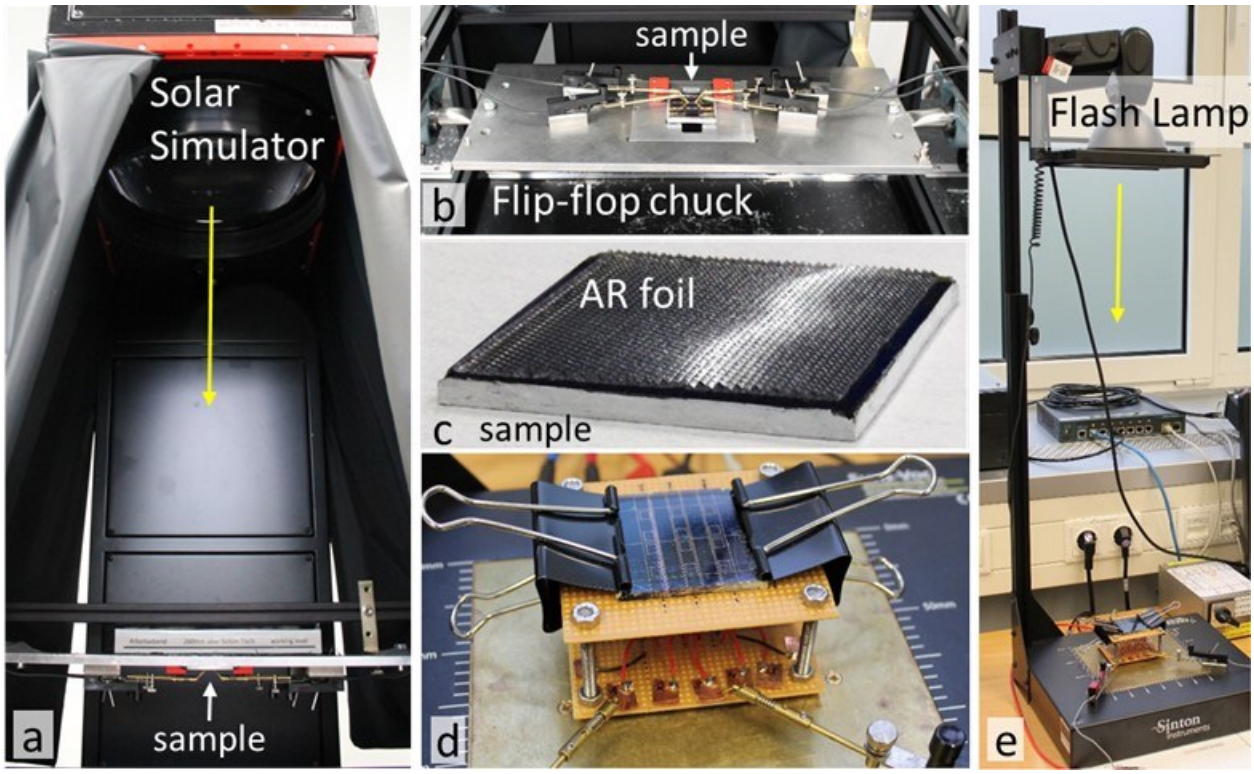


**Figure 2-2.** Solar simulator with flip-flop chuck and 4-point probe (a-b), sample with Tipp-Ex on edges and AR foil on glass (c) and Suns-$V_{OC}$ setup (e) with superstrate contacting unit (d). The arrows indicate the direction of the light.

## 2.2 Pseudo *J-V* Curves and Parameters - Suns-$V_{OC}$

The Suns-$V_{OC}$ measurement (shown in Figure 2-2e) uses a flash lamp to measure the $V_{OC}$ of a solar cell at light intensities between 6 and 0.01 suns. The light intensity is measured with a c-Si reference cell. A special contacting unit was constructed to measure point contact cells in superstrate configuration (Figure 2-2d). The bifacial test and FrontERA cells were (only) measured in substrate configuration. Even though the flash only lasts about 13 ms, this is sufficiently slow for the solar cell to be in a quasi-steady-state [33], allowing for the measurement of the $V_{OC}$ at each intensity (i.e. no current flow). By assuming that the $J_{SC}$ varies linearly with the light intensity (measured by the reference cell and expressed in suns) and using the superposition principle, a pseudo *J-V* curve is constructed using the measured $V = V_{OC}(\text{suns})$ and [33]:

$$J = J_{SC}(1 - suns)\,, \tag{1}$$

where the $J_{SC}$ is an input parameter. This pseudo *J-V* curve is basically a normal *J-V* curve without the influence of series resistance, as the $V_{OC}$ is not influenced by series resistance. From this pseudo *J-V* curve, the *pFF* is derived, which is the *FF* without series resistance.

## 2.3 Reflectance and Transmittance - Spectrophotometer

The reflectance (*R*) and transmittance (*T*) were measured using a PerkinElmer Lambda 1050 spectrophotometer with an integrating sphere as shown in Figure 2-3a. For the cell and AR foil measurements, the light spot was made smaller than the cell area, using a focussing lens ($R_T$) or iris diaphragm (*T*). The inside of the integrating sphere is covered with (white) Spectralon ($R > 99$ %) and the light is reflected many times inside the integrating sphere before being measured by the sensor. The tool is calibrated before starting the measurements with a 0 % (black cover) and Spectralon ($R > 99$ %) *R* measurement or a 0 % and 100 % *T* measurement.

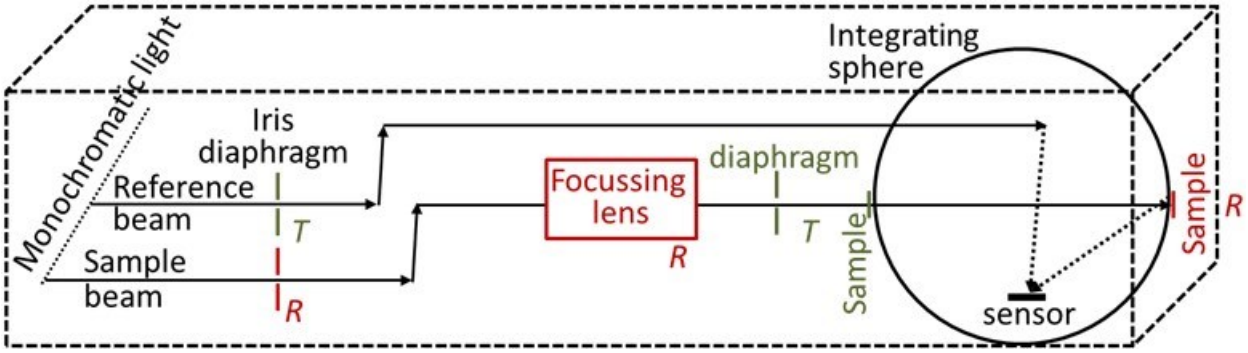


**Figure 2-3.** Schematic representation of the PerkinElmer Lambda 1050 spectrophotometer with integrating sphere. Position of the sample and optical components for the small spot *R* (red) and *T* (green) measurements in indicated in the figure. The light reaches the sensor after many reflections in the integrating sphere.

## 2.4 External Quantum Efficiency

External quantum efficiency (*EQE*) measurements measure for each wavelength which fraction of the incident light is converted to photocurrent. The measurement is calibrated with a calibrated reference cell. For measuring cells with well-defined cell area (point contact cells) and/or strong light scattering, an *EQE* setup was used with a measurement spot much larger than the sample (Figure 2-4b). *EQE* measurements of FrontERA cells on this large area *EQE* tool were corrected for collection outside the cell area (determined by LBIC, next section). The setup uses bandpass filters to create monochromatic light about every 20 nm between 300 and 1200 nm. For test cells, the measurement area is often not clearly defined because of inhomogeneous etching and collection outside the cell area. Therefore, an *EQE* setup with an approximately 2 x 3 $mm^2$ measurement spot (Figure 2-4c) is used, making an accurate determination of the cell area unnecessary. This setup uses a monochromator to create monochromatic light, e.g. every

10 nm between 300 and 1200 nm.

The large area *EQE* uses a halogen lamp that is very weak for short wavelength, causing the *EQE* to be very inaccurate for $\lambda$ < 340 nm. These values are therefore ignored. The small spot *EQE* has a dual light source (Xenon and Halogen), thereby avoiding this problem.

The bias light was varied with a halogen lamp. The bias light intensity was determined by dividing the measured cell current through the product of the $J_{SC}$ (determined with the *EQE* measurement) and the area of the cell (e.g. 3 mA / 24 mA/cm$^2$ / 0.6 cm$^2$ ≈ 0.3 suns). P-type cells have a strong bias light dependence [34] and should therefore be measured with a bias light >0.1 suns. However, too high bias light intensity can also cause measurement errors due to a low signal to noise ratio and sample heating. The optimum bias light intensity for p-type cells (high *EQE*, low noise) was found to be 0.1-0.5 suns. For n-type cells, no fundamental bias light dependence was observed.

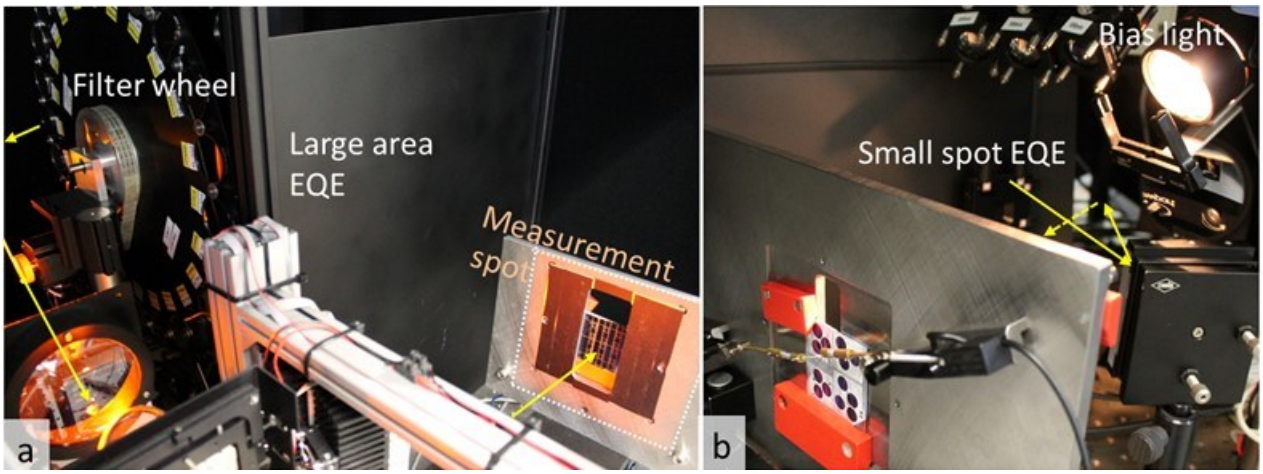


**Figure 2-4.** Figure a and b show the large area (a) and small spot (b) *EQE* measurement setups. The arrows indicate the direction of the light.

All the possible $J_{SC}$ errors mentioned for the *J-V* measurement in section 2.1 also apply to the *EQE* measurement, including the compensation of in- and outscattering. Therefore, the large area *EQE* set-up is more accurate (for long wavelengths) for cells with textured c-Si absorbers and especially with the textured anti-reflection foil.

The internal quantum efficiency (*IQE*) is defined as the *EQE* corrected for the reflectance (*R*) and transmittance (*T*) of the cell: *IQE* = *EQE*/(1-*R*-*T*). In this thesis we distinguish between the *IQE* and the collection efficiency ($\eta_c$), which additionally corrects the *EQE* for the parasitic absorption ($A_{par}$) and the dead area as will be discussed in section 2.7.

## 2.5 Light Beam Induced Current Measurements and Dead Area Fraction

Light beam induced current (LBIC) measurements use a low power laser beam to scan the cell and create a current map showing the relative current contribution for each location. The LBIC setup is shown in Figure 2-5a. All samples were illuminated through the glass. The laser has a wavelength of 532 nm or 904 nm. The laser spot has a full width at half maximum (FWHM) of approximately 30 µm. For each cell, the laser spot is focussed by positioning the beam inside an absorber contact (i.e. a local collection minimum) and moving the lens up and down until the LBIC signal is minimized (i.e. focussed in the local minimum). For most samples, the halogen bias light intensity was set to 0.1-0.5 suns (intensity determined from the cell current). Lock-in technique is used to separate the LBIC current from the bias light current. The bias light mainly influences resistance effects, which become (more) apparent as the current and therefore the resistance loss increase. Increasing the bias light intensity also decreases the signal-to-noise ratio and causes sample heating. A complete cell measurement generally takes 1-3 days, depending on the chosen resolution. Filters are used to reduce the laser beam intensity to a local intensity in the order of 50 suns. Reduction of the laser intensity decreases the signal-to-noise ratio. Therefore, the minimum laser intensity possible for a cell depends on the bias light intensity. In the presence of bias light, variation of the local laser intensity over 2 orders of magnitude (approx. 1-100 sun) did not result in a significant difference between the (relative) LBIC scans. Therefore, the local intensity of 50 suns should not affect the measurement result.

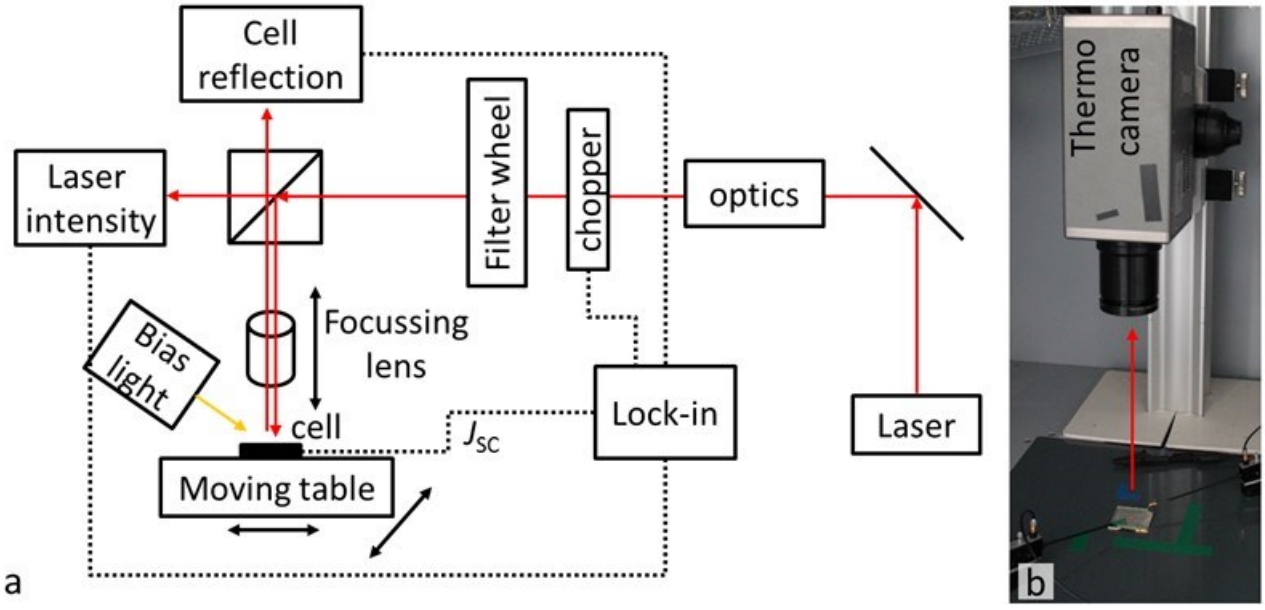


**Figure 2-5.** LBIC (a) and DLIT (b) measurement setups. The arrows indicate the direction of the light.

The LBIC measurement is used, among other things, to determine the dead area fraction due to electrical shading by the absorber contact. In order to quantify the dead area, a Matlab program was written, which

determined the position of the local minima in the LBIC signal formed by the absorber contacts and integrates the relative reduction of the LBIC signal compared to the surrounding cell area for each absorber contact. This relative reduction of the LBIC signal is then used to calculate either the width (FrontERA) or the radius (point contact) of a hypothetical completely dead line/circle which would cause the same total reduction of the LBIC signal. Finally, the median of all the calculated dead area widths/radii for the entire measurement (cell) is taken in order to remove outliers. This results in a value for the dead area which can be compared to the physical width/radius of the absorber contacts and which can be used for optimization of the contact spacing. For the $J_{SC}$ analysis the dead area width/radius is converted to a dead area fraction ($f_{DA}$) using the finger length for the FrontERA cells and the number of point contacts for the point contact cell.

## 2.6 Dark Lock-in Thermography

In thermography measurements a voltage is applied on a cell, which results in a (local) current flow and local heating. This heating is measured by an IR camera (Figure 2-5b). By applying a voltage to a solar cell in the dark, different currents will flow through the cell depending on the voltage: for negative or small positive voltages, a current will only flow through shunts and for voltages close to and larger than the $V_{OC}$, a current will flow through the entire active cell area. For moderate voltages, a current will also flow through regions with higher recombination (i.e. low $V_{OC}$). A shunt can also be non-Ohmic, resulting in a different current for positive and negative voltage. These currents cause resistive heating, which is measured with an IR camera (thermography). The use of the lock-in technique, where the voltage is applied at a certain frequency and the measurement is analyzed correspondingly, improves the sensitivity and spatial resolution of the measurement [35].

## 2.7 Recombination Losses and Diffusion Length - Collection Efficiency ($\eta_c$)

This section describes a method for analysing the *EQE*, *R* and *T* measurements in order to determine the photocurrent loss due to recombination and to estimate the effective diffusion length ($L_{eff}$). The collection efficiency $\eta_c$ is the fraction of the carriers generated in the absorber which are collected at the emitter for each wavelength. The rest is lost due to recombination in the absorber and at the interlayer interface.

### 2.7.1 Experimental $\eta_c$

The experimental $\eta_c$ equals the collected carriers (*EQE*) divided by the generated carriers (1-*R*-*T*-$A_{par}$). Also, the recombination losses were separated into the wavelength independent recombination (dead area, $f_{DA}$, section 2.5) and the wavelength dependent recombination due to recombination in the bulk and at the interlayer interface (*recomb*), which will be described by $\eta_c(\lambda)$). The experimental $\eta_c$ is obtained with the

following equation:

$$\eta_c(\lambda) = \frac{EQE}{1 - R - T - A_{par} - EQE \times f_{DA}} = \frac{EQE}{EQE + recomb}. \quad (2)$$

$A_{par}$ is generally only known with acceptable accuracy in a small wavelength range, e.g. for LPC-Si cells that are illuminated through the glass, the short wavelength light is only absorbed parasitically in the glass, resulting in a small and easily calculated $A_{par}$ for $400 < \lambda < 600$ nm. Fitting the calculated $\eta_c$ to the experimental $\eta_c$ in this small wavelength range, was used to obtain estimates for the effective diffusion length ($L_{eff}$) and an approximate $\eta_c$ for the rest of the wavelength range. This $\eta_c$ was then used to calculate the photocurrent loss due to recombination in the bulk and at the interlayer interface.

### 2.7.2 Calculated $\eta_c$: Equations

The collection probability ($f_c(x)$), i.e. the probability of collecting at the emitter a carrier generated at position $x$, is given by (e.g. [36], [37]):

$$f_c(x) = \frac{SL/_D \sinh(\frac{d-x}{L}) + \cosh(\frac{d-x}{L})}{SL/_D \sinh\left(\frac{d}{L}\right) + \cosh(\frac{d}{L})}, \quad (3)$$

$$D = \mu \frac{kT}{q} = \mu V_T \quad (4)$$

where $D$ is the minority carrier diffusion coefficient, $\mu$ is the minority carrier mobility, $k$ is the Boltzmann constant, $T$ is the temperature, $q$ is the elementary charge, $V_T$ is the thermal voltage, the junction is defined at $x = 0$ and the interlayer-Si interface is defined at $x = d$. For $\mu$, the mobility of mono-Si is assumed [38], because no measurements exists for the minority carrier mobility in LPC-Si. Majority carrier mobility measurements are presented and discussed in appendix A.3.1. In order to calculate the collection efficiency $\eta_c(\lambda)$, $f_c(x)$ must be multiplied by the generation rate ($G(x,\lambda)$), integrated over $x$ and normalized by the total generation:

$$\eta_c(\lambda) = \frac{\int_0^d G(x,\lambda) \times f_c(x) dx}{\int_0^d G(x,\lambda) dx}, \quad (5)$$

In order to solve this equation the generation profile must be known. As was done in ref. [39] the generation profile can be derived without simulation in two extreme cases: if the absorption depth ($1/\alpha$, where $\alpha$ is the absorption coefficient of silicon) is much larger than the absorber thickness $d$, only a small fraction is absorbed for each pass through the absorber. Therefore, the generation rate can be considered uniform. As a result, $G$ drops out of eq. (5) and the collection efficiency is given by [39]:

$$\eta_c = \frac{L}{d}\frac{{}^{SL}/_{D} + \tanh({}^{d}/_{L}) - \frac{{}^{SL}/_{D}}{\cosh({}^{d}/_{L})}}{1 + {}^{SL}/_{D}\tanh({}^{d}/_{L})}\,, \qquad \text{for } \frac{1}{\alpha} \gg d \tag{6}$$

If the absorption depth ($1/\alpha$) is much smaller than $d$, the generation profile $G$ can be calculated with the Lambert-Beer law ($I = I_0 e^{-\alpha x}$). If the light comes from the emitter side (substrate configuration), the generation profile is given by $G(x,\lambda) = G_{0,sub}e^{-\alpha(\lambda)x}$, where the constant $G_{0,sub}$ is irrelevant as it drops out of eq. (5), and $\eta_c$ becomes [39]:

$$\eta_c(\lambda) = \frac{\alpha L}{\alpha^2 L^2 - 1}\left(\alpha L - \frac{{}^{SL}/_{D} + \tanh\left({}^{d}/_{L}\right)}{1 + {}^{SL}/_{D}\,\tanh\left({}^{d}/_{L}\right)}\right), \qquad \text{for } \frac{1}{\alpha} \ll d \;\&\; \text{substrate} \tag{7}$$

If the light comes from the glass/interlayer side, which is called superstrate configuration, the generation profile is given by $G(x,\lambda) = G_{0,sup}e^{\alpha(\lambda)(x-d)}$ and $\eta_c$ becomes [40, pp. 727–729]:

$$\eta_c(\lambda) = \frac{\alpha L}{\alpha^2 L^2 - 1}\left(\frac{L\left(\alpha + {}^{S}/_{D}\right)}{\cosh\left({}^{d}/_{L}\right) + {}^{SL}/_{D}\,\sinh\left({}^{d}/_{L}\right)}\right), \text{for } \frac{1}{\alpha} \ll d \;\&\; \text{superstrate} \tag{8}$$

The influence of a frontside texturing (e.g. textured anti-reflection foil) on the collection efficiency is to change the generation profile. It is possible to correct for this by replacing $\alpha$ in eq. (7)-(8) by $\alpha/\cos\theta$, where $\theta$ is the average angle, relative to the normal, of the light upon entering the silicon [39].

For $d \approx 10$ µm, the $1/\alpha \ll d$ condition for eq. (7) and (8) translates too $\lambda <$ ~600 nm and the $1/\alpha \gg d$ condition for eq. (6) translates to $\lambda >$ ~900 nm. The $\eta_c$ values for the intermittent wavelengths were obtained by fitting the calculated $\eta_c$ values with a hyperbolic tangent function:

$$\eta_c = A\tanh\big(B(\lambda - C)\big) + D\,, \tag{9}$$

where $A$, $B$, $C$ and $D$ are fitting parameters. $A$ equals the difference of $\eta_c$(300 nm) and $\eta_c$(900 nm) and $D$ equals the average of $\eta_c$(300) and $\eta_c$(900). It was determined empirically that $C$ is a value between 500 and 650 nm and $B$ is a value between 0.01 and 0.03. The tanh function was chosen for fitting because of the tanh functions in eq. (6)-(8) and because it results in a good fit, as will be shown in the next section.

### 2.7.3 Calculated $\eta_c$: Example

Figure 2-6 illustrates the $\eta_c$ equations (3)-(8): Figure 2-6a shows $G(x)$, for light coming from the interlayer side (superstrate), and the collection probability $f_c(x)$, for 4 different combinations of $L$ and $S$. $G(x)$ was normalized in such a way that it shows the fraction of the incoming light absorbed each µm, e.g. for $\lambda$ = 900 nm, ~2-3 % of the incoming light is absorbed each µm. For the solid curves, the recombination is completely $L$-limited ($S$ = 1 cm/s) and for the dashed curves, the recombination is completely $S$-limited ($L$

= 1 mm). For the light blue *L*-limited curve $L_{eff} = L$ = 20 µm and for the dark blue *L*-limited curve $L_{eff} = L$ = 10 µm. For the *S*-limited curves, *S* was chosen such that the effective diffusion length ($L_{eff}$) equals 20 µm (light blue) or 10 µm (dark blue), where $L_{eff}$ is given by [41]:

$$L_{\mathrm{eff}} = \sqrt{D\left(\frac{D}{L^2} + \frac{S}{d}\right)^{-1}}. \tag{10}$$

The other input parameters were $d$ = 10 µm and $\mu$ = 317 cm$^2$/Vs (corresponding to $10^{17}$ cm$^{-3}$ doped n-type c-Si). By using eq. (5), i.e. multiplying the $f_c$ and $G$ curves in Figure 2-6a for $\lambda$ < 600 nm, integrating over $x$ from 0 to $d$ and normalizing by the total generation (eq.(8)), the superstrate $\eta_c$ values (orange dots) for $\lambda$ < 600 nm in Figure 2-6b were obtained. By doing the same with $G(x)$ curves for light coming from the emitter side (not shown) (eq. (7)), the $\eta_c$ values (green dots) for $\lambda$ < 600 nm in Figure 2-6b were obtained. $G(x)$ for 900 nm is approximately uniform, so by doing the same for a uniform $G(x)$ (eq. (6)) the $\eta_c$ values (black dots) for $\lambda$ = 900 nm, for both substrate and superstrate configuration, in Figure 2-6b were calculated. The lines connecting the calculated $\eta_c$ values in Figure 2-6b were obtained with the tanh fitting eq. (9). It can be seen that this tanh equation results in a good fit.

It can be seen that the *L*- and *S*- limited $f_c$ curves (blue, Figure 2-6a) with the same $L_{eff}$ are quite similar, except close to the interlayer ($x = d$). It can be seen from the $G$(x) curves in Figure 2-6a that the short wavelength light is absorbed completely within several µm after entering the c-Si. Therefore, $\eta_c$(300 nm) ≈ $f_c(0)$ = 1 for light coming from the emitter side (substrate), while $\eta_c$(300 nm) ≈ $f_c(d)$ for light coming from the interlayer side (superstrate). Therefore, the large $f_c(d)$ difference for the *S*- and *L*- limited curves results in large differences between the *L*- and *S*- limited superstrate $\eta_c$ curves, but almost no difference for the substrate curves.

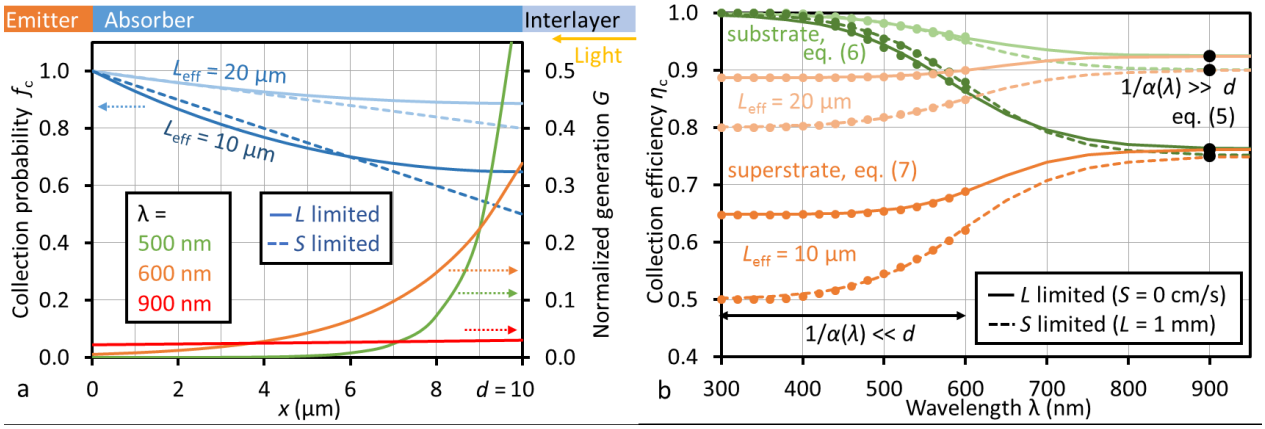


**Figure 2-6.** Fig. a shows the *L*-limited (solid, $S$ = 1 cm/s) and *S*-limited (dashed, $L$ = 1 mm) collection probability ($f_c$) for $L_{eff}$ = 10 µm (dark blue curves) and $L_{eff}$ = 20 µm (light blue curves). It also shows the generation rate $G$(x) for light coming from the interlayer side, normalized such that it shows the fraction of the incoming light absorbed per µm, for $\lambda$ = 500 (green), 600 (orange) and 900 (red) nm. Fig. b shows the collection efficiency ($\eta_c$) for $\lambda$ < 600 nm for superstrate (orange dots) and substrate (green dots) and for $\lambda$ > 900 nm (black dots), calculated from the $f_c$ curves in Fig. a, using the equations referred to in Fig. b. The lines connecting the dots are fitted using the tanh function in eq. (9).

In principle, it is possible to obtain a best fit of the measured substrate or superstrate $\eta_c$ for a unique combination of $L$ and $S$, due to the difference in shape. However, in practice this is only (approximately) possible for cells with a very low $\eta_c$, i.e. very low $L_{eff}$. This changes when simultaneously fitting the measured substrate and superstrate collection efficiency for (bifacial) cells as is done in appendix A.4. If these measurements are not available or possible, it is still possible to estimate the $L_{eff}$ by fitting the measured $\eta_c$ by an *L*-limited and *S*-limited curve and taking the average of both $L_{eff}$ values as will be done in section 3.3.1, 4.1.5 and 5.8. Aside from estimating the $L_{eff}$, the fitted $\eta_c(\lambda)$ will be used to determine the photocurrent loss due to recombination in the bulk and at the interlayer interface. Finally, the $\eta_c$ equations will be used in section 5.8 to estimate the optimum absorber thickness for various $L_{eff}$ values.

# 3 Development of PECVD Interlayers and Precursors using FrontERA Cells

*In this chapter, bifacial, interdigitated FrontERA cells are used to evaluate interlayers and precursor material deposited by plasma enhanced chemical vapor deposition (PECVD) on 3.3 mm BOROFLOAT33 glass substrates. These layers are compared to the standard material, consisting of interlayers deposited by RF magnetron sputtering (physical vapor deposition, PVD), and precursors deposited by electron-beam (e-beam) evaporation. Section 3.1 introduces the LPC-Si development leading up to the research in this chapter. Section 3.2 presents the material and FrontERA cell preparation. In section 3.3 the PECVD material is compared to the PVD/e-beam material, investigating the J-V parameters, absorber doping dependence, grain boundary recombination and shunting behavior. Finally, it is shown how the PECVD material resulted in p- and n-type LPC-Si cells with record efficiencies.*

## 3.1 Introduction

Liquid phase crystalized silicon (LPC-Si) consists of a glass substrate, an interlayer stack and a 5-20 µm c-Si absorber, which is crystallized over a liquid phase by melting a silicon precursor layer with a line shaped energy source. In ref. [19], Amkreutz et al. sputtered 500 nm $SiC_x$:B interlayers on 1.1 mm Corning Eagle XG [42] glass substrates , followed by a 8-13 µm nc-Si precursor deposition by low pressure CVD (LPCVD) at 670 °C. These samples were then crystallized using a line-shaped e-beam. Heterojunction test cells were made on this material, resulting in a highest $V_{OC}$ of 545 mV and $\eta$ of 4.7 %. In ref. [43], Dore et al. found that the $SiO_x$ layer is the best diffusion barrier for impurities from the glass and $SiN_x$ is the best anti-reflection layer. Subsequently, they deposited $SiO_x$ and $SiN_x$ layer stacks by sputtering or PECVD on 3.3 mm Schott BOROFLOAT33 [44] ("Boro33") substrates, combining the best properties of both layers. This was followed by a precursor deposition using e-beam evaporation and crystallization using a line shaped laser beam [45]. It was found that by adding a 15 nm thin $SiO_x$ layer on the $SiN_x$ anti-reflection layer, it is possible to obtain both high $V_{OC}$ and $J_{SC}$. Using a 80/70/15 nm $SiO_x$/$SiN_x$/$SiO_x$ (O/N/O) intermediate layer and point contact cells with diffused homo-emitter, a $V_{OC}$ of 557 mV, $J_{SC}$ of 24.2 mA/cm$^2$ and $\eta$ of 8.4 % were obtained. In ref. [46], Haschke (and Amkreutz) et al. deposited a 200 nm $SiO_x$ and 7-10 $SiC_x$ intermediate layer on a Corning substrate, followed by e-beam evaporation and crystallization of the precursor. Recombination at the interlayer interface was very high, resulting in low $J_{SC}$ for illumination through the glass (superstrate configuration). Therefore, a cell design was developed which allows for illumination through the contacted side (substrate configuration), while minimizing shading losses, by stacking the contact finger grids on top of each other (separated by an insulator). Using these frontside-contacted heterojunction cells on e-beam recrystallized absorbers ("FrontERA") a maximum $V_{OC}$ of 582 mV and $\eta$ of 5.7 % were obtained (on different cells). In ref. [47], Amkreutz et al. deposited 200 nm $SiO_x$ (instead of

$SiC_x$) interlayers on Corning glass substrates by PECVD, followed by e-beam evaporation and crystallization of the precursor. Using FrontERA cells, a $V_{OC}$ of 577 mV and $\eta$ of 7.8 % were obtained. In ref. [20], Dore et al. used PVD O/N/O interlayers on Boro33 substrates with e-beam precursors, laser crystallization and point contact cells to achieve a $V_{OC}$ of 585 mV and initial $\eta$ of 11.7 %. This efficiency degraded to 10 % due to a contact resistance problem. All cell results presented thus far were made on p-type absorber material. By using n-type absorber doping, PVD O/N/O interlayers on Corning substrates, e-beam deposition and crystallization of the precursors, and FrontERA cells, Haschke and Amkreutz et al. obtained a highest $V_{OC}$ of 656 mV [25] and stable $\eta$ of 11.8 % [22]. These latter cells were fabricated during the same time period as the cells described in this chapter.

The heterojunction cells on Corning substrates and e-beam crystallized absorbers by Amkreutz and Haschke et al. ([19], [22], [25], [46]) were made at the Helmholtz Zentrum Berlin (HZB), while the homojunction cells on Boro33 substrates and laser crystallization by Dore et al. ([20], [43], [45]) were made at the University of New South Wales (UNSW). The efficiency progress at both institutes leading up to the results in this chapter is summarized in Figure 3-1a (UNSW) and b (HZB).

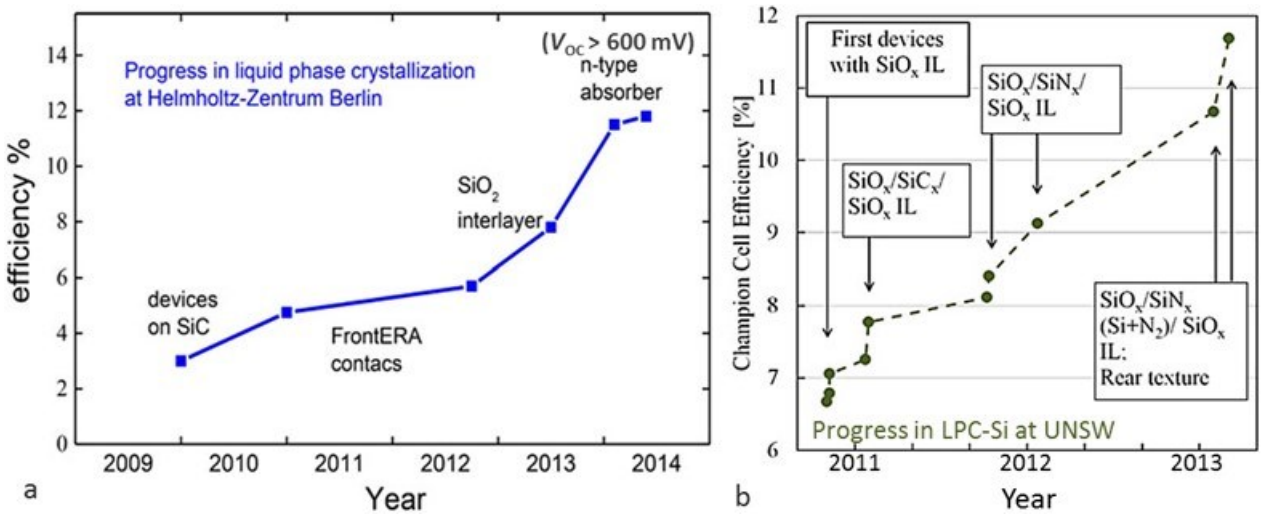


**Figure 3-1.** Chronological summary of the LPC-Si efficiency development at HZB (a) and UNSW (b), including the most important developments resulting in the efficiency improvements. Fig. a was copied from ref. [20] and fig. b was copied from ref. [22].

Except for [19], all of the above cells used a precursor deposited by e-beam evaporation and most cells used interlayers deposited by PVD. E-beam evaporation allows for high rate (~0.5 µm/min) deposition of hydrogen-free silicon and therefore appears very well suited for the precursor deposition. However, no large scale, commercial e-beam evaporation tools have been developed and various challenges exist to develop such a tool. In contrast, PECVD is a well-developed technology used in large scale fabrication of thin film silicon PV modules [6]. Also, it was speculated that deposition of the interlayers and precursor in

the PECVD without vacuum brake, might reduce contamination. In this chapter FrontERA cells are used to evaluate the development of a large scale (30x30 $cm^2$) PECVD interlayer and precursor deposition process, comparing it to the standard PVD/e-beam material. In contrast to the first FrontERA cells [46], crystallization was performed using a line-shaped laser and during the measurements the cells were illuminated through the glass.

## 3.2 Material and Cell Preparation

### 3.2.1 PVD/E-Beam Material

The 100/80/10 nm $SiO_2/SiN_x/SiO_2$ interlayers were deposited by RF (13.56 MHz) magnetron sputtering (PVD) on 1.1 mm Corning Eagle XG substrates. The PVD process takes place at room temperature and a pressure of approximately 1 Pa, using $O_2$ or $N_2$ as a reactant gas. Subsequently, 10-11 µm c-Si precursor layers were deposited by e-beam evaporation with a substrate temperature of 600 °C and a deposition rate of ~0.5 µm/min. Doping was provided during the deposition by a Boron effusion cell heated to 1485-1615 °C for a corresponding (p-type) dopant concentration of $10^{16}$-$10^{17}$ $cm^{-3}$.

Laser crystallisation was performed with a continuous wave, infrared (808 nm), line-shaped laser with a width of 30 mm from Lissotschenko Mikrooptik GmbH in an air atmosphere, using a scanning velocity of 3 mm/s [48]. The rapid, high temperature (> 1400 °C) LPC process results in large thermal stresses [49], which result in bending and even breaking of the Corning substrates. In order to reduce this stress, the samples were annealed at 960°C for 1 min, directly after the crystallization (Corning glass has a softening point of 970 °C). This was followed by a 1 min etch in 30:10:1:15 $HNO_3$(65%):$H_3PO_4$(85%):HF(50%):$H_2O$ (poly-Si etch) [50] and a hydrogen plasma passivation (HPP) at 600 °C for 15-45 min [47]. Finally, the samples were again etched with poly-Si etch for 1 min to remove the damage from the HPP and they were cleaned using a standard RCA procedure, removing metal and organic contamination [51].

### 3.2.2 PECVD Material

The PECVD interlayers and precursors were deposited with an industrial type AKT1600 PECVD cluster tool on 30x30 $cm^2$ substrates, using $SiH_4$, $H_2$, $CO_2$ and $N_2$ as process gasses [52]. Contrary to the PVD/e-beam material, all PECVD material was deposited on 3.3 mm Schott BOROFLOAT 33 substrates. This is because no PECVD recipe was found that resulted in successful crystallization of PECVD precursors on 1.1 mm Corning Eagle XG glass. The used recipes are shown in Table 3-1. The AKT has an electrode area of 1800 $cm^2$ and an RF frequency of 13.56 MHz, as indicated in the table.

Initially it was attempted to reproduce the 100/80/10 nm O/N/O PVD interlayer stack. However, for reliable and repeatable adhesion, it was found necessary to deposit a 10-20 nm $SiN_x$ layer between the

glass substrate and the $SiO_2$ diffusion barrier [52]. Furthermore, the 70/10 nm $SiN_x/SiO_2$ stack was replaced by an $SiO_xN_y$ layer, partly because this resulted in better wetting and adhesion [52] and partly for electrical reasons (see results in section 3.3.1).

The PECVD a-Si:H precursors, deposited at 400 °C, have a high Si-H content of 10-15 %, as determined by Raman Spectroscopy [52]. This hydrogen has to be removed in order to prevent "explosive" effusion of the hydrogen during the liquid phase crystallization. Therefore the samples were annealed for 8/8/8 hours at 450/550/650 °C (>24 hours total), which also resulted in a solid phase crystallization of the precursor. For earlier precursors recipes, the high hydrogen content (15 - 25 %) and/or low density of the precursor resulted in cracks in the absorber after annealing. It was found that a higher deposition rate generally results in a higher hydrogen content and therefore more cracks. All process parameters were varied until a precursor recipe was found (Table 3-1) with a reasonable deposition rate of ~0.74 nm/s (0.044 µm/min), which did not result in cracks after the annealing process.

**Table 3-1.** PECVD (AKT) interlayer & precursor recipes.

| Tool | layer | T (°C) | Power (W) | Pressure (Torr) | Spacing (mm) | $SiH_4$ (sccm) | $H_2$ (sccm) | Other gas (sccm) | Dep. rate (nm/s) |
|---|---|---|---|---|---|---|---|---|---|
| **AKT, ~1800 cm², 13.56 MHz** | **$SiO_x$** | 400 | 600 | 1 | 16.5 | 4 | 200 | 100 ($CO_2$) | 0.24 |
| | **$SiN_x$** | 400 | 250 | 1 | 16.5 | 10 | - | 1200 ($N_2$) | 0.35 |
| | **$SiO_xN_y$** | 400 | 600 | 1 | 16.5 | 10 | 200 | 20 ($CO_2$) / 500 ($N_2$) | 0.49 |
| | **a-Si** | 400 | 100 | 2.5 | 15.2 | 200 | 1000 | - | 0.74 |

Doping was provided by adding doping gas to the final stage of the precursor deposition. For a ~10 µm thick precursor, a ~85 nm layer with 2-8 sccm diluted TMB gas (2 % in $H_2$) was used for a p-type absorber dopant concentration of ~$2\text{-}8\cdot10^{16}$ $cm^{-3}$. For n-type, a ~15-60 nm layer with 2 sccm diluted $PH_3$ (2 % in $H_2$) was used for a dopant concentration of ~$2\text{-}8\cdot10^{16}$ $cm^{-3}$.

Laser crystallization was performed with a scanning velocity of 3-10 mm/s. The 960 °C (1 min) annealing that was used for reducing stress in the Corning substrates is not necessary for the thicker Boro33 substrates. Instead of bending and breaking the glass substrate, the thermal stress created by the LPC process results in long cracks in the LPC-Si absorber, parallel to the crystallization direction [49].

Crystallization was followed by the HPP, poly-Si etching and RCA cleaning process, as described in section 3.2.1. Instead of the poly-Si etch, some samples were textured by etching with an 80 °C potassium hydroxide (KOH) based etch, removing 1-3 µm of c-Si. KOH anisotropically etches silicon with the highest rate for <100> oriented c-Si and the lowest for <111> crystal orientations [53]. Therefore, it creates tilted pyramids with <111> oriented facets and the pyramid tilt depending on the grain orientation.

### 3.2.3 FrontERA Cells

After the RCA cleaning, a thin silicon oxide remains, which was removed in 1 % HF directly before depositing the silicon heterojunction (SHJ) emitter. The SHJ emitter consisted of a 5-10 nm a-Si(i):H layer, which passivates the c-Si/a-Si interface, and a 10-15 nm a-Si(p/n):H layer, which induces a p-n junction in the n-/p-type c-Si [54], [55]. Table 3-2 shows the a-Si(i/p/n):H emitter recipes used in this chapter, deposited with two different PECVD tools, referred to as 'AKT' (see section 3.2.2) and 'FAP' [56]. The doping gas consisted of $PH_3$ for the n-type layers and TMB (AKT) or $B_2H_6$ (FAP) for the p-type layers, all diluted 50:1 in $H_2$.

**Table 3-2.** AKT and FAP PECVD emitter recipes.

| Tool (name, electrode area, freq.) | layer | T (°C) | Power (W) | Pressure (Torr) | Spacing (mm) | $SiH_4$ (sccm) | $H_2$ (sccm) | doping gas (sccm) | Dep. rate (nm/s) |
|---|---|---|---|---|---|---|---|---|---|
| **AKT, ~1800 cm², 13.56 MHz** | **a-Si(i)** | 205 | 30 | 1.5 | 16.5 | 180 | 900 | - | 0.13 |
| | **a-Si(p)** | 205 | 30 | 2 | 20.3 | 55 | 540 | 90 (TMB) | 0.20 |
| | **a-Si(n)** | 185 | 120 | 1.5 | 15.2 | 75 | 645 | 50 ($PH_3$) | 0.25 |
| **FAP, ~280 cm², 60 MHz** | **a-Si(i)** | 170 | 10 | 0.38 | 30 | 10 | 0 | - | ~0.3 |
| | **a-Si(p)** | 150 | 10 | 0.38 | 23 | 10 | 0 | 2 ($B_2H_6$) | |
| | **a-Si(n)** | 150 | 10 | 0.38 | 23 | 10 | 0 | 2 ($PH_3$) | |

For the p-type FrontERA cells, the procedure from ref. [46] was followed, resulting in the cross-section and top view shown in Figure 3-2a and c. First the 5-10 nm a-Si(i) layer was deposited. This was followed by the deposition of a 1 µm thick Al absorber contact grid, using e-beam evaporation through either a lithographic lift-off mask or a metal shadow mask. The latter process was developed as part of this thesis in order to save time and reduce complexity. Subsequently, a photoresist (AZ 4533 [57]) was spin-coated on the sample and structured by photolithography. This resist acts as an insulator, which both defines the cell area and isolates the absorber contact from the emitter contact. The insulator has to be annealed for 30 min at 200 °C to make it insensitive to UV light. During this annealing step the a-Si(i) layer diffuses into the Al, resulting in a low resistivity absorber contact [58]. This was followed by the a-Si:H(n) emitter deposition and RF magnetron sputtering (at room temperature) of an ~80 nm $In_2O_3$:Sn (ITO) layer. Finally, the Ti-Ag emitter contact grid was evaporated through a shadow mask. Each 5x5 $cm^2$ sample contains nine 0.6 $cm^2$ FrontERA cells.

For the n-type FrontERA cells, the procedure from ref. [25] was followed, resulting in the cross-section and top view shown in Figure 3-2b and c. First the 5-10 nm a-Si(i) and ~10-15 nm a-Si(p) layers were deposited The Al does not result in a good absorber contact to the $10^{16}$-$10^{17}$ $cm^{-3}$ doped c-Si(n) and therefore a 10 nm Ti contacting layer was used, followed by a 1 µm Ag layer for lateral conductivity. Ti is generally used for

contacting (highly doped) c-Si(n) emitters, but should be annealed at T > 400° C to form $TiSi_2$ for obtaining a low contact resistivity [59]. As this is not possible without damaging the heterojunction emitters, the c-Si/Ti contact resistivity causes a significant resistance [60]. Subsequently, the lithographic lift-off mask is applied and first used as etch mask to locally remove the emitter layers. This etch mask has an undercut of several µm and the subsequent Ti/Ag deposition by e-beam evaporation is highly directional. This leaves a small (isolating) gap between the Ti/Ag absorber contact and the emitter. The deposition of the absorber contact was followed by the insulator resin, ITO and Ti/Ag contact grid depositions as described above for the p-type cells.

The width of the metal contact is ~44 µm and the distance between the grid fingers is 666 µm, resulting in a contact area fraction of approximately 6.6 %. The gaps on both sides of the contact have a width of about 25 µm each, resulting in an emitter area fraction of approximately 86 %.

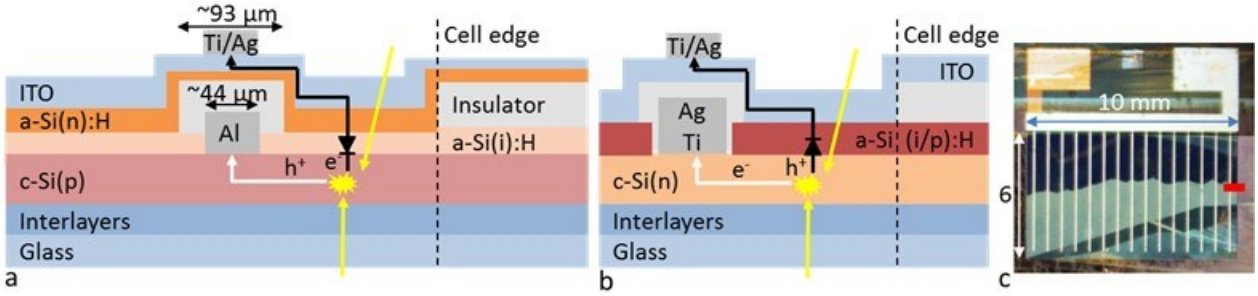


**Figure 3-2.** The figures show FrontERA cross sections for c-Si(p) (a) and c-Si(n) (b) absorbers, as well as a top view image (c) which is identical for both configurations. The arrows in the cross-section indicate that the cell can be illuminated from both sides and indicate the current flow of the generated majority carriers (white arrow) and minority carriers (black arrow). The red line in the top view indicates the position of the cross section and the cell dimensions are given in mm. The left contact pad in the top view image connects to the absorber contact and the right contact pad connects to the TCO. The top-view image is of a KOH textured absorber and the different intensities in the cell area are due to reflection differences, caused by different orientations of the etched pyramids, caused by different crystal orientations of the grains.

## 3.3 Results

### 3.3.1 Comparison of Cells on p-type PECVD and PVD/E-Beam Material

In order to compare PECVD material with PVD/e-beam material, FrontERA cells were fabricated on the following p-type, $(5 \pm 1)\cdot 10^{16}$ $cm^{-3}$ doped, planar LPC-Si absorbers:

- PVD-1: Corning + 100/80/10 nm **O**/**N**/**O** (**PVD**) interlayers + 10-11 µm (**e-beam**) absorber,
- PECVD-1: Boro33 + 150/70/10 nm **O**/**N**/**ON** interlayers + 4-4.5 µm (**PECVD**) absorber,
- PECVD-2: Boro33 + 20/100/80 nm **N**/**O**/**ON** interlayers + 8-9 µm (**PECVD**) absorber (2 samples).

The PECVD precursors were crystallized with a laser velocity of 10 mm/s. The emitter consisted of a 5 nm 'FAP' a-Si(i) layer and a 13 nm 'AKT' a-Si(n) layer. The standard FrontERA process described in ref. [46] was

used.

Figure 3-3 shows the *J-V* parameters for these three samples, measured in superstrate configuration, without reflector. It can be seen that the $V_{OC}$ and $J_{SC}$ of the PVD-1 and PECVD-1 samples (which both have an ONO interlayer stack) is very similar, while the $V_{OC}$ and $J_{SC}$ of the PECVD-2 sample are ~10 mV and ~2 mA/cm$^2$ higher. It can also be seen that the *FF* and $R_{parallel}$ of the PECVD samples are lower than for the PVD-1 sample, indicating that the PECVD samples have more shunts. As a result of the higher $V_{OC}$ and $J_{SC}$, but lower *FF*, $\eta$ is approximately equal for the PECVD-2 and PVD-1 samples.

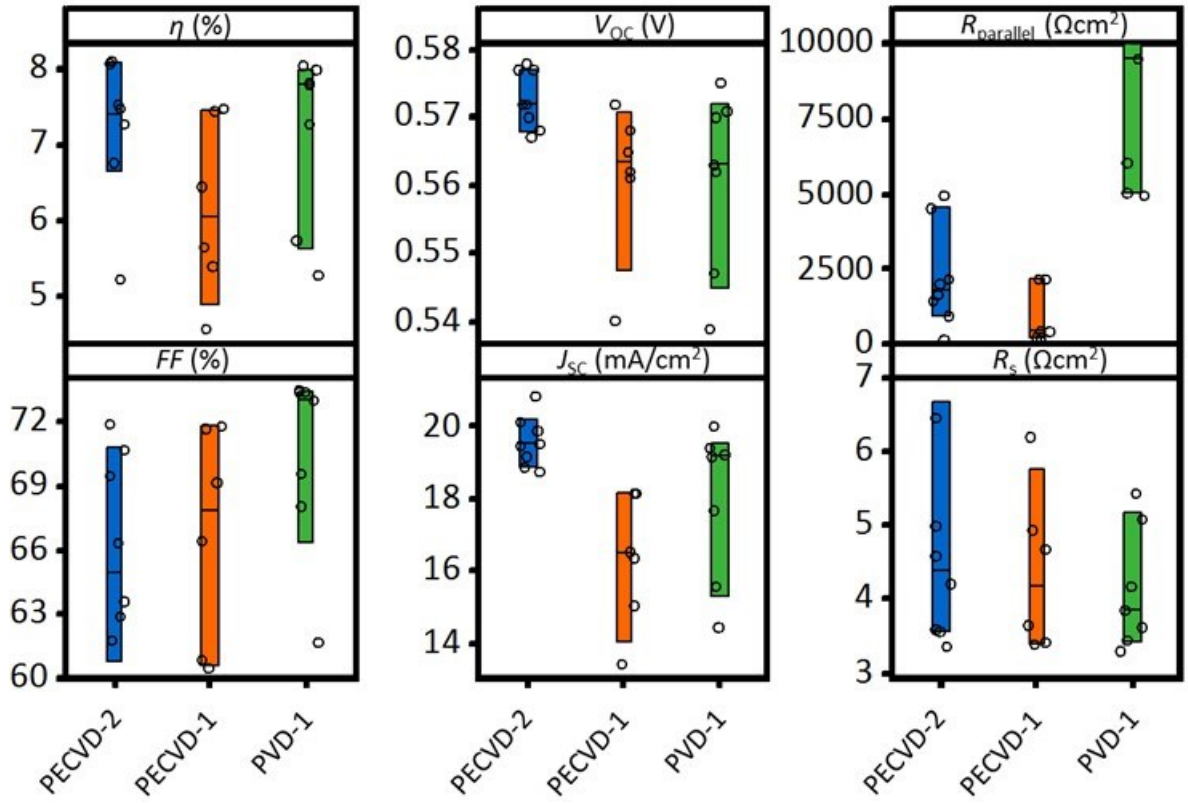


**Figure 3-3.** Boxplots of the *J-V* parameters of 3 planar, 5·10$^{16}$ cm$^{-3}$ doped, p-type, FrontERA cells fabricated on an NO(ON) interlayer + 8-9 µm PECVD absorber (PECVD-2), an ON(ON) interlayer + 4-4.5 µm PECVD absorber (PECVD-1) and an ONO interlayer + 10 µm e-beam absorber (PVD-1). Each open circle represents a cell.

The best cells for each sample were measured with an opaque white paper reflector and a textured anti-reflection foil (ARF) by DSM advanced surfaces [32]. Figure 3-4 shows the *J-V* curves and parameters for these measurements. It can be seen that the $J_{SC}$ gain from the reflector decreases from 20 % to 11 % for an increasing absorber thickness from 4 to 10 µm. All samples gained an additional 13-14 % from the ARF. The increasing $J_{SC}$ also resulted in a small $V_{OC}$ gain. A more detailed analysis of the reflector and ARF is presented in the next chapter. The $\eta$ of 10.8 % and $V_{OC}$ of 601 mV were one of the highest LPC-Si efficiencies

and the highest $V_{OC}$ for a p-type LPC-Si cell at the time, indicating the high quality of the PECVD material (presented in [61] and published in [52]).

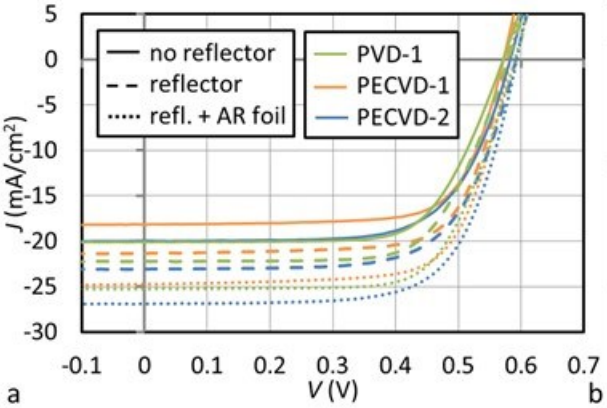


| Material | Optics | $J_{SC}$ (mA/cm²) | | $V_{OC}$ (V) | $\eta$ (%) |
|---|---|---|---|---|---|
| PVD-1: ONO + 10 µm c-Si | - | 20.1 | +11% | 0.571 | 7.8 |
| | Reflector | 22.2 | +14% | 0.579 | 8.7 |
| | Refl. + ARF | 25.2 | | 0.590 | 10.2 |
| PECVD-1: ON(ON) + 4-4.5 µm c-Si | - | 18.1 | +20% | 0.572 | 7.5 |
| | Reflector | 21.9 | +13% | 0.578 | 9.0 |
| | Refl. + ARF | 24.8 | | 0.582 | 10.0 |
| PECVD-2: NO(ON) + 8-9 µm c-Si | - | 20.2 | +14% | 0.577 | 8.1 |
| | Reflector | 23.1 | +14% | 0.591 | 9.1 |
| | Refl. + ARF | 26.3 | | 0.601 | 10.8 |

**Figure 3-4.** *J-V* curves (a) and parameters (b) for the best cells made on the different interlayer + absorber stacks measured without (solid) and with a white paper reflector, without (dashed) and with (dotted) textured anti-reflection foil (ARF). The table also shows the relative $J_{SC}$ gains by the reflector and ARF.

Figure 3-5a shows the *EQE* and 1-Reflectance (1-*R*) for the cells from Figure 3-4, measured with white reflector, the small spot *EQE* and a bias light intensity of approximately 0.1 suns (see section 2.4). Figure 3-5b shows the *IQE* of the cells in fig. a and the fitted collection efficiency ($\eta_c$) curves, using the equations from section 2.7. The effective diffusion length ($L_{eff}$), corresponding to the fitted $\eta_c$, is shown in the figure.

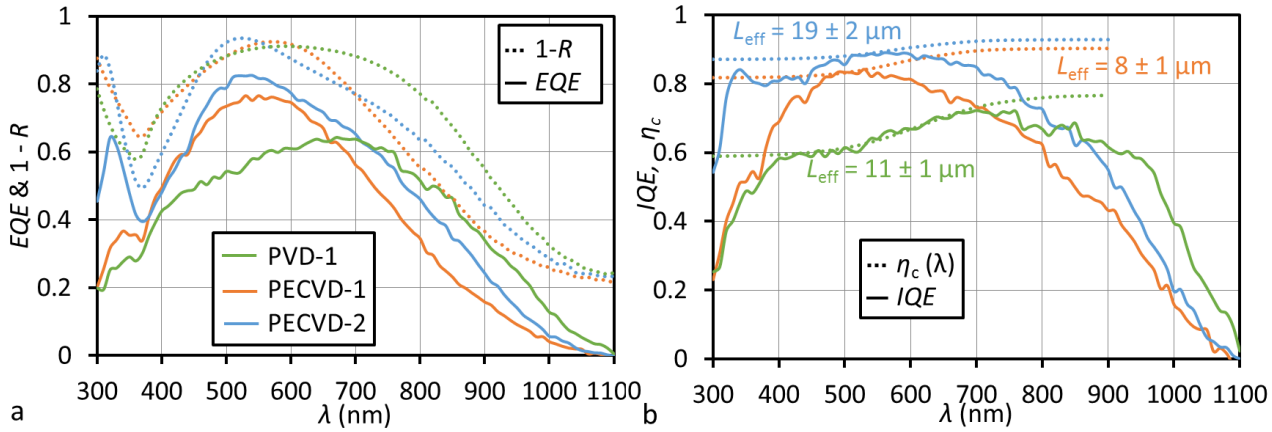


**Figure 3-5.** Fig. a shows the *EQE*, 1-Reflectance (1-*R*) of cells from Figure 3-4, measured with white reflector, the small spot *EQE* and a bias light intensity of approximately 0.1 suns. Fig. b shows the *IQE*, fitted collection efficiency ($\eta_c$), and effective diffusion length ($L_{eff}$) using the equations from section 2.7. The uncertainties indicate the difference between the $L_{eff}$ values determined from the *L*- and *S*-limited $\eta_c$ curves (not shown).

It can be seen that, for λ > 700 nm, the *EQE*, 1-*R* and *IQE* values increase with increasing absorber thickness. It can be seen that the fitted $L_{eff}$ is approximately equal for the PVD-1 and PECVD-1 cells, but significantly higher for the PECVD-2 cell. This fits with the higher $V_{OC}$ and $J_{SC}$ for the PECVD-2 sample. The lower *IQE* of the PVD-1 cell than for the PECVD-1 cell, despite the similar $L_{eff}$, is due to its larger absorber thickness. For

λ < 400 nm, the *IQE* of the PVD-1 and PECVD-1 cells is lower than for the NO(ON) cell. This can be explained at least partly by parasitic absorption in the 70-80 nm $SiN_x$ layers (e.g. [62]).

### 3.3.2 Absorber Doping Experiments

In this section the absorber doping dependence of the *J-V* parameters for p-type FrontERA cells on PVD/e-beam material will be compared to the absorber doping dependence for p- and n-type FrontERA cells on PECVD material. In order to determine the optimum absorber doping, ONO PVD/e-beam samples with four different absorber doping concentrations (i.e. carrier densities (*N*)) were fabricated, one of which was the PVD-1, $(5 \pm 1)\cdot10^{16}$ $cm^{-3}$ doped sample from the previous section. *N* was measured by Hall effect measurements, using 0.25 $cm^2$, square van der Pauw structures, which were fabricated as part of the FrontERA samples. The other *N* were $(1 \pm 0.2)\cdot10^{16}$, $(2 \pm 0.5)\cdot10^{16}$ and $(1 \pm 0.2)\cdot10^{17}$ $cm^{-3}$. The *J-V* parameters are shown in Figure 3-6, measured in superstrate configuration and without reflector.

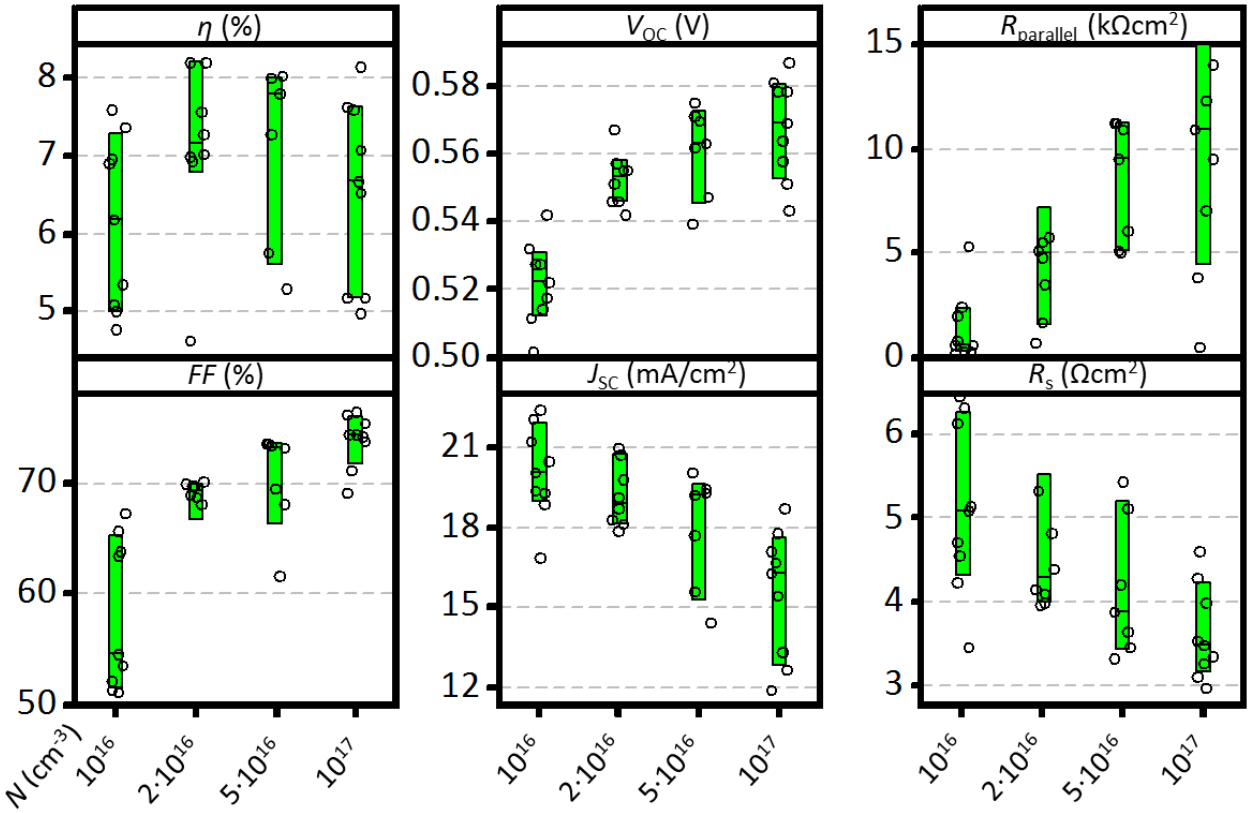


**Figure 3-6**. Boxplots of the *J-V* parameters of 4 FrontERA samples with PVD ONO interlayers and planar, 10-11 µm thick absorbers, with carrier densities $N = 10^{16}$ - $10^{17}$ $cm^{-3}$ as indicated in the figure. Each open circle represents a cell.

It can be seen that the $V_{OC}$ increases with increasing *N* (results published in [21]). It can also be seen that the $J_{SC}$ and $R_s$ decrease and the *FF* and $R_{parallel}$ increase for increasing *N*. For this interlayer stack, absorber

thickness, doping type, cell type and superstrate configuration, the optimum $N$ appears to be approximately $2 \cdot 10^{16}$ cm$^{-3}$.

The increasing $V_{OC}$ can be explained by the logarithmic dependence of the built-in-potential on $N$. The decrease of the $J_{SC}$ can be explained by a decrease of the minority mobility ($\mu$) [38] and perhaps a decreasing effective lifetime ($\tau_{eff}$) for increasing $N$, which both result in a lower $L_{eff}$. Contact resistance measurements, using TLM structures which are part of the FrontERA samples, show that the absorber contact resistivity is smaller than 0.1 Ω cm$^2$ (for all $N$), similar to the contact resistivity determined for this contact type in ref. [63]. The decreasing $R_s$ for increasing $N$ can therefore be explained by the decreasing sheet resistance of the c-Si absorber. The increasing $R_{parallel}$ for increasing $N$ is unexpected, as both bulk and contact resistances generally decrease for increasing $N$. Test cells on ONO (PVD) interlayers with n-type (e-beam) absorbers in ref. [25] show a similar $V_{OC}$ and $J_{SC}$ dependence on $N$.

In order to determine if the same optimum applies to the PECVD NO(ON) interlayer stack, $N$ was varied in the following two experiments:

- p-type: $N = (4 \pm 0.5) \cdot 10^{16}$ and $(7 \pm 1) \cdot 10^{16}$ cm$^{-3}$, using a 10/200/85 nm $SiN_x/SiO_x/SiO_xN_y$ interlayer stack, a planar, 8-9 µm thick absorber, crystallized 10 mm/s LPC velocity and a 9/13 nm a-Si(i/n) 'AKT' emitter.
- n-type: $N = (3 \pm 0.5) \cdot 10^{16}$ and $(9 \pm 1) \cdot 10^{16}$ cm$^{-3}$, using a 20/100/80 nm $SiN_x/SiO_x/SiO_xN_y$ interlayer stack, a textured, ~11 µm thick absorber, 3 mm/s LPC velocity, 9 nm a-Si(i) + $H_2$ plasma + 13 nm a-Si(p) (TMB) 'AKT' emitter.

The resulting $J$-$V$ parameters are shown in Figure 3-7. It can be seen that for the p-type cells, the $V_{OC}$, $R_{parallel}$, $R_s$ and $FF$ dependence is similar to that of the p-type ONO cells (Figure 3-6). The only qualitative difference is that the $J_{SC}$ does not appear to decrease for increasing $N$, resulting in a highest $\eta$ for $N = 7 \cdot 10^{16}$ cm$^{-3}$. A similar $J_{SC}$ dependence was observed on test cells (not shown).

For the n-type cells, the $V_{OC}$ also increases for increasing $N$. Same as for the p-type NO(ON) cell, the $J_{SC}$ appears to be unaffected or even increase with increasing $N$, resulting in a highest $\eta$ for $N = 9 \cdot 10^{16}$ cm$^{-3}$. A similar $J_{SC}$ dependence was observed on test cells (not shown).

Contrary to the p-type cells, for the n-type cells $R_{parallel}$ decreases for increasing $N$ and is generally at a much lower value (i.e. cells are more shunted). $R_s$ is much higher than for the p-type cells and decreases much more steeply with increasing $N$. It should be noted that the $J$-$V$ curve is S-shaped around $V_{OC}$ and the $R_s$ should be considered as more of a qualitative parameter.

The sheet resistance of the n-type absorbers is 3-6 times lower than for p-type cells, mainly due to their 2-4 times higher mobility for the same $N$ (appendix A.3). Therefore the higher $R_s$ of the n-type cells cannot be due to the lateral resistance in the absorber. It might be partly due to the emitter/TCO resistance, but considering the dependence on $N$, $R_s$ is probably mostly caused by the c-Si(n)/Ti contact resistance as was also determined the n-type FrontERA cell in ref. [60].

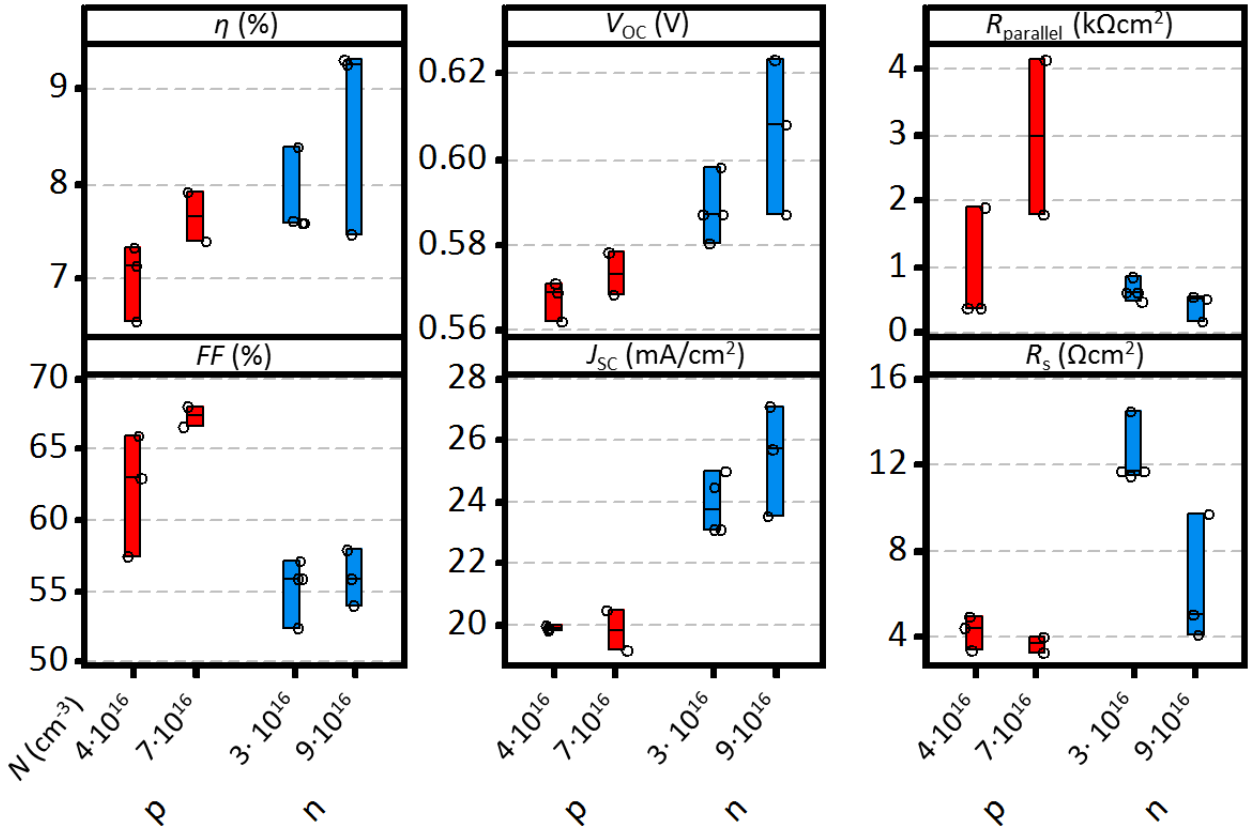


**Figure 3-7.** Boxplots of the *J-V* parameters of 2 p-type and 2 n-type FrontERA samples on PECVD absorbers with NO(ON) interlayers, with different carrier densities $N$. Each open circle represents a cell.

### 3.3.3 Grain Boundaries and Glass Bubbles

Figure 3-8a shows LBIC images of a p-type PVD and PECVD cell from section 3.3.1, an n-type PECVD cell from section 3.3.2 and an n-type PVD test cell (from ref. [21]), all measured with the λ = 532 nm laser. It can be seen that the Corning/PVD/e-beam cells have many grain boundaries with strongly reduced collection, in contrast to the Boro33/PECVD cells. Many more LBIC measurements of PVD and PECVD cells were made and they all show this difference in the electrical activity at the grain boundaries (e.g. [21], [28], [64], [65]). A photoluminescence (PL) and SEM analysis of recombination at grain boundaries and grain boundary related dislocations is presented in ref. [24].

In order to determine if this difference in grain boundary related recombination was caused by the different glass, interlayers or precursor (and corresponding annealing processes), 5×5 $mm^2$, p-type test cells were fabricated on Boro33 glass, using different combinations of a 200/70/20 nm ONO (PVD) or 10/100/80 nm NO(ON) (PECVD) interlayer stack with a 5 µm PECVD or 8.5 µm e-beam precursor. All four samples were annealed for 8/8/8 hours at 450/550/650 °C. A 25 nm a-Si(i) layer was deposited on the PEVCD interlayer stack before breaking the vacuum and depositing the e-beam precursor. Figure 3-8b shows LBIC images for these test cells. It can be seen that both cells with ONO PVD interlayers have many local areas with strongly reduced collection, in contrast to the cells with the PECVD interlayers. This comparison strongly suggests that the interlayer stack, and not the precursor, is causing the difference. From this experiment it cannot be excluded that the Corning substrate and corresponding 960 °C RTA process might have an additional influence.

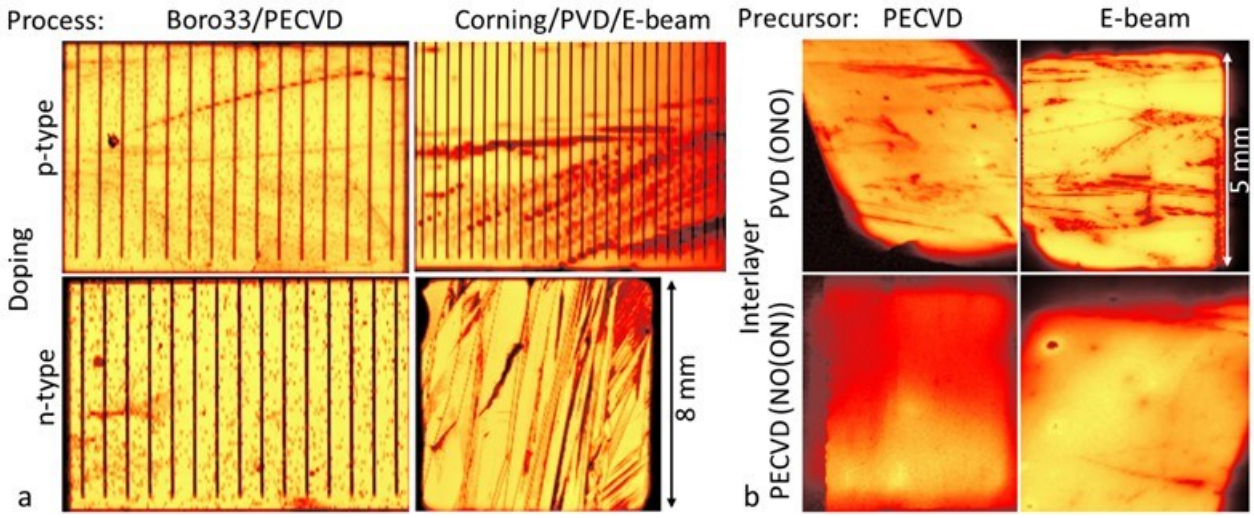


**Figure 3-8.** Fig. a shows LBIC measurements of p- and n-type cells made either on Boro33/PECVD or on Corning/PVD/e-beam material. Fig. b shows LBIC measurements for a p-type test cell experiment using either PVD ONO or PECVD NO(ON) interlayers and either PECVD of e-beam precursors, all on Boro33 substrates.

Another difference between the Boro33/PECVD and Corning/PVD samples that can be seen in Figure 3-8a are the many small spots with reduced LBIC signal for the Boro33/PECVD samples. The LBIC reflection measurement (not shown) reveal that this difference is related to increased reflection. From optical inspection it appears that these spots are caused by bubbles in the glass very close to the interlayers, similar to those reported in ref. [14] for SPC-Si and investigated in ref. [66] for LPC-Si on Boro33/PVD/e-beam samples.

Figure 3-9a shows images of LPC-Si samples that were crystallized with a laser scanning velocity ($v_{laser}$) of 1, 3 and 10 mm/s. In the images from the glass side it can be seen that the bubble density of the glass

substrates increases for decreasing $v_{laser}$. It can also be seen that for 1 mm/s the glass is strongly deformed in the shape of mm-sized waves.

Figure 3-9b shows microscope images of LPC-Si samples with $v_{laser}$ = 3 mm/s from the glass side at different magnifications. It can be seen that the bubbles have many different sizes and (cluster) shapes. The dependency of the bubble density on $v_{laser}$ might be related to the increasing substrate temperature for decreasing $v_{laser}$ (which also causes the wavy glass deformation for 1 mm/s). Corning/PVD/ebeam samples were all crystallized at 3 mm/s, but showed no bubbles in glass. Perhaps this is related to the higher softening point of the Corning glass or a higher hydrogen content in the PECVD layers. It should be noted that $v_{laser}$ and glass type are not the only factors determining the bubble density as different samples with the same $v_{laser}$ and glass type can have very different bubble density [66].

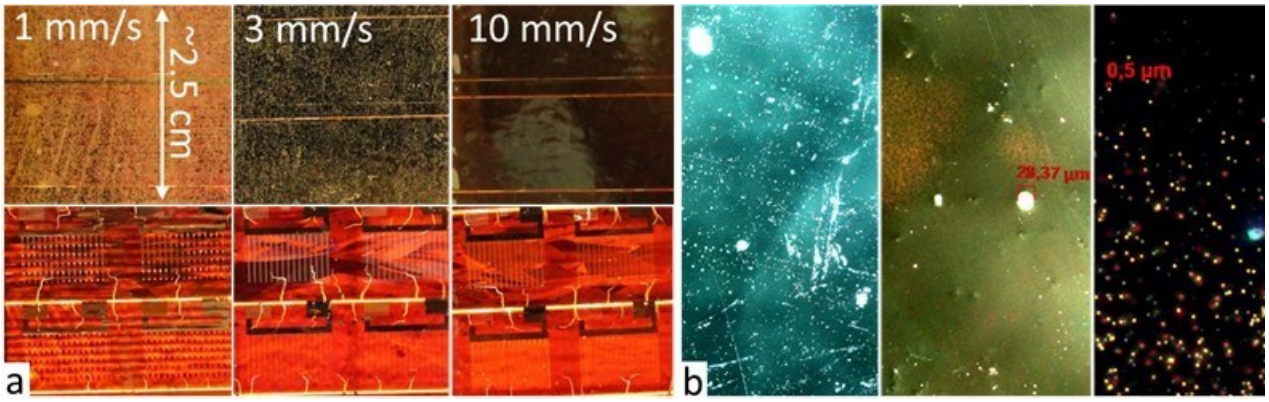


**Figure 3-9.** Fig. a shows images from the glass side (top) and from the Si side (with backlight) (bottom) of Boro33/PECVD samples that were crystallized with different laser crystallization scanning velocities ($v_{laser}$) of 1, 3 and 10 mm/s. Fig. b shows microscope images of the milky glass at different magnifications.

### 3.3.4 The Effect of LPC-Si Cracks on FrontERA Cells

In section 3.3.1 it was observed that the Boro33/PECVD samples result in a lower $R_{parallel}$ than the Corning/PVD samples. The Boro33/PECVD samples also had many cells with very low $J_{SC}$ (< 10 mA/cm$^2$), which were excluded from the boxplot in Figure 3-3, resulting in a lower yield for the Boro33/PECVD cells: ~50 % vs. ~90 % for the PVD samples. In order to determine the reasons for these shunts and the reduced $J_{SC}$, DLIT measurements were made of the Boro33/PECVD cells from section 3.3.1 and these measurements are shown in Figure 3-10. The cells were measured under an applied forward bias of 0.7 V (> $V_{OC}$), resulting in a diode current (and corresponding DLIT signal) in the entire active cell area and not just at the shunts. The white rectangles indicate the cell area. Both cells have an LPC crack (section 3.2.2, ref. [49]) through the metal fingers and it can be seen that the cracks have interrupted the grid fingers, cutting of more than half the cell. The cell in Figure 3-10a also has a crack through the bus bars and, from the heat development below the bus bar, it appears that the crack has resulted in shunts between the (stacked) bus bars. The

shunt is relatively mild as current is still flowing through the rest of the cell. It seems likely that the cracks are at least partly responsible for the lower $R_{parallel}$ (and *FF*) of the Boro33/PECVD cells observed in section 3.3.1 (Figure 3-3).

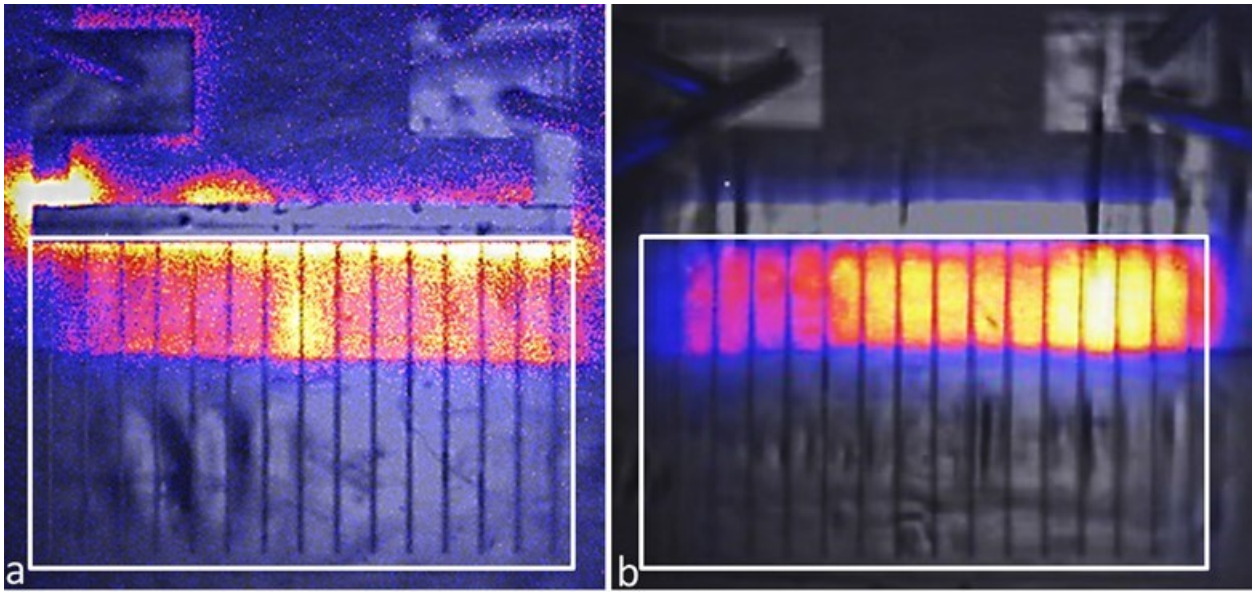


**Figure 3-10.** DLIT images of FrontERA cells fabricated on Boro33 with PECVD interlayers and precursors, measured under a forward bias of 0.7 V.

In order to prevent these cracks from running through the cell area and interrupting the grid fingers, later experiments used laser scribes to prevent cracks in the cell area. These so-called "crack catcher" scribes were made before crystallization and parallel to the crystallization direction, using a 1064 nm ps laser from the glass side. Figure 3-11a shows a backlight photograph of an n-type FrontERA sample (see *J-V* parameters in Figure 3-7) with 5 crack catcher scribes. It can be seen that this mostly prevents the long cracks in the cell area shown in Figure 3-10. However, there are still many smaller "side-cracks", coming out of the crack catchers and extending into the cell area. Figure 3-11b shows the DLIT images corresponding to the cells in Figure 3-11a, again measured with a forward bias of 0.7 V. It can be seen that 6 out of 9 cells are completely shunted, i.e. no DLIT signal except for the hotspot. Comparison of Figure 3-11a and b shows that four of these cells are shunted where a side-crack crosses the bus bars (and 2 cells are shunted at a grid finger). For the cells that are not completely shunted, there are also hotspots where side-cracks cross the grid fingers. For this experiment, out of 142 cells, only 1 cell was unaffected by shunts ($R_{parallel}$ > 2 kΩcm$^2$). This cell resulted in a $\eta$ = 12.1 % record cell (see section 3.3.5).

From the DLIT measurements in Figure 3-10 and Figure 3-11 and from the $R_{parallel}$ in Figure 3-7, it appears that the n-type cells are more strongly affected by shunts than the p-type cells. This can be explained in the following way: for n-type FrontERA cells, if there is an opening in the insulator (e.g. due to an LPC

crack), the Ag absorber contact is in direct contact with the TCO, resulting in a low contact resistance. In contrast, for the p-type FrontERA cell with an opening in the insulator, there is still an a-Si(n) layer between the (Al) absorber contact and the TCO (see Figure 3-2). The high resistance of the a-Si layer and the a-Si/TCO contact can explain why the p-type cells appear to be less affected by shunts than the n-type cells.

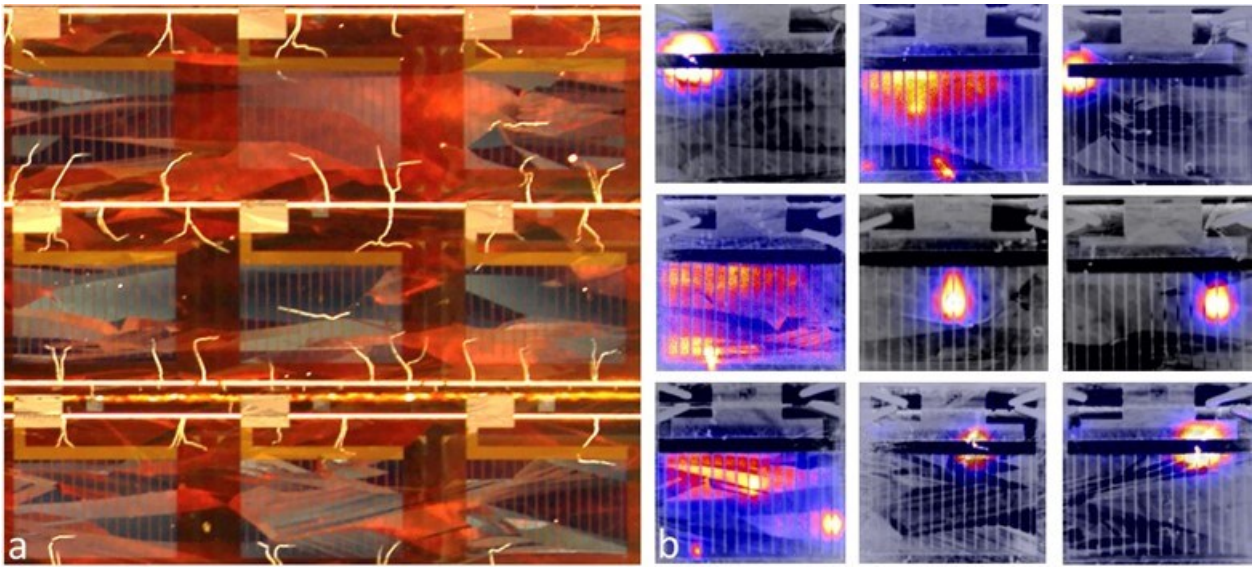


**Figure 3-11.** Backlight photograph (a) and corresponding DLIT images (b) for a textured, n-type FrontERA cell with crack catcher scribes and side-cracks. The DLIT images were made with a bias voltage of 0.7 V.

### 3.3.5 Record Cells

Table 3-3 gives an overview of the p- and n-type FrontERA cells on Corning/PVD/e-beam and Boro33/PECVD material with the highest $\eta$. The corresponding *J-V* and *IQE* curves are shown in Figure 3-12, except for the n-type ONO cell, which was not fabricated as part of this thesis, but taken from ref. [22]. The PECVD cells were published in ref. [67]. All cells were measured with white reflector and textured anti-reflection foil (ARF).

Except for the PVD p-type cell, all cells were measured in superstrate configuration. The p-type PVD cell is the $10^{17}$ $cm^{-3}$ doped cell from section 3.3.2 (Figure 3-6) with the highest $\eta$, measured in substrate configuration with white reflector and ARF. The low *IQE* for $\lambda < 600$ nm is due to the parasitic absorption in the a-Si:H emitter and the low *IQE* for $\lambda > 700$ nm is because the cell was not textured.

The p-type PECVD cell was made on the $7 \cdot 10^{16}$ $cm^{-3}$ doped PECVD material with NO(ON) interlayer from section 3.3.2 (same 30x30 $cm^2$ deposition), but was crystallized with a $v_{laser}$ of 3 mm/s (section 3.3.3) and KOH textured. Other differences were that the AKT emitter was replaced by a 10/10 nm a-Si(i/n) FAP emitter and that the Al absorber contact grid was evaporated through an evaporation mask instead of the

more complicated lithographic lift-off mask. The *J-V* curve shows that the low *FF* is both due to a high $R_s$ and due to a low $J_{MPP}/J_{SC}$ ratio (Figure 3-12a). This latter loss factor has the characteristics of a distributed series resistance [68] as was also observed for the p-type FrontERA cell in ref. [46] where it was attributed to interrupted grid fingers.

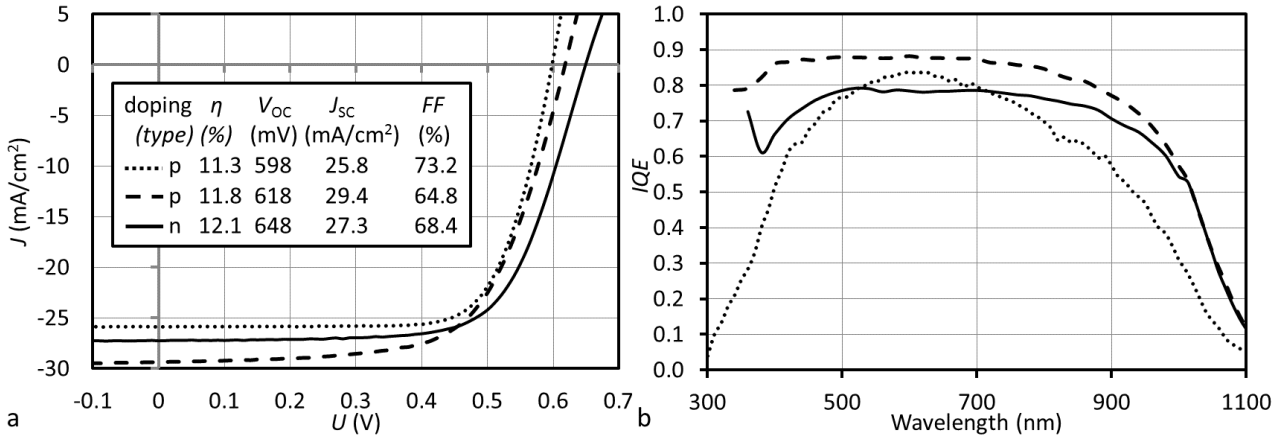


**Figure 3-12.** *J-V* and *IQE* curves of the record p- and n-type FrontERA cells made during this thesis, listed in Table 3-3.

The n-type PECVD cell is identical to that of the $9{\cdot}10^{16}$ cm$^{-3}$ doped cells in section 3.3.2 (Figure 3-7), except for a 5/10 nm a-Si(i/p) 'FAP' emitter instead of the AKT emitter. Due to the very low yield for this series (see section 3.3.4), it could not be determined if the 'FAP' emitter was the reason for the ~ 30 mV higher $V_{OC}$. The higher $V_{OC}$ of the PECVD cell than for the PVD cell can only partially be explained by the higher *N*, as on PVD cells $V_{OC}$ values of ~650 mV were only published for a doping densities of $10^{18}$ cm$^{-3}$ [21], [25]. The reflection loss was higher for the PECVD (NO(ON)) cell than for the PVD (ONO) cell as can be seen in Figure 3-5a. The maximum *IQE* of the PVD cell was 90 % [22], compared to ~80 % for the PECVD cell. These $J_{SC}$ losses for the PECVD cell are compensated by the better light trapping of the PECVD cell, due to the KOH texturing, resulting in a similar $J_{SC}$ for both cells.

**Table 3-3.** Overview of highest *η* FrontERA cells

| Interlayer (IL) type | IL (nm) | p/n-type | *N* (cm$^{-3}$) | *d* (µm) | KOH text. | $v_{laser}$ (mm/s) | $J_{SC}$ (mA/cm$^2$) | $V_{OC}$ (mV) | *FF* (%) | *η* (%) |
|---|---|---|---|---|---|---|---|---|---|---|
| **PVD: ONO** | **100/80/10** | **p** | **$10^{17}$** | **10** | **No** | **3** | 25.8 | 598 | 73 | 11.3 |
| | **250/70/10** | **n [7]** | **$4{\cdot}10^{16}$** | **10** | **No** | **e-beam** | 27.8 | 632 | 67 | 11.8 |
| **PECVD: NO(ON)** | **15/200/85** | **p** | **$6{\cdot}10^{16}$** | **7.5** | **Yes** | **3** | 29.4 | 618 | 65 | 11.8 |
| | **20/100/80** | **n** | **$9{\cdot}10^{16}$** | **11** | **Yes** | **3** | 27.3 | 649 | 68 | 12.1 |

## 3.4 Conclusions

It was shown that the PECVD material can result in cell with similar *η* as those made with the established PVD/e-beam material. Aside from this overall similarity, several differences were also identified. Absorber doping experiments using PECVD material indicated that the $J_{SC}$ was unaffected (or even increased) for

increasing carrier density, contrary to the decreasing $J_{SC}$ observed for cells based on PVD/e-beam material. LBIC measurements showed that cells with a PVD ONO interlayer stack had a strongly reduced carrier collection near the grain boundaries, contrary to cells with a PECVD NO(ON) interlayer stack, for which the collection was not visibly affected by the grain boundaries. It was further found that, for PECVD material on Boro33 substrates, a reduction of the laser crystallization scanning velocity resulted in an increasing density of bubbles in the glass.

So far, the PECVD material could only be crystallized successfully on BOROFLOAT33 substrates, which resulted in elongated cracks in the LPC-Si absorber. It was shown that these cracks resulted in interrupted grid fingers and increased shunting. “Crack catcher” laser scribes were implemented, attempting to prevent this. However, for many samples, large side cracks still crossed the bus bars and grid fingers, causing interrupted grid fingers and shunts.

Using PECVD material, new LPC-Si $\eta$ and $V_{OC}$ records for p-type (11.8 %, 618 mV) and n-type (12.1 %, 649 mV) cells were obtained, indicating the high quality of the PECVD material.

# 4 Photocurrent Analysis of FrontERA Cells

*In this chapter the photocurrent of the FrontERA LPC-Si cells will be analysed in detail. Section 4.1 presents a photocurrent analysis of a planar p-type and textured n-type cell, showing how the photocurrent is affected by the absorber contact, LPC-Si cracks, the interlayers, the anti-reflection foil, the white reflector, KOH texturing, parasitic absorption and recombination. It is argued that, for the best KOH textured FrontERA cells, the largest photocurrent losses are due to electrical shading by the absorber contact, reflection and parasitic absorption, while the light trapping efficiency is close to the theoretical limit. This photocurrent loss analysis is followed by a discussion of the photocurrent potentials. In section 4.2 a detailed LBIC and EQE analysis is presented of p-type FrontERA cells with $SiO_xN_y$ or $Al_2O_3$ based interlayer stacks. Simulation is used to argue that the measured carrier collection and bias light dependence, outside and inside the cell area, can be explained by a frontside charge inversion layer. The research in section 4.1 was published in* [67] *and section 4.2 is a preprint version of* [69]*.*

## 4.1 Photocurrent Losses and Potentials

The goal of this section is to show and discuss the photocurrent losses and potentials for LPC-Si cells in general and FrontERA cells specifically. Figure 4-1 shows a schematic cross section of the LPC-Si FrontERA cell and all the components that are part of the photocurrent analysis:

1. Collection (*EQE*)
2. Electrical losses
    - Dead area / electrical shading
    - The loss due to recombination in the bulk and at the interlayer interface
3. Optical losses
    - The (direct) reflectance of light that does not enter the c-Si absorber: $R_{\text{direct}}$
    - Light which escapes after entering the c-Si absorber: $T$ and $R_{\text{esc}}$
    - Parasitic absorption ($A_{\text{par}}$)

Together these components add up to 1:

$$1 = A_{\text{Si}} + R_{\text{direct}} + R_{\text{esc}} + T + A_{\text{par}}\,, \tag{11}$$

where the absorption in the silicon ($A_{\text{Si}}$) equals the *EQE* + the electrical losses. The yellow arrows in Figure 4-1 represent the incoming and reflected light, the red arrows represent the (poorly absorbed) long wavelength light and the black arrows represent the transport of the minority carriers.

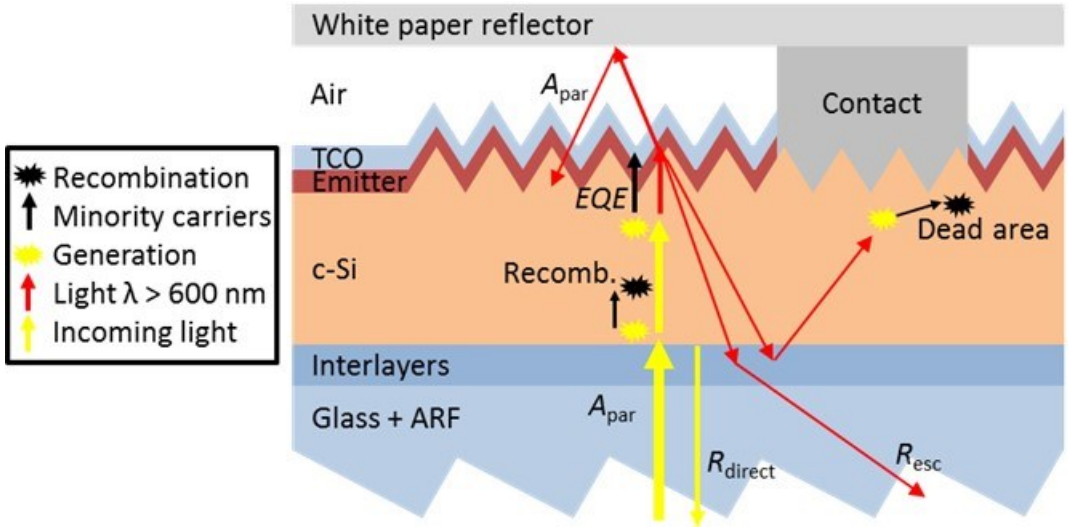


**Figure 4-1.** Schematic cross section of the LPC-Si (FrontERA) cell, with detached white paper reflector and textured anti-reflection foil, and all the components making up the $J_{SC}$ analysis: *EQE*, direct reflection ($R_{direct}$), reflection due to incomplete light trapping ($R_{esc}$), parasitic absorption ($A_{par}$), recombination due to bulk and interlayer recombination and dead area due to the absorber contact.

Section 4.1.1 presents the investigated cells. This is followed by an LBIC analysis in section 4.1.2, investigating the dead area losses due to the absorber contact and LPC-Si cracks. In section 4.1.3 the effect of the interlayers and the anti-reflection foil on the reflection losses is investigated, using simulation to separate the measured total reflectance ($R_T$) into $R_{direct}$ and $R_{esc}$. Section 4.1.4 presents the absorptance properties of the substrate, contacting layers and light trapping layers. Also, *IQE* measurements will be used to study the effect of light trapping on the parasitic absorption. In section 4.1.5, the *IQE*, corrected for the dead area and parasitic absorption in the glass, will be used to determine the recombination losses and the effective diffusion length (as explained in section 2.7). At this point all the aforementioned components of the photocurrent analysis have been determined, except for the $A_{par}$ in the layer stack (for λ > 600 nm). Therefore, the remainder equals $A_{par}$ (± all potential inaccuracies) (see eq. (11)). In section 4.1.6 ray tracing simulations are used to compare the light trapping of the cells to the theoretical light trapping limit for geometrical optics. This is needed to determine realistic photocurrent losses and potentials, as even with perfect light trapping not all the light can be absorbed in the silicon. Subsequently, the simulations are also used to estimate the contribution of the individual layers to the total $A_{par}$. Finally, section 4.1.7 presents an overview of the photocurrent losses, followed by a discussion of the photocurrent potentials in section 4.1.8.

### 4.1.1 Investigated Cells

Table 4-1 shows the properties and *J-V* parameters of the investigated planar p-type cell (A) and textured n-type cell (B). The record p- and n-type cells were added for comparison (in grey). Cell A and B were both

part of the experiments presented in section 3.3.2 and were selected for their above average current. The differences in KOH texturing and doping type between cell A and cell B were selected, in order to illustrate how these difference influence the photocurrent losses. The differences in crystallization speed, thickness and doping concentration were unavoidable, given the available cells. In ref. [70] it was shown how the interlayer thicknesses were optimized to minimize reflection. The p- type cells in Table 4-1 had these optimized IL thicknesses, while the n-type cells still had IL thicknesses that were not optimized for anti-reflection.

**Table 4-1.** Investigated (A and B) & record (grey) FrontERA cells.

| Cell ID | Glass + IL | IL (nm) | p/n-type | $N$ ($cm^{-3}$) | $d$ (µm) | KOH text. | $v_{laser}$ (mm/s) | $J_{SC}$ ($mA/cm^2$) | $V_{OC}$ (mV) | $FF$ (%) | $\eta$ (%) |
|---|---|---|---|---|---|---|---|---|---|---|---|
| **A** | Boro 33 + NO (ON) | 15/200 /85 | p | $4 \cdot 10^{16}$ | 9 | no | 10 | 26.2 | 590 | 58 | 8.9 |
| - | | | | $6 \cdot 10^{16}$ | 7.5 | yes | 3 | 29.4 | 618 | 65 | 11.8 |
| **B** | | 20/100 /80 | n | $9 \cdot 10^{16}$ | 11 | yes | 3 | 28.9 | 568 | 56 | 9.2 |
| - | | | | | | | | 27.3 | 649 | 68 | 12.1 |

### 4.1.2 Dead Area due to the Absorber Contact and LPC-Si Cracks

In this section LBIC measurements will be used to determine the photocurrent loss due to local effects (dead area) like electrical shading by the absorber contact and interrupted grid fingers due LPC-Si cracks. Figure 4-2a and b show the LBIC measurements of cell A and B, measured from the glass side with a bias light intensity of approximately 1 sun and the λ = 532 nm laser. Figure 4-2c and d show the corresponding pictures of the cells from the Si side of cell A (c) with backlight and of cell B (d) without backlight.

For textured cell B, the different grain orientations result in differently tilted pyramids, resulting in different reflection, which is visible in the image. The visible grain boundaries are indicated as dashed lines in Figure 4-2b. It can be seen that areas with locally reduced current collection in Figure 4-2b (cell B) are mostly extending from the grain boundaries or limited to certain grains. These are probably dislocation-rich areas as determined in ref. [24]. As the effect is relatively small and hard to quantify it is not included in the dead area fraction ($f_{DA}$). Therefore these losses are automatically included in the (wavelength dependent) loss due to bulk and surface recombination which will be determined in section 4.1.5.

It can be seen in Figure 4-2c that cell A has an LPC-Si crack (see section 3.3.4) through the lower-left part of the cell and three smaller “side-cracks” extending from the main crack. The LBIC measurement in Figure 4-2a shows that these cracks result in areas with strongly reduced LBIC signal. By comparing the LBIC signal in the affected areas with unaffected neighbouring areas, the $f_{DA}$ caused by the cracks was estimated at 7 ± 1 %. For an LBIC measurement without bias light (not shown), the LBIC signal was approximately equal on both sides of the cracks, indicating that the cell area below the cracks is not completely cut off, but

connected to the rest of the cell with a large resistance.

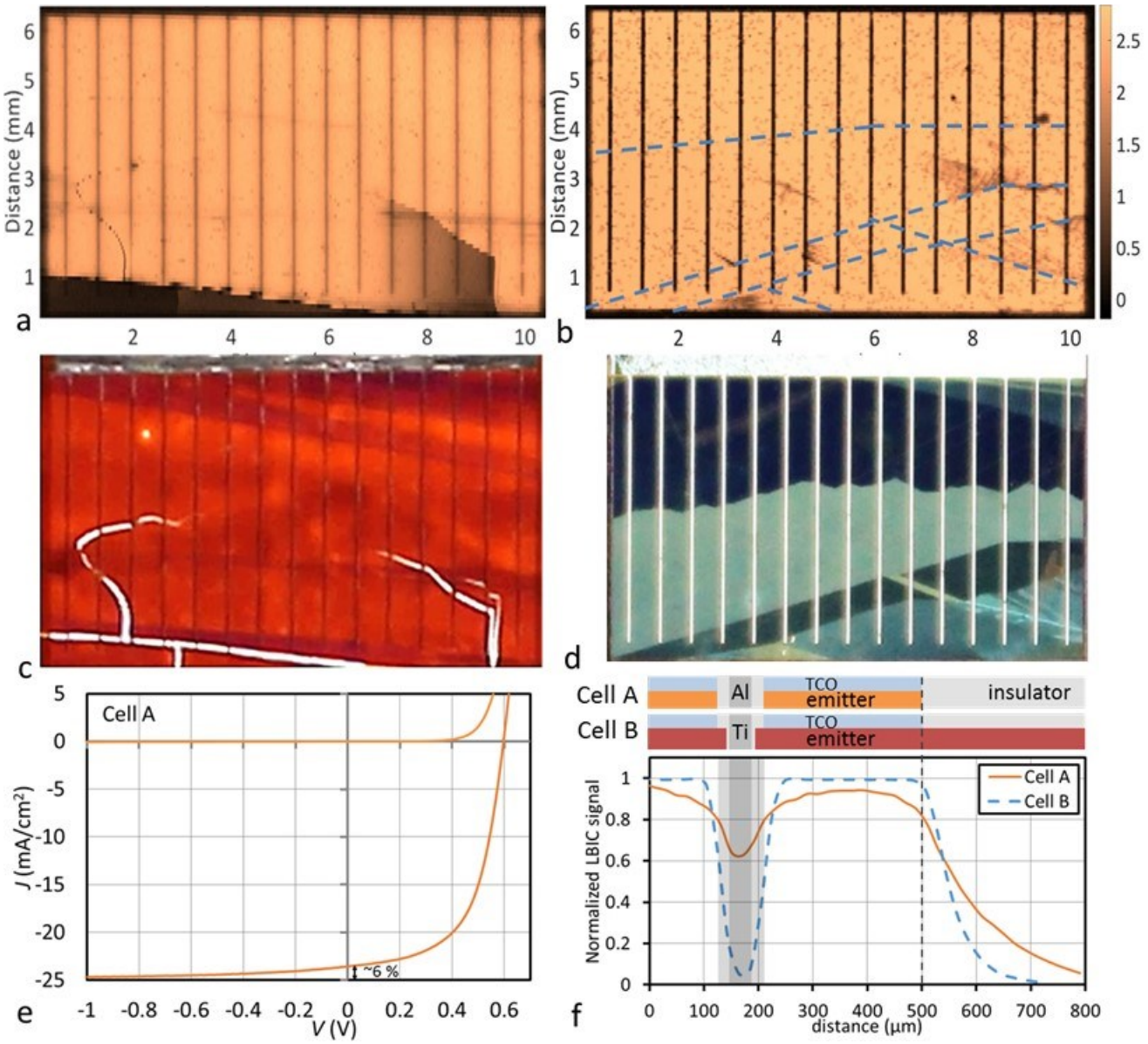


**Figure 4-2**. LBIC measurements of cell A (a) and cell B (b) as well as the corresponding images of planar cell A (c) with backlight (in order to show the cracks) and of textured cell B (d) without backlight (in order to show the grain boundaries). The scale bar next to Fig. b shows the current generated by the LBIC laser. The dashed lines represent the grain boundaries visible in Fig. d. The LBIC images have been mirrored to match the photograph from Fig c and d, which were taken from the silicon side. Fig. e shows the dark and light *J-V* curves of cell B, showing the distributed series resistance effect (slope at $J_{SC}$) and how it affects the $J_{SC}$. Fig. f shows LBIC linescans and corresponding simplified schematic cross-sections of the cell edge and neighboring absorber contact for cell A and B (see Figure 3-2 for comparison).

Figure 4-2e shows the dark and light *J-V* curves of cell A. The light *J-V* curve has a large slope at $J_{SC}$, but the dark *J-V* curve does not, showing that the cell is not shunted. In ref. [46] it was speculated for a p-type FrontERA cell that such a *J-V* curve can be explained by a distributed resistance, caused by interrupted grid

fingers. The $J_{SC}$ loss due to the distributed series resistance estimated from the *J-V* curve is ~6 %, which fits with the 7 ± 1 % estimated from the LBIC measurement. This confirms the hypothesis that the slope in the *J-V* curve around $J_{SC}$ is caused by a distributed series resistance that is caused by (partially) interrupted grid fingers. It can be seen in the *J-V* curve that the resistance/photocurrent loss due to the interrupted grid fingers is larger at the maximum power point than at $J_{SC}$, thus resulting in a reduction of the *FF*.

Figure 4-2f shows normalized LBIC linescans and simplified schematic cross-sections of the cell edge and neighboring absorber contact for cell A and B. The linescans clearly indicate that the dead area fraction ($f_{DA}$) due to electrical shading by the absorber contact is much smaller for cell A (p-type) than for cell B (n-type). The $f_{DA}$ due to the absorber contact was estimated at 7.1 ± 0.5 % and 11.0 ± 0.5 % for cell A and B respectively, using the method described in section 2.5. The measurement in Figure 4-2f was also used to correct the *EQE* measurement for the collection outside the cell area, which was estimated at 6.5 ± 1 % for cell A and 2.6 ± 0.5 % for cell B. The reason for the higher collection below the absorber contact and outside the cell area for the p-type cell (A) compared to n-type cell (B) will be discussed in section 4.2.

As discussed in section 3.3.3, the many small spots of reduced LBIC signal are caused by bubbles in the glass below the interlayers, created during laser crystallisation. They are more numerous and appear to be larger for cell B, which is related to the lower $v_{laser}$ for cell B (3 mm/s) compared to cell A (10 mm/s) (see section 3.3.3). As this loss is also part of the reflection loss (next section) it is not included in $f_{DA}$.

### 4.1.3 Reflection

In this section the impact of the optimized interlayer thicknesses and the ARF on the reflection will be investigated. Simulation will be used to divide the measured total reflectance $R_T$ into the $R_{direct}$, defined as the reflected light which has *not* entered the c-Si absorber, and $R_{esc}$, defined as the light escaping the cell after entering the c-Si absorber. This division is made, because these losses are caused by different effects, requiring different solution, i.e. anti-reflection vs. light trapping.

A simulated $R_{direct}$ ($R_{direct,sim}$) was calculated with PV Lighthouse's OPAL2 [71], simulating a glass halfspace, followed by the intermediate layers, followed by a silicon halfspace. The reflection of the glass-air interface was added to the simulated reflectance, taking into account multiple reflections and absorption in the glass. The simulated interlayer thicknesses were adjusted until $R_{direct,sim}$ fitted the measured $R_T$ for $\lambda <$ 600 nm, as for $\lambda <$ 600 nm all the light is absorbed in a single pass and therefore $R_{esc} = 0$, i.e. $R_T = R_{direct}$. $R_{direct}$ and $R_{esc}$ were defined as:

$$R_{direct} \equiv R_T \quad \text{, for } \lambda < 600 \text{ nm,} \tag{12}$$

$$R_{direct} \equiv R_{direct,sim} \quad \text{, for } \lambda > 600 \text{ nm,} \tag{13}$$

$$R_{esc} = R_T - R_{direct} \tag{14}$$

i.e. $R_{direct,sim}$ is only used for λ > 600 nm. Figure 4-3 shows $R_T$ (solid) and $R_{direct,sim}$ (dashed) for cell A (fig. a) and cell B (fig. b), with ARF (blue) and without ARF (red). All measurements were made with back reflector. It can be seen from the differences in the interference peaks that different interlayer thicknesses were used for cells A and B: 15/200/85 vs. 20/100/80 nm. The optimization of the interlayer thicknesses to minimize reflection was presented in ref. [70]. It can be seen that cell A has two reflection minima, thereby "spreading" the anti-reflection effect over a wider wavelength range. From $R_{direct}$ it was calculated that the optimized IL thicknesses for cell A reduced the direct reflection loss by 1.1 ± 0.2 mA/cm$^2$.

It can be seen how the ARF strongly reduced $R_{direct}$ for both samples. The $R_{direct,sim}$ with ARF could not be simulated and was instead fitted to the measured $R_T$ by shifting the $R_{direct,sim}$ without ARF by 40 nm to shorter wavelengths and reducing the reflectance by 65 % for cell A and 50 % for cell B. From $R_{direct}$ it was calculated that the ARF reduced the direct reflection loss by 3.8 ± 0.2 mA/cm$^2$ for both cells.

The ARF has a mm-sized texturing and therefore falls in the geometrical scattering domain. The schematic ray tracing examples in Figure 4-3b (similar to ref. [16]) shows how the ARF can reduce both the "$R_{direct}$ loss caused by the glass/air interface" (1) and the "$R_{direct}$ loss caused by the glass/interlayer/Si interface" (2): by texturing the glass/air interface, the ~4 % reflectance at this interface can be reduced to $0.04^2 = 0.0016$, as the light is reflected upon a neighbouring pyramid, getting a "second chance" for transmission ("multiple bounce"). However, this reduction cannot explain the magnitude, nor the wavelength dependence, of the observed reduction. A reduction of the "$R_{direct}$ loss caused by the glass/interlayer/Si interface" can be explained by light trapping, i.e. total internal reflection, at the textured ARF/air interface as is shown in Figure 4-3b. In other words, the ARF changes both the incoupling (1) and the outcoupling (2) at the glass/air interface. For Lambertian light trapping (randomized light), the fraction of the light outside the escape cone for total internal reflection, i.e. the fraction which is reflected back into the cell, is given by 1-1/n$^2$ [72]. For glass ($n_{glass}$ = 1.47 [44]) this equals $1 - 1/n_{glass}^2 = 0.54$, which can explain the observed 50-65 % reflectance reduction by the ARF, indicating that the ARF is very effective at trapping the light. The wavelength shift can be explained by a shift of the interference peaks as scattering by the ARF increases the effective optical pathlength in the interlayer stack.

Cell A has a planar Si backside, resulting in a large $R_{esc}$ (poor light trapping), and cell B has a KOH textured Si backside, resulting in a small $R_{esc}$. It can be seen that the ARF reduces $R_{esc}$ for cell A, but not (significantly) for cell B. This will be discussed in more detail in section 4.1.6.

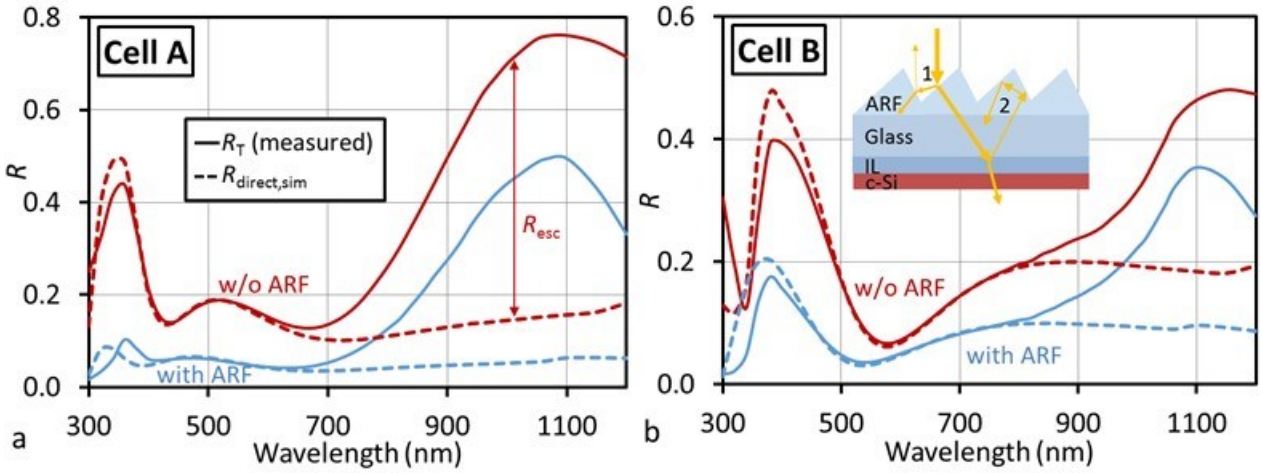


**Figure 4-3:** Fig. a and b show the measured total reflectance ($R_T$) and the simulated direct reflectance ($R_{direct}$) with and without textured anti-reflection foil (ARF) for cell A (a) and for cell B (b). The inset in fig. b schematically shows how the ARF can reduce both the incoupling (1) and the outcoupling (2) at the glass/air interface.

### 4.1.4 Parasitic Absorption

In this section we present the absorptance properties of the layers in the FrontERA cells. Subsequently, the *IQE* measurement are used to show the effect of light trapping on parasitic absorption. The actual $A_{par}$ loss in the cells and in the individual layers for $\lambda > 600$ nm, cannot be determined yet in this section as it requires the determination of the recombination losses (section 4.1.5) and optical simulation (section 4.1.6).

The absorptances of the ARF, glass and $SiN_x$ layer are shown in Figure 4-4a. The $SiN_x$ interlayer is the only interlayer with a significant absorptance. A logarithmic axis is used in order to show both the very high absorptance (up to 80 %) for $300 < \lambda < 400$ nm and the low absorptance (< 2 %) in the rest of the wavelength range.

The high parasitic absorption for $300 < \lambda < 400$ nm only represents a relatively small $J_{SC}$ loss (0.1-0.3 mA/cm$^2$), as the photon flux of the AM1.5 spectrum is very low in this wavelength range. The roughly 1 % absorptance of the Boro33 glass and ARF for $\lambda > 400$ nm both cause an approximately 0.3-0.4 mA/cm$^2$ $J_{SC}$ loss on the first pass. The absorptance in the Corning glass for $\lambda > 400$ nm is less than 0.1 mA/cm$^2$.

Figure 4-4b shows the simulated absorptance of a 5/10 nm a-Si(i/p) emitter, the measured absorptance of the ITO layer and the white paper reflector and the transmittances of cell A and B. The transmittance curve of planar cell A shows how much light reaches the back of the c-Si absorber. It can be seen that, in the wavelength range where the a-Si emitter shows relevant absorptance, very little light actually reaches the emitter, making the parasitic absorption in the emitter negligible. The figure also shows the absorptance

of the ITO layer and the white paper reflector[1]. The low transmittance of textured cell B without reflector indicates that the backside texturing traps most of the light in the cell. As only the transmitted light reaches the reflector, this strongly limits the possible parasitic absorption in the reflector for cell B.

In addition to the layers presented in Figure 4-4b there is one more potentially important cause of parasitic absorption: the 10/1000 nm Ti/Ag absorber contact. The (simulated) absorptance of a textured Si / 10 nm Ti / Ag interface is ~70 % and the surface coverage of the absorber contact is ~6 %, resulting in an area weighted absorptance of about 4 %. For comparison: this is higher than the absorptances of the ITO (~1.5 %) and white paper (~3 %).

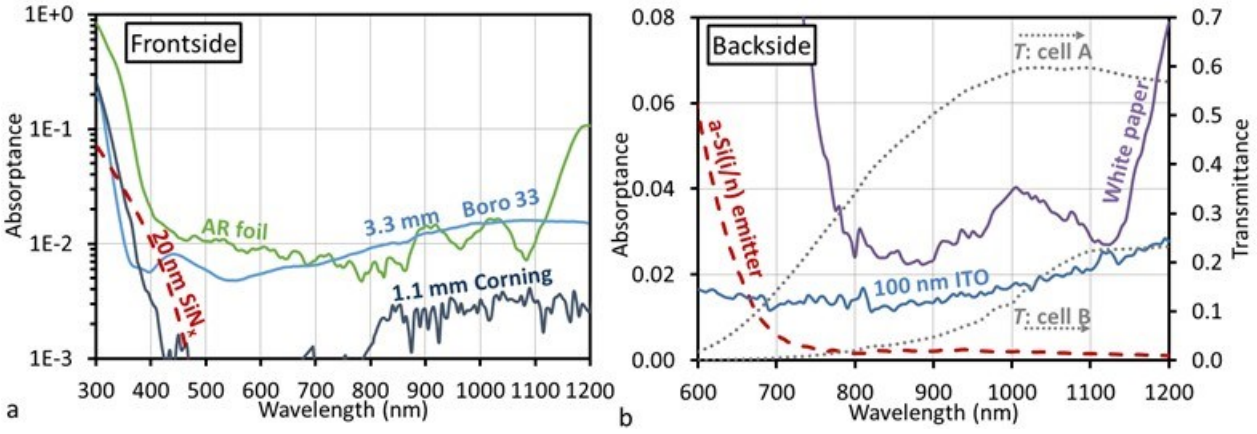


**Figure 4-4.** The calculated (dashed) and measured (solid) absorptance in the frontside (a) and backside (b) layers. Figure b also includes the transmittance (dotted) of textured cell A and planar cell B, both measured w/o ARF and reflector. Due to the strong light scattering, the uncertainty for the ARF measurement is approximately ± 1 %, i.e. the absorptance for 400 < λ < 800 nm is 0-2 %. For the backside layers, the absorptance is only shown for λ > 600 nm.

Figure 4-5a and b show the internal quantum efficiency (*IQE)* of both cells, with (dashed) and without (solid) reflector and with (blue) and without (red) ARF, measured with the large area *EQE* set-up (see section 2.4). For cell B, there was no bias light dependence between 0.4 and 1 suns (not shown), so the bias light was set to 0.4 suns in order to improve the signal to noise ratio. For cell A, there was a strong bias light dependence between 0.4 and 1 sun, mainly due to the interrupted grid fingers (as discussed in section 4.1.2). Therefore, the bias light intensity was set to ~1 suns.

It can be seen that the ARF strongly reduced the *IQE* for $\lambda < 400$ nm as would be expected from the absorptance measurement shown in Figure 4-4. The ARF decreased the *IQE* for $500 < \lambda < 700$ nm by approximately 2 % for cell A and 1 % for cell B, which fits with the expected loss due to the parasitic absorption in the ARF.

It can be seen that, for the planar cell (A), the addition of the ARF and the back reflector strongly decreased



[1] From a comparison of white reflectors it was found that, for $800 < \lambda < 1100$ nm, white paper has the lowest absorptance (~3 %), followed by white PVB foil (~6-7 %) and white paint (~9 %).

the *IQE* for λ > 700 nm. For the textured cell (B), the *IQE* does not decrease with the addition of the reflector or ARF. For λ > 700 nm, the *IQE* for cell B is approximately equal to that of cell A without reflector or ARF.

The observation that the $A_{par}$ for cell B is not increased by the reflector and ARF can be explained by the low transmittance of textured cell B without reflector in Figure 4-4b, i.e. very little light is absorbed in the (detached) reflector and ARF because the KOH texturing traps most of the light in the c-Si/TCO stack. It can be concluded that texturing the Si absorber strongly reduces the relative parasitic absorption by trapping most of the light within the absorber (and TCO) layer.

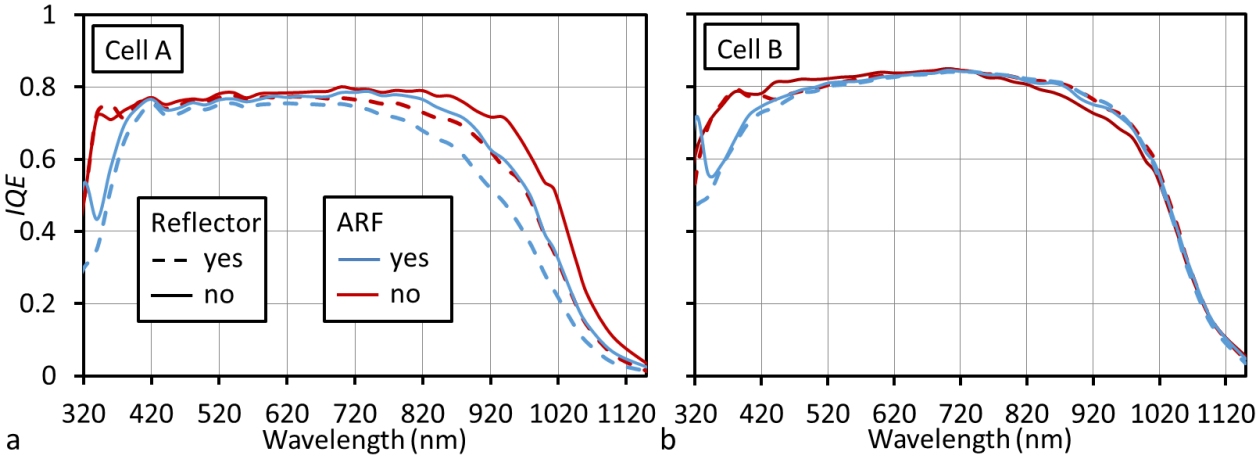


**Figure 4-5:** *IQE* of (a) cell A and (b) cell B, with (dashed) and without (solid) reflector and with (blue) and without (red) anti-reflection foil (ARF).

### 4.1.5 Recombination and Effective Diffusion Length

In the previous sections the measured *EQE*, *R* and $f_{DA}$ were presented and these measured quantities are shown in Figure 4-6a for cell B, without reflector or ARF. The remainder (white area) consists of the losses due to parasitic absorption ($A_{par}$) and recombination in the bulk and at the interlayer interface. For $400 < \lambda < 600$ nm the parasitic absorption consist only of the (small) absorption in the glass and the remaining loss is due to recombination.

Using the equations in section 2.7, this can be used to estimate the recombination loss in the entire wavelength range by fitting a calculated collection efficiency ($\eta_c$) to the experimental $\eta_c$ for $400 < \lambda < 600$ nm, as is shown in Figure 4-6b. Aside from the experimental $\eta_c$ (dots) for cell A (blue) and B (green), the figure also shows the fitted $\eta_c$ curves, for the assumptions that the recombination is either completely determined by the bulk diffusion length (*L*-limited, light, dashed curves, $S$ = 0 cm/s) or completely determined by the surface recombination velocity at the interlayer interface (*S*-limited, dark, dashed curves, $L$ = 1 mm). This is similar to what was done in ref. [60] by using AFORS-HET. All possible fitted $\eta_c$ curves are between the two dashed curves, thereby showing the maximum inaccuracy of the fit.

Ignoring the measurement uncertainties, the fitted effective diffusion length ($L_{eff}$) is 30 ± 4 µm for cell B and 20 ± 3 µm for cell A. The solid lines show the fitted $\eta_c$ used for the $J_{SC}$ analysis.

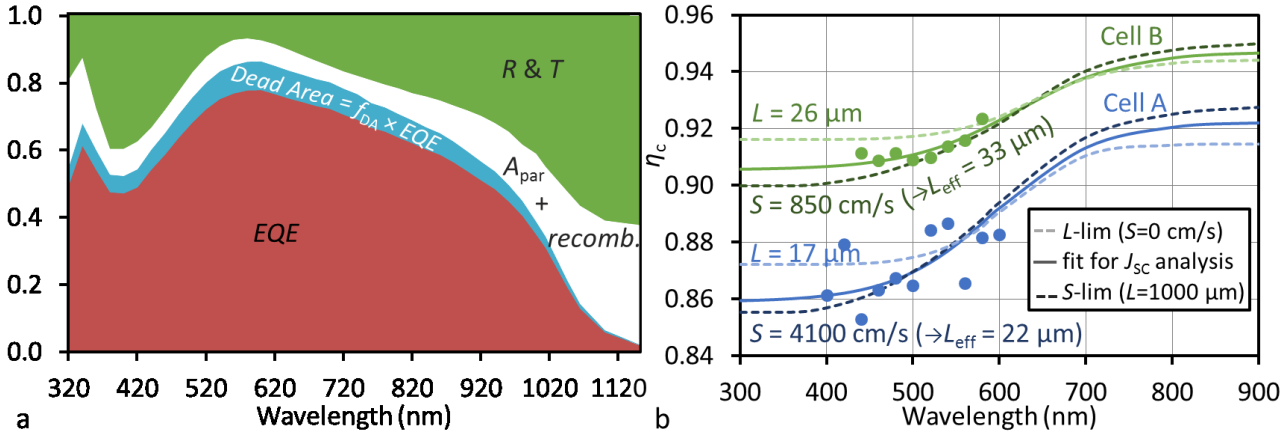


**Figure 4-6:** Fig. a shows the measured *EQE* (orange), $f_{DA}$ × *EQE* (green) and *R*+*T* (blue), for cell B without reflector and ARF. The remainder (white) consists of recombination and $A_{par}$. Fig. b shows the experimental $\eta_c$ (dots), for cell A (blue) and B (green), and the fitted $\eta_c$ curves (dashed), for the assumptions that $\eta_c$ is either completely determined by the bulk diffusion length (*L*-lim) (light green/blue) or completely determined by the surface recombination velocity at the interlayer interface (*S*-lim) (dark green/blue). The used *L* and *S* values for the *L* and *S* limited curves are indicated in the graph. The *S* values were converted to $L_{eff}$ using eq. (10), allowing for comparison to the fitted *L* (= $L_{eff}$) values.

The recombination loss can be calculated with the following equation:

$$recomb. = EQE\left(\frac{1}{\eta_c} - 1\right), \tag{15}$$

The fitted $\eta_c$ for the measurements without reflector or AR foil, were also used to calculate the recombination loss for the measurements with reflector and/or AR foil, as both optical improvements do not significantly affect $\eta_c$. After calculating the recombination loss, the remainder is the loss due to parasitic absorption (eq. (11)):

$$A_{\mathrm{par}} = 1 - A_{\mathrm{Si}} - R_{\mathrm{T}} - T = 1 - EQE\left(\frac{1}{\eta_c} + f_{\mathrm{DA}}\right) - R_{\mathrm{T}} - T\,, \tag{16}$$

### 4.1.6 Simulation of Light Trapping Limits and Parasitic Absorption

Geometrical light trapping has a theoretical limit [72]. Hence, even with perfect light trapping, only part of the long wavelength light can be absorbed in the silicon. Therefore, counting the entire optical losses determined in the previous sections (*T*, $R_{esc}$, $R_{direct}$ and $A_{par}$) as a $J_{SC}$ loss, would create an unrealistic expectation about the $J_{SC}$ potential. In order to determine which fraction of the optical losses can be gained by improved light trapping, a theoretical light trapping limit must first be determined. Light trapping by a an attached Lambertian reflector is generally considered the maximum light trapping obtainable with geometrical optics, and is also referred to as the Yablonovitch [72] or $4n^2$ limit. In order to compare

Lambertian light trapping for the LPC-Si structure with light trapping by (mono-Si) backside pyramid texturing and the experimentally observed light trapping, simulations were made with PV Lighthouse's online ray tracer [73]. The ray tracer simulations were also be used to estimate the $J_{SC}$ losses due to parasitic absorption in the backside layers.

In order to compare the light trapping for the experimental and simulated structures, it is necessary to calculate a light trapping efficiency ($\eta_{LT}$), showing the light absorbed in the silicon ($A_{Si}$) as a fraction of the escaped light + the light absorbed in the silicon:

$$\eta_{\mathrm{LT}} = \frac{A_{\mathrm{Si}}}{A_{\mathrm{Si}} + (R_{\mathrm{esc}} + T)} = \frac{A_{\mathrm{Si}}}{1 - R_{\mathrm{direct}} - A_{\mathrm{par}}} \,. \tag{17}$$

For the experimental $\eta_{LT}$, the input parameters for this equation are derived with eq. (11)-(16) and for the simulated $\eta_{LT}$, the input parameters follow directly from the simulation. The simulated layer stack consisted of: air, Boro33 glass, the intermediate layers, 11 µm c-Si (9 µm for cell A), 2 µm high, non-periodic pyramids, 15 nm a-Si:H (p), 75 nm ITO, and a detached white (Lambertian) reflector with a reflectance of 97 %, which represents the white paper (see measured absorptance in Figure 4-4b). For the simulation of Lambertian light trapping, the Si was planar and the emitter/ITO/reflector stack was replaced by an attached Lambertian reflector with $R$ = 100 %. The attached Lambertian randomizes the light in the silicon absorber, thereby trapping it in the cell by total internal reflection. This is in contrast to a detached Lambertian reflector which randomizes the light in the air layer, contributing very little to light trapping as the angular distribution of the scattered light is strongly reduced upon refraction into the silicon.

Figure 4-7 shows the experimental $\eta_{LT}$ curves (solid) for cell A (a) and cell B (b), with and without reflector and with and without ARF. These curves are compared to the simulated $\eta_{LT}$ curves (dashed) for the Lambertian reflector and for the pyramid textured cell with and without detached reflector. Figure a also includes two calculated $A_{Si}$ curves (dotted) for 1 and 3 passes through the absorber, using the Lambert-Beer law: $A_{Si} = 1 - e^{-\alpha d Z}$, where $\alpha$ is the absorption coefficient of c-Si, $d$ is the absorber thickness and $Z$ is the number of passes through the absorber.

In Figure 4-7a it can be seen that the light trapping for planar cell A without reflector (light red) only slightly exceeds the calculated single pass absorptance (dotted curve). Adding a diffuse reflector increases the optical pathlength enhancement to about 3 passes. Adding the textured ARF mainly increased the $\eta_{LT}$ for the measurement with reflector, as without reflector most of the light escapes at the back of the cell, which is not affected by the ARF. The simulated $\eta_{LT}$ for cell A, but with pyramid texture, was added as a reference.

Figure 4-7b shows that the ARF has no significant effect on the $\eta_{LT}$ of the textured cell (B). The experimental $\eta_{LT}$, could be reproduced quite well by the simulated $\eta_{LT}$. For wavelengths between 800-1000 nm, the measured $\eta_{LT}$ is lower than the simulated $\eta_{LT}$, especially without a reflector. It can also be seen that the pyramid texturing results in slightly better light trapping than the Lambertian light trapping. Therefore, instead of an attached Lambertian reflector, we assume the simulated $\eta_{LT}$ for the (non-periodic) pyramid textured backside (with a detached Lambertian reflector) to be the maximum achievable light trapping with geometrical optics ($\eta_{LT,lim}$). This limit results in a $J_{SC,lim}$ of 40.2 mA/cm$^2$ for the 9 µm thick c-Si absorber of cell A and 40.6 mA/cm$^2$ for the 11 µm thick absorber of cell B.

The better light trapping for the pyramid textured c-Si than for the Lambertian reflector can be explained using the schematic ray tracing examples in Figure 4-7b: for the first reflection at the backside, the pyramid texturing reflects all the light beyond the critical angle of the opposite interface, while, for the Lambertian reflector (which scatters the light uniformly in all directions) $1/n^2$ = 8 % [74] of the light is reflected within the escape cone of c-Si to air [75].

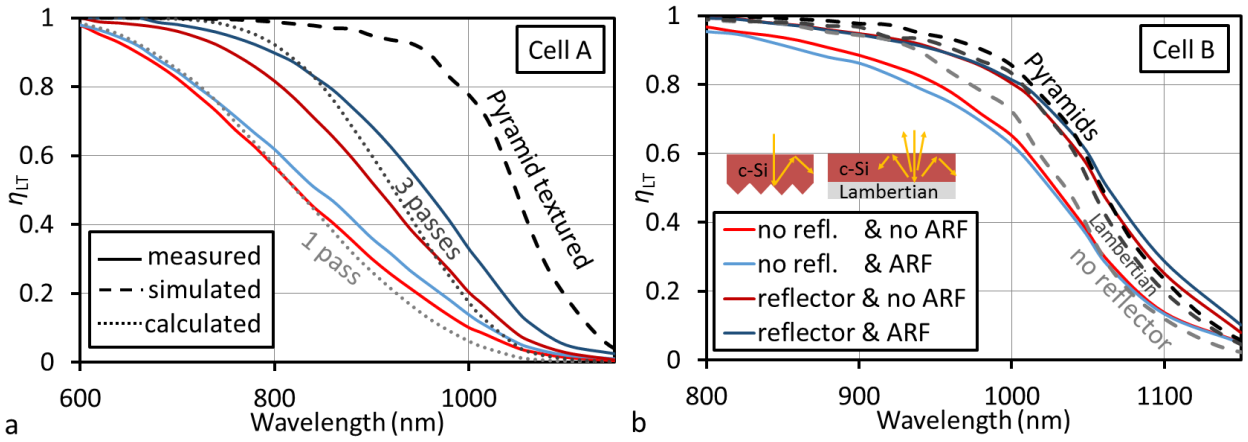


**Figure 4-7.** The experimental $\eta_{LT}$ curves for cell A (a) and cell B (b) (solid), with reflector (dark blue/red) and without reflector (light blue/red) and with ARF (blue) and without ARF (red). These experimental curves are compared to the simulated $\eta_{LT}$ curves (dashed) for the Lambertian reflector and for the pyramid textured cell with and without detached reflector. Figure a also includes two calculated $A_{Si}$ curves (dotted) for 1 and 3 passes through the absorber, using the Lambert-Beer law: $A_{Si} = 1 - e^{-\alpha dZ}$, where α is the absorption coefficient of c-Si, $d$ is the absorber thickness and $Z$ is the number of passes through the absorber, as indicated in the figure.

The difference between the experimental and simulated $\eta_{LT}$ can be explained by the randomly tilted pyramids (or even some planar areas) of the polycrystalline LPC-Si cell, compared to the simulated monocrystalline Si pyramids (pyramid angle = 54°). The tilted pyramids will let part of the light escape at the first reflections, especially without a back reflector. After multiple internal reflections the direction of the light becomes randomized [75] and the experimental $\eta_{LT}$ ($\lambda > 1000$ nm) more closely resembles the

simulated $\eta_{LT}$. The difference between the experimental $\eta_{LT}$ and the simulated $\eta_{LT,lim}$ will be used in the next section to calculate the loss due to incomplete light trapping.

The simulation with pyramids and reflector for cell B was also used to estimate the parasitic absorption in the emitter, ITO and reflector. It could not be used to determine the parasitic absorption in the Boro33 glass, as it was not possible to simulate a 3.3 mm thick glass layer. The 9 µm Boro33 glass layer, which was used instead, resulted in the small interference peaks every ~30 nm in Figure 4-7, i.e. the effect on $\eta_{LT}$ was negligible. The simulation confirmed the conclusion in section 4.1.4 that the emitter has no significant contribution to the parasitic absorption (< 0.05 mA/cm$^2$). From the simulation is it was estimated that the $J_{SC}$ loss (for cell B) due to parasitic absorption in the ITO and detached reflector is approximately 1 and 0.2 mA/cm$^2$ respectively. It should be noted that the $\eta_{LT}$ curves indicated that for the LPC-Si cells, more light reached the back reflector than for the simulation. Therefore the actual absorption is the reflector was probably slightly larger. Nonetheless, the small simulated parasitic absorption in the reflector fits with the unaffected *IQE* for addition of the reflector observed in Figure 4-5, indicating that the absorptance in the reflector is indeed small.

### 4.1.7 $J_{SC}$ Loss Overview

In this section the measurements and simulations presented in the previous sections are used to derive the $J_{SC}$ losses for cell A and cell B, with and without reflector and with and without ARF.

In order to obtain the $J_{SC}$ loss due to incomplete light trapping ($LT_{loss}$), the difference between the experimental $\eta_{LT}$ and simulated $\eta_{LT,lim}$ is multiplied by 1-$R_{direct}$-$A_{par}$ to convert the efficiency back into a current loss as follows from eq. (17). The $J_{SC}$ loss due to direct reflection was obtained by multiplication of $R_{direct}$ by $\eta_{LT,lim}$. As in eq. (16) the remainder, corrected for the $\eta_{LT,lim}$, equals the loss due to parasitic absorption (± all potential inaccuracies):

$$LT_{\mathrm{loss}} = \left(\eta_{\mathrm{LT,lim}} - \eta_{\mathrm{LT}}\right)\left(1 - R_{\mathrm{direct}} - A_{\mathrm{par}}\right), \tag{18}$$

$$R'_{\mathrm{direct}} = \eta_{\mathrm{LT,lim}} R_{\mathrm{direct}}, \tag{19}$$

$$A'_{\mathrm{par}} = 1 - A_{Si} - LT_{\mathrm{loss}} - R'_{\mathrm{direct}} \tag{20}$$

Figure 4-8 shows examples of the $J_{SC}$ loss analysis for the planar cell A, without reflector or AR foil, and for the textured cell B with reflector and AR foil. Table 4-2 gives an overview of all the $J_{SC}$ losses.

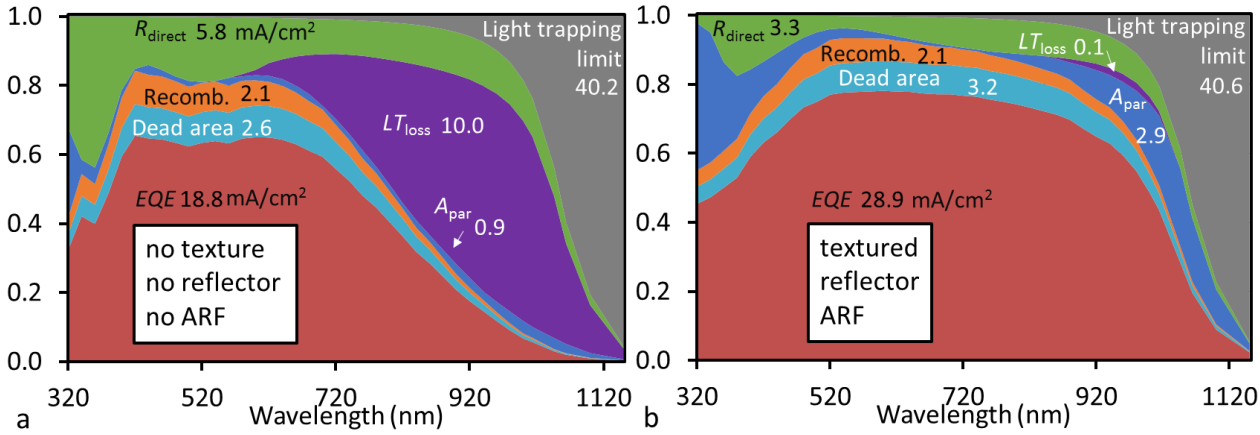


**Figure 4-8.** Wavelength dependent analysis of $J_{SC}$ losses for planar cell A without reflector and AR foil (a) and for textured cell B with reflector and AR foil (b). The corresponding losses in mA/cm² are indicated in the figures.

Without texturing, reflector or ARF (Figure 4-8a), incomplete light trapping ($LT_{loss}$) is the largest loss factor, and $A_{par}$ is very small. Table 4-2 shows how, by using the ARF and reflector, the $LT_{loss}$ decreases from 10 to 3.3 mA/cm² and $R_{direct}$ decreases from 5.8 to 1.9 mA/cm², but at the same time $A_{par}$ increases from 0.9 to 5.5 mA/cm², partly compensating these gains. The *EQE* and electrical losses (dead area and recombination) increase for increased light trapping because they scale with the absorption in the silicon.

**Table 4-2.** Overview of $J_{SC}$ losses (mA/cm²). The colours indicate the high (red), average (orange/yellow) and low (green) $J_{SC}$ losses for each column.

| Cell | ARF | Refl. | *EQE* | Dead area | Recomb. | $A_{par}$ | $LT_{loss}$ | $R_{direct}$ | $J_{SC,lim}$ |
|---|---|---|---|---|---|---|---|---|---|
| A | No | No | 18.8 | 2.6 | 2.1 | 0.9 | 10.0 | 5.8 | 40.2 |
| | | Yes | 21.2 | 3.0 | 2.3 | 2.5 | 5.5 | | |
| | Yes | No | 21.3 | 3.0 | 2.3 | 2.2 | 9.5 | 1.9 | |
| | | Yes | 23.7 | 3.3 | 2.5 | 5.5 | 3.3 | | |
| B | No | No | 25.5 | 2.8 | 1.9 | 2.0 | 1.2 | 7.1 | 40.6 |
| | | Yes | 26.4 | 2.9 | 1.9 | 2.1 | 0.2 | | |
| | Yes | No | 27.9 | 3.1 | 2.1 | 2.5 | 1.7 | 3.3 | |
| | | Yes | 28.9 | 3.2 | 2.1 | 2.9 | 0.1 | | |

For the textured cell (B) with reflector and AR foil (Figure 4-8a), the most important causes for current loss are direct reflection (3.3 mA/cm²), the dead area loss due to the absorber contact (3.2 mA/cm²), parasitic absorption (3 mA/cm²) and bulk and interface recombination (2 mA/cm²). It can be seen that the light trapping loss is negligible for the KOH textured FrontERA cell (with reflector). Using simulation, it was estimated that 1 mA/cm² of $A_{par}$ was due to the TCO and 0.2-0.3 mA/cm² was due to the white paper reflector. From the measured absorptance in the ARF and Boro33, $A_{par}$ losses of ~0.4-0.7 mA/cm² were estimated for both (0.1-0.3 mA/cm² for $\lambda < 450$ nm and 0.3-0.4 mA/cm² for $\lambda > 400$ nm), leaving 0.1-1 mA/cm² for absorption by the absorber contact (and the measurement uncertainties).

### 4.1.8 Discussion of $J_{SC}$ Potentials

In this section the $J_{SC}$ potentials will be discussed. For cell B, the largest $J_{SC}$ loss was the direct reflection loss. It can be seen from $R_{direct}$ for cell A that this loss can be decreased from 3.3 to ~1.9 mA/cm$^2$, by using the optimized interlayer thicknesses. Using simulation in OPAL2, it was determined that this loss can be reduced further to ~1.5-1.6 mA/cm$^2$ by using an optimized $SiO_2/SiN_x/SiO_2$ (PVD) or $SiN_x/SiO_x/SiN_x/SiO_xN_y$ (PECVD) interlayer stack. A possible solution for further reduction of $R_{direct}$ is presented in ref. [76], where a high angle glass/interlayer texturing is made smooth with a $TiO_2$ solgel (n ≈ 2), creating a geometrically smooth surface that is needed for a low defect LPC process [31], while preserving its optical roughness for anti-reflection.

The second largest $J_{SC}$ loss for cell B was the dead area loss. The LBIC measurements indicated that $f_{DA}$ can be reduced from ~11 % to ~7 % by using p-type cells (without interrupted grid fingers). However, the p-type cells generally result in lower $V_{OC}$ values [21]. Alternatively, the dead area loss could be reduced by increasing the spacing between the absorber contacts, but this will also increase both the lateral resistance and the contact resistance, which are already high for the FrontERA cells (see section 3.3.2). The approach chosen in this thesis was to use the point contact device concept, which has an absorber contact area of only 2-4 %.

The third largest $J_{SC}$ loss for cell B was $A_{par}$. Glass absorption could be reduced by replacing the BOROFLOAT33 glass by Corning Eagle glass (Figure 4-4a) or thinning and texturing the glass by sandblasting and HF etching as was done for the record 10.4 % SPC-Si module in ref. [16]. Texturing the glass/air interface could also be used to replace the ARF, which would strongly reduce parasitic absorption. Absorption by the absorber contact will be mostly prevented by switching to the point contact cell concept, due to the smaller contact area and higher reflectivity of the contacts. The optical properties of the ITO are already relatively good, but the absorptance could be reduced further by decreasing the carrier density [77]. This would increase the sheet resistance of the ITO, but that will not cause a significant $R_s$ loss as long as the TCO sheet resistance remains much smaller than the sheet resistance of the c-Si absorber (as the contact spacing is identical for the c-Si and TCO contact fingers).

Considering the high material quality ($L_{eff}$ ≈ 30 ± 4 µm) determined for cell B in section 4.1.5, a reduction of the 2 mA/cm$^2$ recombination loss will require either a fundamental improvement in the LPC-Si material quality or a reduction of the LPC-Si absorber thickness. In section 5.8.6 the optimum absorber thickness will be estimated, using the models described in this chapter and measured (point contact cell) input parameters for the light trapping and parasitic absorption.

## 4.2 Influence of the Frontside Inversion Layer on the Minority Carrier Collection in p-Type LPC-Si Cells

This section is a preprint version of [69] (DOI: https://doi.org/10.1002/solr.201700100). In this section *EQE* and LBIC measurements are used together with electrical simulations to investigate the bias light dependent collection of p-type FrontERA cells inside and outside the cell area.

In the previous section, LBIC measurements indicated that, for the p-type cell (A), the collection below the majority carrier contact and the collection outside the cell area is 2-3 times higher than for the n-type cell (B) (section 4.1.2, Figure 4-2f). Both cells had a $SiN_x/SiO_x/SiO_xN_y$ interlayer stack. Capacitance-voltage (*C-V*) measurements of a 20/100/80 nm $SiN_x/SiO_x/SiO_xN_y$ LPC-Si interlayer stack revealed a high positive fixed charge density at mid gap ($Q_{f,MG}$) of $1.4 \cdot 10^{12}$ $cm^{-2}$ [78], which is similar to the values reported for $SiN_x$:H layers on c-Si wafers [79]. On p-type wafers, such $Q_{f,MG}$ values result in a charge inversion layer [80]. In refs. [81], [82] it was argued with 2D simulation and through experimental results, that it is possible for a backside contacted cell to collect minority charge carriers by conduction through a front floating emitter (FFE), which is similar to a frontside inversion layer. In this section we present evidence supporting the hypothesis that it is possible for a backside contacted (p-type, LPC-Si) cell to collect minority charge carriers by conduction through a frontside inversion layer.

In ref. [34] a strong bias light dependence of the *EQE* was observed for p-type LPC-Si cells with $SiO_2$ interlayer. It was speculated that this is related to the excess carrier density ($\Delta n$) dependence of the effective surface recombination velocity ($S_{eff}$) observed for p-type wafers with $SiO_2$ passivation [83]. Ref. [84] presented p-type LPC-Si cells with a $SiO_2/Al_2O_3/SiO_2$ interlayer stack. It was shown that the bias light dependence of the *EQE* for the cells with $Al_2O_3$ interlayer is much smaller than for the reference cells with $SiO_2/SiN_x/SiO_2$ interlayer stack. $Al_2O_3$ layers have a negative fixed charge density ($Q_{f,MG} \approx -10^{13}$ $cm^{-2}$ on wafers [85]). On p-type silicon, this negative $Q_f$ results in a charge accumulation, instead of the aforementioned charge inversion caused by $SiN_x$ layers on p-type wafers.

In this section, a p-type LPC-Si cell with a $SiO_xN_y$ based interlayer stack ($\eta$ = 11.8%, see section 3.3.5, Table 3-3) and a p-type cell with $Al_2O_3$ based interlayer stack described in ref. [84] are compared using external quantum efficiency (*EQE*) and LBIC measurements (section 4.2.2). Simulation is used to argue that the measured collection and bias light dependence outside the cell area (section 4.2.3) and inside the cell area (section 4.2.4) can be explained by a frontside charge inversion layer.

### 4.2.1 Investigated Cells

The material properties of the two investigated p-type FrontERA cells are summarized in Table 4-1. For the sample with $SiO_xN_y$ interlayer, a 10/200/85 nm $SiN_x/SiO_x/SiO_xN_y$ interlayer stack and 9 µm Si layer were deposited by PECVD on Boro33 glass. For the sample with $Al_2O_3$ interlayer, the first 200 nm $SiO_x$ was deposited by PVD on Corning glass, followed by 30 nm $Al_2O_3$ by atomic layer deposition (ALD) and 10 nm $SiO_2$ by PVD. Subsequently 10 µm silicon was deposited by e-beam evaporation. After this, both samples were crystallized with a laser crystallization scanning velocity of 3 mm/s. The Si absorber of the sample with the $SiO_xN_y$ interlayer (called "$SiO_xN_y$ cell" in this section) had a measured acceptor density ($N_A$) of $6 \cdot 10^{16}$ $cm^{-3}$ and the silicon was textured with KOH, etching away ~1.5 µm. The sample with the $Al_2O_3$ interlayer (called "$Al_2O_3$ cell" in this section) had a measured $N_A$ of $1.5 \cdot 10^{17}$ $cm^{-3}$ and was not textured. FrontERA cells were simultaneously fabricated on these LPC-Si materials.

**Table 4-3.** Investigated Cells

| Cell name & ref. | Glass | Interlayers | | | $N_A$ ($cm^{-3}$) | $d_{abs}$ (µm) | KOH text |
|---|---|---|---|---|---|---|---|
| | | $d_{IL}$ (nm) | Materials | Deposition | | | |
| **$SiO_xN_y$ [10]** | **Boro33** | **15/200/85** | **$SiN_x/SiO_x/SiO_xN_y$** | **PECVD** | **$6 \cdot 10^{16}$** | **7.5** | **yes** |
| **$Al_2O_3$ [15]** | **Corning** | **200/30/10** | **$SiO_2/Al_2O_3/SiO_2$** | **PVD/ALD/PVD** | **$1.5 \cdot 10^{17}$** | **10** | **no** |

### 4.2.2 *EQE* and LBIC Measurements

Figure 4-9a shows the large area *EQE* measurement results of the $SiO_xN_y$ (blue curves) and $Al_2O_3$ (red curves) cells, for a bias light intensity of 0.3 suns (dark curves) and ~$5 \cdot 10^{-4}$ suns (light curves). For the $SiO_xN_y$ cell, the *EQE* curves are shown with a mask (dashed curves) and without a mask (solid curves) that had an opening slightly smaller than the cell area. The difference between the *EQE* curve without and with mask represents the collection outside the cell area.

For the $SiO_xN_y$ cell, it can be seen that the *EQE* measured with mask (dashed) decreases when the bias light intensity is decreased from 0.3 to ~$5 \cdot 10^{-4}$ suns, e.g. at λ = 600 nm the *EQE* decreases from ~70 % to ~60 %. In contrast, for the measurement without mask (solid), it can be seen that the reduction of the bias light intensity results in an increase of the *EQE* from ~70 % to ~120 % (at λ = 600 nm). As mentioned, the difference between the *EQE* curve without and with mask represents the collection outside the cell area, explaining the *EQE* > 100 %. Thus it can be seen that the collection outside the cell area strongly increases with decreasing bias light intensity in case of the $SiO_xN_y$ based interlayer stack. For the $Al_2O_3$ cell, the *EQE* shows almost no bias light dependence, as was published in ref. [84].

Figure 4-9b shows the normalized *EQE* signal, measured at λ = 600 nm, for the $Al_2O_3$ and $SiO_xN_y$ FrontERA cells, with and without mask, as a function of bias light intensity. The *EQE* signal was normalized to the average of the *EQE* signals with and without mask at 0.3 suns. The lowest intensity of $10^{-4}$ suns corresponds

to the intensity of the *EQE* measurement spot at λ = 600 nm (i.e. no bias light).

For the $SiO_xN_y$ cell, the *EQE* measurement with mask shows a steadily decreasing *EQE* for decreasing bias light intensity. It can be seen that the collection outside the cell area ($EQE_{no\ mask} - EQE_{masked}$) increases steadily for decreasing bias light intensities, reaching a maximum at ~$3 \cdot 10^{-4}$ suns. For the $Al_2O_3$ cell, the *EQE* with and without mask is identical, indicating that the collection outside the cell area is negligible. It can also be seen that the bias light dependence of the *EQE* measurement (with mask) is much smaller for the $Al_2O_3$ cell than for the $SiO_xN_y$ cell.

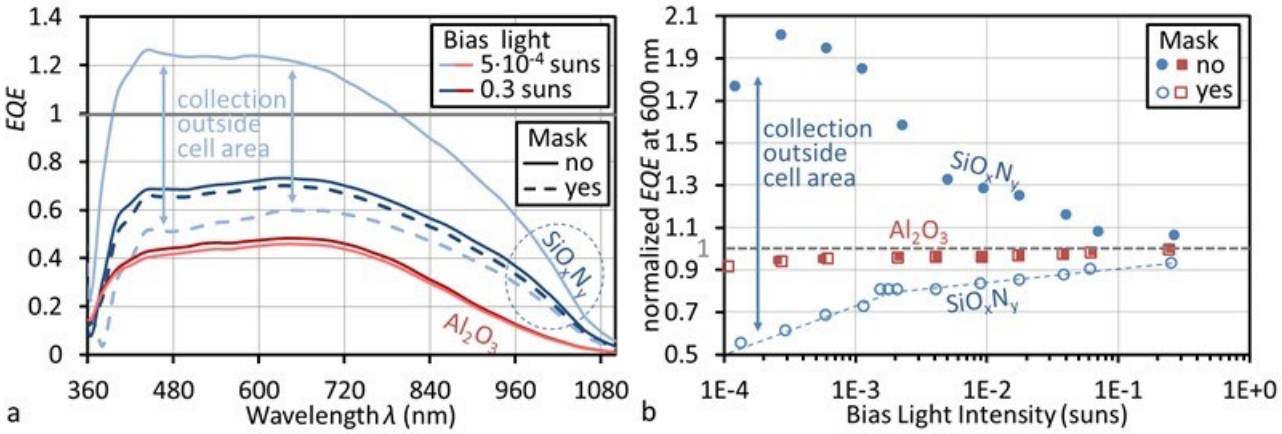


**Figure 4-9.** Figure a shows large area *EQE* measurements of the $SiO_xN_y$ (blue) and $Al_2O_3$ (red) cells, with low bias light intensity ($5 \cdot 10^{-4}$ suns, light curves) and high bias light intensity (0.3 suns, dark curves) and, for the $SiO_xN_y$ cell, with mask (dashed) and without mask (solid). The difference between the *EQE* with and without mask represents the collection outside the cell area. Figure b shows normalized *EQE* measured at $\lambda$ = 600 nm for the $SiO_xN_y$ (blue) and $Al_2O_3$ (red) cells, measured with mask (open symbols) and without mask (closed symbols), as a function of the bias light intensity in suns. The dashed lines are a guide to the eye.

Figure 4-10 shows the normalized LBIC signal for line-scans across the absorber contact and cell edge (see Figure 3-2a) with and without (~0.5 suns) bias light, for the $SiO_xN_y$ and $Al_2O_3$ cells. The grey dotted curves are the calculated collection probabilities ($f_c = e^{-x/Leff}$ [65]) for effective diffusion lengths $L_{eff}$ = 20, 200 and 1000 µm.

It can be seen that, for the $SiO_xN_y$ cell, the LBIC signal outside the cell area is large and strongly bias light dependent. For the $Al_2O_3$ cell, the LBIC signal outside the cell area is small and bias light independent. It can also be observed that the collection from below the (Al) absorber contact is much larger for the $SiO_xN_y$ cell than for the $Al_2O_3$ cell and that this collection is not bias light dependent.

The collection outside the cell area for the $Al_2O_3$ cell can be fitted by the calculated $f_c$ for a diffusion length of 20 µm, which is in line with the typical LPC-Si $L_{eff}$ of 10-40 µm [24], [65], [86] (though it should be noted that the LBIC FWHM spot size is ~30 µm). For the $SiO_xN_y$ cell, the collection outside the cell is 1-2 orders of

magnitude larger and also doesn't quite follow the exponential $f_c$ curves. Instead, (without bias light) the signal drops off at the cell edge by about 30-40 %, followed by a much slower decay.

In section 4.2.3 it will be discussed how the collection outside the cell area can be explained and in section 4.2.4 it will be discussed how the bias light dependence of the collection inside the cell area can be explained.

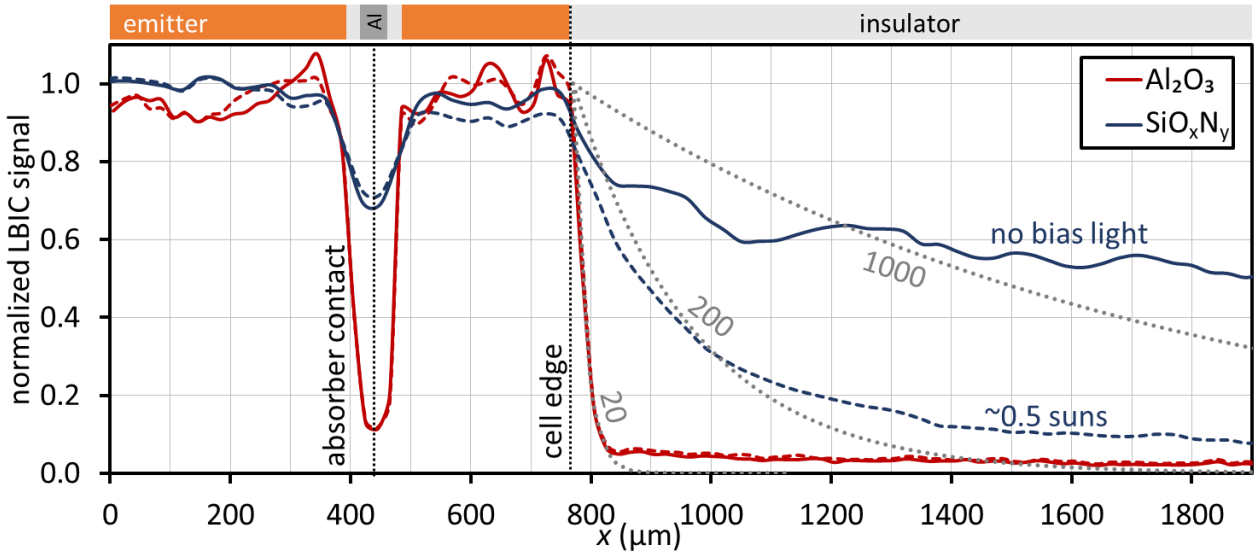


**Figure 4-10.** The normalized LBIC linescan and simplified schematic cross-section of the Al absorber contact and cell edge (see Figure 3-2a) for the $SiO_xN_y$ (blue) and $Al_2O_3$ (red) cells with (dashed line) and without (solid line) bias light (~0.5 suns). The calculated collection probability ($f_c = e^{-x/Leff}$) curves (grey, dotted), for effective diffusion length $L_{eff}$ = 20, 200 and 1000 µm, are plotted for comparison.

### 4.2.3 Collection Outside the Cell Area

In this section we provide an explanation for the observed collection of charge carriers from outside the cell area using three arguments: a comparison of the $Al_2O_3$ and $SiO_xN_y$ cells (A), wavelength dependence of the collection outside the cell area (B) and bias light dependence of the collection outside the cell area (C).

#### A. Comparison of the $Al_2O_3$ and $SiO_xN_y$ Cells

There are three potential collection paths for the charge carrier collection from outside the cell area: the back, the bulk and the front, i.e. collection through a hypothetical backside inversion layer, diffusion within the absorber and collection through a frontside inversion layer (generated by the positive charge in the $SiO_xN_y$ interlayer).

The backside of the $Al_2O_3$ and $SiO_xN_y$ cells is identical, as they were processed simultaneously. As the $Al_2O_3$ cell doesn't show a large charge carrier collection outside the cell area, collection through a backside layer

cannot explain the carrier collection observed for $SiO_xN_y$ cell. In Figure 4-10 it can be seen that the charge carrier collection outside the cell area is still high far away (> 200 µm) from the cell edge. An $L_{eff}$ of 200-1000 µm would be required to explain this with collection by diffusion within the LPC-Si absorber, which is not realistic since $L_{eff}$ = 10-40 µm for LPC-Si [24], [65], [86]. Also, the $L_{eff}$ would have to increase from ~200 to ~1000 µm for decreasing bias light intensity, instead of decreasing as would be inferred from the decreasing collection (*EQE*) inside the cell area. Therefore, by exclusion of the back and the bulk, it can be concluded that the observed charge carrier collection from outside the cell area is related to the frontside.

### B. Wavelength Dependence

Figure 4-11a shows a schematic cross-section of the FrontERA cell with $SiO_xN_y$ based interlayer. The arrows indicate the uniform bias light (yellow) and local LBIC laser light (red) coming through the glass. The figure includes representations of four factors which determine the collection from outside the cell area:

I. The collection efficiency ($\eta_c(\lambda)$), for diffusion towards the inversion layer,
II. The collection probability ($f_c(d)$, where $d$ is the absorber thickness) for diffusion from the inversion layer to the emitter,
III. The operating voltages and corresponding currents of the p-n junctions created by the charge inversion layer. In Figure 5a it can be seen how the current has to flow in opposite directions through the diode inside the cell area (orange) and the diode outside the cell area (green). Appendix A.1 provides a qualitative explanation of this effect (adapted to our cells from ref. [81]).
IV. The resistance loss $\Delta V = IR$ in the inversion layer, where $I$ is the current and $R$ is the resistance of the inversion layer. In section 4.2.3C simulation will be used to determine if the observed bias light dependence of the collection outside the cell area can be explained by the resistance in the inversion layer ($R$).

Of these four factors only the first factor depends on the wavelength of the incoming light: short wavelength light is absorbed close to the inversion layer and therefore has a higher collection efficiency for diffusion toward the inversion layer than the long wavelength light, which is absorbed more uniformly in the LPC-Si material (see section 2.7). The opposite wavelength dependence is expected for collection at the backside.

Figure 4-11b shows *IQE* curves measured inside (orange) and outside (green) the cell area of the $SiO_xN_y$ cell, with a low bias light intensity of ~$3 \cdot 10^{-3}$ suns. The *IQE* curves were fitted with the $\eta_c(\lambda)$ equations that describe collection at the frontside (section 2.7, eq. (6)-(7)) and collection at the backside (eq. (6)-(8)). The comparison between measured *IQE* and calculated $\eta_c(\lambda)$ confirms that the minority carriers generated

outside the cell area are initially collected at the frontside (and the minority carriers generated inside the cell area are collected at the backside).

The short wavelength light (λ < 450 nm) is absorbed very close to the interlayer. If this light is absorbed outside the cell area, the generated minority carriers are directly collected at the inversion layer, resulting in a calculated $\eta_c$ (λ < 450 nm) ≈ 100 %. The calculated $\eta_c$ was therefore multiplied by the measured *IQE* at 450 nm (48 %) to account for the three wavelength independent loss factors (Figure 4-11a, factors II-IV)). If the short wavelength light is absorbed inside the cell area, the generated minority carriers subsequently diffuses from the interlayer to the emitter. Therefore, the *IQE* inside the cell area for λ = 450 nm approximately equals the collection probability for diffusion from the interlayer to the emitter $f_c(d)$ (II). In Figure 4-11b it can be seen that the 1 - $f_c(d)$ loss can explain most of the observed *IQE*(450 nm) = 48 %. The remainder is presumable caused by the diodes (factor III) and the resistance in the inversion layer (IV).

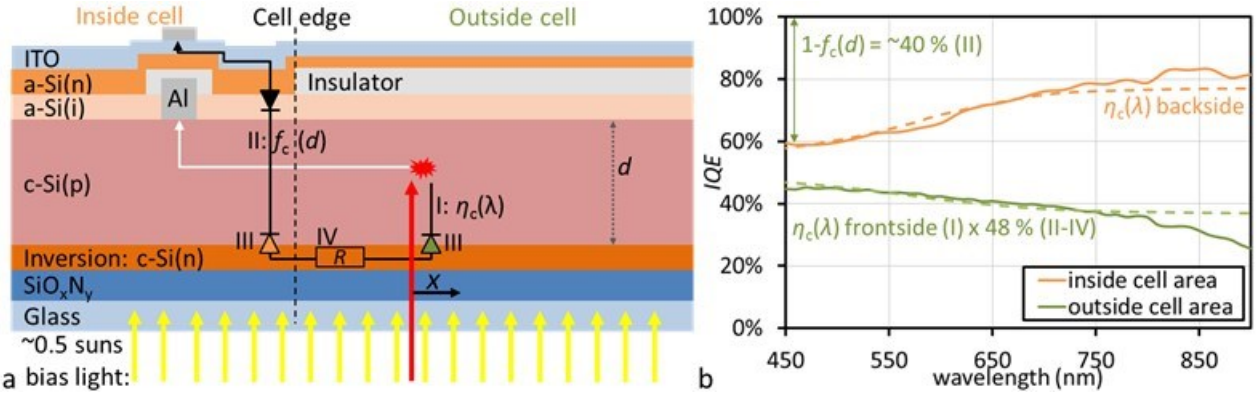


**Figure 4-11.** Figure a shows schematic cross-section of the FrontERA edge and absorber contact (for the $SiO_xN_y$ cell). The yellow and red arrows indicate the bias and LBIC laser light. The black and white arrows indicate the collection path for the generated minority and majority carriers. The roman numerals (I-IV) indicate the different factors determining the collection probability through the inversion layer. Figure b shows small spot *IQE* measurements inside and outside the cell area of the $SiO_xN_y$ cell (solid lines). The dashed lines are calculated collection efficiency ($\eta_c$) curves, using equations for collection at the frontside (section 2.7, eq. (6)-(7)) and for collection at the backside (eq. (6), (8)). The calculated $\eta_c(\lambda)$ for frontside collection (factor "I") was multiplied by the measured *IQE*(λ = 450 nm) ≈ 48 % (presumably caused by the wavelength independent factors "II-IV"). The collection probability for diffusion from the inversion layer to the emitter ($f_c(d)$) (factor "II") approximately equals the backside $\eta_c$ at 450 nm.

### C. Bias Light Dependence

In this section, simulations are performed in order to determine if the sheet resistance of the inversion layer can quantitatively explain the measured bias light dependence outside the cell area. In order to determine the sheet resistance of the inversion layer, the electron and hole densities ($n$(x) and $p$(x)) of the inversion layer at the $SiO_xN_y$/LPC-Si(p) interface were simulated in AFORS-HET [87]. As input parameters we used the measured $Q_{f,MG}$ = 1.4·10$^{12}$ cm$^{-2}$ and defect density at midgap $N_{it,MG}$ = 4·10$^{11}$ cm$^{-2}$, based on the

*C-V* measurements in ref. [78]. In AFORS-HET, a 1 nm c-Si defect layer, with a defect density of $4 \cdot 10^{18}$ cm$^{-3}$ was used to simulate $N_{it}$. The hole/electron capture cross sections ($\sigma_{p/n}$) of the $SiO_xN_y$/LPC-Si interface were not measured, nor are there (to our knowledge) corresponding literature values. For a charge inversion in c-Si(p), holes are the minority charge carriers and therefore, $\sigma_p$ will determine $S_{eff}$. Literature values for $\sigma_p$ vary from $10^{-17}$ cm$^2$ for the $SiO_x$/c-Si interface [88], to $\sigma_p \approx 10^{-13}$ cm$^2$ for the $SiN_x$/c-Si interface [89]. For our simulations, we assumed $\sigma_{p/n} = 10^{-15}$ cm$^2$.

Figure 4-12a shows the simulated $E(x)$, $n(x)$ and $p(x)$ for the $SiO_xN_y$/LPC-Si(p) charge inversion layer. It can be seen how the positive fixed charges in the $SiO_xN_y$ repel the positive charges in the c-Si(p) and induce negative charges in the c-Si(p) near the surface, causing a charge inversion. A strong charge inversion, as shown in figure 7 ($p_{surface} << n_{bulk}$), can passivate the silicon surface just as well as a charge accumulation [90].

By integrating the simulated $n(x)$ in the inversion layer, it is possible to estimate the sheet resistance of the inversion layer [91]. The majority carrier mobility ($\mu$) in the inversion layer is relatively low, which is mainly due to Coulomb scattering. Based on the data in ref. [92], we estimate $\mu \approx 150$ cm$^2$/Vs. This results in an order of magnitude estimate for the sheet resistance of the inversion layer of $10^5$ Ω/□. A variation of $\sigma_p$ from $10^{13}$ to $10^{17}$ cm$^{-2}$ did not affect this estimate.

In order to determine if the bias light dependence of collection outside the cell area in Figure 4-9 can be explained by the sheet resistance of the inversion layer, resistance simulations were performed with Quokka 2 [93]. In order to compare the simulated collection to the measured collection outside the cell area, the measured *EQE* (λ = 600 nm) data from Figure 4-9b was converted into the ratio of the collection outside the cell area to the collection inside the cell ($EQE_{out/in}$) using:

$$EQE_{out/in} = \frac{EQE_{no\ mask} - EQE_{mask}}{EQE_{mask}}. \qquad (21)$$

In the 2D Quokka simulations, the $J_{SC}$ was determined for a 10 µm thick, 1.5 cm long solar cell structure with a single contact on the left, for uniform illumination intensities between $10^{-3}$ and 1 sun and an absorber sheet resistance of $10^5$ Ω/□. The simulated structure is shown in Figure 4-12b. The sheet resistance of the emitter was set to 20 Ω/□ to ensure that the resistance in the emitter was negligible. The $J_{SC}$ (for full collection and 1 sun illumination) was reduced optically to 15 mA/cm$^2$, in order to roughly approximate the collected current density through the inversion layer, which is lower than the cell $J_{SC}$ due to factors I-III. The diffusion length was set to 20 µm. The obtained current collection in mA/cm was divided by the relative illumination intensity (suns) and multiplied by the circumference of the cell without the bus

bar (2.2 cm) to obtain the approximate total current collected outside the cell area in mA. This was then divided by the approximate total current from within the cell area (22 mA/cm$^2$ × 0.6 cm$^2$) to obtain the ratio of the collection outside/inside the cell area.

The measured $EQE_{out/in}$ and the simulation result, for $10^5$ Ω/□, is shown in Figure 4-12c. It can be seen that the simulation fits the measured data very well. Variation of the estimated input parameters shifts the simulated $EQE_{out/in}$ vs bias light intensity curve up and down, but doesn't significantly change its slope (not shown). This indicates that the bias light dependence of the collection outside the cell area can be explained by the resistance in the inversion layer.

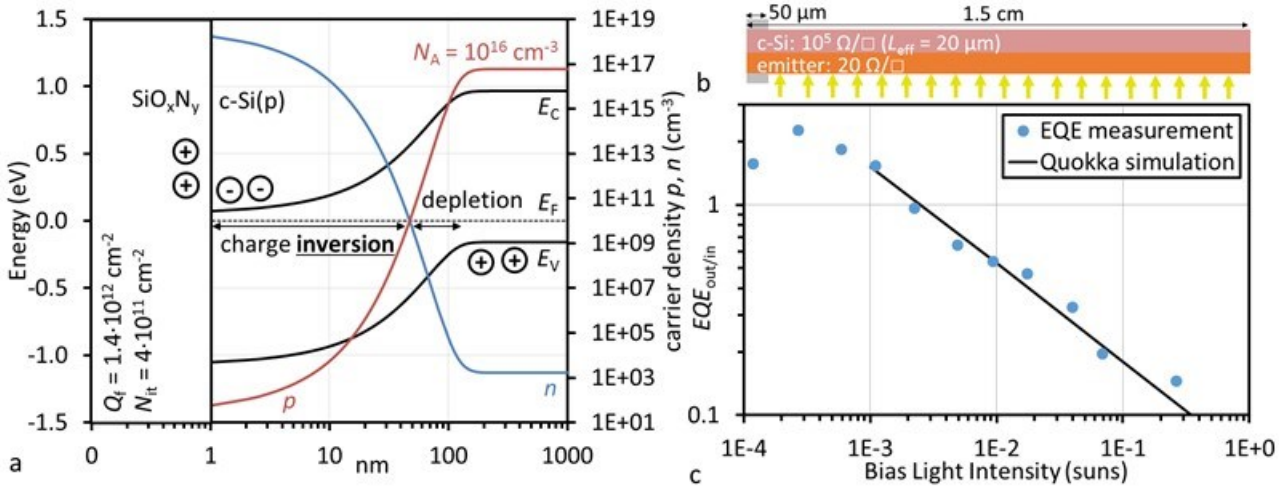


**Figure 4-12.** Fig a shows the simulated band diagrams and hole ($p$) and electron ($n$) densities for a $SiO_xN_y$/c-Si(p) charge inversion using AFORS-HET[87]. The fixed charge density ($Q_f$), interface trap density ($N_{it}$) and c-Si(p) acceptor density ($N_A$) are given in the figure. Fig. b shows a cross-section of the structure simulated in Quokka. Fig. c shows the collection outside the cell area divided by the collection inside the cell area ($EQE_{out/in}$), for the $EQE$ measurements from Figure 4-9b (dots) and for the 2D simulation in Quokka (line).

### 4.2.4 Bias Light Dependent Collection Inside the Cell Area

In this section, it will be attempted to explain the bias light dependence of the $EQE$ inside the cell area for the $SiO_xN_y$ and $Al_2O_3$ cells. For this purpose the excess carrier density ($\Delta n$) dependence of the effective surface recombination velocity ($S_{eff}$) will be modelled, using the extended Shockley-Read-Hall surface recombination model, solved according to ref. [94].

Figure 4-13 shows the modelled $S_{eff}$ vs. the bulk excess charge carrier density ($\Delta n$) for the $SiO_xN_y$ and $Al_2O_3$ interlayers, using the aforementioned input parameters for the $SiO_xN_y$ interlayer and also for a reduced $Q_f$ of $10^{12}$ cm$^{-2}$. For the $Al_2O_3$ interlayer, there is no $C$-$V$ measurement data and therefore $N_{it} = 4 \cdot 10^{11}$ cm$^{-2}$ and $Q_f = -10^{11}$, $-10^{12}$ or $-10^{13}$ cm$^{-2}$ were used as input parameters. The uncertainty of $Q_f$ and $N_{it}$ for the $Al_2O_3$ interlayer and of $\sigma_{p/n}$ for both interlayers (see section 4.2.3.C) introduces a quantitative inaccuracy, but

the purpose of this calculation is to determine the qualitative dependence of $S_{eff}$ on $\Delta n$.

It can be seen that, for the $SiO_xN_y$ structure, $S_{eff}$ increases for decreasing $\Delta n$, especially for the simulation with $Q_f = 10^{12}$ cm$^{-2}$. In contrast, the $S_{eff}$ of the "$Al_2O_3$" layer is unaffected by $\Delta n$, for $\Delta n < 10^{12}$ cm$^{-3}$, independent of the chosen $Q_f$. This fits with the much lower BL dependence for the *EQE* of the $Al_2O_3$ cell. It can be concluded that the increasing $S_{eff}$ for decreasing $\Delta n$ (for $\Delta n < 10^{12}$ cm$^{-3}$) is typical for the inversion type passivation.

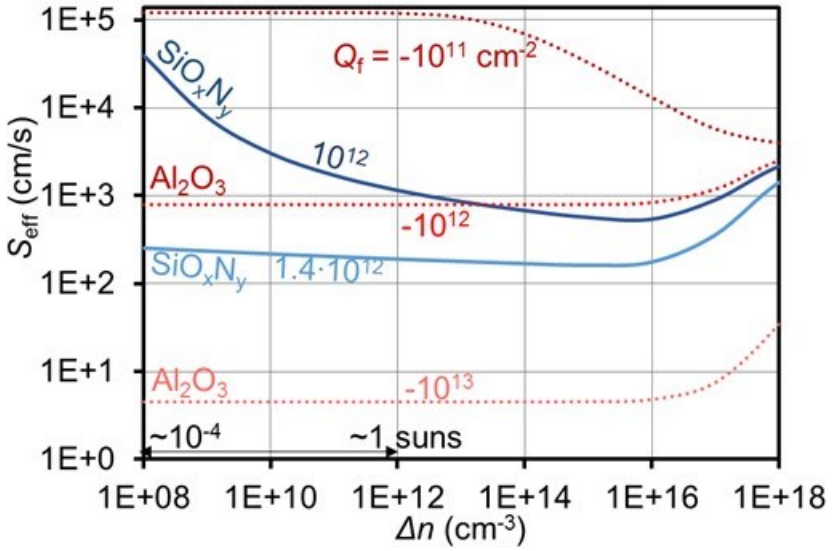


**Figure 4-13.** Effective surface recombination velocity $S_{eff}$ vs. the bulk excess carrier density $\Delta n$ for the $SiO_xN_y$ (blue) and $Al_2O_3$ (red) samples for the fixed charge densities ($Q_f$) indicated in the figure. The approximate bias light intensities in suns corresponding to the $\Delta n$, as simulated for $J_{SC}$ conditions in AFORS-HET, are indicated in the figure.

In order to estimate $\Delta n$ for the *EQE* measurements in Figure 4-9b, AFORS-HET simulations of a 10 µm c-Si(p) absorber with $L$ = 20 µm were made, for 0 V ($J_{SC}$) and light intensities between $10^{-4}$ and 1 sun. This resulted in a simulated $\Delta n$ of ~$10^8$ – $10^{12}$ cm$^{-3}$. Therefore, it can be concluded that the bias light intensity of $10^{-4}$ to 1 sun in Figure 4-9b roughly corresponds to $\Delta n = 10^8 – 10^{12}$ cm$^{-3}$ in Figure 4-13. By comparison of these figures it can be seen that the dependence of $S_{eff}$ on $\Delta n$, for $Q_f = 10^{12}$, roughly corresponds to the decreasing *EQE* for decreasing bias light intensity. This doesn't necessarily mean that the actual $Q_f$ is lower than the $Q_f$ determined by the *C-V* measurements. Alternatively, $N_{it}$ or $\sigma_p$ might be higher than the values used in the simulation.

In addition, the AFORS-HET simulations were also made at $V_{OC}$ and MPP conditions, resulting in a simulated $\Delta n$ of ~$10^{14}$ and ~$10^{13}$ cm$^{-3}$ respectively. In Figure 4-13 it can be seen that this results in a higher $S_{eff}$ (more recombination) at MPP than at $V_{OC}$, thereby reducing the *FF* [95].

### 4.2.5 Conclusions

*EQE* and LBIC measurements of a p-type FrontERA cell on LPC-Si with $SiO_xN_y$-based interlayer, showed a large, bias light dependent collection outside the cell area. This was in contrast to a simultaneously fabricated FrontERA cell with an $Al_2O_3$ based interlayer stack. The measured collection from below the absorber contact was also much higher for the $SiO_xN_y$ cell.

Using these two p-type LPC-Si cells, we argued that, for backside contacted solar cells, minority carriers can be collected through a frontside charge inversion layer:

1. The very small and bias light independent collection outside the cell area for the $Al_2O_3$ cell showed that the collection outside the cell area for the $SiO_xN_y$ cell cannot be due to collection through a backside layer. The magnitude of the collection showed that the collection cannot be due to diffusion within the bulk. By exclusion, the only remaining collection path is through the frontside inversion layer.
2. The wavelength dependence of the *IQE* measurement outside the cell area could be fitted by the collection efficiency ($\eta_c(\lambda)$) equations for collection at the frontside.
3. Using AFORS-HET, it was simulated that, for the investigated p-type LPC-Si with a $SiO_xN_y$-based interlayer stack, the measured positive fixed charges in the interlayer result in a passivating charge inversion layer, with a sheet resistance of ~$10^5$ Ω/□. Using 2D resistance simulations in Quokka, the measured bias light dependence of the collection outside the cell area could be explained by the resistance in the ~$10^5$ Ω/□ inversion layer.

The *EQE* of the $SiO_xN_y$ cell inside the cell area also showed a strong bias light dependence. Simulation of the effective surface recombination at the $SiO_xN_y$/LPC-Si interface for excess carrier densities between $10^8$ and $10^{12}$ $cm^{-3}$ could explain this bias light dependence between $10^{-4}$ and 1 sun.

## 4.3 Conclusions

In this chapter the photocurrent of LPC-Si FrontERA cells was investigated, using LBIC, *EQE* and optical measurements. The measurement results were analysed using optical simulation in PV Lighthouse's OPAL2 and online ray tracer and electrical simulations in AFORS-HET and Quokka.

Using LBIC measurements, it was shown that the collection from below the absorber contact and from outside the cell area is 2-3 larger for p-type than for n-type FrontERA cells. Using simulation and bias light dependent *EQE* and LBIC measurements of p-type cells with $SiO_xN_y$ or $Al_2O_3$ based interlayer stacks, it was argued in three different ways that this collection could be explained by a frontside charge inversion layer, induced by fixed charges in the $SiO_xN_y$ layer. Using the calculated $\Delta n$ dependence of the $S_{eff}$, it was further argued that this inversion layer is also responsible for the bias light dependence (and reduced *FF*) of the

p-type LPC-Si cells.

Using LBIC measurements, a slope in the *J-V* curve at $J_{SC}$, for a p-type FrontERA cell, could be explained as a distributed series resistance caused by grid fingers that were interrupted by LPC-Si cracks, confirming a hypothesis from ref. [46].

The large dead area losses due to electrical shading by the absorber contact and interrupted grid fingers, as well as the measurement difficulties due to collection outside the cell area, provide part of the motivation for switching to the point contact cell concept.

Reflection measurements indicated that the textured anti-reflection foil causes a reduction of $R_{direct}$ by 50-65 % and a shift of ~40 nm to shorter wavelengths. It was argued that this is caused by a combination of (1) reduction of the reflection at the glass-air interface and (2) total internal reflection at the glass-air interface of light that was reflected by the glass/interlayer/Si interface. Using optimized NO(ON) interlayer thicknesses and the ARF, the $R_{direct}$ loss could be reduced to 1.9 mA/cm$^2$. Simulation indicated that this could be reduced further to 1.5 mA/cm$^2$ by using an ONO or NON(ON) interlayer stack.

For the KOH textured cell (with detached white paper reflector), it was shown that the light trapping efficiency ($\eta_{LT}$) was higher than the simulated $\eta_{LT}$ for a Lambertian reflector and very close to the simulated $\eta_{LT}$ for mono-Si pyramids. As it was argued that the $\eta_{LT}$ for these mono-Si pyramids constitutes the light trapping limit for geometrical optics, the incomplete light trapping loss was estimated at 0.1 mA/cm$^2$.

From the *IQE* measurement it could be seen that, contrary to the planar cell, the addition of the reflector and ARF did not significantly increase the parasitic absorption for $\lambda > 700$ nm. It was concluded that texturing the Si absorber strongly reduces the relative parasitic absorption ($A_{par}$) by trapping most of the light within the absorber layer. The $A_{par}$ loss for the textured cell with reflector and ARF was estimated at 3 mA/cm$^2$. Using simulation, it was estimated that 1 mA/cm$^2$ of this was due to the TCO and 0.2-0.3 mA/cm$^2$ was due to the white paper reflector. From the measured absorptance in the ARF and Boro33, $A_{par}$ losses of ~0.4-0.7 mA/cm$^2$ were estimated for both, leaving 0.1-1 mA/cm$^2$ for absorption by the absorber contact (and the measurement uncertainties). It was proposed that the $A_{par}$ losses could be reduced by thinning and texturing the glass as was done for the 10.4 % CSG mini-module in ref. [16] and by reducing the carrier density in the ITO.

The $J_{SC}$ analysis methods and results presented in this chapter will be used in section 5.6 to analyse the point contact cells and to estimate the optimum absorber thickness and LPC-Si $J_{SC}$ potential.

# 5 Solar Cells with Laser Fired Absorber Point Contacts and Heterojunction Emitters for Textured LPC-Si

*This chapter describes the development and analysis of backside contacted LPC-Si cells with heterojunction emitters and laser fired absorber point contacts. The starting point for this cell development is an 11.5 %, planar, $2{\cdot}10^{16}$ $cm^{-3}$ doped, n-type point contact cell* [30]*, which was mainly limited by a high $R_s$. In this chapter we describe the implementation new emitters to reduce $R_s$, a higher absorber doping to increase $V_{OC}$ (and reduce $R_s$) and KOH texturing to increase $J_{SC}$. Measurements and simulations are used to determine the $R_s$ losses and potentials and to estimate the optimum point contact spacing as a function of absorber doping. A passivated isolation scribe is implemented to prevent an observed recombination problem and a new point contact cell with an efficiency of 12 % is presented and compared to the 11.5 % cell from ref.* [30]*. Comparison of the photocurrent losses of the point contact cells to those of the FrontERA cells from section 4.1 reveals that parasitic absorption and light trapping losses are higher for point contact cells. It is argued that this is mainly due to the attached white reflector and several solutions are discussed to prevent these losses. It is also argued that, for the LPC-Si absorbers in this study, the absorber thickness should be reduced to ~6 µm to reduce recombination losses.*

## 5.1 Introduction

Development of crystalline silicon on glass (CSG) at UNSW included the development of a corresponding backside point contacting scheme on which the device in this chapter is based [13], [96]. A 30×40 $cm^2$ mini-module pilot plant by Pacific Solar [97], and subsequent industrial production of 1.38 $m^2$ point contacted, solid phase crystallized silicon (SPC-Si) modules by CSG Solar AG [16], showed the industrial compatibility of the point contact process.

For SPC-Si, the initial doping profile is more or less maintained during crystallization and it was therefore possible to create thin, highly doped crystalline silicon layers, acting as front side emitter and back surface field. After the SPC process, a laser isolation scribe (isoscribe) was made to separate the SPC-Si into cells and a hydrogen plasma passivation was used to reduce the defects [23]. A white resin was applied on the film and point contact openings to the emitter and BSF were made by inkjet printing with a KOH based ink. This was followed by the deposition of an Al layer, contacting the emitter and BSF. Finally, a laser was used to structure the Al layer into interdigitated fingers. This process resulted in a 94 $cm^2$ mini-module with an independently verified record efficiency of 10.4 % by CSG Solar [16]. The $V_{OC}$ of this SPC-Si module was only 492 mV/cell, showing the need for a higher material quality, e.g. LPC-Si. The schematic cross-section and top view image of this SPC-Si point contact module are shown in Figure 5-1a and b. It can be seen that

the BSF point contacts of cell 1 are connected to the emitter point contacts of cell 2, thereby creating a module interconnection between the cells.

Contrary to SPC-Si, LPC-Si results in a uniformly doped c-Si layer, requiring a separate emitter formation. At UNSW this was solved by using a high temperature phosphorus diffusion process on an LPC-Si (p) absorber to create a homo-junction, resulting in a cell efficiency of 11.7 % with a $V_{OC}$ of 585 mV, a $J_{SC}$ of 27.6 mA/cm$^2$ and a *FF* of 72.4 %. This cell, shown schematically in Figure 5-1c, was made on a ~8·10$^{15}$ cm$^{-3}$ doped, planar, p-type absorber and sputtered ONO interlayer stack [20], using a point contacting scheme based on that of CSG Solar. However, this cell efficiency was not stable, degrading over time to 10 % due to a problem with the c-Si(p)/Al absorber contact.

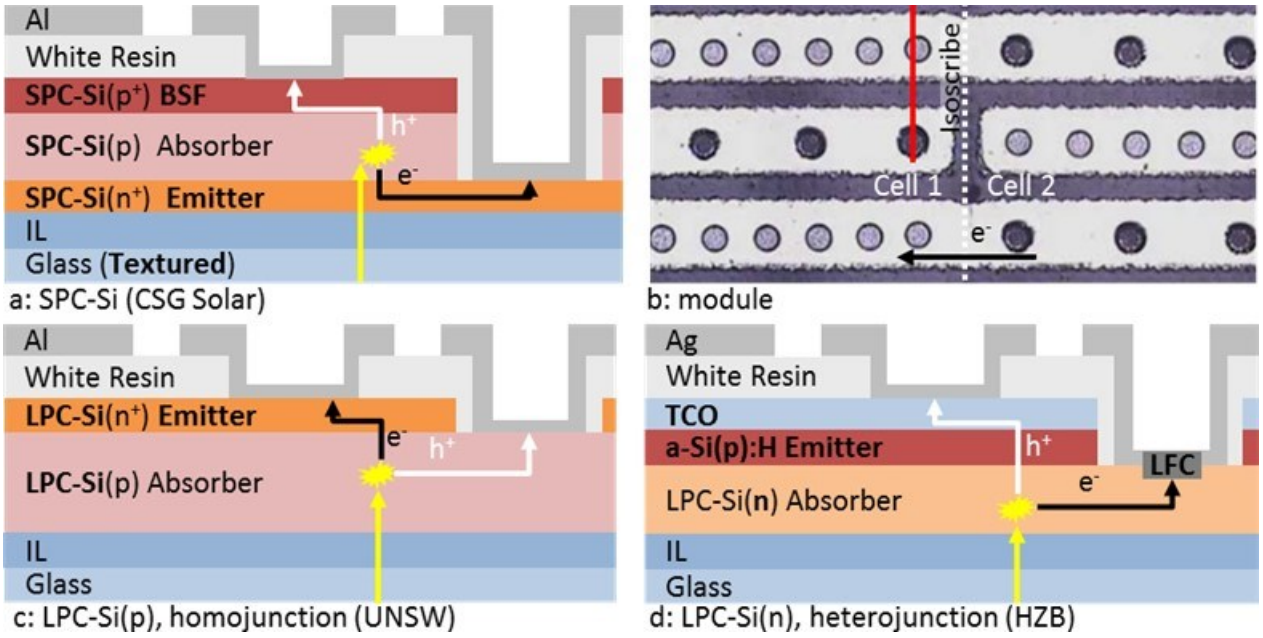


**Figure 5-1.** Figure a shows a schematic cross-section of the p-type SPC-Si point contact cell, developed at CSG Solar [16]. Figure b shows a top-view image from ref. [12] of the mini-module interconnection. The red line indicates the position of the cross-section in fig. a. Figure c shows a schematic cross-section of the p-type LPC-Si point contact cell with diffused homo-emitter developed at UNSW [20]. Figure d shows a schematic cross-section of the n-type LPC-Si point contact cell with silicon heterojunction (SHJ) emitter and laser fired contacts (LFC) developed at HZB [30]. The arrows indicate the direction of the light (yellow) and of the generated electrons (black) and holes (white).

At HZB, the absorber contacts of p-type point contacts cells from UNSW were laser fired, resulting in a stable, low contact resistivity without increasing the point contact opening [29]. The point contact cell concept at HZB was further adapted from homo- to hetero-junction emitters and from p- to n-type absorbers, resulting in a cell efficiency of 11.5 % with a $V_{OC}$ of 619 mV, a $J_{SC}$ of 28.2 mA/cm$^2$ and a *FF* of 65.5 % [30]. This cell, shown schematically in Figure 5-1d, was made on a planar, 9 µm thick, ~2·10$^{16}$ doped, n-type absorber with a 15/200/60/20 nm NON(ON) PECVD interlayer stack. The efficiency of this cell was

mainly limited by the low *FF* of 65.5 %, caused by an $R_s$ of 5.2 Ωcm$^2$, determined from the slope of the *J-V* curve at $V_{OC}$. The measured $R_s$ contributions by the absorber and TCO point contacts were only 0.2 and 0.1 Ωcm$^2$ respectively and it was therefore argued that the high cell $R_s$ was caused by the a-Si(p)/TCO contact resistance. It was also discussed that the lack of backside texturing resulted in a lower *EQE* in the long wavelength region.

In this chapter a modified point contact process is presented with the following elements: an improved absorber contact etch process, new emitters to decrease the $R_s$, an increase of the absorber doping to increase the $V_{OC}$ and decrease the $R_s$, KOH texturing to increase the $J_{SC}$ and an adapted isoscribe process to increase the *FF*. Analysis of the $R_s$ and $J_{SC}$ losses in the resulting device, led to the identification of several other potential efficiency improvements.

Section 5.2 describes the fabrication of the material, point contact cells and test structures used in this chapter, followed by an overview of the investigated cells. In section 5.3 the etching in the absorber point contact opening is investigated for different emitter/TCO combinations and etch solutions, attempting to prevent shunting without increasing the dead area loss. In section 5.4, measurements and simulations are used to show how the point contact resistance depends on the absorber doping. The dead area and resistance results from section 5.3 and 5.4, are then used to estimate the optimum point contact spacing as a function of absorber doping. In section 5.5 test structures are used to analyse many different emitter/TCO combinations, attempting to reduce the $R_s$ without reducing the $V_{OC}$. Also, the resistance of n-type point contact cells with different emitters is analysed, resulting in an overview of the $R_s$ losses and potentials. In section 5.6 a recombination problem at the isolation scribe is identified, requiring the introduction of passivated isolation scribes. In section 5.7 a resulting point contact cell with an efficiency of 12 % is compared to the 11.5 % cell from ref. [30], indicating how the developments described in this chapter increased the cell efficiency. In section 5.8 the photocurrent losses of textured point contact cells are analysed and compared to those of the FrontERA cells from chapter 4, which is followed by a discussion of the $J_{SC}$ potentials and optimum absorber thickness.

## 5.2 Fabrication

Section 5.2.1 describes the interlayer and absorber fabrication and section 5.2.2 the emitter/TCO deposition, insofar they deviate from the fabrication process described in chapter 3. Section 5.2.3 describes the fabrication of the point contact cells and TLM structures, which is followed by the fabrication of the test (quasi) cells in section 5.2.4 and emitter/TCO resistivity test structures in section 5.2.5. Section 5.2.6 will present an overview of the six experiments which provided the investigated cells in this chapter.

### 5.2.1 Interlayer and Absorber

The fabrication of the PECVD (AKT) (and PVD/e-beam) material was described in section 3.2 and also applies to the material used in this chapter. Unless mentioned otherwise, all the absorbers in this chapter are KOH textured. All PECVD (AKT) absorbers on Boro33 glass were crystallized with 10 mm/s to minimize bubbles in the glass (see section 3.3.3), which can interrupt the isolation scribe by scattering the laser beam.

Some of the interlayers in this chapter were deposited in a different PECVD tool, which will be referred to as "PC1". These 200/60/10 nm $SiO_x/SiN_x/SiO_x$ interlayers (recipes in Table 5-1) were deposited both on Corning and on Boro33 substrates. Subsequently, the precursors for these interlayers were deposited by e-beam evaporation. The absorber doping was determined by deposition of a thin a-Si(n) layer on the precursor before crystallization, similar to the PECVD precursors (see section 3.2.2).

**Table 5-1.** Recipes of the PECVD Interlayers from the "PC1".

| Tool, area, freq. | layer | T (°C) | Power (W) | Pressure (mbar) | Spacing (mm) | $SiH_4$ (sccm) | $H_2$ (sccm) | Other gas (sccm) (gas) | DR (nm/s) |
|---|---|---|---|---|---|---|---|---|---|
| **PC1, 314 $cm^2$, 13.56 MHz** | **$SiO_x$** | 400-600 | 160 | 0.5 | 13 | 8 | 0 | 100 ($CO_2$) + 100 ($N_2O$) | 1.1 |
| | **$SiN_x$** | 400-600 | 130 | 0.8 | 13 | 3 | 0 | 100 ($N_2$) + 3.5 ($NH_3$) | 0.29 |

### 5.2.2 Emitter and TCO

Several different emitter and TCO layers were used than in chapter 3 in an attempt to reduce the emitter/TCO resistance and for compatibility with the point contact etching process. The emitter layers in this section are either amorphous (a-Si) or nano-crystalline (nc-Si), where the latter can potentially result in a lower resistance [98]–[100]. The nc-Si layer has a deposition process which can damage the underlying layers [101]. The rate at which the nc-Si layer nucleates during the deposition can be influenced by many factors like surface treatment, morphology and doping gas [98], [102], [103]. For the p-type emitters, the doping gas was either TMB or $B_2H_6$, where the latter is known to result in much higher conductivity [104], potentially resulting in lower resistance losses. The emitter recipes, deposited in the AKT PECVD, are listed in Table 5-2. The nc-Si(p) layer consists of a 10 s (~1-2 nm) nucleation step, followed by a ~28 nm thick layer and finished by a 1-2 nm, higher doped contacting layer. The deposition rate was estimated for textured wafers by division of the measured deposition rate on planar wafers by a geometry factor of 1.7 [105]. It should be noted that for the tilted pyramids on textured LPC-Si the geometry factor and corresponding deposition rate depend on the pyramid/grain orientation. None of these recipes were developed as part of this thesis, but they were used in new combinations. Unless mentioned otherwise, the emitters in this chapter consisted of a ~6 nm a-Si(i) layer, followed by a ~6 nm a-Si(n/p) layer and a

20/30 nm nc-Si(n/p) layer.

**Table 5-2.** Emitter Recipes from the "AKT"

| layer | T (°C) | Power (W) | Pressure (Torr) | Spacing (mm) | $SiH_4$ (sccm) | $H_2$ (sccm) | doping gas | | Dep. rate (nm/s) | Thick. (nm) |
|---|---|---|---|---|---|---|---|---|---|---|
| | | | | | | | type | (sccm) | | |
| **a-Si(i)** | 205 | 30 | 1.5 | 16.5 | 180 | 900 | - | - | 0.11 | 6 |
| **a-Si(p)** | 205 | 30 | 2 | 20.3 | 55 | 540 | TMB/ $B_2H_6$ | 90 | 0.20 | 6-12 |
| **nc-Si(p)** | 205 | 400 | 9 | 16.5 | 10 | 6100 | TMB/ $B_2H_6$ | 2 | *(10 s)* | 30 |
| | 205 | 330 | 5 | 15.2 | 12 | 4800 | | 4 | 0.12 | |
| | 205 | 400 | 9 | 16.5 | 10 | 6100 | | 4 | *(10 s)* | |
| **a-Si(n)** | 185 | 120 | 1.5 | 15.2 | 75 | 645 | $PH_3$ | 50 | 0.25 | 6-12 |
| **nc-Si(n)** | 185 | 500 | 9 | 16.5 | 10 | 2000 | | 6 | 0.30 | 20 |

The TCO's used in this chapter are ZnO:Al (AZO) and $In_2O_3$:Sn (ITO). The AZO was deposited at room temperature (~25°C) and the ITO was deposited at 200°C in a Leybold AV600 pulsed DC magnetron sputtering tool. The recipes are shown in Table 5-3. Unless mentioned otherwise, the TCO stack in this chapter consisted of a 10 nm 200 °C ITO contacting layer and a 250 nm 25°C AZO layer for lateral conductivity (and high etch rate) ("ITO-AZO").

**Table 5-3.** TCO Recipes from the "Leybold"

| Layer | Freq. | Target area (cm) | T (°C) | Power (kW) | Pressure (µbar) | Ar (sccm) | $O_2$ (sccm) | Dep. rate (nm·m/min) | Thick (nm) |
|---|---|---|---|---|---|---|---|---|---|
| **ITO** | 40 kHz | 60 × 12.5 | 200 | 0.5 | 6.7 | 500 | 2 | ~9 | 10 |
| **AZO** | | 60 × Ø 15.3 | 25 | 2 | 5.2 | 570 | 0.07 | ~23 | 250 |

### 5.2.3 Point Contact Cells

This first process step in the point contact cell process consists of the laser isolation scribe (isoscribe). In this thesis three different methods were used for making the isolation scribes:

- Method 1: one laser scribe after TCO deposition (as used in ref. [30]),
- Method 2: two slightly overlapping scribes after LPC and a 3rd scribe (within the first two scribes) after TCO deposition,
- Method 3: one scribe before LPC (i.e. crack catcher scribe) and a 2nd scribe after TCO deposition,

where the second and third method were developed during this thesis in order to passivate the isolation scribes (section 5.6). The scribes that remove the c-Si were made with a 1064 nm, picosecond pulse (ps) laser, while the scribes that remove only the emitter and TCO were made with a 532 nm ps laser, because the a-Si emitter is transparent for 1064 nm light. For method 1 and 2, separate crack catcher scribes were made just outside the cell area before LPC to reduce cracks through the cell area (see section 3.3.4).

As described in the introduction, after the emitter/TCO isoscribe, a roughly 5 µm thick white resin (P150W)

layer was applied by spin coating and structured by inkjet printing with a KOH based ink. The P150W was made in-house, by mixing $TiO_2$ particles into a protective coating resin (Clariant AZ® P150). The opening of the P150W was followed by a TCO etch (1 min, 5 % HF for standard ITO-AZO) and an emitter etch, using a HF + $KMnO_4$ (purple etch) solution or an HF + $HNO_3$ (poly-Si etch) solution. Etch times are presented in section 5.3. The sample was then placed in a solvent atmosphere for several minutes, allowing the P150W to "reflow" several µm, covering the TCO and emitter edge within the point contact opening. Subsequently, the resin was opened for the TCO point contacts (with the inkjet printer) and annealed at 150°C, which is the maximum temperature the P150 can withstand. Figure 5-2a and b show a schematic cell cross section (a) and top view image (b) after these process steps. The etch and reflow steps are indicated in the cross-section, numbered in chronological order.

Subsequently, the absorber and TCO were contacted by depositing a 100 nm Ag layer for the n-type samples, or 20/100 nm Ag/Al for the p-type samples, using the Leybold sputtering tool. It is not possible to do an HF etch to remove the native oxide before depositing the metal, as the HF would etch away the AZO in the TCO point contact openings. In combination with the low c-Si doping, the impossibility to anneal at T > 150 °C and the small contact area, this results in a very high absorber point contact resistance. In order to reduce this contact resistance, each absorber point contact was fired with a 532 nm ns laser. Only laser firing of the absorber contact is insufficient to strongly reduce the contact resistance; it is also necessary to supply dopants for a local $n^+$ or $p^+$ c-Si doping. For p-type cells, the 100 nm Al layer provided the doping source [29] (and the 20 nm Ag layer is needed for a low contact resistivity to the AZO). For n-type cells, an adenosine diphosphate (ADP) sodium salt layer was applied on the sample from a solution (before the laser firing). Subsequently, a heat gun (200 °C) was used to quickly evaporate the water, before the corrosive ADP solution can damage the TCO and TCO/Ag contact. After laser firing, the metal layer was patterned into interdigitated metal fingers, using a 355 nm ps laser. The result is shown in Figure 5-2c and d. The cell area is 1 $cm^2$ (1.8 × 0.56 $cm^2$). The standard point contact spacing in the x-direction is 564 µm (for both the TCO/Ag and c-Si/Ag contacts) and the standard spacing in the y-direction is 141 µm for the TCO/Ag contacts and 282 µm for the c-Si/Ag contacts. The top-view images (fig. b and d) include one cell and, below that, two transfer length measurement (TLM) structures, which were used to measure the TCO sheet resistance and TCO/Ag contact resistivity (left TLM structure) and the c-Si sheet resistance and c-Si/Ag contact resistivity (right TLM structure), as will be explained in section 5.4.1.

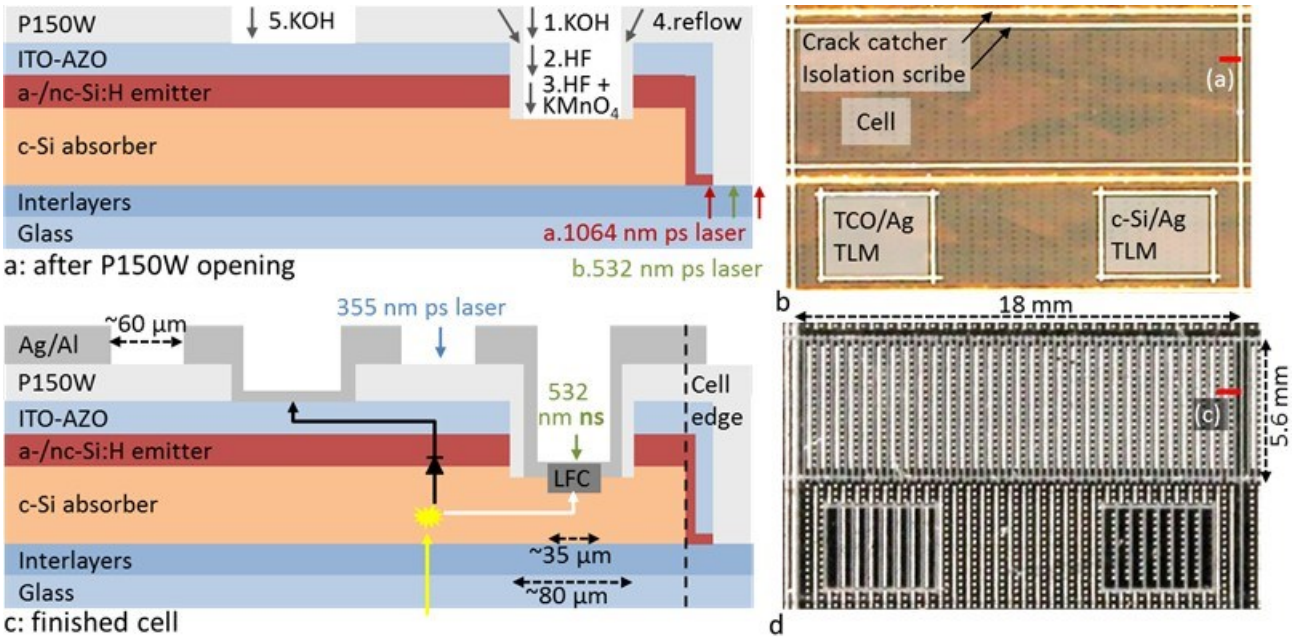


**Figure 5-2.** Schematic cross sections of the point contact cell after making the TCO point contact opening (a) and after structuring the metal (c and d). The structuring processes are indicated in fig. a and c, with the etch and reflow processes numbered chronologically. The laser steps are described by laser wavelength and approximate pulse duration: nanosecond (ns) or picosecond (ps). Fig. b and d show the top view images of a point contact cell and both the TCO/Ag and c-Si/Ag TLM structures after making the absorber point contacts opening (b) and after structuring the metal (d).The red lines in the figures show the position of the cross-sections. The arrows indicate the direction of the light (yellow) and of the generated minority carriers (black) and majority carriers (white).

### 5.2.4 Quasi Cells

In addition to the point contact cells, simple test cells (quasi-cells) were made to quickly characterize the $V_{OC}$ (and *pFF*) for different emitters using a process similar to the process described in ref. [34]: circular Kapton dots with a diameter of 8 mm were applied on the TCO. Subsequently, the TCO outside these Kapton dots was etched away by HF (or HCl) and the emitter was etched away using the HF + $HNO_3$ (poly-Si etch) solution. In order to reduce shunts a second Kapton dot was applied (on top of the first) with a diameter of 9 mm before depositing the metal, thereby creating a ~0.5 mm gap between the metal and cell. For n-type cells, 10 nm Ti + a several 100 nm thick Ag layer was evaporated. The resulting cross-section and top-view image are shown in Figure 5-3a and b. Finally, the Kapton is removed and the cell can be measured by contacting the TCO inside the cell area and the Ag outside the cell area.

### 5.2.5 Emitter/TCO Resistivity Test Structures

For determination of the emitter/TCO resistivity ($\rho_c$), the emitter and TCO layers were co-deposited on textured c-Si wafers with same doping type as the emitter. A thick (1.5 µm) metal layer was deposited on top of the TCO in order to prevent significant lateral resistance within the metal. This was followed by a

lithographically structured resin (AZ4533) etch mask. The Ag was etched away using $NH_4OH + H_2O_2$, the TCO was etched away with HF and the emitter was etched away with poly-Si etch. After the etching, the resin mask is removed with acetone, resulting in the structure shown in Figure 5-3c and d.

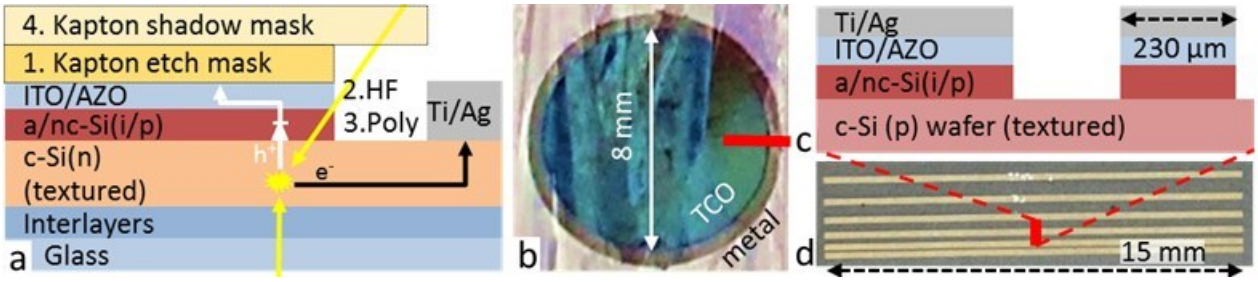


**Figure 5-3**. Figure a and b show the cross-section (a) and top view image (b) of the n-type Kapton dot quasi cell. The masking and etching steps are indicated in the figure, numbered chronologically. The arrows indicate the direction of the light (yellow) and of the generated electrons (black) and holes (white). Figure c and d show the cross-section (c) and top view image (d) of the emitter/TCO resistivity test structure. The red lines indicate the position of the cross-sections.

The measured resistance between two metal fingers ($R$) is composed of 2× the emitter/TCO resistance ($R_c$) and the lateral resistance within the wafer: $R_{wafer} / w \times \Delta x$, where $R_{wafer}$ is the sheet resistance of the wafers, $w$ is the width of the metal finger (15 mm) and $\Delta x$ is the distance between the finger. The wafers had a thickness of 400-500 µm and a doping of ~$5 \cdot 10^{16}$ $cm^{-3}$, resulting in a very low $R_{wafer}$ of 3-7 Ω/□. This makes the lateral resistance negligible for even the lowest emitter/TCO $\rho_c$, allowing for the calculation of $\rho_c$ ($\Omega cm^2$) from the median of the measured resistances between the fingers: $\rho_c = R / 2 \times w \times l$, where $l$ is the length of the finger (230 µm). The low wafer $R_{wafer}$ also ensures that the transfer length ($L_T$) (e.g. [106]) is always much larger than the physical contact length, i.e. that the physical contact length can be used as the effective contact length. The $\rho_c$ determined by these emitter/TCO test structures includes both the emitter/TCO contact resistance and the resistance within the emitter, which can be significant in some emitters.

### 5.2.6 Investigated Cells

Table 5-4 presents an overview of the 6 experiments which provided the investigated cells for this chapter, showing the cell type, glass type, interlayer type and thickness, absorber doping type and concentration, thickness and texturing, laser crystallization velocity ($v_{laser}$), emitter type, TCO type, isoscribe method, absorber point contact emitter etching type and duration and other intentional (and unintentional) process variations. In addition, emitter/TCO $\rho_c$ test structures were fabricated by co-deposition with the cells. In each result section the experiment number (1-6) will be specified, together with the relevant cell parameters, which will be presented in more detail than in the table. The unintentional variations, which mostly resulting in increased resistance, will be briefly discussed in the relevant result sections.

**Table 5-4.** Overview Point Contact and Quasi Cell Experiments.

| **Exp** | Cell type | Glass | Interlayers | Doping ($cm^{-3}$) | *d* (µm) & Texturing | $v_{laser}$ (mm/s) | emitter | TCO | Isocribe Method | Emitter etching (s) | other |
|---|---|---|---|---|---|---|---|---|---|---|---|
| **1** | Point Contact | Boro33 | 20/100/60/20 NON(ON) | **n, $2\cdot10^{16}$** | 7.5 µm, KOH textured | 10 | **nc-Si (AKT) and a-Si (FAP)** | ITO-AZO, with ITO depo at 25 °C | 1 | purple etch, a-Si(n): 20 nc-Si(n): 40 a-Si(p): 60 nc-Si(p): 120 | -**Point contact spacing and radius variation** -p-type: 100 nm Al (no Ag) n-type: long ADP contact |
| | | | 20/100/80 NO(ON) | **p, $2\cdot10^{16}$** | | | | | | | |
| | | | 10/200/85 NO(ON) | **n, $10^{17}$** | 8.5 µm, KOH | 3 | | | | | |
| | | | | **p, $10^{17}$** | | | | | | | |
| **2** | Point contact | Boro33 | 10/200/85 NO(ON) | **p/n**, $8\cdot/10\cdot10^{16}$ | 8.5 µm, KOH | 10 | **a-Si vs. nc-Si (AKT)** | **ITO vs AZO** | 1 | purple etch, 40-120 s | -misalignment -metal problem |
| | Quasi cell | | 10/200/60/20 NON(ON) | **p**, $8\cdot10^{16}$ | 7.5 µm, KOH | | | | - | | Emitter in cell gap |
| | | | 20/100/80 NO(ON) | **n**, $10^{17}$ | | | | | | | |
| **3** | Point contact | Boro33 | 10/200/85 NO(ON) | **p/n**, $8\cdot/10\cdot10^{16}$ | 8.5 µm, KOH | 10 | a-/nc-Si | p:AZO n:ITO-AZO | **2,3, exp.** | purple etch, 40-120 s | n-type: Ag corroded away by ADP |
| | Quasi cell | | | | | | **a-Si vs. nc-Si (AKT)** | **ITO vs. AZO** | - | | - |
| **4** | Point contact | Boro33 | 10/200/85 NO(ON) | p/n, $7\cdot/9\cdot10^{16}$ | p: 7.5, n: 11 µm KOH | 10 | **a-Si vs. nc-Si, TMB vs. $B_2H_6$ (AKT)** | ITO-AZO | 2 | purple etch, 40-120 s | evaporated Ag → high $R_s$ |
| **5** | Point contact | Boro33 | 10/200/60/20 NON(ON) | n, $10^{17}$ | 8 µm, KOH | 10 | **a-Si ($B_2H_6$) a-/nc-Si** | ITO-AZO | 2 | **poly-Si etch, 90 s** | **-Different a-Si(i)** -low LFC energy |
| | | Corning | 200/60/10 ONO (PVD) | n, $1.5\cdot10^{17}$ | 13 µm, various | 3 | a/nc-Si | | | | |
| **6** | Point contact | Boro33 | 10/200/60/20 nm NON(ON) | n, $10^{17}$ | 8 µm, KOH | 10 | a-Si($B_2H_6$) a/nc-Si | ITO-AZO | **2 & 3** | **poly-Si etch, 40 s & exp.** | **1 $cm^2$ cells vs. 4 and 10 $cm^2$ mini-modules** |
| | | Corning | 200/60/10 ONO (PC1) | n, $1.5\cdot10^{17}$ | 13 µm, KOH | 3 | | | | | |
| | | Boro33 | | | | | | | | | |

"a-/nc- Si" refers to the 5 nm a-Si(p/n) + 20-30 nm nc-Si(p/n) (TMB/$PH_3$) emitter stack. "ITO-AZO" refers to the 10 nm 200 °C ITO + 250 nm 25 °C AZO TCO stack. A lot of emitter/TCO experiments were repeated several times, as these experiments were difficult to evaluate. A new a-Si(i) layer was developed, for which the first 1-2 nm was deposited with 2-6 times the normal power, as will be discussed in appendix A.5. This new a-Si(i) layer was implemented in experiment 5.

## 5.3 Etching of the Absorber Point Contact Opening

The point contact device requires etching of the TCO and emitter layers in the absorber point contact openings after opening the P150W with the inkjet printer. Too short etching will result in shunting and too long etching will result in etching of the emitter/TCO layers below the P150W, resulting in increased dead area losses. In this section, *J-V* curves and LBIC measurements are used to show how the etching of the emitter and TCO layers in the absorber point contact influences both shunting and the dead area loss. Section 5.3.1 presents the etch rates and etch uniformity for different emitter and TCO layers and section 5.3.2 shows the shunting and dead area losses for different emitter layers and etch processes. Finally, a new process will be presented which allows for longer etching and a small dead area loss.

### 5.3.1 Etch Rate and Uniformity

In order to determine the etch rates, emitter stacks were co-deposited on glass during device fabrication, followed by co-deposition of the TCO layers. Table 5-5 shows the approximate etch time required to completely remove the indicated layer and the corresponding etch homogeneity, using either purple or poly-Si etch for the emitter layers and 5 % HF for the TCO's. It can be seen that the purple etch resulted in short etch times and good homogeneity for n-type emitters, but long etch times and poor homogeneity for the p-type emitter. The opposite was observed for poly-Si etch, indicating that purple etch should be used for the n-type emitters and poly-Si etch should be used for the p-type emitter.

The long etch time for the a-Si ($B_2H_6$) emitter with the purple etch solution, might be related to the observation that even very long HF etching of emitters with $B_2H_6$ as doping gas does not result in dewetting. This would normally indicate that the $SiO_x$ is not yet removed. The poly-Si etch also resulted in yellowing of the P150W, but so far no negative effect of this yellowing on the cell performance was observed.

With regard to the TCO etching, a relatively high concentration (5 %) HF solution was used to minimize the etch time. The test results indicate that the ITO has a very low etch rate of about ~0.4 nm/s, while the AZO has a high etch rate of about 50 nm/s. Other etch tests of 100 nm ITO layers on textured LPC-Si (with a-/nc-Si emitter) showed that, aside from the inhomogeneity on planar samples, the ITO has an etch rate

that is much lower for the textured LPC-Si areas than for the planar areas of the LPC-Si sample.

**Table 5-5.** Etch time and homogeneity of indicated layers on glass substrate.

| **Layer stack** | **Purple Etch** | | **Poly-Si Etch** | |
|---|---|---|---|---|
| **Emitters** | **Etch time** | **Homogeneity** | **Etch time** | **Homogeneity** |
| ~10/34 nm a-/nc-Si(**n**) – $PH_3$ | ~20 s | + | ~40 s | - |
| ~10/50 nm a-/nc-Si(i/**p**) – **TMB** | ~45 s | - | ~20 s | + |
| ~20 nm a-Si(**p**) – **$B_2H_6$** | ~150 s | - | ~15 s | + |
| **TCO** | **5 % HF** | | | |
| ~10 nm 200 °C **ITO** | ~25 s | - | | |
| 250 nm 25 °C **AZO** | ~ 5 s | + | | |

As the ITO has better electrical properties than the AZO (e.g. section 5.5), it was attempted to replace the 250 nm AZO with a 100 nm ITO stack for 1 sample from exp. 2. However, LBIC measurements of the point contacts cells from this sample showed that etching for 10 min in 5 % HF resulted in a dead area radius ($r_{DA}$, section 2.5) up to 100 µm and even partial lift-off of the P150W due to excessive etching in some areas. In other areas the $r_{DA}$ was only about the size of the point contact opening, suggesting that significantly shorter etching would have resulted in shunting due to incomplete etching. Because of these etching problems, a very thin 10 nm ITO contacting layer was combined with a 250 nm AZO layer for lateral conductivity (and high etch rate) and this TCO stack could be removed successfully by etching for 1 min in 5 % HF.

### 5.3.2 Shunting and Dead Area

The etch tests in the previous section indicated that, for etching the p-type emitters, the purple etch should be replaced by poly-Si etch. After experiment 4 it was found out by etch tests that the purple etch solution was “used up” and that probably the emitters from experiment 3-4 had not been etched away completely (a new solution was used for the experiment in Table 5-5). The fact that the cells from exp. 4 were not completely shunted can be explained by the high $\rho_c$ of the (oxidized) emitter/Ag contact and the laser firing of the Ag and phosphorous doping through the emitter. The emitters in experiment 5 were etched for 90 s with poly-Si etch instead of purple etch. A problem with the ITO-AZO stack is that the 250 nm AZO layer is etched away within ~5 s (in 5 % HF), while the thin ITO layer requires about ~25 s (Table 5-5). Together with the emitter etch (1 % HF) this causes etching of the AZO below the P150W. In order to prevent this, in experiment 6 the poly-Si etch time was reduced to 40 s, which is still 2 times the etch time in Table 5-5, and one sample was etched with an adapted etching process: it was etched for 30 s in 5 % HF, followed by a 90 s reflow, to remove any “high etch rate layers” from the opening and protect them from further etching. This was followed by a 90 °C anneal and the same etch process as the reference samples: 1 min in 5 % HF and 40 s in poly-Si etch, followed by a 5 min reflow. As the 30 s, 5 % HF etch does

not etch the emitter and most of the reflow takes place in the first 90 s, this adapted process leaves a passivating emitter layer below most of the reflow area. This etch-reflow-etch-reflow process will be abbreviated as "e-r-e-r". All investigated cells in this section had an ITO-AZO TCO stack. As shunts represented a larger loss than dead area, longer etching times were used than the (minimum) etch times indicated in Table 5-5.

Figure 5-4a and b show the *J-V* curves for point contact cells from exp. 4 (old purple etch) and exp. 5 (90 s poly-Si etch), using three different emitters: 6/30 nm a-Si/nc-Si(p) (TMB), 12 nm a-Si(p) ($B_2H_6$) and 6/30 nm a-Si/nc-Si(p) ($B_2H_6$). It can be seen that the shunts are non-ohmic, i.e. non-linear and different for forward and reverse bias. It can also be seen that the cells with the $B_2H_6$ emitters are more shunted than the cells with the TMB emitter. Finally, it can be seen that the 90 s poly-Si etch (exp. 5) strongly reduced shunting compared to the old purple etch solution (exp. 4). The best cell from Figure 5-4b, measured with anti-reflection foil, resulted in a 12 % efficiency cell, which will be presented in more detail in section 5.7.

Figure 5-4c shows the dead area radius ($r_{DA}$) determined by LBIC (see section 2.5), for various cells from exp. 3 (old purple etch), exp. 5 (90 s poly-Si etch) and exp. 6 (40 s poly-Si etch and e-r-e-r). Each point represents a single point contact. All cells are from different samples and the number of measured cells for each process (*n*) is indicated in the figure together with the median $r_{DA}$ and corresponding dead area fraction $f_{DA} = N_p \pi r_{DA}^2 / A_{cell}$, where $N_p$ is the number of absorber point contacts in the cell (558) and $A_{cell}$ is the area of the cell (1 $cm^2$).

It can be seen that the $r_{DA}$ for experiment 3 is very small, especially for the p-type sample. However, in Figure 5-4a it was shown that cells with this etch process were all shunted. The 90 s poly-Si etch in exp. 5 prevented these shunts, but in Figure 5-4c it can be seen that this process also resulted in an $f_{DA}$ of about 8 % (= relative $J_{SC}$ loss). It can be seen that by reducing the poly-Si etch time from 90 s to 40 s in exp. 6, the $r_{DA}$ was reduced from 68 to 54 µm and by using the e-r-e-r process, the $r_{DA}$ was decreased further to 42 µm.

Figure 5-4d shows the *J-V* curves of the cells with the e-r-e-r process (dashed) and of the reference cells (solid). Both samples used Corning substrates with PC1 ONO interlayers and a textured, $1.5 \cdot 10^{17}$ $cm^{-3}$ doped, 13 µm thick absorber. It can be seen that, compared to the reference sample, the cells with the e-r-e-r process have a higher $J_{SC}$, lower $R_s$ and no completely shunted cells. The *J-V* curves also show that most of the e-r-e-r samples are affected by non-Ohmic shunting, similar to the shunts in Figure 5-4a. DLIT images (not shown) reveal that, for both samples, the shunts occur in the middle of the cell and might therefore be due to the absorber point contacts.

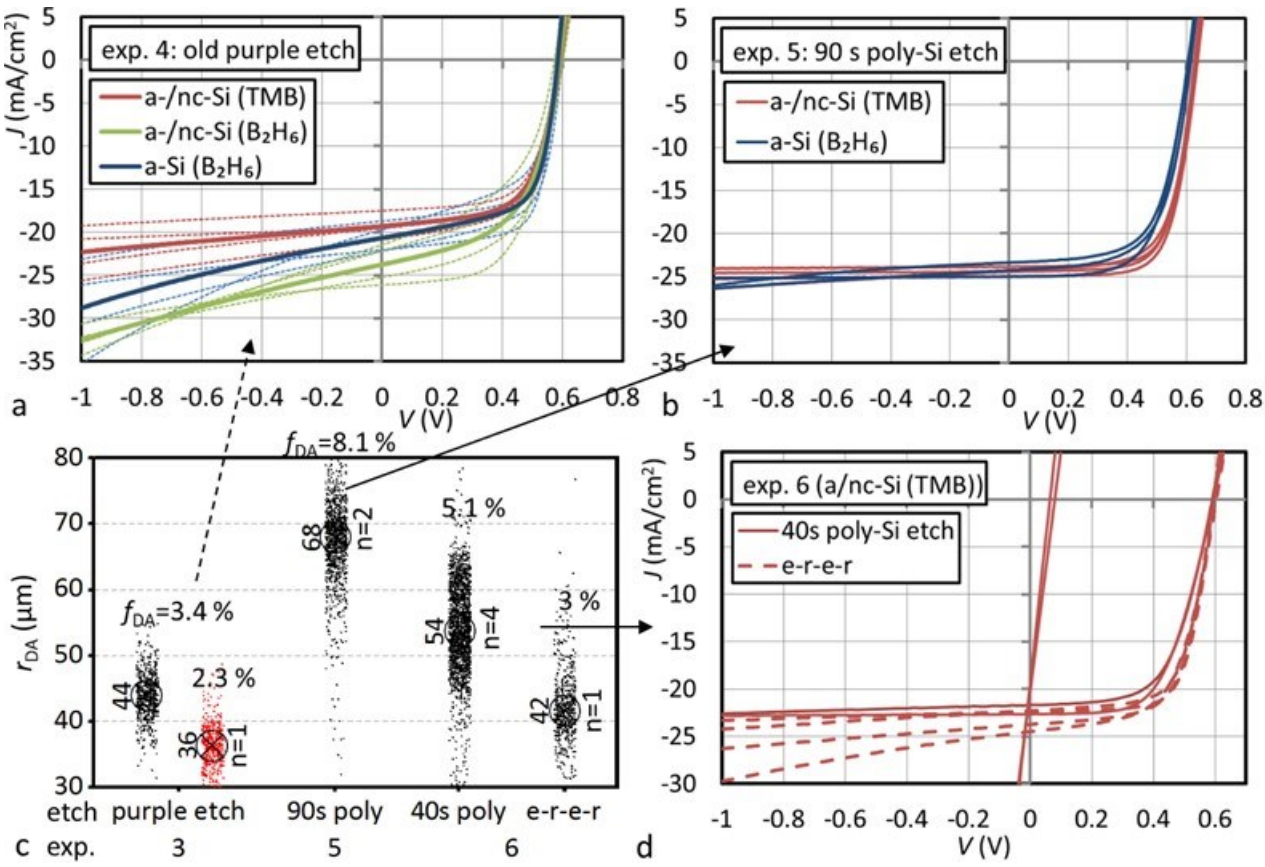


**Figure 5-4.** Figures a, b and d shows *J-V* curves of point contact cells with different emitters and emitter etch processes (indicated in the figures) from experiments 4 (a), 5 (b) and 6 (d). The dotted lines in fig. a are the individual *J-V* curves and the thick, solid lines are the average of these curves. Figure c shows the dead area radius ($r_{DA}$, see section 2.5) measured by LBIC, for a p-type (red) and an n-type cell from exp. 3 (old purple etch), for 2 n-type cells from exp. 5 (90 s poly-Si etch), for 4 n-type cells from exp. 6 (40 s poly-Si etch) and for the cell from exp. 6 with the etch-reflow-etch-reflow (e-r-e-r) process. The number of cells for each process ($n$) is indicated in the figure together with the median $r_{DA}$ and corresponding dead area fraction ($f_{DA}$).

### 5.3.3 Discussion and Conclusions

It was attempted to implement 100 nm Leybold ITO layer to replace the 250 nm AZO, but inhomogeneous etching (10 min. in 5 % HF) resulted in >50 µm etching below the P150W (at some locations) and a corresponding dead area loss. This etching problem was solved by combining a thin 10 nm ITO contacting layer with a thick 250 nm AZO layer.

For the emitter etch experiments, the $r_{DA}$ was reduced from ~68 to ~54 µm ($\Delta r_{DA}$ = 14 µm) for a reduction of the poly-Si etch time from 90 to 40 s ($\Delta t$ = 50 s). Based on the ITO and AZO etch rates, the maximum etching below the P150W should be ~400 nm for the 10 min etch of the ITO and 2.5 µm for the 50 s poly-Si etch process, instead of the observed >50 µm and 14 µm. These observations seem to indicate that either the lateral etch rate of these layers is much higher than the vertical etch rate or that some other layer is being etched.

Etch tests showed that the poly-Si etch resulted in faster and more homogeneous etching of p-type emitters than purple etch. Therefore the purple etch was replaced by a 90 s poly Si etch. This resulted in shunt free cells and a 12 % efficiency record, but it also resulted in an $f_{DA}$ increase of ~3.4 % to ~8 %. In order to prevent this, the etch process was modified to a short etch and reflow to etch any "high etch rate layers" and protect them from further etching, followed by a longer etch and reflow to etch and cover any "low etch rate layers". This e-r-e-r process resulted in a low $f_{DA}$ of 3 % and generally better cell results than with the reference process, though the cells with the e-r-e-r process still had some non-Ohmic shunts. The reduced $f_{DA}$ for the e-r-e-r process can be explained by a combination of reduced etching below the P150W and not etching the emitter below most of the reflow area. With the new etch process it should be possible to further increase the duration of the second etch to prevent shunting, without increasing $f_{DA}$.

## 5.4 Absorber Point Contact Resistance and Spacing

As mentioned in the introduction, the 11.5 % LPC-Si point contact cell from ref. [30] was mainly limited by a *FF* of only 65.5%, caused by an $R_s$ of 5.2 Ωcm$^2$. This section presents an analysis of the absorber point contact resistance, laying the groundwork for a cell $R_s$ analysis in section 5.5. In section 5.4.1 the point contact TLM structures are used to analyse the dependence of the c-Si/Ag point contact resistance on the c-Si doping and point contact radius. In section 5.4.2 simulation is used to determine the lateral resistance in the c-Si, which is then used to analyse a point contact spacing experiment and estimate the optimum point contact spacing as a function of absorber doping.

### 5.4.1 Point Contact Resistance

As mentioned in section 5.2.3, the point contact samples include transfer length measurement (TLM) structures for measuring the sheet resistance ($R_{layer}$) of the c-Si (and TCO) and the contact resistance ($R_c$) of the c-Si/Ag contact (and TCO/Ag contact). Figure 5-5a and b show a schematic cross-section and a top view image of the c-Si/Ag absorber contact TLM structure. By plotting the measured resistance against the distance between the finger ($\Delta x$), $R_{layer}$ can be determined from the slope of the curve (i.e. the resistance which depends on $\Delta x$) and $R_c$ can be determined from the intersection with the y-axis (i.e. the resistance which doesn't depend on $\Delta x$):

$$R = \frac{R_{\mathrm{layer}}}{w}\Delta x + 2R_C = \mathrm{slope} \cdot \Delta x + \mathrm{intersection\ with\ y\ axis}\,, \tag{22}$$

where *w* is the width of the TLM structure (3.5 mm). Compared to the standard rectangular contact TLM structure, the current flow in point contact TLM structures is more complicated due to both the point contact geometry and current crowding near the point contacts. Current crowding refers to the fact that the local resistive power loss depends on the square of the local current and therefore, local high current

densities contribute disproportionally to the power loss. In ref. [107] it is shown that most of the resistive power loss in the absorber takes place very close to the point contact, where the current density is highest. This increased resistance next to the point contact does not depend on $\Delta x$ and will therefore be interpreted as a contact resistance. The measured contact resistance, must be corrected for this apparent contact resistance ($R_{c,apparent}$).

In ref. [108], the program SourceField was used to correct a point contact TLM structure. SourceField uses a semi-analytical model with point sources and sinks to calculate the potential drop ($\Delta V$) between two point contacts [109]. These source-sink pairs are mirrored many times in order to create a rectangular unit cell. SourceField was used to simulate $R$ vs $\Delta x$, which was subsequently analyzed as a TLM measurement, resulting in a $R_{c,apparent}$. Figure 5-5c shows an example of a measured and a simulated $R$ vs $\Delta x$ curve. The actual $R_c$ is the difference between the measured $R_{c,measured}$ and the simulated $R_{c,apparent}$. In order to obtain a more easily interpretable value, the $R_c$ values were converted to a cell $R_s$ contribution (in $\Omega cm^2$) using:

$$R_{s,c} = R_c \frac{N_{TLM}}{N_{cell}} A_{cell} = \left(R_{c,measured} - R_{c,apparent}\right) \frac{N_{TLM}}{N_{cell}} A_{cell}\,, \tag{23}$$

where $N_{TLM}$ is the number of point contacts in a TLM finger (10), $N_{cell}$ is the number of point contacts in the cell (588) and $A_{cell}$ is the area of the cell (1 $cm^2$). The distance between the c-Si/Ag point contacts on a TLM finger ($\Delta y$) is 282 µm (same distance as for the cells), but for the upper contact the distance to the isoscribe is 423 µm ($\Delta y_{upper}$) and for the lower point contact the distance is 282 µm ($\Delta y_{lower}$) (see Figure 5-5b). The $R_{s,c}$ for these outer regions was simulated separately and the total $R_{s,c}$ for these parallel resistance was calculated by:

$$\frac{1}{R_{s,c}} = \frac{1}{R_{s,c,upper}} + \frac{8}{R_{s,c,middle}} + \frac{1}{R_{s,c,lower}}\,, \tag{24}$$

Figure 5-5d shows the $R_{s,c,apparent}$ for the c-Si/Ag TLM with and without $\Delta y_{upper/lower}$ as a function of $R_{layer}$. It can be seen that $\Delta y_{upper/lower}$ have a significant influence on the $R_{s,c,apparent}$. The addition of $\Delta y_{upper/lower}$ also increased the slope of the simulated TLM curve by about 4 %. The measured $R_{layer}$ was therefore obtained by:

$$R_{layer} = \text{slope} \cdot w \,/1.04\,, \tag{25}$$

For the TCO/Ag point contact TLM structure, which will be used for the cell $R_s$ analysis in section 5.5.2, the point contacts are almost touching (see Figure 5-2d) and therefore there is no significant $R_{s,c,apparent}$ due to current crowding, i.e. the structure can be analyzed as a standard TLM structure.

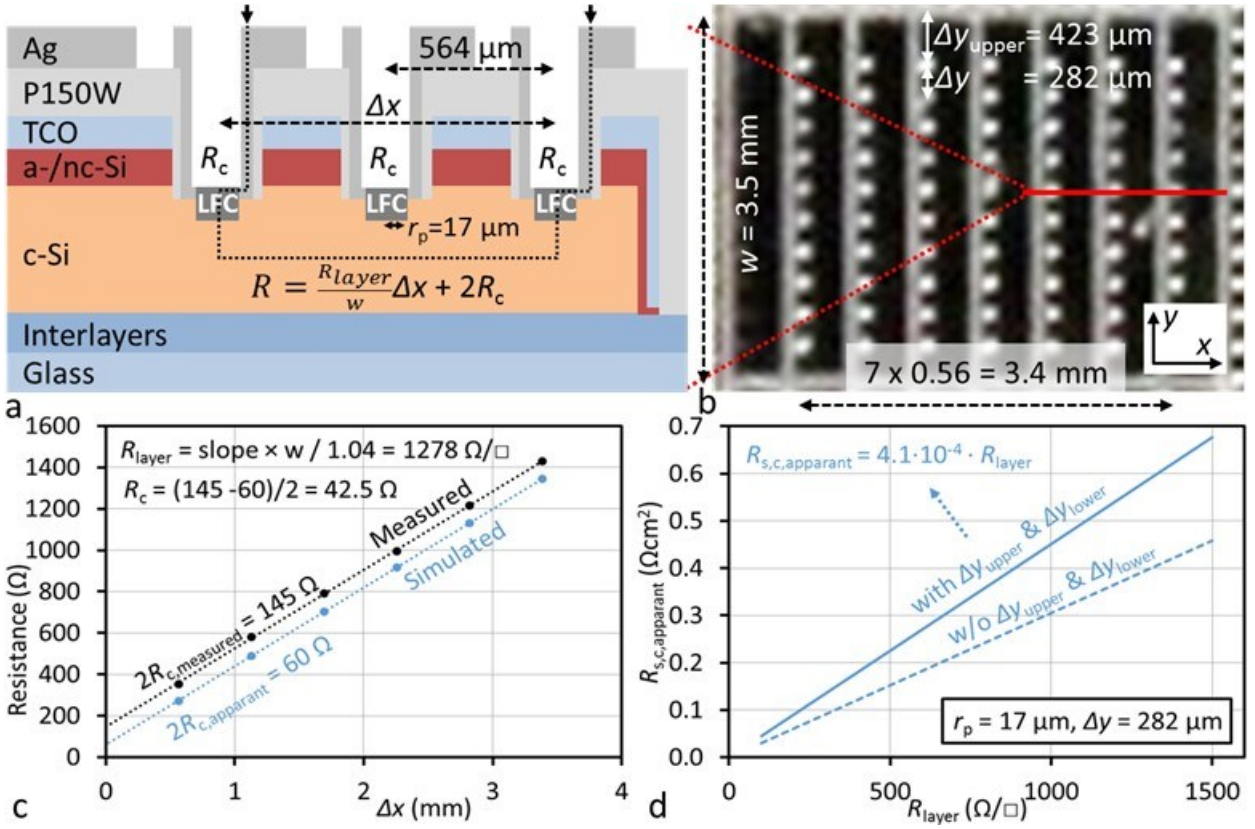


**Figure 5-5.** Figure a and b show a schematic cross-section and a top view image of the point contact (c-Si/Ag) TLM structure. Figure c shows a measured and a simulated TLM measurement with the same sheet resistance (1278 Ω/□). The actual $R_c$ is the difference between $R_{c,measured}$ and $R_{c,apparent}$. From the simulation it followed that the slope not only had to be multiplied by the width of the TLM structure ($w$) (eq. (22)), but also divided by 1.04 to reproduce the $R_{layer}$ (input parameter). Figure d shows the $R_{s,c,apparent}$ for the c-Si/Ag TLM with (solid) and without (dashed) $\Delta y_{upper/lower}$ as a function of $R_{layer}$.

Figure 5-6a shows the measured and corrected $R_{s,c}$ of the c-Si/Ag contact, measured by TLM for p- and n-type samples (from exp. 1, 3 and 4), plotted against $R_{layer}$ (also determined by TLM). Each point represents 2-5 TLM structures from a single sample. The absorber doping was approximately $2 \cdot 10^{16}$ - $10^{17}$ $cm^{-3}$, which corresponds to an $R_{layer}$ of ~400-1300 Ω/□ for the p-type samples and ~100-400 Ω/□ for the n-type samples (see Hall mobility ($\mu_{Hall}$) measurements in appendix A.3). It can be seen that both the p- and the n-type $R_{s,c}$ appear to have a very similar, approximately linear dependence on $R_{layer}$, which appears to go through 0 for $R_{layer}$ ≈ 75-200 Ω/□ (i.e. not 0 Ω/□). This corrected $R_{s,c}$ (linear interpolation) will be used in the next section as input for the optimization of the point contact spacing as a function of $R_{layer}$.

The radius of the point contact opening (~40 µm) is much larger than the LFC radius ($r_p$ ≈ 17 µm). Therefore, if the LFC radius can be increased, the resistance could probably be reduced without increasing the dead area radius ($r_{DA}$ ≈ 40 µm, see section 5.3.2). As the LFC radius cannot be increased significantly without making hardware changes to the laser, it was increased by making 3 slightly overlapping LFC in the same

contact opening. Figure 5-6b shows the measured and corrected $R_{s,c}$ for either 1 or 3 LFC's on p-type samples, with an $R_{layer}$ of ~1250 Ω/□ (experiment 1). Microscope images of the contacts are included in the figure: the white circles are the openings made with the inkjet and the black dots in the middle are the laser fired contacts. It is estimated that the effective radius $r_p$ for the 3 LFC contact is 30 µm and the measured $R_{s,c}$ is corrected correspondingly. Both the measured and corrected $R_{s,c}$ for the 3 LFC's is 40 ± 20 % lower than for 1 LFC, which is less than the 66 % that would be expected from the tripling of the LFC area.

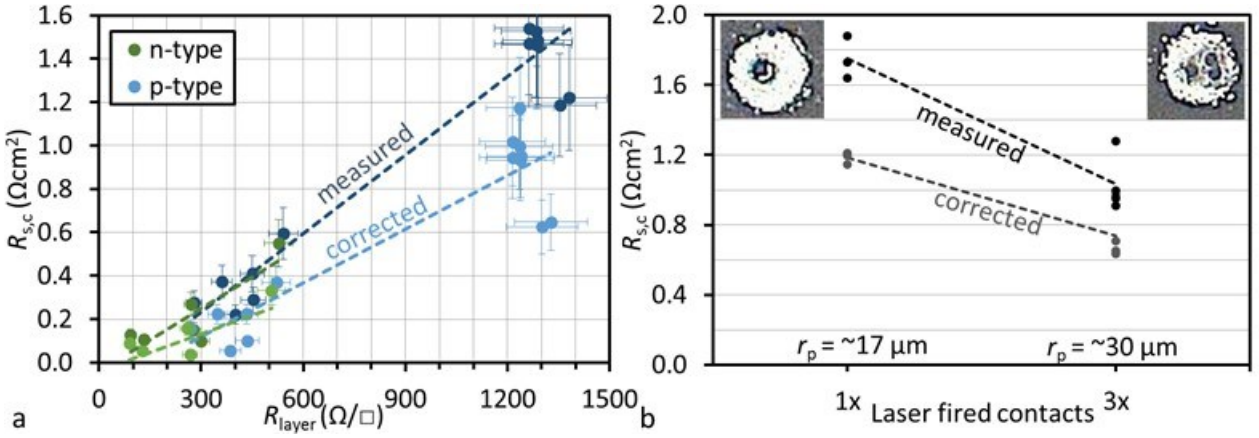


**Figure 5-6.** Fig. a shows the measured and corrected $R_{s,c}$ of the c-Si/Ag contact, for p-type (blue) and n-type (green) samples plotted against the measured $R_{layer}$ of the c-Si. Each point represent 2-5 TLM structures from a single sample. Fig. b shows the $R_{s,c}$ of the c-Si/Ag contact for either 1 LFC or 3 slightly overlapping LFC within the same point contact opening on p-type samples with an $R_{layer}$ of ~1250 Ω/□. Microscope images of the point contact openings (white) and LFC (black) are included in the figure.

In this section the TLM measurement was corrected for current crowding effects and it was observed that the c-Si/Ag point contact resistance can be reduced by decreasing the c-Si $R_{layer}$ or by using multiple LFC to effectively increase the point contact radius.

### 5.4.2 Point Contact Spacing

Point contact cells were fabricated with a c-Si/Ag point contact spacing $\Delta y$ = 141, 282 (standard) and 564 µm, for several p-type cells with an $R_{layer}$ of approximately 1250 Ω/□ (experiment 1). Microscope images of the point contact spacing (for $\Delta y$ = 141 and 564 µm) are shown in Figure 5-7a.

In order to determine the contribution of the lateral resistance in the c-Si to the cell $R_s$ ($R_{s,l}$) from the measured $R_{layer}$, 3D solar cell simulations were made in Quokka2 [93]. The $R_{s,l}$ was simulated for $R_{layer}$ = 500 Ω/□ and scaled linearly to the measured $R_{layer}$ (see appendix A.2.2 for more details regarding the simulation). Similar to the TLM structures, at the edge of the cell the distance of the point contacts to the isoscribe is larger than $\Delta y/2$ and $\Delta x/2$ in the rest of the cell. These outer regions with larger unit cells, shown in the top view cell image in Figure 5-7b, are simulated separately and their $R_{s,l}$ is added relative to

their ractions. Table 5-6 shows the simulated $R_{s,l}$ for the difference regions and the resulting total $R_{s,l}$, which will be used to analyze the experimental results. The TCO/Ag point contact geometry ($\Delta y$ = 141 µm, $\Delta x$ = 564 µm) was also simulated as it will be needed for the $R_s$ analysis in section 5.5. By comparison of $R_{s,l,middle}$ and $R_{s,l,total}$, it can be seen that, for $R_{layer}$ = 500 Ω/□, the outer regions add about 0.1 Ωcm$^2$ (for all values of $\Delta y$). For the standard point contact spacing, this represents an addition of about 50 %.

**Table 5-6.** Simulated $R_{s,l}$ (in Ωcm$^2$) for different point contact spacing $\Delta x$ and $\Delta y$ (for $R_{layer}$ = 500 Ω/□). The results for the standard point contact spacing are underlined.

| Contact | $r_p$ (µm) | $\Delta y$ (µm) | $R_{s,l,middle}$ | $R_{s,l,top/bottom}$ | $R_{s,l,left}$ | $R_{s,l,right}$ | $R_{s,l,total}$ |
|---|---|---|---|---|---|---|---|
| | | | **$\Delta x$: 564 µm** | **$\Delta y$: 694 µm** | **$\Delta x$: 1404 µm** | **$\Delta x$: 864 µm** | |
| | | | **Area: 82 %** | **11.8 %** | **4 %** | **2.4 %** | **100 %** |
| **c-Si/Ag** | **17** | **141** | 0.09 | 0.77 | 0.90 | 0.32 | 0.21 |
| | | **282** | 0.21 | | 1.21 | 0.49 | 0.32 |
| | | **564** | 0.58 | | 2.12 | 1.02 | 0.67 |
| **TCO/Ag** | **45** | **141** | 0.03 | 0.39 | 0.76 | 0.10 | 0.10 |

Figure 5-7c shows the cell $R_s$ of the aforementioned $\Delta y$ experiment (black), the $R_{s,l}$ calculated with the Quokka simulation (red), the corrected $R_{s,c}$ from the TLM contact resistance measurements (blue) and the sum of both $R_s$ contributions (purple) as a function of $\Delta y$. The cell $R_s$ values, determined from the *J-V* curve at 0.9 V (see section 2.1), are from two different samples, each containing a cell for each $\Delta y$. The high cell $R_s$ can be explained by a high TCO/Al $R_{s,c}$ for this experiment. In order to better see if the observed dependence of the cell $R_s$ on $\Delta y$ can be explained by the sum of the $R_{s,l}$ and $R_{s,c}$, the purple curve was shifted up (purple, dashed) to the cell $R_s$ curve (black, dotted).

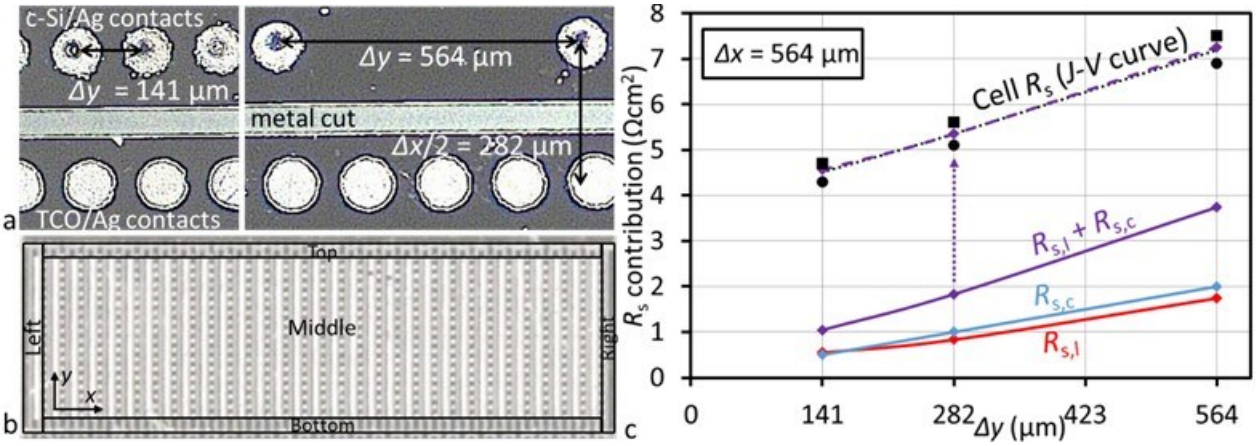


**Figure 5-7.** Fig. a shows microscope images of point contact cells with $\Delta y$ = 141 µm (left) and 564 µm (right). The white circles are the openings made with the inkjet and the black dots in the middle are the laser fired contacts. Figure b shows a top view image of the point contact cells, divided into regions with different $\Delta x$ or $\Delta y$. The curves in fig. c show the average cell $R_s$ determined from the *J-V* curves (dotted, black), the $R_{s,l}$ contribution calculated with Quokka (red), the corrected $R_{s,c}$ from the TLM measurements (blue) and the sum of both $R_s$ contributions (purple). The dashed curve was shifted up to the cell $R_s$ curve for easier comparison of the $\Delta y$ dependence. The black circles correspond to the cell $R_s$ from one point contact sample and the black squares to the cell $R_s$ of the other point contact sample.

It can be seen that the sum of the $R_{s,l}$ and $R_{s,c}$ accurately reproduces the observed cell $R_s$ dependence on $\Delta y$ for both samples (black circles/squares). This experiment indicates that the corrected TLM $R_{s,c}$, together with the simulated $R_{s,l}$, can accurately determine the (combined) c-Si/Ag contact and lateral c-Si resistance.

In order to optimize the point contact spacing, the lateral and contact resistance losses must be balanced with the dead area loss. For the point contact cells, the point contact opening and corresponding dead area has a radius ($r_{da}$) of approximately 40 µm (section 5.3). In order to optimize the point contact spacing $\Delta y$ and $\Delta x$, the dead area and the resistances must be converted to the relative power losses $P_{DA}$ and $P_{R,rel}$ according to:

$$P_{\mathrm{DA}} = \frac{\text{dead area}}{\text{unit cell area}} = \frac{\pi r_{\mathrm{DA}}^2}{\Delta x \Delta y}, \tag{26}$$

$$P_{\mathrm{R,rel}} = \frac{P_{\mathrm{R}}}{P_{\mathrm{M}}} = \frac{R_{\mathrm{s}} J_{\mathrm{M}}^2 \Delta x \Delta y}{I_{\mathrm{M}} V_{\mathrm{M}}} = \frac{R_{\mathrm{s}} J_{\mathrm{M}}}{V_{\mathrm{M}}}, \tag{27}$$

where $P_M$, $J_M$, $I_M$ and $V_M$ are the power, current density, current and voltage at the maximum power point. It is assumed that the corrected $R_{s,c}$ depends linearly on the total contact area and, for $R_{layer} > 150$ Ω/□, depends linearly on $R_{layer}$ (trendline in Figure 5-6a).

The 3D solar cell simulations are too time intensive for simulating the large parameter space required for optimizing the point contact spacing. Also, the relative uncertainty of the simulated $R_{s,c}$ increases for decreasing resistance and mesh re-optimization is needed for different unit cell sizes. Therefore, an analytical model was developed to calculate the lateral resistance for uniformly generated current flowing to a point contact from a rectangular unit cell. This model is explained and compared to the Quokka simulation in appendix A.2.2. It was found that the model can reproduce the simulated $R_{s,l}$, within the uncertainty of the simulation for a unit cell aspect ratio of 1 ($\Delta y = \Delta x$) and overestimates the resistance for an aspect ratio diverging from 1.

Figure 5-8a shows the relative power losses $P_{R,lateral}$, $P_{R,contact}$, $P_{DA}$ and the combined (total) relative power loss $P_{total}$ as a function of $\Delta y$, for $\Delta x = 500$ µm and $R_{layer} = 300$ Ω/□. It can be seen that there is a minimum $P_{total}$ at $\Delta y \approx 500$ µm, i.e. an aspect ratio of 1 ($\Delta y = \Delta x$). Figure 5-8**c** shows the relative total power loss as a function of $\Delta y$ and $\Delta x$. It can be seen that, for each cross-section (fixed $\Delta y$ or $\Delta x$), the minimum power loss is at $\Delta y = \Delta x$. For $\Delta y = \Delta x$, (dashed line), the optimum spacing is found at $\Delta y = \Delta x \approx 480$ µm.

This optimum spacing was found for $R_{layer} = 300$ Ω/□, but for different values of $R_{layer}$, the optimum spacing will be different. In Figure 5-8**d**, the relative total power loss is shown as a function of $R_{layer}$ and the point contact spacing ($\Delta y = \Delta x$). It can be seen that, as $R_{layer}$ increases, the optimum spacing decreases, the power loss increases and the power loss depends more strongly on the spacing. Figure 5-8**b** shows the optimum

spacing and corresponding relative total power loss as a function of $R_{layer}$. The figure also includes reference lines for the currently standard values for $\Delta x$ = 564 µm and $\Delta y$ = 282 µm. Above the figure the approximate n- and p-type carrier densities ($N$), corresponding to the $R_{layer}$ values, are indicated for an absorber thickness ($d$) of 10 µm: $10^{17}$ cm$^{-3}$ doped LPC-Si(n) results in $R_{layer}$ ≈ 100 Ω/□, $2 \cdot 10^{16}$ cm$^{-3}$ doped LPC-Si(n) and $10^{17}$ cm$^{-3}$ doped LPC-Si(p) both result in $R_{layer}$ ≈ 375 Ω/□ and $2 \cdot 10^{16}$ cm$^{-3}$ doped LPC-Si(p) results in $R_{layer}$ ≈ 1400 Ω/□ (see $\mu_{Hall}$ measurements in appendix A.3).

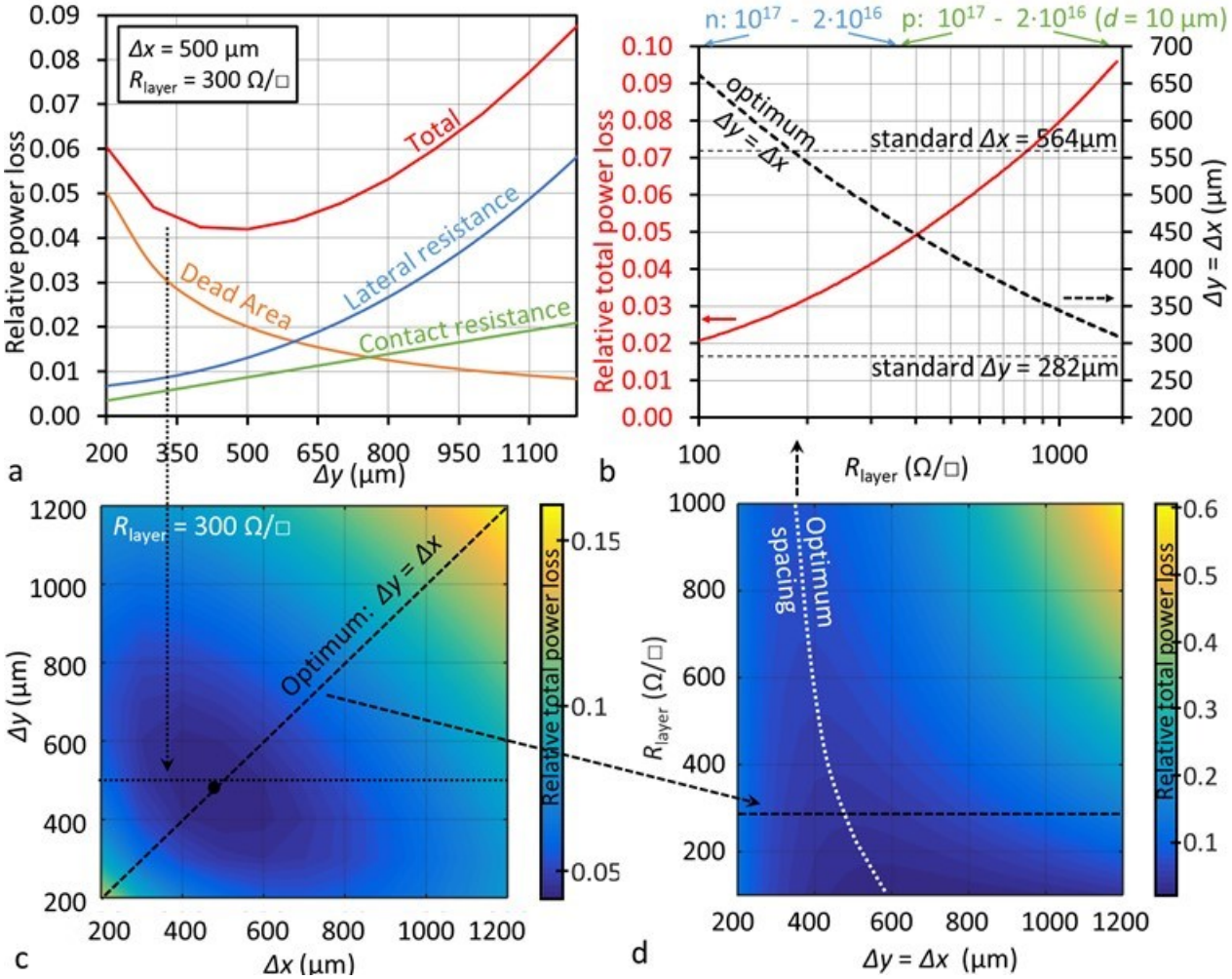


**Figure 5-8.** Fig. a shows the relative power losses due to lateral resistance, contact resistance, dead area and the total relative power loss, as a function of the point contact spacing in the x direction $\Delta x$, for $\Delta y$ = 500 µm and $R_{layer}$ = 300 Ω/□. Fig. b shows the relative total power loss as a function of $\Delta y$ and $\Delta x$. In fig. c the relative total power loss is shown as a function of $R_{layer}$ and the point contact spacing ($\Delta y = \Delta x$). Fig. d shows the optimum spacing and corresponding relative total power loss as a function of $R_{layer}$. The figure also includes reference lines for the current standard point contact spacing: $\Delta x$ = 564 µm and $\Delta y$ = 282 µm. Above the figure the approximate n- and p-type carrier densities (in cm$^{-3}$), corresponding to the $R_{layer}$ values are indicated for an absorber thickness $d$ = 10 µm.

Based on this optimization, the average of the standard spacing ($\Delta y$ = 282 µm and $\Delta x$ = 564 µm) is close to the optimum distance for highly doped p-type samples and lowly doped n-type samples. For the lowly

doped p-type samples $\Delta x$ should be reduced and for the highly doped n-type samples, $\Delta y$ should be approximately doubled to 564 µm. However, the potential gain from these optimizations is relatively small: it was estimated that the relative total power loss can be reduced from ~11.5 % to 9.5 % for the p-type $N = 2{\cdot}10^{16}$ cm$^{-3}$ material and from ~3.1 % to 2 % for n-type $N = 10^{17}$ cm$^{-3}$ material.

The potential gain for increased absorber doping from $2{\cdot}10^{16}$ to $10^{17}$ cm$^{-3}$ is ~2.5 times larger: in Figure 5-8b the relative power loss decreases from ~10 % to ~4.5 % for p-type, and from 4.5 % to ~2 % for n-type cells ($d$ = 10 µm).

### 5.4.3 Discussion and Conclusions

Simulations were made to correct the point contact TLM measurement for current crowding effects, enabling the measurement of the contact and sheet resistances. 3D solar cell simulations were made to determine the lateral resistance from the measured sheet resistance. For both the TLM and the cell simulations it was found that the large distances of the point contacts to the edge of the structure, strongly affected the simulated resistance. This increased distance at the edge of the cell was implemented because of processing problems due to a thinner P150W layer near the isoscribe. Reducing these cell edge distances could reduce the $R_{s,l}$ by ~50 % for the standard point contact spacing.

It was observed that the $R_{s,c}$ appears to depend linearly on $R_{layer}$, varying from 0.8 Ωcm$^2$ for $R_{layer} \approx 1250$ Ω/□ to 0.1 Ωcm$^2$ for $R_{layer} \approx 300$ Ω/□. This dependence of $R_{s,c}$ on $R_{layer}$ is not expected for the laser fired contacts (LFC), because the c-Si at the contact is doped $p^+$ or $n^+$ by the LFC process (using Al for p-type and APD for n-type cells). Furthermore, it seems unlikely that the p and n-type contact resistances would have exactly the same dependence on the sheet resistance. These observations indicate that there might be some additional lateral resistance effect influencing the TLM measurement. Nonetheless, the sum of the corrected $R_{s,c}$ and simulated $R_{s,l}$ could accurately predict the measured cell $R_s$ vs spacing ($\Delta y$) dependence.

A spacing optimization was performed for a dead area radius of 40 µm and $R_{layer}$ = 100-1400 Ω/□, using the measured $R_{s,c}$ and a calculated $R_{s,l}$. The lowest relative total power loss was always found for $\Delta y = \Delta x$. For lowly doped p-type ($2{\cdot}10^{16}$ cm$^{-3}$) material, it was found that a decrease of the spacing should result in a relative power gain of ~2 % and, for highly doped n-type ($10^{17}$ cm$^{-3}$) material, it was found that the doubling of the spacing should result in a relative power gain of ~1 %, i.e. in this range the power is relatively insensitive to a spacing variation. The relative power gain for increasing the absorber doping from $2{\cdot}10^{16}$ to $10^{17}$ cm$^{-3}$, was estimated at ~5.5 % for p-type samples and ~2.5 % for n-type samples.

## 5.5 Emitter-TCO Resistance

As mentioned in the introduction, in ref. [30] it was argued that the high $R_s$ of 5.2 Ωcm$^2$, for the 11.5 % point contact cell, was caused by the a-Si(p)/TCO resistivity ($\rho_c$), where the a-Si(p) emitter was deposited with TMB as doping gas. In this section it is attempted to reduce the emitter/TCO $\rho_c$ (without reducing the $V_{OC}$) by replacing the TMB by $B_2H_6$ and the a-Si by nc-Si.

In ref. [104] it was determined that a-Si emitters with $B_2H_6$ as doping gas have a much higher conductivity than emitters with TMB as doping gas, which resulted in a much higher *FF* on the corresponding c-Si wafer silicon heterojunction (SHJ) cells. In ref. [98] it was attempted to reduce the emitter/TCO $\rho_c$ of interdigitated backside contacted (IBC) SHJ cells by using a 20 nm nc-Si(p) layer, combined with a 6 nm a-Si(p) layer between the a-Si(i) and nc-Si(p) (using $B_2H_6$ as doping gas). A thickness of 6 nm was used because it was determined (on test structures) that an increase of the thickness from 2 to 6 nm in resulted in an increase of the effective lifetime from 1.5 to 1.8 ms and a further increase of the thickness did not affect the lifetime. Test structures indicated that the addition of the nc-Si(p) layer reduced the $\rho_c$, but efficiency of the corresponding IBC-SHJ cells was mainly increased (to 23.4 %) by an increase of the $V_{OC}$ and $J_{SC}$. In a subsequent paper the authors applied the nc-Si layer on both the a-Si(i/p) emitter and a-Si(i/n) back surface field (BSF). Test structures were used to measure the $\rho_c$, which was found to increase from 0.38 to 0.49 Ωcm$^2$ for the p-type emitter and decrease from 0.37 to 0.10 Ωcm$^2$ for the n-type BSF. This latter reduction was confirmed by a corresponding $R_s$ reduction of the IBC cell.

In section 5.5.1 the emitter/TCO $\rho_c$ will be investigated for various emitter and TCO combinations, using quasi cells (see section 5.2.4) to determine the $V_{OC}$ and emitter/TCO test structures (see section 5.2.5) to determine the corresponding emitter/TCO resistivity ($\rho_c$). In section 5.5.2 it will be attempted to verify the TLM results by analysing the $R_s$ losses of point contact cells for different emitters. This $R_s$ loss analysis also shows the $R_s$ potential for the LPC-Si point contact cells. The investigation focusses on n-type cells (with p-type emitters). Parts of this section were published in ref. [110].

### 5.5.1 Emitter/TCO $V_{OC}$ and Resistivity

Figure 5-9 shows the $V_{OC}$ values, measured by Suns-$V_{OC}$, for textured LPC-Si quasi cells from experiment 2 using either 30 nm nc-Si(p), 12 nm a-Si(p) or 6 nm a-Si(p) + 30 nm nc-Si(p) as emitter. For the cell with the 12 nm a-Si emitter the doping gas was either TMB or $B_2H_6$. The cells had a 6 nm a-Si(i) layer and a 100 nm ITO layer.

It can be seen that nc-Si emitter results in a ~80 nm $V_{OC}$ loss compared to the a-Si emitter, which was confirmed by similar $V_{OC}$ losses in point contact experiment 1 (~70 mV) and quasi cell experiment 3 (~50

mV) (not shown). By adding a 6 nm doped a-Si layer between the a-Si(i) and nc-Si(p), this $V_{OC}$ loss could be prevented. It can be seen that the doping gas type does not significantly affect the $V_{OC}$, which was confirmed in subsequent experiments. No significant $V_{OC}$ differences were found for a variation of the TCO (ITO vs AZO).

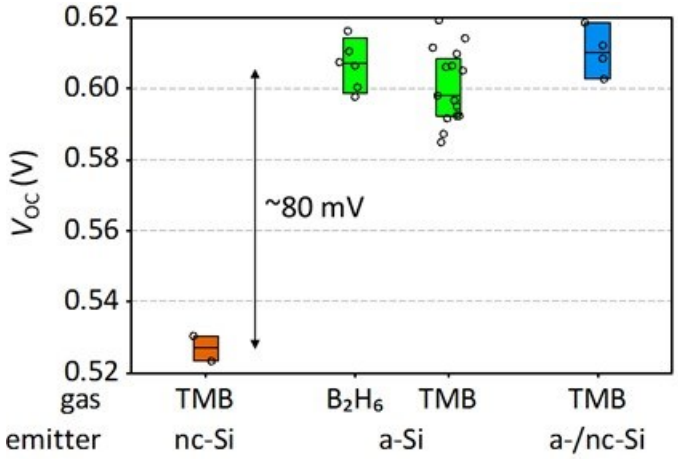


**Figure 5-9.** Boxplot of the $V_{OC}$ values, measured by Suns-$V_{OC}$, for quasi cells from experiment 2, using either 30 nm nc-Si(p) (orange), 12 nm a-Si(p) (green) or 6 nm a-Si(p) + 30 nm nc-Si(p) (blue) as emitter. For the cell with the 12 nm a-Si emitter the doping gas was either TMB or $B_2H_6$. The cells had a 6 nm a-Si(i) layer and a 100 nm ITO layer.

The emitter/TCO $\rho_c$ test structures on textured wafers were co-processed with the quasi and point contact cell experiments 2-5. For each structure, one *I-V* curve was measured to evaluate whether the contact was Ohmic or non-Ohmic. It was found that almost all the *I-V* curves were S-shaped (non-Ohmic) to a certain degree. The $\rho_c$ (slope of the *I-V* curve / 2 × contact area) was calculated for each *V* and is plotted in Figure 5-10a for various a-Si and nc-Si emitters with ITO or AZO as TCO. It can be seen that the S-shapes add a (large) uncertainty to the $\rho_c$ measurements, but can still be used to compare different emitter/TCO combinations and derive a $\rho_c$ estimate. As it is impractical to measure and compare a statistically meaningful number of $\rho_c$ curves, the $\rho_c$ was subsequently measured with a multi-meter and these $\rho_c$ values are listed in Figure 5-10b (table) for several experiments, each involving many TLM samples. The $\rho_c$ range in the table refers both to differences between samples and the uncertainty due to the S-shapes. The a-Si($B_2H_6$) and a-Si/nc-Si(TMB) emitters with ITO as TCO were also tested on a planar wafer (without changing the deposition time).

It can be seen that:

- Changing the doping gas from **TMB** to **$B_2H_6$**
  - strongly decreased $\rho_c$ for the a-Si emitter,
  - had no significant effect for the a-/nc-Si emitter.

- Changing the emitter material from **a-Si** to **nc-Si** reduced the $\rho_c$ to ~0.05 Ω cm$^2$.
- **Adding a 6 nm a-Si(p)** layer between the a-Si(i) and nc-Si(p)/ITO increased the $\rho_c$ by 0.6-2 Ω cm$^2$,
  - which is lower than the 12 nm a-Si emitter with TMB as doping gas,
  - but higher than the 12 nm a-Si emitter with $B_2H_6$ as doping gas.
- **ITO** generally resulted in lower $\rho_c$ than **AZO.**
  - (The same $\rho_c$ was obtained for samples with 100 nm ITO or 10 nm ITO + 250 nm AZO)
- The $\rho_c$ for **planar** wafers was ~4 times higher than for **textured** wafer.

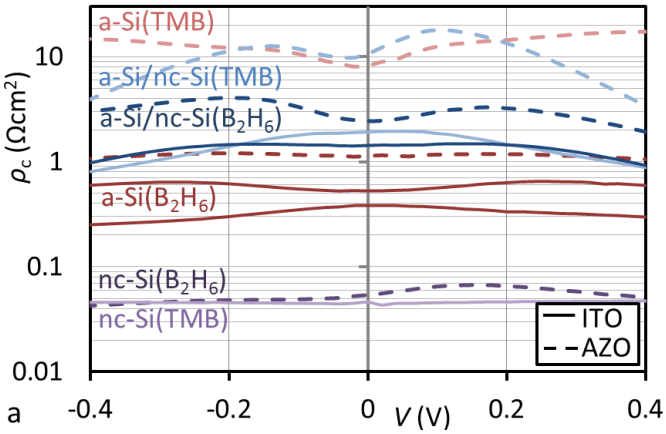


| Emitter stack | Gas | $\rho_c$ (Ω cm²) ITO | AZO |
|---|---|---|---|
| 12 nm **a-Si** | TMB | 3-10 | 4-15 |
| | $B_2H_6$ | 0.2-0.6<br>2-3 (planar) | 1-1.5 |
| 30 nm **nc-Si** | TMB | ~0.05 | - |
| | $B_2H_6$ | - | ~0.05 |
| 6 nm **a-Si** +<br>30 nm **nc-Si** | TMB | 0.8-2<br>4-7 (planar) | 2-10 |
| | $B_2H_6$ | 0.6-1.5 | 1-4 |

**Figure 5-10.** Figure a shows $\rho_c$ curves, derived from the slope of the *I-V* curves of emitter/TCO $\rho_c$ test structures on textured wafers, for a-Si (red), nc-Si (purple) and a-Si/nc-Si (blue) emitters with ITO (solid), AZO (dashed) as TCO. For the p-type emitters the doping gas was either TMB (light) or $B_2H_6$ (dark). The table in fig. b presents an overview of the emitter-TCO $\rho_c$ for the different emitter/TCO combinations on textured or planar (indicated in table) c-Si wafers.

The nc-Si emitter results in the lowest $\rho_c$ values, but strongly reduces the $V_{OC}$. Therefore, the best emitter-TCO layer stacks appear to be a-Si(p)($B_2H_6$)/ITO.

### 5.5.2 Cell $R_s$ Analysis

In the previous section the emitter/TCO $\rho_c$ was estimated using test structures on c-Si wafers, allowing for the comparison of many different emitter/TCO combinations. However, aside from the measurement uncertainty, the TLM structures were made on textured mono-crystalline wafers instead of textured poly-crystalline LPC-Si (with tilted pyramids) and also the lack of a p-n junction might affect the resistance measurement. Therefore, in this section the $R_s$ of point contact cells with different emitters will be compared to the emitter/TCO $\rho_c$ determined with the wafer test structures ($\rho_{c,wafer}$). Due to variations in the point contact resistances it was necessary to make a full analysis of the resistance components of the cells, instead of just comparing the cell $R_s$. Figure 5-11 schematically shows all the components making up the series resistance of the point contact cell:

1. Lateral transport in c-Si to point contact ($R_{s1}$)

2. Lateral transport in TCO to point contact ($R_{s2}$)
3. Resistance in the metal fingers ($R_{s3}$)
4. c-Si/Ag contact resistance ($R_{s4}$)
5. TCO/Ag contact resistance ($R_{s5}$)
6. Emitter/TCO (contact) resistance ($R_{s6}$)

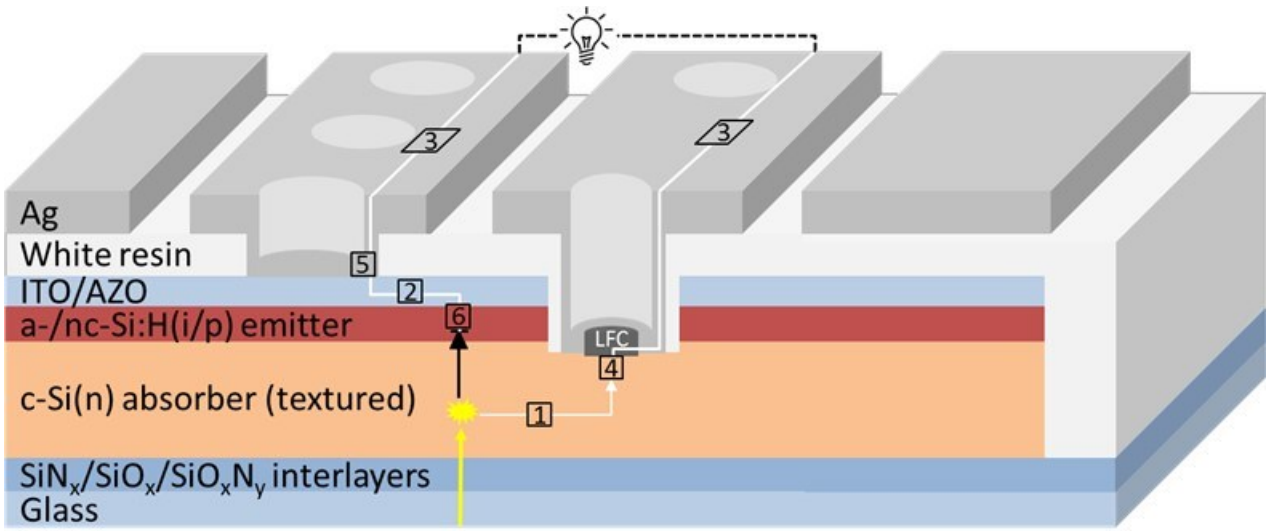


**Figure 5-11.** All the components ($R_{s1}$-$R_{s6}$) making up the series resistance of the point contact cell.

The point contact and sheet resistance were obtained from the point contact TLM structures as described in section 5.4.1. The lateral resistance was calculated from the measured sheet resistances, using the simulations presented in section 5.4.2. Finally, the metal finger resistance contribution was calculated in appendix A.2.1 to be 0.09 Ωcm$^2$. The cell $R_s$ was obtained from the *J-V* curve at 0.9 V (see Figure 2-1b). After subtracting $R_{s1}$-$R_{s5}$ from the cell $R_s$, the remainder should be due to $R_{s6}$, i.e. the emitter/TCO $\rho_c$ ($\rho_{c,cell}$).

The result is shown in Table 5-7 for n-type, ~9·10$^{16}$ doped samples from experiment 3 and 4. The TCO consisted of 10 nm ITO + 250 nm AZO (see section 5.3). The values are the median + standard deviation ($\sigma$) values for 5-6 TLM structures (or 4 cells) per sample. The cells were affected by the following $R_s$ issues:

a) For experiment 3, the ADP salt layer was left on too long and corroded away almost the entire Ag layer. After LFC and metal cut, a 2$^{nd}$ Ag layer was deposited and the metal cut was repeated. This resulted in a very low $R_s$.

b) For experiment 4, the c-Si/Ag ($R_{s4}$) and TCO/Ag ($R_{s5}$) contact resistance were higher than usual. It is suspected that this was due to the use of e-beam evaporated Ag instead of the sputtered Ag

The $V_{OC}$ values (in the table) confirm the quasi cell result that these emitters do not significantly affect the $V_{OC}$. It can be seen that the $R_{s6}$ (remainder) for the cell with the a-Si/nc-Si (TMB) emitter is significantly smaller than the smallest $\rho_c$ determined on the wafer test structures ($\rho_{c,wafer}$). For the a-Si ($B_2H_6$) emitter,

$R_{s6}$ fits with $\rho_{c,wafer}$. It can be concluded that the $\rho_{c,cell}$ difference between the a-Si/nc-Si (TMB) and a-Si ($B_2H_6$) emitters is smaller than was determined with the wafer based $\rho_c$ test structures. From the individual $R_s$ components, a cell $R_s$ of 0.6 Ωcm$^2$ appears to be achievable for n-type, ~$9 \cdot 10^{16}$ doped, LPC-Si point contact cells (by combining the 0.8 Ωcm$^2$ cell with the a-Si ($B_2H_6$) emitter).

**Table 5-7.** Cell resistance analysis showing the $R_s$ contributions (Ωcm$^2$) for cells with different emitters. The $V_{OC}$ and $R_s$ values are the median ± σ values for 5-6 TLM structures (or 4 cells) per sample.

| **Emitter type** | **a-Si(p)/nc-Si(p)** | **a-Si(p)** |
|---|---|---|
| **Doping gas type** | **TMB** | **$B_2H_6$** |
| **Experiment** | **3** | **4** |
| **$V_{OC}$ (mV)** | 600 ± 21 | 582 ± 9 |
| **c-Si (Ω/□)** | 115 | 100 |
| **$R_{s1}$: c-Si lateral (Ωcm$^2$)** | 0.07 ± 0.02 | 0.06 ± 0.02 |
| **$R_{s4}$: c-Si/Ag (Ωcm$^2$)** | 0.05 ± 0.05 | 0.26 ± 0.05 |
| **TCO (Ω/□)** | 151 | 320 |
| **$R_{s2}$: TCO lateral (Ωcm$^2$)** | 0.03 ± 0.00 | 0.06 ± 0.01 |
| **$R_{s5}$: TCO/Ag (Ωcm$^2$)** | 0.04 ± 0.02 | 0.15 ± 0.15 |
| **$R_{s3}$: Ag fingers (Ωcm$^2$)** | 0.09 | 0.09 |
| **Total ($R_{s1}$-$R_{s5}$) (Ωcm$^2$)** | 0.28 ± 0.09 | 0.62 ± 0.23 |
| **Cell $R_s$ (Ωcm$^2$)** | 0.79 ± 0.04 | 0.93 ± 0.05 |
| **$R_{s6}$: Remainder (Ωcm$^2$)** | 0.51 ± 0.13 | 0.31 ± 0.28 |
| **$\rho_{c,wafer}$ (Ωcm$^2$) ($R_{s6}$)** | 0.8-2 | 0.2-0.6 |

### 5.5.3 Discussion and Conclusions

The a-Si/ITO $\rho_{c,wafer}$ could be reduced to 0.2-0.6 Ωcm$^2$ by switching from TMB to $B_2H_6$ as doping gas and to ~0.05 Ωcm$^2$ by switching from a-Si to nc-Si emitters. However, the nc-Si emitter also resulted in a 50-80 mV $V_{OC}$ loss. This loss could be prevented by adding a 6 nm doped a-Si layer between the a-Si(i) and nc-Si layer, but that also increased the $\rho_{c,wafer}$ to 0.6-2 Ωcm$^2$. Further optimization should be attempted to reduce the $\rho_c$ for the a-Si(p)/nc-Si(p) emitter to the $\rho_c$ of the nc-Si(p) emitter (0.05 Ωcm$^2$), e.g. by reducing the a-Si thickness and/or the $B_2H_6$ flow in the nc-Si layer (to increase crystallinity [98]).

In order to determine if these emitter/TCO $\rho_{c,wafer}$ values (measured on textured wafers) correspond with the actual $\rho_{c,cell}$ for the LPC-Si point contact cells, the $R_s$ of point contact cells with a-Si/nc-Si (TMB) or a-Si ($B_2H_6$) emitters were analyzed. It was found that $\rho_{c,cell}$ is significantly lower than $\rho_{c,wafer}$ for the a-Si/nc-Si (TMB) emitter and roughly equal to the $\rho_{c,wafer}$ for the a-Si ($B_2H_6$) emitter.

The emitter/TCO $\rho_{c,wafer}$ measurements showed a ~4 times higher $\rho_c$ for planar than for textured wafers. This higher $\rho_c$ can be explained partly by a ~1.7 [105] times smaller contact area and partly by the (~1.7 times) higher deposition rate for the planar wafers, resulting in increased layer thicknesses and probably different material properties (e.g. crystallinity). Contrary to the wafers, the LPC-Si samples have many

different pyramid orientations (including planar areas for <111> oriented grains) as can be seen in the microscope image in Figure 5-12a. The tilted pyramids of the LPC-Si samples mean that these pyramids have both surfaces with larger and smaller angles than the 54° of the mono-Si pyramids on the textured wafers. Based on the texture dependence observed for the $\rho_{c,wafer}$ measurements, it seems likely that the areas with pyramid angles > 54° on the LPC-Si samples have a lower $\rho_c$ than the $\rho_{c,wafer}$. These differently tilted LPC-Si pyramid surfaces should form parallel resistances with high $\rho_c$ for the low angle surfaces and low $\rho_c$ for the high angle surfaces (shown schematically in Figure 5-12b). As the diffusion length is larger than the pyramid size, a large fraction of the current should flow through the low $\rho_c$ areas. Diffusion, together with conduction through the charge inversion layer [111], can transport minority carriers from planar areas to textured areas. This might explain the lower $\rho_{c,cell}$ than $\rho_{c,wafer}$ for the samples with a-Si/nc-Si emitter.

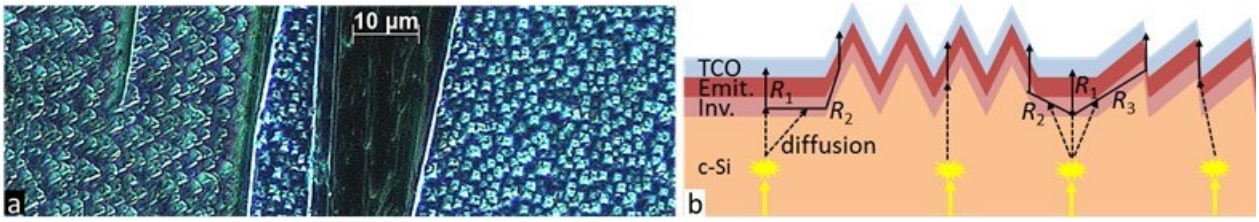


**Figure 5-12.** Figure a shows a microscope image of a KOH textured LPC-Si sample. Figure b shows a schematic cross-section of the textured LPC-Si sample with different pyramid orientations. The black arrows schematically show the different paths the minority carriers can take through the c-Si absorber, inversion layer, emitter and TCO, with the corresponding parallel resistances $R_1$-$R_3$.

It was found that the $\rho_c$ on the textured LPC-Si cells is approximately 0.51 ± 0.13 Ωcm$^2$ for the a-Si(i/p)/nc-Si(p)(TMB)/ITO/AZO stack and 0.31 ± 0.28 Ωcm$^2$ for the a-Si(i/p)($B_2H_6$)/ITO/AZO stack. For ~9·10$^{16}$ cm$^{-3}$ doped n-type cells, an $R_s$ of 0.8 Ωcm$^2$ was obtained with the a-Si/nc-Si (TMB) emitter and 0.6 Ωcm$^2$ should be obtainable with the a-Si ($B_2H_6$) emitter.

## 5.6 Passivated Isoscribe

The 11.5 % point contact cell from ref. [30] was made, using a planar, 2·10$^{16}$ cm$^{-3}$ doped absorber and the isoscribes were made with a single laser scribe after the TCO deposition. Based on the absorber doping and KOH texturing experiments on FrontERA cells presented in chapter 3, it was concluded that, in order to improve the cell efficiency, the absorber doping had to be increased to about 9·10$^{16}$ cm$^{-3}$ and the absorber had to be textured. In section 5.6.1 it will be shown how the resulting textured LPC-Si cells were affected by a *FF* loss that was related to the isoscribe. In section 5.6.2 it will be shown how a passivated isoscribe process was implemented to prevent this problem. The investigation will focus on n-type cells.

### 5.6.1 Isoscribe Recombination

In experiment 1 all the absorber layers were textured and the doping of some samples was increased to $8{\cdot}10^{16}$ cm$^{-3}$. The emitter consisted of an nc-Si layer and the TCO of 10 nm 25°C ITO + 250 nm AZO. Figure 5-13a shows the light *J-V* curve of the 11.5 %, $2{\cdot}10^{16}$ cm$^{-3}$ doped, n-type, planar point contact cell from ref. [30] and the light and dark *J-V* curves of textured a $2{\cdot}10^{16}$ cm$^{-3}$ and a $8{\cdot}10^{16}$ cm$^{-3}$ doped, n-type point contact cell from experiment 1. The corresponding $V_{OC}$, *FF* (measured with the solar simulator) and *pFF* (measured by Suns-$V_{OC}$) are included in the figure.

It can be seen that the (*p*)*FF* for the textured cells are much lower than for the planar cell. Especially the $8{\cdot}10^{16}$ cm$^{-3}$ doped cell had a very low *pFF*. From the slope of the *J-V* curve for reverse bias it can be seen that this low *FF* is not caused by Ohmic shunting. The $V_{OC}$ of the textured cells is also lower than for the planar cell, but this can (partly) be explained by the nc-Si emitter (see section 5.5.1).

Figure 5-13b shows DLIT measurements at different bias voltages (-0.4, 0.4 and 0.7 V) (see section 2.6) of the $8{\cdot}10^{16}$ cm$^{-3}$ doped cell from fig. a. The goal of the DLIT measurement is to determine the location of the high dark current at 0.4 V, which is reducing the *FF* (see dark *J* at 0.4 V in fig. a). The DLIT measurement shows many hotspots at the isoscribe for 0.4 V, indicating that the *FF* problem is related to the isoscribe.

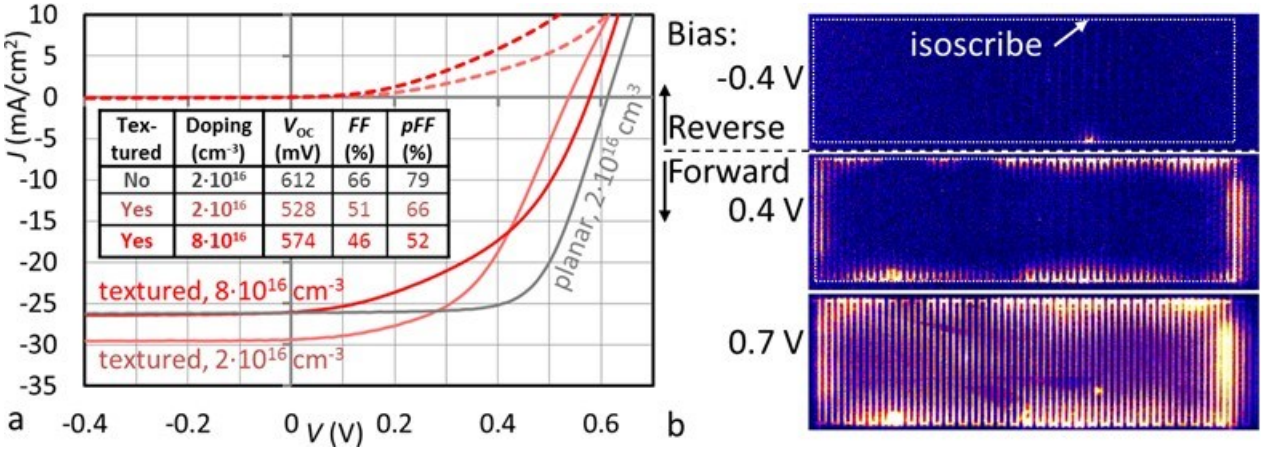


**Figure 5-13.** Figure a shows the *J-V* curve of the 11.5 %, $2{\cdot}10^{16}$ cm$^{-3}$ doped, n-type, planar cell from ref. [30] and dark and light *J-V* curves of textured $2{\cdot}10^{16}$ and $8{\cdot}10^{16}$ cm$^{-3}$ doped, n-type, KOH textured cells from experiment 1. Figure b shows DLIT images at different bias voltages (-0.4, 0.4 and 0.7 V) of the $8{\cdot}10^{16}$ cm$^{-3}$ doped cell from fig. a. The DLIT measurements are made from the metallized side and the infrared light only comes through the openings in the metal layer as the metal itself has very low emissitivity.

The dark *J-V* curves were fitted using the "resistance limited ($R_H$), locally increased recombination ($J_{0H}$)" feature in the PV Lighthouse equivalent circuit simulator. The equivalent circuit for this $R_H$-$J_{0H}$ model is shown in Figure 5-14a. The model was originally developed to characterize, among other things, the effect of edge recombination on the *J-V* curves of (<6 cm$^2$) wafer based c-Si solar cells [112]. Figure 5-14 shows

the measured (red) and fitted (grey) dark *J-V* (a) and *m-V* (b) curves of the textured cells from Figure 5-13a, where *m* is the local ideality factor that was derived from the dark *J-V* curves using $m = \frac{J}{V_T}\frac{dV}{dJ}$. The *m-V* curve is used in combination with the $R_H$-$J_{0H}$ model as it results in much more accurate and meaningful fitting results [112]. The fitted $J_{0H}$ and $R_H$ are listed in Figure 5-14b, together with the dark saturation current density ($J_{01}$, ideality factor = 1) and $R_s$. The ideality factor for the $J_{0H}$ diode was set to 2 as it resulted in a much better fit of the *m-V* curve for $V < 0.2$ V.

It can be seen that the $R_H$-$J_{0H}$ model can accurately reproduce the dark *J-V* and *m-V* curves. The fit results indicate that the higher dark current (lower *FF*) for higher absorber doping is due to a combination of a higher recombination ($J_H$) and a (~2x) lower resistance ($R_H$). The same *FF* loss and absorber doping dependence was also observed for textured, 2-7·10$^{16}$ cm$^{-3}$ doped p-type cells in experiment 1.

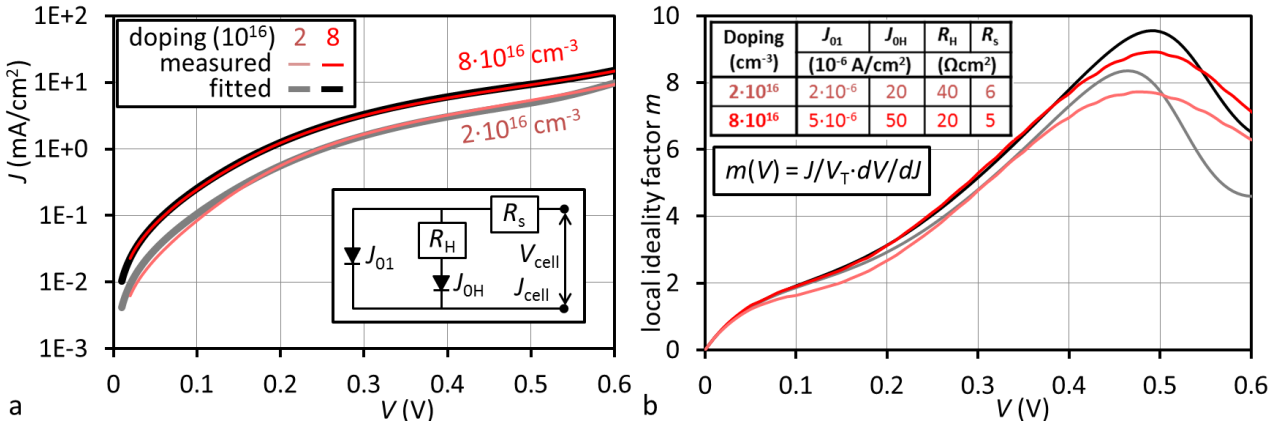


**Figure 5-14.** The measured (red) and fitted (grey) dark *J-V* (a) and *m-V* (b) curves of the textured cells from Figure 5-13a, where *m* is the local ideality factor. The curves were fitted with the "resistance limited ($R_H$), locally increased recombination ($J_{0H}$)" feature in the PV Lighthouse equivalent circuit simulator (shown in fig. a). The resulting fitting parameters are listed in fig. b.

Figure 5-15 shows LBIC measurements (using the 904 nm laser) of a p-type cell (a) and an n-type cell (b) (same cell as above) as well as two corresponding LBIC linescans near the isolation scribe (c). Both cells are 7-8·10$^{16}$ cm$^{-3}$ doped cells from experiment 1 with NO(ON) interlayer stacks. It can be seen that the p-type cell has a lower carrier collection close to the isoscribe, while for the n-type cell, collection near the isolation scribe appears to be unaffected. This reduction near the isoscribe for the p-type cell looks qualitatively similar to the DLIT measurement at 0.4 V in Figure 5-13b. It can also be seen that the LBIC signal of the p-type cell is reduced 200-2000 µm from the isoscribe, which is much too far to be explained by the typical LPC-Si diffusion length of 10-40 µm. This can be explained by conduction of minority carriers to the isoscribe through the charge inversion layer that is induced in the c-Si(p) by positive fixed charges in the $SiO_xN_y$ interlayer (see section 4.1.2). From the reduction of the LBIC signal near the isoscribe, the relative $J_{SC}$ loss for the p-type cells was estimated at 5-15 %.

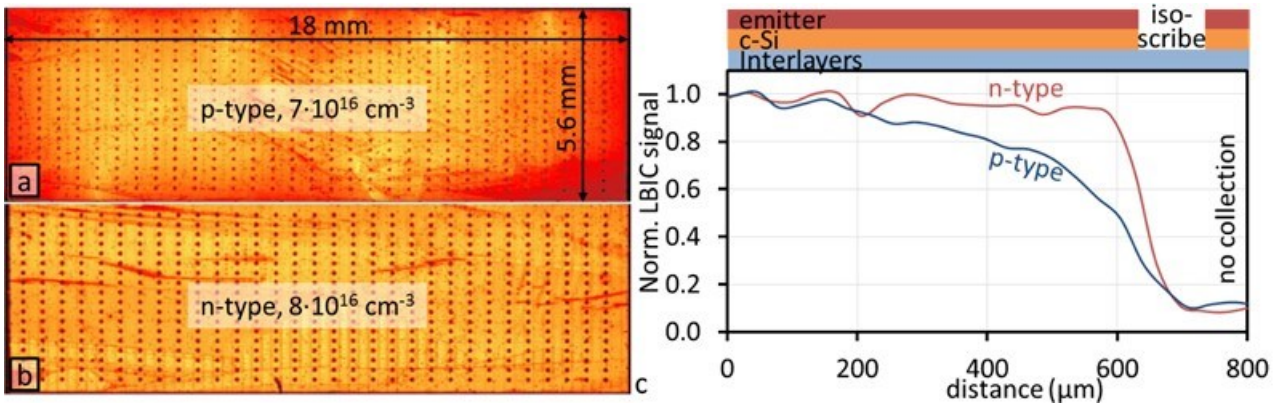


**Figure 5-15.** The LBIC images of a p-type cell (a) and an n-type cell (b) as well as two corresponding LBIC linescans near the isolation scribe (c). In fig. a and b red represent low and yellow represents high carrier collection. The grid of points with reduced carrier collection is caused by the absorber contacts. The schematic cross-section above fig. c indicates the position of the isoscribe.

Finally, laser scribes were made through finished, textured, p- and n-type quasi-cells from experiment 3 with a-Si or nc-Si emitters and ITO or AZO TCO layers. Suns-$V_{OC}$ measurements before and after the isoscribe process showed that this resulted in a similar *J-V* curve as in Figure 5-13a (after the isoscribe process), a $V_{OC}$ loss of ~50-70 mV and a *FF* loss of 20-25 %, independent of doping type, emitter or TCO.

Together, the results in this section indicate that the *FF* loss of the textured point contact cells is caused by increased recombination at the isoscribe.

### 5.6.2 Passivated Isoscribes

The isoscribe process was adapted in order to prevent the increased recombination at the isoscribe. The single step isoscribe after TCO deposition process was changed to a two-step process where the 1st isoscribe is made before the hydrogen passivation and the 2nd isoscribe is made within the 1st isoscribe after the TCO deposition. This way, the KOH texturing removes the surface damage created by the 1st isoscribe process, and the hydrogen plasma passivation and emitter deposition passivate the flank of the 1st isoscribe, while the 2nd isoscribe remove the TCO (and emitter) inside the 1st isoscribe.

Figure 5-16 show typical cross-section SEM images of the isoscribe (using finished cells) for the old (a) and new (passivated) (b) isoscribe processes. The layers are labelled in the figures. The isoscribe is made with a 1064 nm ps laser through the glass. The laser evaporates the lower part of the absorber and the rest is explosively broken off by the expanding plasma/vapour. It can be seen that the flanks of the isoscribe are shaped very irregularly and for the old process (a) there are many micro-cracks along the c-Si breakage line. The passivated isoscribe (b) does not shown these micro-cracks and the TCO (and presumably emitter) covers the isoscribe flanks, even if this flank is vertical (marked in fig. b by black circles).

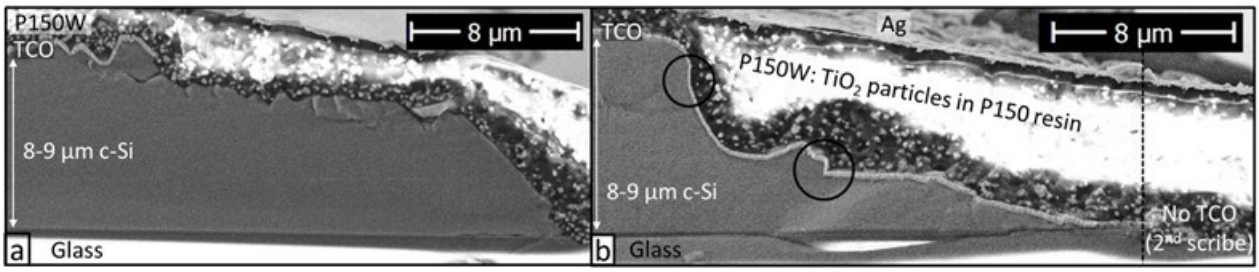


**Figure 5-16.** Fig. a and b show SEM cross section images of typical isolation scribe flanks using the "single scribe after TCO" (a) and "passivated isoscribe" (b) methods. The images show the irregular and even horizontal breakage of the c-Si absorber by the isoscribe process. The black circles in fig. b mark the areas where the c-Si surface is vertical, but nonetheless appears to be covered by a (thin) TCO layer.

Figure 5-17a shows schematic representations of the different isoscribe methods uses in this thesis:

1. Method 1: isoscribe after TCO deposition (width ≈ 50 µm) , not passivated (added for comparison)
2. Method 2: **double** 1st isoscribes after LPC with ~10 µm overlap + 2nd isoscribe inside 1st isoscribes
3. Method 3: isoscribe before LPC parallel to LPC scanning direction ("**crack catcher**") + isoscribe perpendicular to LPC scanning direction after LPC + 2nd isoscribe inside 1st isoscribes.

For the 2nd isoscribe, a 532 nm ps laser was used (from the glass side), as 1064 nm laser light is not absorbed by the a-Si emitter. In experiment 3, point contacts cells were fabricated on textured, ~$10^{17}$ $cm^{-3}$ doped, n-type absorbers with NO(ON) interlayers, using either method 2 or method 3 for the isoscribe.

Figure 5-17b and c show microscope images of the isoscribes of these cells, using method 2 (double scribe) (b) or method 3 (crack catcher) (c). In fig. b it can be seen how the 2nd scribe (black) fits inside the 1st two scribes. In fig. c it can be seen in how small grains and many small side cracks originate from the crack catcher scribe. (In chapter 6 LBIC measurements will be used to determine the photocurrent loss due to the crack catcher and isoscribe.) Figure c shows an example of an optical inhomogeneity (e.g. a bubble in the glass, section 3.3.3) interrupting the 1st isoscribe and bending the 2nd isoscribe from its path. It can be seen how a narrow crack follows a straight line, ignoring the interruption in the 1st scribe.

Figure 5-17d shows DLIT measurements made with ± 0.4 V bias voltage for a cell with the crack catcher as isoscribe (method 3). It can be seen that the cell is no longer affected by increased recombination at the isoscribe. *J-V* and Suns-$V_{OC}$ measurements resulted in an average $V_{OC}$ of 625 mV and *pFF* of ~68 % for both isoscribe methods 2 and 3, indicating that both methods can be used to passivate the isoscribe.

The remaining *pFF* loss is due to the non-Ohmic hotspots shown in the DLIT measurements (Figure 5-17d). In section 5.3.2 it was concluded that these non-Ohmic shunts were due to incomplete etching of the emitter (see Figure 5-4a).

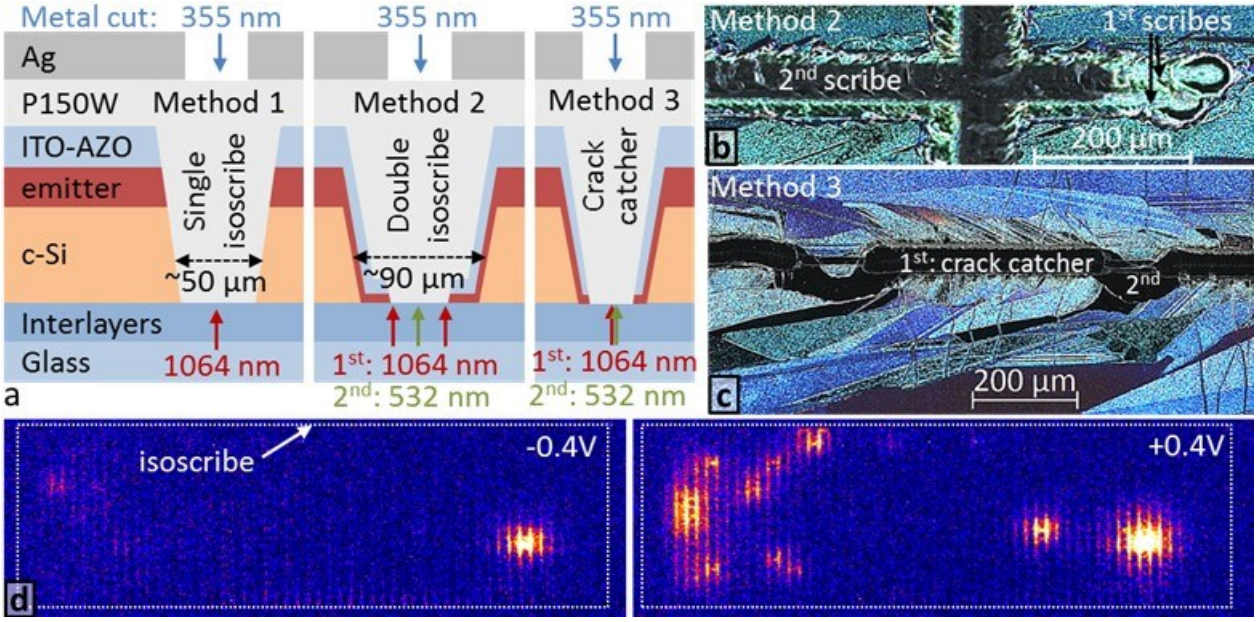


**Figure 5-17.** Figure a and b show microscope images of the double scribe (a) and the crack catcher (b-c) as 1st isoscribe. Figure d shows DLIT measurements at -0.4 and 0.4 V for a cell with crack catcher as isoscribe.

### 5.6.3 Conclusions

It was determined that the textured point contact cells were affected by a FF loss that was related to the isoscribe and it was argued that this could be explained by increased recombination at many positions along the isoscribe. A passivated isoscribe process was successfully developed to prevent the isoscribe recombination problem, featuring a 1st isoscribe of the c-Si absorber before hydrogen passivation and a 2nd isoscribe after the TCO deposition. The 1st isoscribe consisted either of two slightly overlapping scribes or of the crack catcher scribe. These two different passivated isoscribe processes will also be compared on mini-modules in chapter 6.

For the p-type cells, the current collection next to the isoscribe was also reduced, indicating that conduction of minority carriers through the frontside inversion layer can also decrease the $J_{SC}$ in the presence of locally increased recombination. It should be investigate if other forms of locally increased recombination, e.g. at the grain boundaries (see section 3.3.3), result in similar *FF*, $V_{OC}$ and $J_{SC}$ losses as determined in this section for increased recombination at the isoscribe.

## 5.7 Cell Efficiency Improvement

Using the passivated isoscribe process, a ~$10^{17}$ $cm^{-3}$ doped, n-type, KOH textured absorber, an a-Si/nc-Si (TMB) emitter and a 90 s poly-Si emitter etch, a new record $\eta$ for point contact LPC-Si cells of 12.0 % was obtained in experiment 5. The cell also used an a-Si(i) layer process for which the 1st nm was deposited with 4x the normal power (i.e. 120 W). The results in appendix A.5 indicate that this a-Si(i) layer resulted

in a higher *pFF* and $V_{OC}$, but also a higher $\rho_c$. The *J-V* curve of this cell and of the old, $2 \cdot 10^{16}$ $cm^{-3}$ doped, planar, 11.5 % cell [30] are shown in Figure 5-18a. The *J-V* parameters are indicated in the figure and the *pFF* was 81.2 %. Both cells had an NON(ON) interlayer stack and were measured with ARF, i.e. had similar direct reflection losses. It can be seen that the 12.0 % cell has a higher $V_{OC}$, *FF* and $\eta$, which can mainly be explained by the higher doping and new emitter. Figure 5-18b shows the *EQE* and 1-*R* curves of the 11.5 % cell and of the 12.0 % cell. It can be seen that the texturing resulted in the expected long wavelength *EQE* and 1-*R* gain, but this is overcompensated by the *EQE* loss for low wavelengths, which can mainly be explained by a higher recombination loss. The photocurrent losses will be analyzed in more detail in the next section.

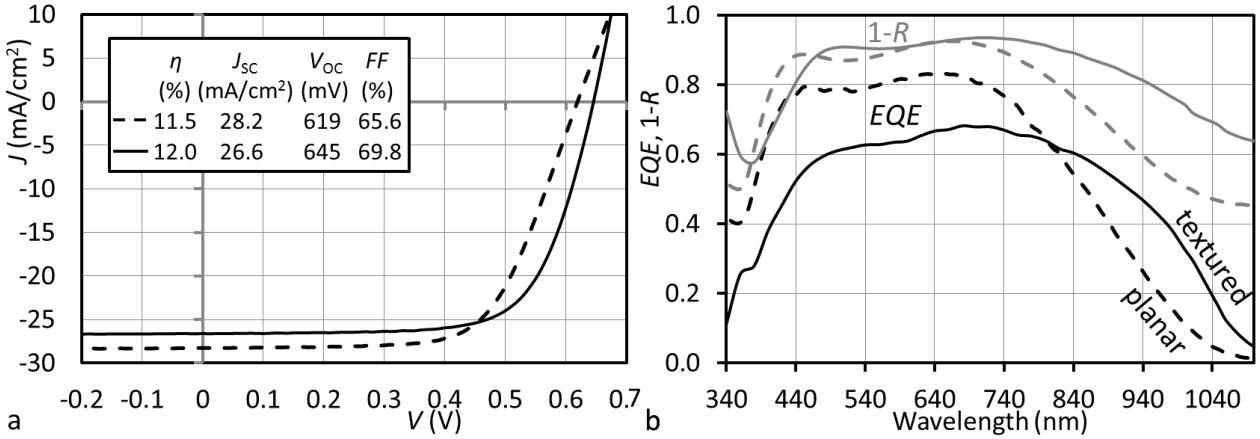


**Figure 5-18.** The *J-V* (a) and the *EQE* and 1-*R* (b) curves of the $2 \cdot 10^{16}$ $cm^{-3}$ doped, planar, 11.5 % cell from ref. [30] (dashed) and of a ~$10^{17}$ $cm^{-3}$ doped, KOH textured 12.0 % cell (solid). Both *J-V* curves are measured with ARF and the *EQE* curves are not.

## 5.8 Photocurrent Analysis

In this section the photocurrent losses of the textured point contact cells will be analysed and compared to the textured FrontERA cell from section 4.1, focusing on the impact of the back reflector on the light trapping and parasitic absorption losses. In section 5.8.1 the investigated cells are presented, together with the fitted interlayer thicknesses and $L_{eff}$ values, which is directly followed by the $J_{SC}$ loss overview in section 5.8.2. The absorptance properties of the P150W/metal reflector is presented in section 0 and the light trapping and parasitic absorption are investigated in more detail in sections 5.8.4 and 5.8.5. This is followed by a discussion of the $J_{SC}$ potentials in section 5.8.6.

### 5.8.1 Investigated Cells

The photocurrent was analyzed for 6 different point contact cells (from experiments 3-6) to show that point contact cells from different series on different materials result in similar light trapping and parasitic absorption behavior (compared to the FrontERA cell). The cells will be analyzed without ARF, as the ARF

was already analyzed in section 4.1 and requires a significant additional measurement effort. The cell ID's used in this section and the properties of the cells are shown in Table 5-8. The cell ID's indicate: doping-glass-experiment, e.g. n-c-6 for an **n**-type cell on **C**orning glass from the experiment **6**. Cell n-b-5 is the $\eta$ = 12.0 % cell from the previous section.

The table shows both the intended and the fitted interlayer thicknesses, and also the fitted refractive indices (n) of the $SiN_x$ layers at λ = 700 nm, using the method described in section 4.1.3 (simulation in OPAL2). The difference of the fitted thicknesses for the same interlayer type indicate the non-uniformity of the interlayer deposition. The PECVD $SiN_x$ interlayer had the n (~2.09) and this n was also higher than the n for the PVD $SiN_x$ layer (1.99, not shown in table).

The table also includes the fitted effective diffusion lengths ($L_{eff}$) (± 15 %) using the same method as in section 4.1.5 (average of *L*- and *S*-limited fit). All the point contact cells could best by fitted by completely *S*-limited $\eta_c$ curves (*L* = 10 ms). The effect of the different emitter etch procedures was described in section 5.3.2: the old purple etch solution did not completely remove the emitter, resulting in very low $f_{DA}$, but also shunting. The 90 s poly-Si etch prevented the shunts, but resulted in a large $f_{DA}$ (n-b-5). The 40 s poly-Si etch and the etch-reflow-etch-reflow (e-r-e-r) process were used to reduce the $f_{DA}$ to ~3 %.

**Table 5-8.** Overview of the investigated cells. The fitted/measured values are indicated in grey.

| **cell ID** | **n-b-FE** | **p-b-3** | **p-b-4** | **n-b-4** | **n-b-5** | **n-b-6** | **n-c-6** |
|---|---|---|---|---|---|---|---|
| **Glass** | Boro33 | Boro33 | | | | | Corning |
| **Interlayer type** | AKT N/O/ON | AKT N/O/ON | AKT N/O/N/ON | | | | PC1 O/N/O |
| **Intended. IL thickness (nm)** | 20/ 110/ 85 | 20/ 110/ 85 | 15/ 200/ 60/20 | | | | 200/ 60/ 10 |
| **Fitted IL thickness (nm)** | 20/ 135/ 80 | 25/ 125/ 88 | 15/ 217/ 52/17 | 15/ 245/ 52/20 | 15/ 235/ 59/15 | 10/ 250/ 60/17 | 200/ 45/ 33 |
| **$SiN_x$ (n@700 nm)** | - | - | 2.08 | | | | 1.85 |
| **Doping type** | n | p | | n | | | |
| ***N* ($10^{16}$ $cm^{-3}$)** | 9 | 8 | 6 | 10 | | | 15 |
| ***d* (µm)** | 11 | 8 | | 11 | 8 | | 13 |
| **Fitted $L_{eff}$ (µm)** | 30 | 13 | 13 | 20 | 10 | 14 | 19 |
| **Emitter etch** | - | old purple etch | | | 90 s | 40 s | e-r-e-r |
| **$f_{DA}$ (Dead area)** | 11 % | 2.3 % | | 3.4 % | 8.3 % | 4.2 % | 3.0 % |
| **Texture** | KOH | KOH | | | | | |
| **Reflector** | White paper | P150W/Ag/Al | | P150W/Ag | | | |

### 5.8.2 $J_{SC}$ Loss Overview

Using the methods described in section 4.1, the measured *EQE*, *R*, *T* and $f_{DA}$ were used to determine the $J_{SC}$ losses. Figure 5-19 shows examples of the $J_{SC}$ loss analysis for the n-type (a) and p-type (b) cells with the

highest $J_{SC}$, both from experiment 4. Table 5-9 gives an overview of all the $J_{SC}$ losses, including for the textured n-type FrontERA cells with reflector and without ARF from section 4.1.

The approximately 2 mA/cm$^2$ lower dead area loss of the point contact cells (except n-b-5) compared to the FrontERA cell, shows one of main reasons for switching to the point contact cells. Unfortunately, this was overcompensated by the higher recombination losses for these point contact cells, due to the lower material quality (lower $L_{eff}$). In addition, the parasitic absorption ($A_{par}$) and light trapping losses ($LT_{loss}$) are larger for the point contacts cells: the average $A_{par}$ is 4.1 mA/cm$^2$ for the p-type and 3.1 mA/cm$^2$ for the n-type point contact cells, compared to 2.2 mA/cm$^2$ for the textured FrontERA cell. The average $LT_{loss}$ was 1 mA/cm$^2$ for the point contact cells, compared to 0.1 mA/cm$^2$ for the textured FrontERA cell. About half of this $LT_{loss}$ was due to transmittance through the metal scribes.

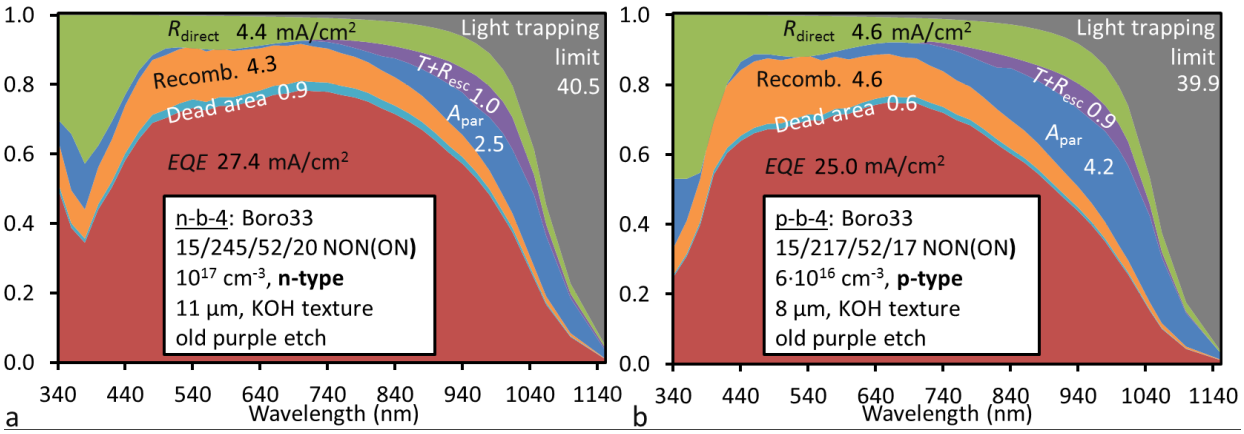


**Figure 5-19.** Wavelength dependent analysis of the photocurrent losses for the n-type (a) and p-type (b) point contact cells with the highest $J_{SC}$. The most relevant material parameters and the photocurrent losses in mA/cm$^2$ are indicated in the figures.

**Table 5-9.** Overview of $J_{SC}$ losses (mA/cm$^2$) for the cell from Table 5-8.

| Cell ID | *d* (µm) | IL type | *EQE* | $J_{SC,lim}$ | Dead area | Recomb. | $A_{par}$ | $LT_{loss}$ | $R_{direct}$ |
|---|---|---|---|---|---|---|---|---|---|
| **n-b-FE** | **11** | **NO(ON)** | 26.4 | 40.6 | 2.9 | 1.9 | 2.2 | 0.2 | 7.1 |
| **p-b-3** | **8** | **NO(ON)** | 22.7 | 39.9 | 0.5 | 4.2 | 4.0 | 0.8 | 7.7 |
| **p-b-4** | **8** | **NON(ON)** | 25.0 | 39.9 | 0.6 | 4.6 | 4.2 | 0.9 | 4.6 |
| **n-b-4** | **11** | | 27.4 | 40.5 | 0.9 | 4.3 | 2.5 | 1.0 | 4.4 |
| **n-b-5** | **8** | | 23.2 | 39.9 | 1.9 | 6.0 | 3.5 | 1.2 | 4.1 |
| **n-b-6** | **8** | | 25.6 | 39.9 | 1.1 | 4.4 | 4.1 | 0.7 | 4.0 |
| **n-c-6** | **13** | **ONO-PC1** | 24.0 | 40.8 | 0.7 | 5.6 | 3.0 | 0.9 | 6.6 |

The $R_{direct}$ loss for NON(ON) interlayer stack is relatively low due to the optimized interlayer thicknesses and the high refractive index of the $SiN_x$ layer (see Table 5-8). In section 4.1 it was shown that the ARF reduces this $R_{direct}$ loss by about 60 %, while adding about 0.4-0.7 mA/cm$^2$ to the $A_{par}$ loss. Therefore, with ARF, $A_{par}$ and recombination are the largest losses.

In the next sections the parasitic absorption and light trapping losses will be investigated in more detail in

order to understand why these losses are higher for the point contact cells and discuss ways to reduce them. Finally, it will be discussed how the recombination loss can be reduced by optimizing the absorber thickness.

### 5.8.3 Absorptance of the P150W/Metal Reflector

The absorptances of the ARF, glass, $SiN_x$, emitter and ITO layers were presented and discussed in section 4.1.4. The layers in the point contact device that were not yet presented are the P150W/metal reflector and the 250 nm AZO layer. The absorptance of the 250 nm AZO layer (not shown) is ~0.4 $\%_{abs}$ or 25 $\%_{rel}$ lower than that of the 100 nm R&R ITO layer used in the FrontERA cell and therefore cannot explain the higher parasitic absorption in the point contact cells.

Point contact cells use a ~5 µm P150W diffuse/white reflector, combined with a 100 nm Ag layer for the n-type cells and a 20 nm Ag / 100 nm Al layer for the p-type cells. The 20 nm Ag layer was added in order to reduce the AZO/metal point contact resistance. In order to measure the absorptance (1-*R*) of the P150W/metal reflector, P150W was spin coated on 100-200 nm Ag and Al layers that were sputtered on a glass substrate. Figure 5-20a shows the measured absorptance (1-*R*) of this P150W/Ag reflector, for ~5 and ~16 µm P150W. Figure 5-20b shows the measured absorptance for the same ~5 µm P150W/Ag reflector and for a ~5 µm P150W/Al reflector. For comparison, fig. a also shows the simulated absorptances of various Ag reflectors that were simulated with PVLighthouse's OPAL2 [71], using a planar or pyramid textured, 1 µm Ag layer in contact with a non-absorbing air (n = 1), $SiO_2$ (n ≈ 1.5), or AZO (n ≈ 2) halfspace. Fig. b also shows the simulated absorptances of a pyramid textured AZO/Ag/Al reflector for Ag thicknesses between 0 and 60 nm. For Ag thicknesses ≥ 60 nm, the simulated absorptance no longer changes significantly. The measured and simulated structures are shown schematically in Figure 5-20a.

It can be seen that the measured P150W/Ag absorptance is ~8 %, which is much higher than the absorptance of the white paper reflector (~3 %) that was used for the FrontERA cells (see section 4.1.4). It can also be seen that increasing the P150W layer thickness has almost no effect. Finally, it can be seen that the measured P150W/Ag absorptance is very similar to that of the simulated, textured AZO/Ag reflector and that the measured P150W/Al absorptance is very similar to that of the simulated textured AZO/Al reflector. These observations show that the metal has a very strong influence on the measured absorptance, indicating that the P150W is very transparent. (The transmittance of the P150W layer on glass could not be measured reliably due to light trapping in the glass substrate.)

It can be seen that the simulated absorptance of the Ag reflector increases from ~ 2 % to ~3.5 % by changing the refractive index of the material it is in contact with from 1 (air) to 2 (AZO). For the pyramid

textured AZO/Ag reflector, the light is reflected from the AZO/Ag interface of one pyramid onto the AZO/Ag interface of a neighboring pyramid, thereby doubling the total absorptance by the AZO/Ag reflector ("multiple bounce"). P150W consists of $TiO_2$ particles (n ≈ 2.7) in a P150 resin (n ≈ 1.5), resulting in an effective refractive index close to or slightly higher than that of AZO (n ≈ 2). The similarity of the planar P150W/metal reflectors to the textured AZO/metal reflectors can be explained by the light being scattered back and forth within the P150W, causing multiple reflections at the P150W/metal interface. By removing the $TiO_2$ particles from the P150W, the resulting planar P150/Ag interface is optically very similar to that of the simulated planar $SiO_2$/Ag interface, which has an absorptance of ~3 %. This indicates how the reflector absorptance might be reduced.

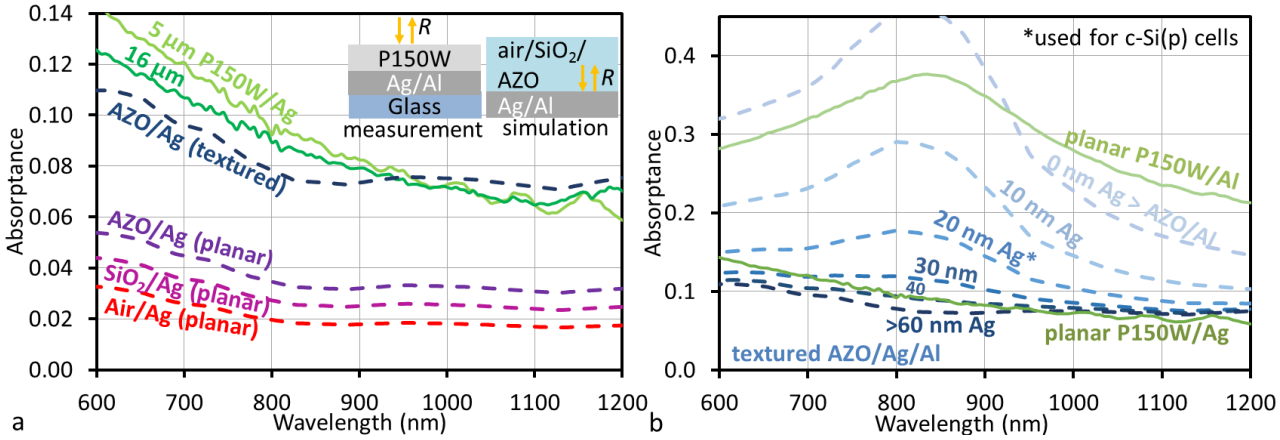


**Figure 5-20**. Figure a compares the measured absorptance (1-*R*) of the P150W/Ag reflector (solid curves) to the absorptance of various Ag reflectors that were simulated with OPAL2 (dashed curves). Schematic representation of the measured and simulated structures are included in the figure. Figure b shows the measured absorptance of the P150W/Al and P150W/Ag reflectors (solid), as well as the simulated absorptance of a textured AZO/Ag/Al reflector for Ag thicknesses between 0 and 60 nm (dashed).

The simulated AZO/Ag/Al absorptance curves in Figure 5-20b show how the absorptance decreases for increasing Ag thickness. It can also be seen that the 20 nm Ag layer, which is used for p-type cells, is not thick enough to completely prevent absorption in the Al. This can explain the (~1 mA/cm$^2$) higher $A_{par}$ in the p-type cells than in the n-type cells. It can be seen that this absorptance could be reduced to that of the n-type cells by increasing the Ag layer thickness to 40-60 nm.

### 5.8.4 Light Trapping in KOH Textured LPC-Si Cells

In this section the light trapping of the textured point contact cells will be compared in more detail to that of the textured FrontERA cells. First, a new concept must be introduced to allow for the comparison of relatively small light trapping differences between the textured cells with different absorber thicknesses ($d$). Figure 5-21a shows the light trapping efficiency ($\eta_{LT}$), simulated with the PV Lighthouse ray tracer for a pyramid textured LPC-Si cell with $d$ = 11 µm (see section 4.1.6), compared to the calculated absorption

probability in silicon ($a_{Si}$) (as introduced in ref. [113]). Here, $a_{Si}$ was calculated for a "fraction of the light escaping every $d$" ($f_{esc}$) of 1.3 %, using:

$$a_{\mathrm{Si}} = \frac{\alpha_{\mathrm{Si}}}{\alpha_{\mathrm{Si}}+\alpha_{\mathrm{esc}}}, \tag{28}$$

$$f_{\mathrm{esc}} = 1 - e^{-\alpha_{\mathrm{esc}} d} \rightarrow \alpha_{\mathrm{esc}} = \frac{-\ln(1-f_{\mathrm{esc}})}{d}. \tag{29}$$

Eq. (29) uses the Lambert-Beer law and eq. (28) is similar to eq. (7) in ref. [113] (where $\alpha_{esc}$ was fixed at $1/(4n^2d)$, i.e. the Yablonovitch limit). It can be seen in Figure 5-21a that the $f_{esc}$ = 1.3 % $a_{Si}$ curve (dotted) provides a very good fit for the $\eta_{LT}$ curve (solid), especially for λ > 950 nm. For the pyramid texturing ($\eta_{LT}$ curve), no light escapes the cell ($f_{esc}$ = 0 %) after the first reflection, because all the light is reflected beyond the critical angle of c-Si to air (16°). This results in a small underestimation for λ < 950 nm by the $a_{Si}(f_{esc})$ model, which assumes a fixed fraction of the light continuously escaping the cell. After several internal reflection in the simulated pyramid textured cell, the light becomes randomized and, based on the good fit in Figure 5-21a, ~1.3 % escapes the cell every $d$. Figure 5-21b shows the light trapping limit in mA/cm$^2$ using $f_{esc}$ = 1.3 %, for $d$ = 2-50 µm The $a_{Si}(f_{esc})$ model and $J_{SC,lim}$ curve will also be used in the absorber thickness optimization in section 5.8.6.

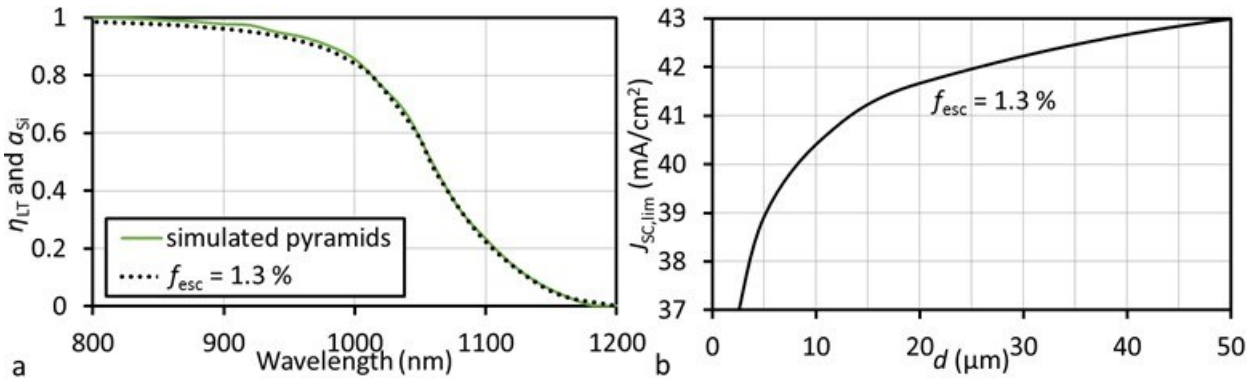


**Figure 5-21.** Fig a shows the absorption probability in silicon ($a_{Si}$) for $f_{esc}$ = 1.3 %, for an 11 µm c-Si layer and the light trapping efficiency ($\eta_{LT}$) for the simulation from Figure 4-7 (section 4.1.6) with a detached reflector and a pyramid textured Si backside. Fig. b shows the light trapping limit ($J_{SC,lim}$) vs. $d$ for $f_{esc}$ = 1.3 %.

Having shown that the $f_{esc}$ model can reproduce the simulated $\eta_{LT}$, it will now be used to compare the light trapping differences for the LPC-Si cells. $f_{esc}$ will be calculated for each wavelength from the experimental $\eta_{LT}$, using eq. (17), (28) and (29) and defining $a_{Si} \equiv \eta_{LT}$ (see Figure 5-21a):

$$f_{\mathrm{esc}} = 1 - e^{-\alpha_{\mathrm{esc}} d} = 1 - e^{-\frac{\alpha_{\mathrm{Si}}(R_{\mathrm{esc}}+T)d}{A_{Si}}}. \tag{30}$$

This way, the $A_{Si}$, $R_{esc}$ and $T$ are not only corrected for $R_{direct}$ and $A_{par}$ as was done with the $\eta_{LT}$ in section 4.1.6, but also for the absorber layer thickness $d$. Furthermore, $f_{esc}$ is a physically meaningful quantity (fraction of the light that escapes every $d$) and is much better suited than $\eta_{LT}$ for comparing relatively small light trapping difference.

Figure 5-22 shows the $f_{esc}$ without (a) and with (b) transmission for all the cells from Table 5-8. A planar point contact (on Corning glass with PVD interlayers, from exp. 5) and a planar FrontERA cell (from section 4.1) were added as reference. The relevant wavelength region is approximately between 850 and 1050 nm, as for λ < 850 nm little light escapes the cell (even without light trapping) and for λ > 1050 nm little light is absorbed, even with perfect light trapping. It can be seen that the best light trapping (lowest $f_{esc}$) is obtained for the textured FrontERA cell ($f_{esc}$ ≈ 1.5 %, $LT_{loss}$ ≈ 0.2 mA/cm$^2$), followed by the textured point contact cells ($f_{esc}$ ≈ 2-3.5 % w/o *T* and 3-4.5 % with *T*, $LT_{loss}$ ≈ 1 mA/cm$^2$), the planar point contact cell ($f_{esc}$ ≈ 8-9 %, $LT_{loss}$ ≈ 2 mA/cm$^2$) and the planar FrontERA cell ($f_{esc}$ ≈ 22 %, $LT_{loss}$ ≈ 5.5 mA/cm$^2$). (Note that the pyramid texture light trapping limit results in an $f_{esc}$ of 1.3 %.)

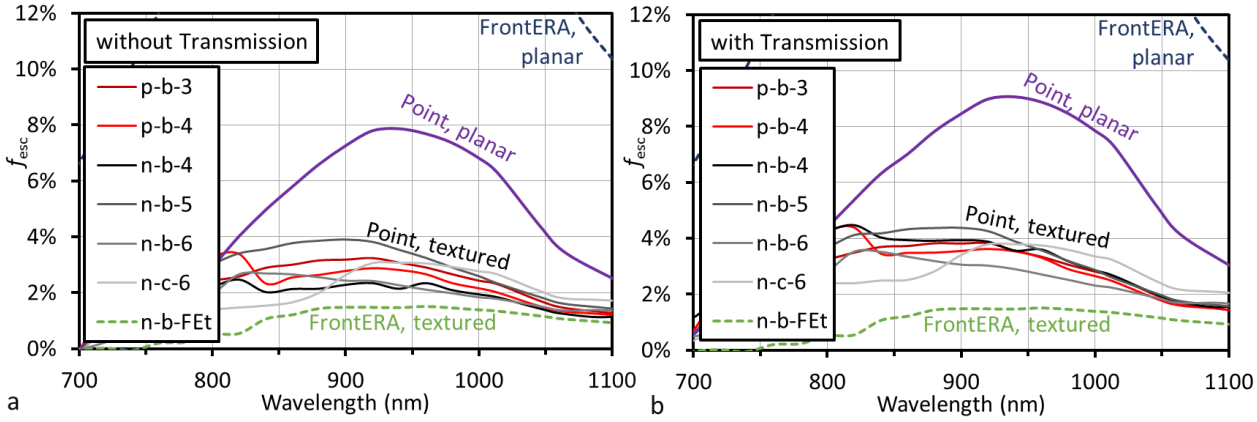


**Figure 5-22.** Experimental $f_{esc}$ with (a) and without transmission (b) for the point contact cells (solid line) and FrontERA cells (dashed).

With regard to light trapping, the fundamental difference between the FrontERA and the point contact cell, is that the point contact cell has an attached white reflector and the FrontERA cell has a detached (white) reflector. The lower $f_{esc}$ for the planar point contact cell than for the planar FrontERA cells indicates that the attached white reflector increases light trapping for a planar cell. The higher $f_{esc}$ for the textured point contact cell than for the textured FrontERA cell indicates that the attached white reflector decreases light trapping for a (KOH) textured cell. This would be rather unexpected as for the CSG solar cell, the P150W/Al reflector was considered a significant reason for the excellent light trapping properties [16].

A reduced light trapping due to the attached white reflector can be explained in the following way (shown schematically in Figure 5-23a):

- For KOH textured (poly-crystalline) LPC-Si there are many **different pyramid angles (θ)**.
- **For θ > 8°**, the pyramids scatter the light at an angle larger than the critical angle of c-Si to air (16°), thereby trapping the light in the cell. **Any additional random scattering by the white reflector should decrease light trapping** by scattering some of the light within the critical angle.
- **For θ > 34°** the light is totally reflected at the Si/TCO interface, i.e. **the reflector doesn't affect the**

**light trapping**.

- For an attached white reflector (**point contact cells**) and θ < 34°, the light is scattered by the reflector →
    - **For 34° > θ > 8°, light trapping is reduced by the white reflector**
    - For θ < 8° (planar), light trapping is improved by the white reflector
- For a detached white reflector (**FrontERA**) and
    - 34° > θ > 16°, the light is totally reflected at the TCO/air interface,
    - θ > 16°, the light is scattered by the detached reflector →
        - **For 16° > θ > 8°, light trapping is reduced by the white reflector**
        - For θ < 8° (planar), light trapping is improved by the white reflector

In other words: the attached reflector has a 3 times larger pyramid angle range where the light trapping is reduced due to "scattering where no scattering is needed". In addition, the isotropic light scattering by the white reflector is better preserved for the attached reflector, which scatters isotropically into the TCO (n ≈ 2), than for the detached reflector, which scatters isotropically into air (n = 1). This means that both the light trapping reduction for θ > 8° and the light trapping improvement for θ < 8° should be larger for the attached reflector. These arguments can explain why the attached white reflector (point contact cells) results in higher $f_{esc}$ than the detached white reflector (FrontERA).

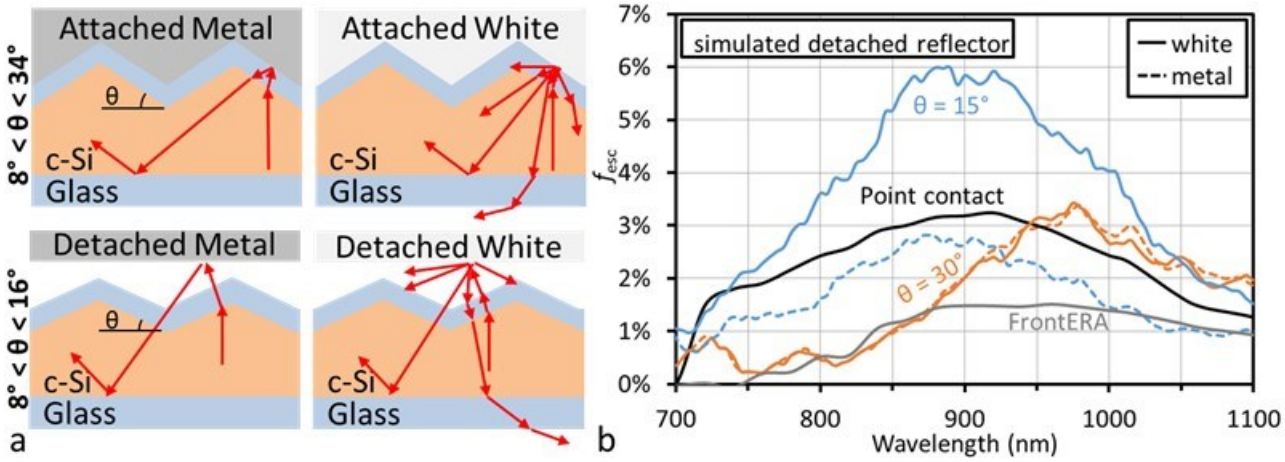


**Figure 5-23.** Figure a shows schematic representations of scattering at the backside for different reflectors, indicating how a white (diffuse) reflector can reduce light trapping compared to a metal (specular) reflector. The pyramid angle (θ) range corresponding to the attached and detached reflector examples is indicated next to the figures. (For lower angles, the white reflector increases light trapping and for higher angles the reflector has no influence on the indicated reflection.) Figure b show the simulated $f_{esc}$, using the PV Lighthouse ray tracer, for detached white (solid) and metal (dashed) reflectors and for θ = 15 ° (blue) and θ = 15 ° (orange). The experimental $f_{esc}$ for a textured point contact cell (n-b-3) and the textured FrontERA cell were added as reference.

Simulations were made with the PV Lighthouse ray tracer in order to confirm the light trapping reduction

by the white reflector described above and to estimate its magnitude. Figure 5-23b shows the simulated $f_{esc}$ for a detached white reflector (solid curves) or metal reflector (dashed curves), and for θ = 15 ° (blue) and θ = 15 ° (orange). The experimental $f_{esc}$ for a textured point contact cell (n-p-3) and FrontERA cell were added as reference. For the simulations with θ = 15°, $f_{esc}$ is increased from 3 % to 6 % by the (detached) white reflector compared to a metal reflector, proving that a white reflector can significantly decrease light trapping for certain pyramid angles. As predicted above, for θ > 16° there is no significant $f_{esc}$ difference between white and metal detached reflectors. It can be seen that the θ = 15° simulations are similar to the experimental point contact $f_{esc}$ and these simulations will therefore be used in the next section to estimate the absorption in the reflector and TCO.

### 5.8.5 Parasitic Absorption

In this section, the same method as in the previous section is applied to the parasitic absorption, using the following eq. (based on eq. (17), (28)-(28)) to determine the fraction absorbed parasitically every *d* ($f_{par}$):

$$\eta_{par} = \frac{A_{Si}}{A_{Si} + A_{par}} \equiv \frac{\alpha_{\mathrm{Si}}}{\alpha_{\mathrm{Si}} + \alpha_{\mathrm{par}}} \tag{31}$$

$$\rightarrow\ f_{\mathrm{par}} = 1 - e^{-\alpha_{\mathrm{par}} d} = 1 - e^{-\frac{\alpha_{\mathrm{Si}} A_{par} d}{A_{Si}}}, \tag{32}$$

The second part of eq. (31) is similar to eq. (8) in ref. [113] (where $\alpha_{par}$ is used to include the free carrier absorption in the c-Si). Figure 5-24a shows $f_{par}$ for all the point contact cells (solid lines) and for the FrontERA cells with (dashed) and without (dotted) ARF. It can be seen that that the p-type point contact cells have higher $f_{par}$ than the n-type point contact cells, which in turn have a higher $f_{par}$ than the FrontERA cell. For λ = 960 nm, $f_{par}$ is about 6 % for the p-type cells, 4 % for the n-type cells and 2 % for the FrontERA cell.

These observations can partly be explained by the different absorptances in the reflectors: ~14 % for P150W/Ag/Al (p-type), ~8 % for P150/Ag (n-type) and ~3 % for white paper (FrontERA) (see section 5.8.2). In the previous section it was argued that more light reaches the attached reflector of the point contact cell than the detached reflector of the FrontERA cell (resulting in a lower $f_{esc}$). If more light reaches the reflector, then this also results in a larger parasitic absorption in the reflector, which provides an additional explanation for the higher parasitic absorption in the point contact cells.

Ray tracing simulations were made to estimate which fraction of the light is absorbed in the TCO and which fraction is absorbed in the reflector. Figure 5-24b shows the simulated $f_{par}$ for the ray tracing simulations of the detached white (solid curve) and metal (dashed) reflectors described in the previous section. The simulated $f_{par}$ curves are shown for different absorptances (*A*) of the detached reflector (0.15 or 0.25) and

for different pyramid angles (θ = 15° or 30°). Several point contact $f_{par}$ curves (grey, long dash) are added as reference.

It can be seen that the $f_{par}$ for the p-type point contact cells is best fitted with $A$ = 0.25, while the $f_{par}$ for the n-type point contact cells are best fitted with $A$ = 0.15. This is roughly 50 % higher than the absorptances determined in section 5.8.2, which can be explained by the fact that the simulated reflectors are detached and the actual reflectors are attached: more light will reach the attached reflector and the attached reflector reflects part of the light onto the reflector of the neighbouring pyramid. It can also be seen that changing θ from 15° to 30 ° resulted in a large reduction in the total $f_{par}$, as less light reaches the reflector. The $A_{par}$ in the TCO (0.6-0.8 mA/cm$^2$) was relatively unaffected by the change in θ. Note that this is ~30 % lower than the ~1 mA/cm$^2$ $A_{par}$ simulated for the 100 nm ITO layer in the FrontERA cell (section 4.1.6), which fits with the ~25 % lower absorptance in the 250 nm AZO layer compared to the 100 nm ITO layer (section 5.8.3). The simulations for the 15° pyramids with detached reflector resulted in an $A_{par}$ due to the reflector of 1.9 mA/cm$^2$ for the n-type reflector ($A$ = 0.15, dark blue curves) and 3 mA/cm$^2$ for the p-type reflector ($A$ = 0.25, light blue curves).

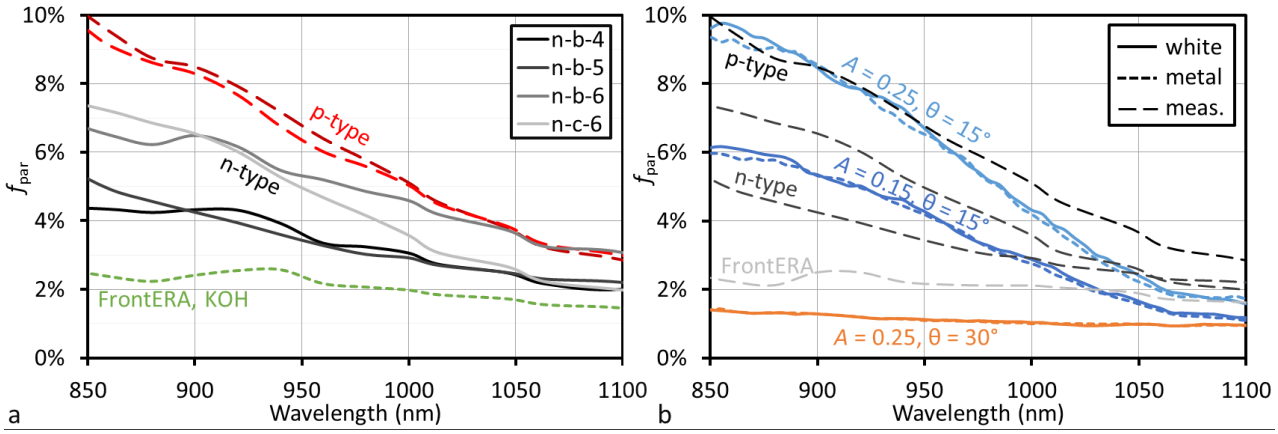


**Figure 5-24.** Fig. a shows the fraction absorbed every $d$ ($f_{par}$) for the KOH textured n-type (grey, solid lines) and p-type (red, long dash) point contact cells and FrontERA cell (green short dash). Fig. b shows the simulated $f_{par}$ for the ray tracing simulations with detached white (solid curves) and metal (short dash) reflector from section 5.8.4. The absorptance (1-$R$) of the detached reflectors ($A$ = 0.15 or 0.25) and the pyramid angles (θ = 15° or 30°) are indicated in the figure.

### 5.8.6 Discussion of $J_{SC}$ Potentials

The $J_{SC}$ loss overview indicated that the $LT_{loss}$ for textured point contact cells is about ~1 mA/cm$^2$ and the $f_{esc}$ results indicated that about half of this loss is due transmission through the (~60 µm wide) metal cut scribes. Test scribes indicate that the metal cut width and corresponding transmission loss can be reduced by about 40-50 % (0.2-0.3 mA/cm$^2$) by changing the laser spot energy profile from “top head” to Gaussian. Further hardware changes would allow for even narrowed metal cuts scribes.

In section 5.8.2 it was shown through optical simulation that it is possible to reduce the absorptance in the P150W/Ag/Al reflector for p-type cells to that of the P150W/Ag reflector (n-type cells) by increasing the Ag thickness from 20 nm to 40-60 nm. Based on the $J_{SC}$ loss analysis this should reduce the $A_{par}$ loss for p-type cells by approximately 1 mA/cm$^2$.

It was observed that the textured, n-type point contact cells have a larger $A_{par}$ loss than the textured FrontERA cells. It was argued that this was due to a combination of the higher absorptance of the P150W/Ag reflector (~8 %) compared to the white paper reflector (~3 %) and because more light reaches the attached (P150W/Ag) reflector than the detached (white paper) reflector. Based on the optical simulations and the $J_{SC}$ loss analysis we estimate the $A_{par}$ loss due to the attached P150W/Ag reflector, (compared to the detached white paper reflector) at 1.4 ± 0.3 mA/cm$^2$. In section 5.8.4 it was further argued that the additional $R_{esc}$ loss for the point contact cells compared to the FrontERA cell is also due to the attached P150W/Ag reflector, adding another ~0.3 mA/cm$^2$ loss that can be attributed to the reflector.

We expect that these reflector losses can (mostly) be prevented by removing the $TiO_2$ particles from the P150W, thereby turning the white, attached P150W(n≈2.1)/Ag reflector into a P150(n≈1.5)/Ag reflector. This reflector is optically similar to a detached Ag reflector, but with the air layer replaced by the transparent P150 resin. The simulated absorptance of the P150(n≈1.5)/Ag reflector is ~3 %, i.e. similar to the white paper reflector. The (specular) Ag reflector should also prevent the additional $R_{esc}$ loss of the textured point contact cell compared to the textured FrontERA cell.

A problem with removing the $TiO_2$ particles is that the P150W protects the emitter from the 355 nm ps laser that is used for the metal cut scribe and that the P150 resin itself is completely transparent at this wavelength. A solution to this problem would be to use a colouring pigment which only absorbs for short wavelength (e.g. Sudan IV or Congo Red).

An alternative solution for reducing the parasitic absorption and light trapping losses would be to deposit an Ag layer on the TCO before the resin deposition. This will reduce the $A_{par}$ loss less than removing the $TiO_2$ particles as the absorptance is slightly higher (~4 %) and the reflector is still attached to the TCO. How much less will have to be determined experimentally and/or by using different simulation software. However, this approach has several other advantages: it should reduce the transmittance to about 0 % and it would reduce both the $R_{s,l}$ contribution by the TCO and the $R_{s,c}$ contribution by the TCO/Ag contact to about 0 Ωcm$^2$, as the current will flow through the Ag and Ag/Ag contact and the Ag should protect the AZO from the ADP process, which could significantly improve process repeatability. It would also be possible to reduce the AZO thickness, as it is no longer needed for lateral conductivity, thereby further reducing parasitic absorption. Both approaches are shown in Figure 5-25.

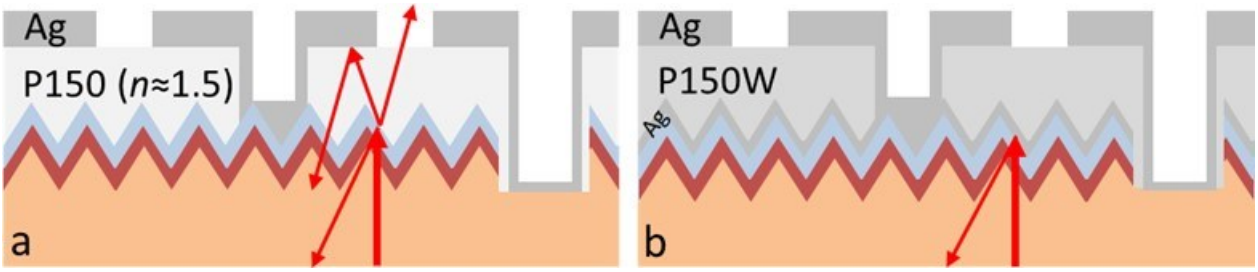


**Figure 5-25.** Schematic representation of both solution proposed for improving the reflector of the point contact cells: removing the $TiO_2$ particles from the P150W (a) and depositing an Ag layer on the TCO before applying the P150W (b). The red arrows show possible light paths.

One of the largest $J_{SC}$ losses in Table 5-9 is the recombination loss. One way to reduce this loss is to reduce the absorber thickness ($d$), but this will increase the light trapping and parasitic absorption losses. In the following, the photocurrent analysis models will be used to estimate the optimum $d$ and corresponding $J_{SC}$ potential for different $f_{esc}$ and $f_{esc}$ scenarios and for different material quality ($L_{eff}$) scenarios.

In order to use the photocurrent analysis models to simulate the photocurrent, $R_{direct}$ was simulated in OPAL2, reduced by 60 % and shifted by 40 nm to lower wavelengths to model the effect of the ARF (see section 4.1.3). Also, a fixed parasitic absorption percentage ($A_{par,fix}$) was added, representing absorption in the glass and the ARF. By solving eq. (11), (17) and (31), it was found that $A_{Si}$, $A_{par}$ and $T+R_{esc}$ can be calculated from $\eta_{LT}$ ($f_{esc}$, $d$) and $\eta_{par}$ ($f_{par}$, $d$) using:

$$A_{\mathrm{Si}} = \frac{1 - R_{\mathrm{direct}} - A_{\mathrm{par,fix}}}{\frac{1}{\eta_{\mathrm{LT}}} + \frac{1}{\eta_{\mathrm{par}}} - 1}\,, \tag{33}$$

$$A_{\mathrm{par}} = \frac{A_{\mathrm{Si}}}{\frac{1}{\eta_{\mathrm{par}}} - 1} + A_{\mathrm{par,fix}}\,, \tag{34}$$

$$T + R_{\mathrm{esc}} = \frac{A_{\mathrm{Si}}}{\frac{1}{\eta_{\mathrm{LT}}} - 1}\,, \tag{35}$$

The $\eta_c$ can be calculated from the equations in section 2.7 and the *EQE* can be obtained by using (derived from eq. (16)):

$$EQE = \frac{A_{\mathrm{Si}}}{\frac{1}{\eta_{\mathrm{c}}} + f_{\mathrm{DA}}}\,, \tag{36}$$

The different simulation scenarios are listed in Table 5-10. In the first scenario it was estimated that the "current" $f_{esc}$ ≈ 3 %, $f_{par}$ ≈ 4 % and $A_{par,fix}$ ≈ 2 % can be reduced to $f_{esc}$ ≈ 1.5-2 %, $f_{par}$ ≈ 1.5-2.5 % and $A_{par,fix}$ ≈ 0.5 % by removal of the $TiO_2$ particles from the P150W and by texture etching of the glass as was done in ref. [16]. The latter potential was briefly discussed in section 4.1.8 as a means of replacing the ARF and reducing the glass absorption. The second scenario consists of three different material qualities, with

approximately equal impact of $L$ and $S$ on $L_{eff}$. The $L_{eff}$ in the table, added for reference, was calculated with eq. (10), for $d$ = 7 µm and $\mu$ = 333 cm$^2$/Vs (n-type, 8·10$^{16}$ cm$^{-3}$). The $L_{eff}$ for the point contact cells in this chapter varied from "Low" to "Middle" ($L_{eff}$ = 12-20 µm. Aside from the input parameters in Table 5-10, the $f_{DA}$ was 3 % and the reflectance corresponded to a NON(ON) interlayer stack with ARF. For scenario 1 the "High 1" material parameters were used and for scenario 2 the "Potential 1" $f_{esc}$, $f_{par,}$ and $A_{par,fix}$ values were used.

**Table 5-10.** Input parameters for simulation scenarios 1 and 2 and the resulting max. $J_{sc}$ (mA/cm$^2$) and optimum $d$ (µm) ($d_{opt}$).

| **Scenario 1** | $f_{esc}$ | $f_{par}$ | $A_{par,fix}$ | $J_{SC}$ | $d_{opt}$ | **Scen. 2** | $L$ (µm) | $S$ (cm/s) | ~$L_{eff}$ | $J_{SC}$ | $d_{opt}$ |
|---|---|---|---|---|---|---|---|---|---|---|---|
| **Current** | 3.0 % | 4.0% | 2.0 % | 30.3 | 7.5 | **Low** | 15 | 1500 | 12 | 30.1 | 4.5 |
| **Potential 1** | 2.0 % | 2.5% | 0.5 % | 32.1 | 7.0 | **Middle** | 25 | 500 | 20 | 32.1 | 7.0 |
| **Potential 2** | 1.5 % | 1.5% | 0.5 % | 33.1 | 6.5 | **High** | 40 | 200 | 32 | 33.4 | 10 |

Figure 5-26a and b shows the modelled *EQE* and photocurrent losses before (a) and after (b) applying the light trapping limit, for $d$ = 7 µm, the "Potential 1" photocurrent scenario and the "Middle" material quality. Figure 5-26c shows the $J_{SC}$ and $J_{SC}$ losses as a function of the thickness for the "Current" (dashed), "Potential 1" (solid) and "Potential 2" (dotted) scenario. The light trapping limit is plotted as "43 – $J_{SC,lim}$" in order to convert it into a photocurrent loss that can be compared directly to the other $J_{SC}$ losses. It can be seen that for increasing $d$, the light trapping and parasitic absorption losses are slowly decreasing, while the recombination loss is rapidly increasing. The combination of these $J_{SC}$ losses, results in a $J_{SC}$ vs. $d$ curve, with a maximum $J_{SC}$ of ~32.1 mA/cm$^2$ at $d$ ≈ 7.0 µm for the "Potential 1" scenario (solid), ~30.3 mA/cm$^2$ at $d$ ≈ 7.5 µm for the "Current" scenario (dashed) and ~33.1 mA/cm$^2$ at $d$ ≈ 6.5 µm for the "Potential 2" scenario (dotted). Reduction of $f_{esc}$ and $f_{par}$ reduces the $A_{par}$ and $T$+$R_{esc}$ losses, but has only a very small effect on the optimum absorber thickness ($d_{opt}$). These $J_{SC}$ values (included in Table 5-10) provide an indication of the potential $J_{SC}$ improvement due to the removal of the $TiO_2$ particles and the texture etching of the Boro33 substrate. The $J_{SC}$ of 32 mA/cm$^2$, together with a $V_{OC}$ of 650 mV and *FF* of 77 %, would result in an $\eta$ of 16.0 %.

Figure 5-26d shows the $J_{SC}$ and recombination losses as a function of $d$ for the "Low" (dashed), "Middle" (solid) and "High" (dotted) material quality scenarios from Table 5-10. It can be seen that optimum absorber thickness ($d_{opt}$) is very strongly affected by the material quality, doubling from 4.5 µm ($L_{eff}$ = 12 µm) to 10 µm ($L_{eff}$ = 32 µm). From these results it appears that $d_{opt}$ ≈ $L_{eff}$/3 (in combination with "Potential 1"). Considering that the fitted $L_{eff}$ for the point contact cells in Table 5-8 was between 10 and 20 µm, the optimum $d$ appears to be around 6 µm. A reduction of $d$ from 8-13 µm to 6 µm would also strongly reduce the impact of low material quality on the $J_{SC}$, thereby decreasing the $J_{SC}$ variation. It should be noted that the $V_{OC}$ decreases for increasing $d$, thereby shifting the optimum $d$ to even lower values. The

combination of the "High" and "Potential 2" scenarios results in a maximum $J_{SC}$ of 34.4 mA/cm$^2$, which, together with a $V_{OC}$ of 650 mV and *FF* of 77 %, would result in an $\eta$ of 17.2 %.

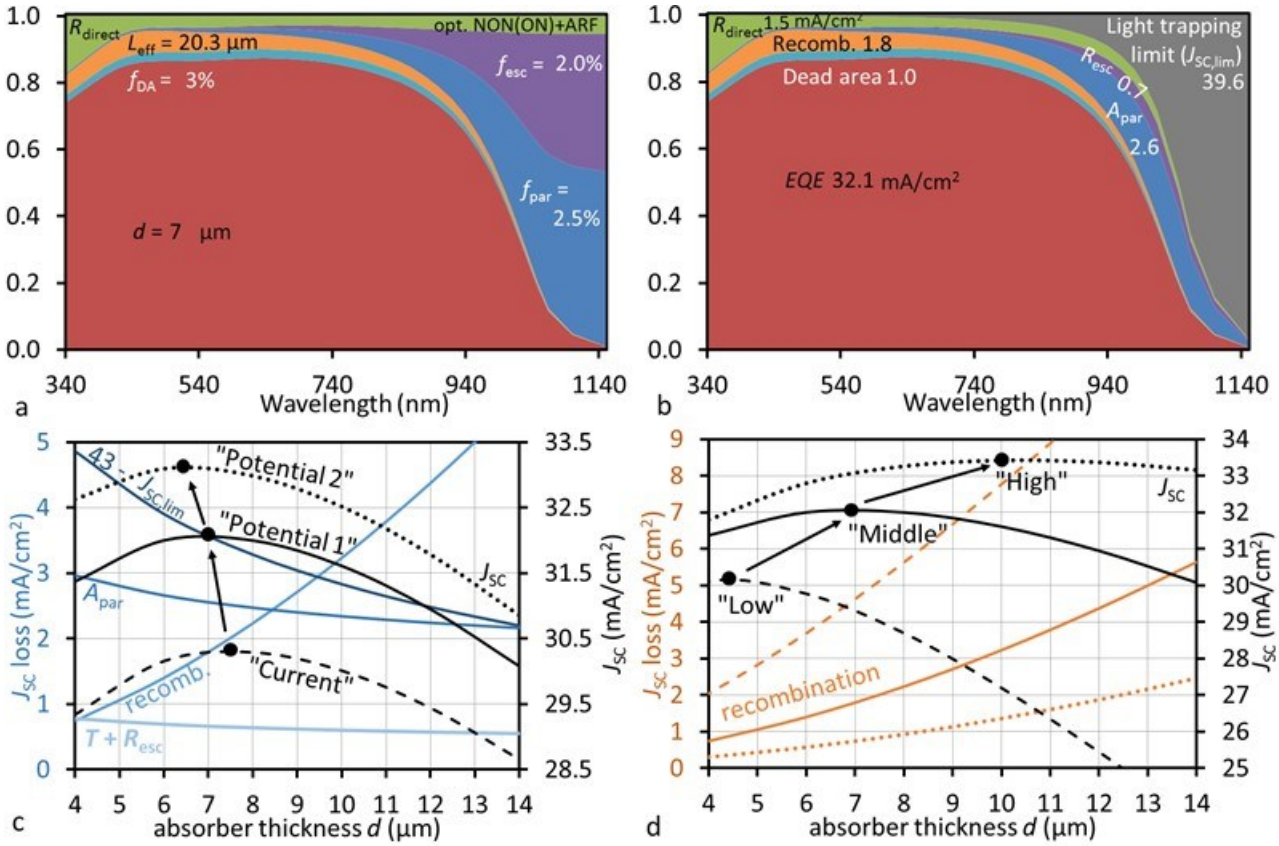


**Figure 5-26.** Figure a and b show the modelled *EQE* and photocurrent losses before (a) and after (b) applying the light trapping limit, for the input parameters indicated in figure a (scenarios "Potential 1" and "High", see Table 5-10). Figure c shows the $J_{SC}$ losses (blue) and $J_{SC}$ (black) as a function of the thickness for the "Current" (dashed), "Potential 1" (solid) and "Potential 2" (dotted) scenarios. Figure d shows the recombination losses (orange) and $J_{SC}$ (black) as a function of the thickness for the "Low" (dashed, $L_{eff}$ = 12 µm) and "Middle" (solid, 20 µm) and "High" (dotted, 32 µm) material quality scenarios. The corresponding parameters are listed in Table 5-10.

## 5.9 Summary

The starting point for the cell development in this chapter was an 11.5 %, 2·10$^{16}$ cm$^{-3}$ doped, planar point contact cell, with a relatively high $J_{SC}$ and $V_{OC}$, but low *FF* due to a high $R_s$. The main goals in this chapter were to reduce the $R_s$ by introducing new emitters, to increase the $V_{OC}$ and decrease the $R_s$ by increasing the absorber doping and to increase the $J_{SC}$ by introducing absorber texturing.

In section 5.3 the etch properties of different emitter and TCO layer were compared, indicating how long and/or inhomogeneous etching results in shunting and increased dead area losses. In order to obtain a short, uniform etching process a 10 nm ITO contacting layer (with a low etch rate) was combined with a 250 nm AZO layer for lateral conductivity (and a high, uniform etch rate). Also, for the p-type emitters, the

$KMnO_4$ + HF etch solution (purple etch) was replaced by a faster and more homogeneous $NHO_3$ + HF etch solution (poly-Si etch). Finally, a new etch process was tested, consisting of a short etch and reflow to remove and protect the high etch rate layers, followed by a longer etch and reflow to remove and isolate the low etch rate layers. This process resulted in a high yield and low dead area fraction ($f_{DA}$) of ~3 % ($r_{DA}$ ≈ 42 µm).

In section 5.4, simulations were used to correct the point contact TLM measurements for current crowding effects and to calculate the $R_s$ contribution for lateral resistance in the c-Si (and TCO). Using the simulation results, the measured $R_s$ contribution by the absorber contact and $r_{DA}$ ≈ 40 µm, the optimum point contact spacing was estimated for a wide range of absorber doping concentrations. For lowly doped p-type ($2 \cdot 10^{16}$ $cm^{-3}$) material, it was found that a decrease of the spacing should result in a relative power gain of ~2 % and for highly doped n-type ($10^{17}$ $cm^{-3}$) material, it was found that the doubling of the spacing should result in a relative power gain of ~1 %. Hence, in this range the power is relatively insensitive to a spacing variation. The relative power gain for increasing the absorber doping from $2 \cdot 10^{16}$ to $10^{17}$ $cm^{-3}$, was estimated at ~5.5 % for p-type samples and ~2.5 % for n-type samples.

In section 5.5, it was attempted to reduce the emitter/TCO resistance of the n-type cells by replacing the a-Si by nc-Si and replacing the TMB doping gas by $B_2H_6$. Using emitter/TCO $\rho_c$ test structures on textured wafers, nc-Si and $B_2H_6$ were found to reduce the $\rho_{c,wafer}$ to ~0.05 and ~0.3 $\Omega cm^2$ respectively. Using quasi cells it was found that replacing a-Si by nc-Si results in a ~80 mV $V_{OC}$ loss, which could be prevented by adding a 6 nm a-Si(p) layer between the a-Si(i) and nc-Si(p) layers. However, this a-Si layer also increased $\rho_{c,wafer}$ to ~0.8-2 $\Omega cm^2$.

Subsequently, the cell $R_s$ was analysed for point contact cells with different emitters, subtracting the point contact and lateral $R_s$ contributions from the cell $R_s$ to obtain an emitter/TCO $\rho_{c,cell}$ estimate. It was found that $\rho_{c,cell}$ (~0.5 $\Omega cm^2$) is significantly lower than $\rho_{c,wafer}$ for the a-Si/nc-Si (TMB) emitter and roughly equal to the $\rho_{c,wafer}$ (~0.3 $\Omega cm^2$) for the a-Si ($B_2H_6$) emitter. It was argued that the low $\rho_{c,cell}$ for the a-Si/nc-Si emitter may be explained by the tilted pyramids of KOH textured LPC-Si, resulting in high $\rho_c$ in the "low-pyramid-angle-areas" and low $\rho_c$ in the "high-pyramid-angle-areas". From the individual $R_s$ components, a cell $R_s$ of ~0.6 $\Omega cm^2$ appears to be obtainable for ~$9 \cdot 10^{16}$ $cm^{-3}$ doped n-type LPC-Si point contact cells.

In section 5.6 it was shown that the textured point contact cells were affected by a *FF* loss that was related to the isoscribe. It was argued that this could be explained by increased recombination at many positions along at the isoscribe. A passivated isoscribe process was successfully developed to prevent the increased recombination at the isoscribe, featuring a 1st isoscribe of the c-Si absorber before hydrogen passivation

and a 2nd isoscribe (within the 1st) after the TCO deposition. It was shown that the crack catcher scribe can be used as the 1st isoscribe.

Using the passivated isoscribe process, an $8 \cdot 10^{16}$ $cm^{-3}$ doped, n-type, KOH textured absorber, an a-Si/nc-Si emitter and a 90 s poly-Si emitter etch, a new record $\eta$ for point contact LPC-Si cells of 12.0 % was obtained, despite a high recombination loss (section 5.7).

In section 5.8 the photocurrent losses were analyzed for textured point contact cells and compared to the textured FrontERA cell analyzed in section 4.1. It was found that the point contact cells have higher light trapping losses (~1 mA/$cm^2$) and parasitic absorption losses (~3-4 mA/$cm^2$) than the FrontERA cell (0.2 and 2.2 mA/$cm^2$) and it was argued that this was mainly due to attached white P150W/Ag reflector compared to the detached white paper reflector for the FrontERA cells. This was explained by the combination of a high absorptance in the reflector and more light reaching the reflector because it is attached instead of detached. It was proposed to reduce these light trapping and parasitic absorption losses by (a) removing the $TiO_2$ particles from the P150W, thereby changing the attached white reflector into a quasi-detached (P150/) Ag reflector with an absorptance of ~3 %, or (b) by depositing an Ag layer on the TCO before applying the P150W, thereby preventing all transmission, reducing the absorptance of the reflector to ~4 % and reducing the resistance by the TCO and at the TCO/Ag point contacts. It was argued that by implementing these potentials, together with texture etching the glass, the $J_{SC}$ potential could be increased from ~30 mA/$cm^2$ to 33 mA/$cm^2$ for $L_{eff} \approx 20$ µm (34.4 mA/$cm^2$ for $L_{eff} \approx 32$ µm)

Together with the parasitic absorption, the largest loss for the point contact cells was the recombination loss. It was argued that the absorber thickness should be reduced to ~6 µm in order to increase the efficiency for the typical material quality ($L_{eff} \approx$ 10-20 µm) found for the point contact cells in this chapter. The absorber doping experiments (and $\eta$ records) with PECVD material and FrontERA cells in chapter 3 led to the conclusion that the absorber doping of the point contact cells should be increased to ~$9 \cdot 10^{16}$ $cm^{-3}$. Considering the high recombination losses in this section, these doping experiments should be repeated on the current material and point contact cells.

# 6 Point Contact LPC-Si Mini-Modules

*In this chapter the first LPC-Si mini-modules are presented, using either "separate isoscribes and crack catchers" or using "the crack catchers as isoscribes". LBIC measurements are used to determine the $J_{SC}$ loss (dead area) due to the isoscribe and crack catcher scribe. J-V curves, DLIT and PL measurements are used to discuss the low shunt sensitivity of the mini-module interconnection.*

## 6.1 Investigated Modules

An important advantage of the point contact device is that it is a module concept, allowing for the fabrication of mini-modules without any additional process steps. In order to demonstrate this advantage and test the influence of different crack catcher and isoscribe configuration, two different types of mini-modules were fabricated during experiment 6 (see section 5.2.6):

- 4 $cm^2$ mini-modules consisting of four 1 $cm^2$ cells connected in series, using the "double isoscribe" process (method 2, see section 5.6), with separate crack catcher scribes going through the cell area. This way, there is room for two mini-modules (and 4 TLM structures) on each sample. Figure 6-1a shows a backlight image of one of these sample after laser crystallization. It can be seen that for "cell 2" there are two crack catcher scribes in the cell area and for "cell 4" there is one crack catcher scribe in the cell area. An advantage of this configuration is that it possible to determine separately the $J_{SC}$ losses due to the isoscribe and crack catcher.
- 10 $cm^2$ mini-modules consisting of five 2 $cm^2$ cells connected in series, using the "crack catcher as isoscribe" process (method 3), allowing for one mini-module on each sample (see Figure 6-1b).

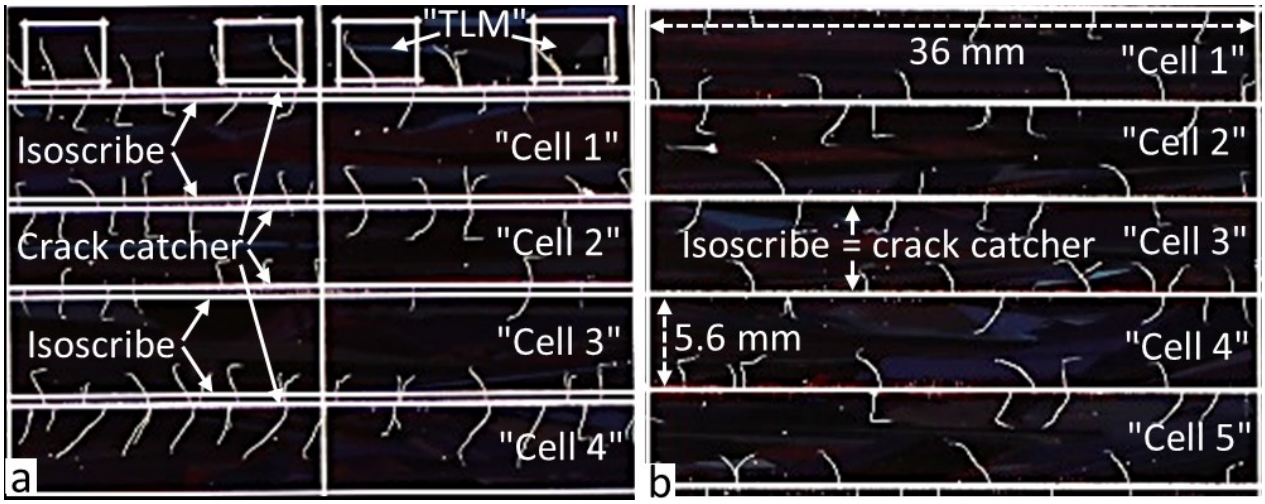


**Figure 6-1.** Photographs with backlight after the LPC process for a 2x4 $cm^2$ mini-module sample with separate isoscribes and crack catcher scribes (a) and for a 10 $cm^2$ mini-module sample with crack catcher scribes as isoscribes (b). The positions of the scribes and the subsequently fabricated cells and TLM structures are indicated in the figures. The "side-cracks" are coming out of the crack catcher scribes.

The material consisted of PC1 ONO interlayers on Boro33, with textured, ~13 µm thick, ~$1.5 \cdot 10^{17}$ $cm^{-3}$ doped, n-type absorbers, crystallized with a laser scanning velocity of 3 mm/s. The emitter was a-Si/nc-Si and the TCO was ITO-AZO.

Figure 6-2 shows top view images (a and b) and a schematic cross-section (c) of the point contact module interconnection. It can be seen how a series connection is obtained by connecting the TCO/Ag contact grid fingers of cell 4 to the c-Si/Ag contact fingers of cell 5.

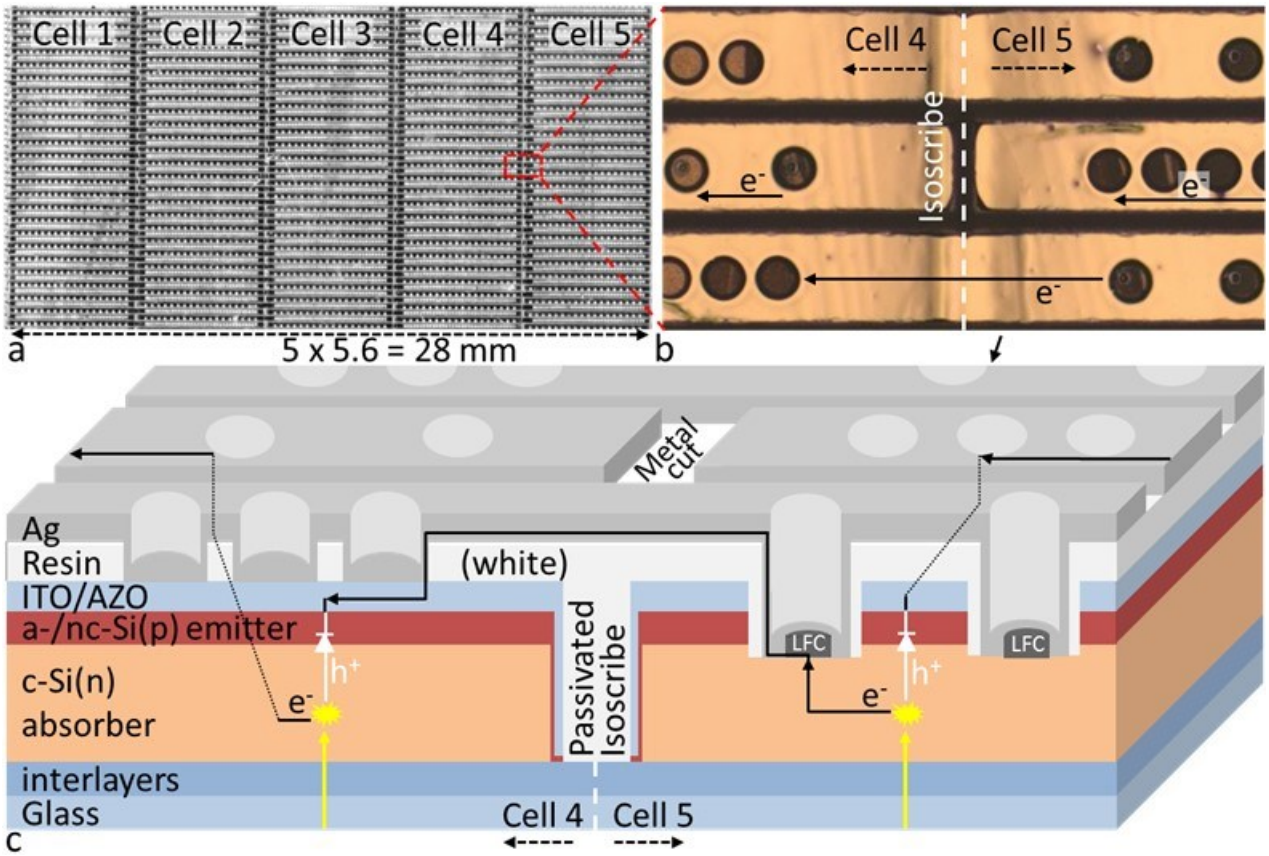


**Figure 6-2.** Figure a and b show top view images of a point contact module (a) and module interconnection (b), for a 10 $cm^2$ mini-module, which uses the crack catcher as isoscribe. Figure c shows a schematic cross-section of the module interconnection. The lines and arrows in the cross-section indicate the direction of the light (yellow), electrons (black) and holes (white).

## 6.2 Results

As mentioned above, the use of separate isoscribes and crack catcher scribes (inside the cell area) for the 4 $cm^2$ mini-modules, allow for the separate determination of the $J_{SC}$ losses (dead area) due to both scribes. Figure 6-3a and b show LBIC measurements (λ = 904 nm) with and without ~0.1 suns bias light (BL) for a 4 $cm^2$ mini-module. The arrows indicate the positions of the isoscribes, crack catchers and side-cracks. The metal cut scribe is made on top of the isoscribe for every other finger (see Figure 6-2). It should be noted that series connected cells all operate at the same current, which means that (normally) the module $J_{SC}$ is

limited by the cell with the lowest individual $J_{SC}$. For LBIC measurements, this means that the additional light added by the laser should only results in additional current (LBIC signal) for the current limiting cell. Without bias light, the only illuminated cell is the measured cell, which is therefore never current limiting. The observation in Figure 6-3a and b that all cells for this particular mini-module nonetheless result in a similar LBIC signal can be explained by shunts, which provide a conductive path for the generated current through the current limiting cells (for several other modules only 1 or 2 cells resulted in an LBIC signal).

It can be seen that large parts or the narrow cell area between the isoscribes and crack catchers is dead area (black). It can be seen that side-cracks separate these dead areas from other areas between the scribes that are not dead. Presumably, the difference between the dead and the active areas is the presence of connected absorber and TCO point contacts for the active areas. Some area's still appear active in the LBIC measurement without bias light, but show strongly reduced collection at 0.1 suns BL intensity. This indicates that they are contacted, but with a high resistance (distributed series resistance, see section 4.1.2). The dead area's between the crack catcher and the isoscribe can be prevented by using the crack catcher as isoscribe, as was done for the 10 $cm^2$ mini-module.

Figure 6-3c shows averaged, normalized LBIC linescans through the (~50 µm wide) crack catcher and a neighboring grain boundary, measured at the indicated position in fig. a and b. It can be seen that LBIC signal near at the crack catcher and grain boundary decreases strongly for increased bias light intensity. The dashed areas in the figure indicate how the dead area width due to the crack catcher is estimated by integrating the relative reduction of the LBIC signal in the ~400 µm wide region that appears to be affected by the isoscribe and calculating the width of a completely dead area that would cause the same relative reduction, i.e. the sum of the dashed areas above the curve equals the dashed area below the curve. This way it is estimated that the crack catcher causes a ~200 µm dead area width. Using this dead area width it can be calculated that, for a cell width of 5.6 mm, a single crack catcher scribe results in a relative $J_{SC}$ loss of 4 %.

Figure 6-3d shows averaged, normalized LBIC linescans through the (~90 µm wide) isoscribe with or without Ag on the P150W reflector in the isosribe (i.e. without or with metal cut scribe), measured at the indicated position in fig. a. The dead area width for the double isoscribe is ~11 µm with Ag and ~22 µm w/o Ag, resulting in a $J_{SC}$ loss of approximately 0.3 % (for a cell width of 5.6 mm). It can be seen that the dead width due to the (double) isoscribe is much smaller than that of the crack catcher, despite being physically almost twice as wide.

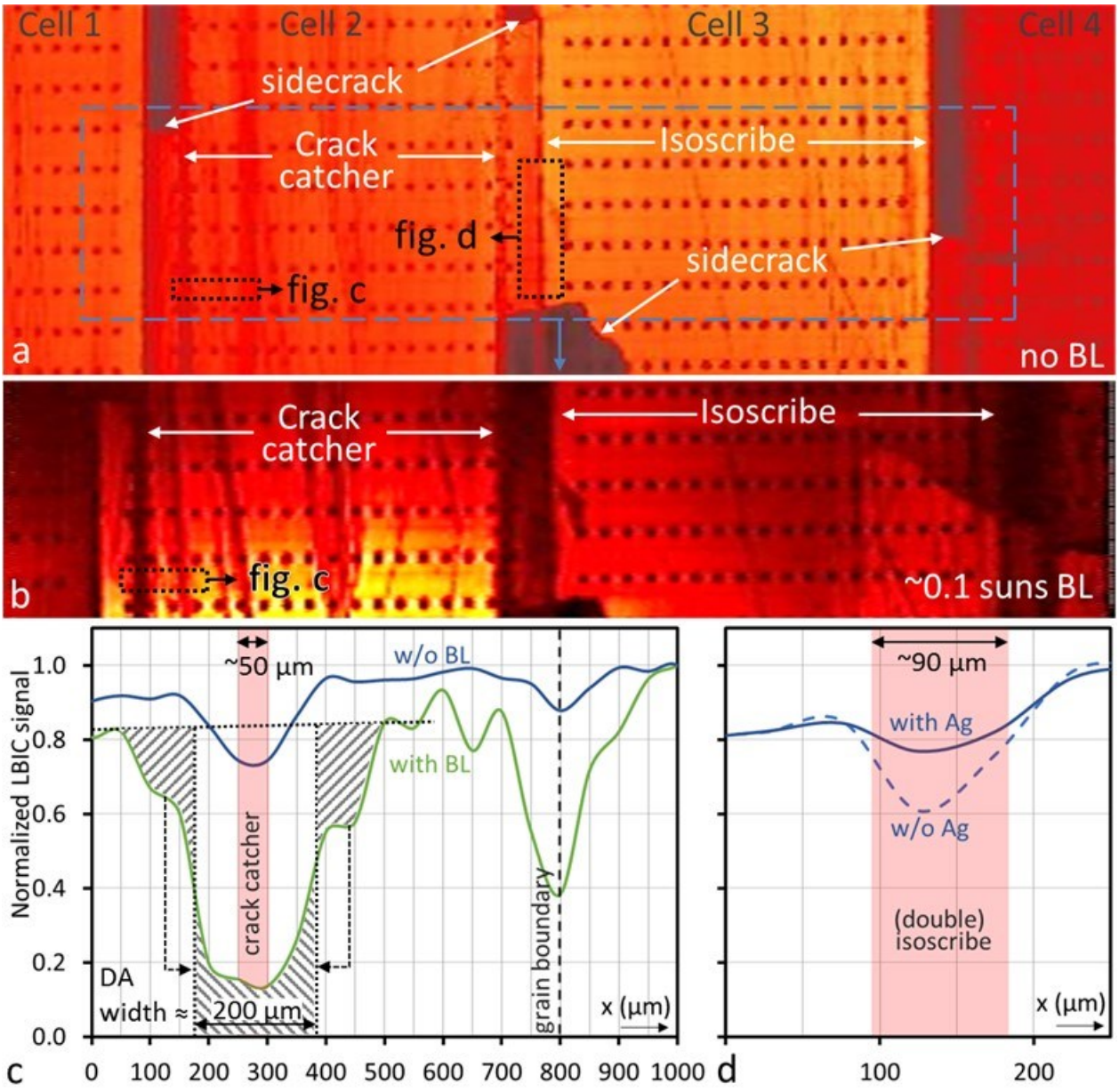


**Figure 6-3.** Figure a and b show LBIC measurements without (a) and with (b) 0.1 suns bias light (BL). Figure c and d show the normalized, average linescans of a (~50 µm wide) crack catcher and neighboring grain boundary with BL (green) and without (blue) (c) and of a (~90 µm wide) double isoscribe with Ag (solid) and w/o Ag (dashed) on the P150W in the isoscribe (d). The approximate positions of the averaged linescans in fig. c and d are highlighted in fig. a and b. The dashed areas in fig. c indicate how the 200 µm dead area (DA) width was determined: the sum of the dashed areas above the curve equals the dashed area below the curve.

The large dead area for the crack catcher can be explained by the small grain size next to the crack catcher (see section 5.6.2, Figure 5-17), indicating a low material quality in these regions. The increasing dead area for increasing bias light might be due to a bias light dependent recombination or a (very) high resistance in the small grained area. Considering the very similar bias light dependence of the dead area at the grain boundary, the former possibility is much more likely. The mini-module could not be measured successfully

at higher bias light intensity than 0.1 suns due to current matching and noise problems, but it is possible that the loss at 1 sun is even larger.

The relatively small dead area for the isoscribe can be explained by the diffuse reflector in the isoscribe. This P150W/Ag reflector scatters part of the light back into the cell, reducing the dead area. The very small loss due to the isoscribe can in principle be reduced further by positioning the metal cut scribe directly next to the isoscribe, thereby leaving the P150W in the entire isoscribe covered by Ag.

Figure 6-4a shows the measured *J-V* parameters of the 4 and 10 $cm^2$ mini-modules, compared to 1 $cm^2$ reference cells on the same material (using the double isoscribe process). It can be seen that all the 1 $cm^2$ cells, with 2 exceptions, are completely shunted (*FF* < 50 %), while the mini-modules are not (with 1 exception). The mini-modules have a $V_{OC}$/cell of ~600 mV. The 4 $cm^2$ mini-modules have a higher *FF* and a ~4 mA/$cm^2$ (~17 %) lower $J_{SC}$ than the 10 $cm^2$ mini-modules. Despite these differences, both mini-modules result in approximately the same $\eta$. The highest $\eta$ of 9.2 % (without ARF) was obtained for a 4 $cm^2$ module, with a $V_{OC}$ of 603 mV/cell, a $J_{SC}$ of 20.8 mA/$cm^2$ and a *FF* of 73.2 %.

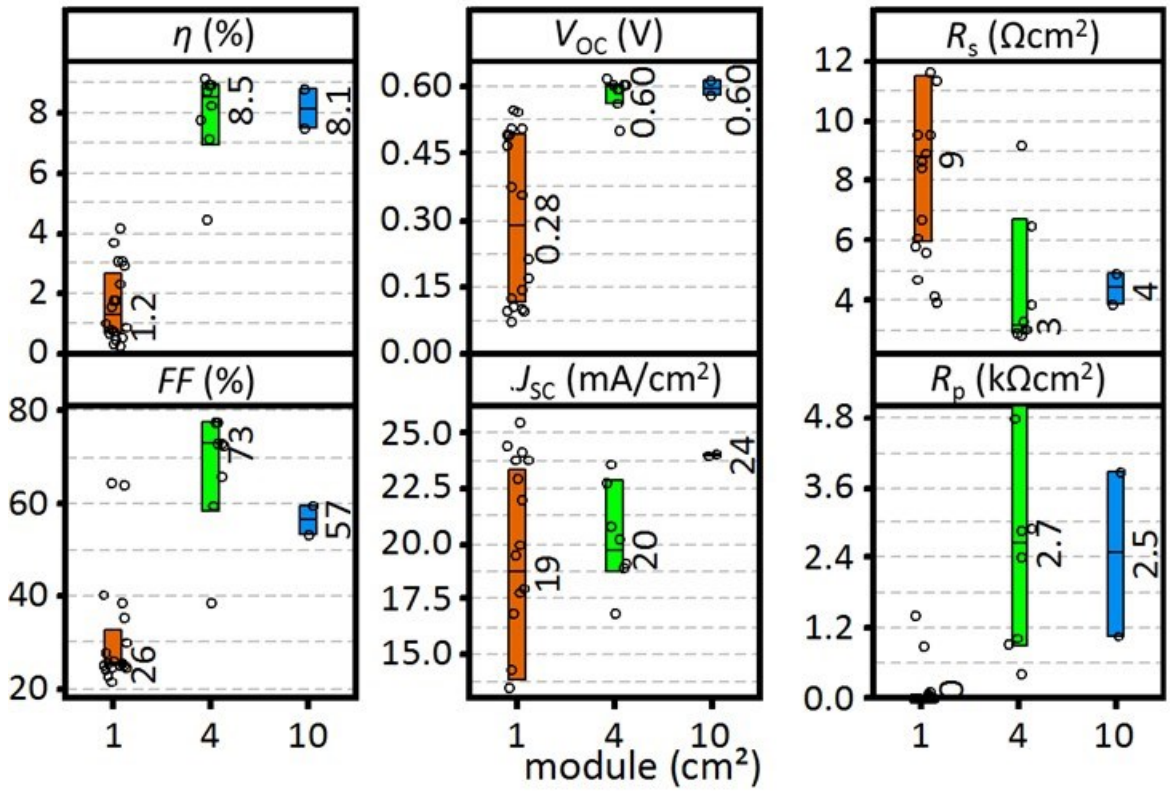


**Figure 6-4.** Boxplot of the *J-V* parameters of the 4 and 10 $cm^2$ mini-modules and reference 1 $cm^2$ cells.

The lower $J_{SC}$ of the 4 $cm^2$ modules compared to the 10 $cm^2$ modules can be explained by the dead area due to the crack catcher scribes and the dead areas between the crack catchers and isoscribes (see Figure

6-3). The module $J_{SC}$ is limited by the cell with the lowest $J_{SC}$, which is probably cell 2, as it has two crack catcher scribes running through it. For the cells that are not current-limiting, the reduction of their $J_{MPP}$ by the low $J_{MPP}$ of current-limiting cell shift the MPP operating point on their *J-V* curve to a higher $V_{MPP}$, thereby partly compensating the $J_{MMP}$ loss and increasing the *FF*. In other words, the high *FF* of the 4 $cm^2$ modules can at least partly be explained by the large $J_{MMP}$ loss for the cells with crack catcher scribes in the cell area.

The higher parallel resistance ($R_p$) of the point contact modules compared to the cells can be explained in the following way: if a cell that is not part of a module has a shunted grid finger (with a low resistance), all the current will flow through this shunted finger as all fingers (of the same type) are connected to each other through the metal outside the cell. In contrast, for a module, the effect of the shunt is mostly limited to the shunted finger, as the fingers are not connected to each other, except through the TCO and the c-Si, i.e. the relatively high resistance perpendicular to the metal fingers (in the TCO and c-Si) effectively shields the rest of the cell from the effects of the shunt [114]. In a way, the point contact module consists of parallel connected rows of series connected cells. This is depicted schematically by a (simplified) equivalent circuit in Figure 6-5a.

Figure 6-5b shows the DLIT images of a 4 $cm^2$ mini-module, measured at a forward bias of 2.8 V. As follows from the high $R_p$ of the module, there is no significant DLIT signal for reverse bias (not shown), and therefore the measurement is made at forward bias. The image shows both hotspots and more uniformly radiating areas. For a single cell, these effects would be interpreted as shunts and areas with increased recombination (lower $V_{OC}$). However for a module DLIT image there are various complications, e.g.:

- The locally applied voltage in the module can vary strongly for different positions (is “floating” [114]): the same voltage is applied to each “rows of series connected cells/fingers”, but if one of the cells in a row is shunted, all the other cells in the row experience a higher bias voltage. This locally increased bias voltage is a possible explanation for the uniformly radiating areas in the DLIT image.
- The same current flows through all the series connected cells/finger. If one of the fingers is shunted with a low shunt resistance, the relatively low current that can pass through the other cells may not be enough to cause significant radiative heating at the shunt. Therefore, many shunts may be invisible in the DLIT image.

Another method for imaging shunts, which does not suffer from these problems, is photoluminescence (PL) imaging. In PL imaging, carriers are generated optically and the subsequent radiative recombination

is measured with a camera. If the carriers recombine by any other path than radiative recombination (e.g. defect recombination or shunting), the PL signal at that position is reduced, resulting in a dark area in the PL image. Figure 6-5c shows a PL image of the same cell as in fig. b.

The image shows many line shaped dark areas, which can be explained by recombination at grain boundaries and related dislocations [24]. The image also shows other dark areas that are not line shaped and more or less bounded by the laser scribes. These can be explained by shunting. There are many dark areas between the isoscribe and the crack catcher for cell 2, suggesting the presence of shunts. The dark region in the middle of cell 2 can be explained by a shunt whose effect is limited to about 4 grid fingers. As mentioned before, this limited effect of the shunt can be explained by the relatively high resistance in the c-Si and TCO perpendicular to the grid fingers.

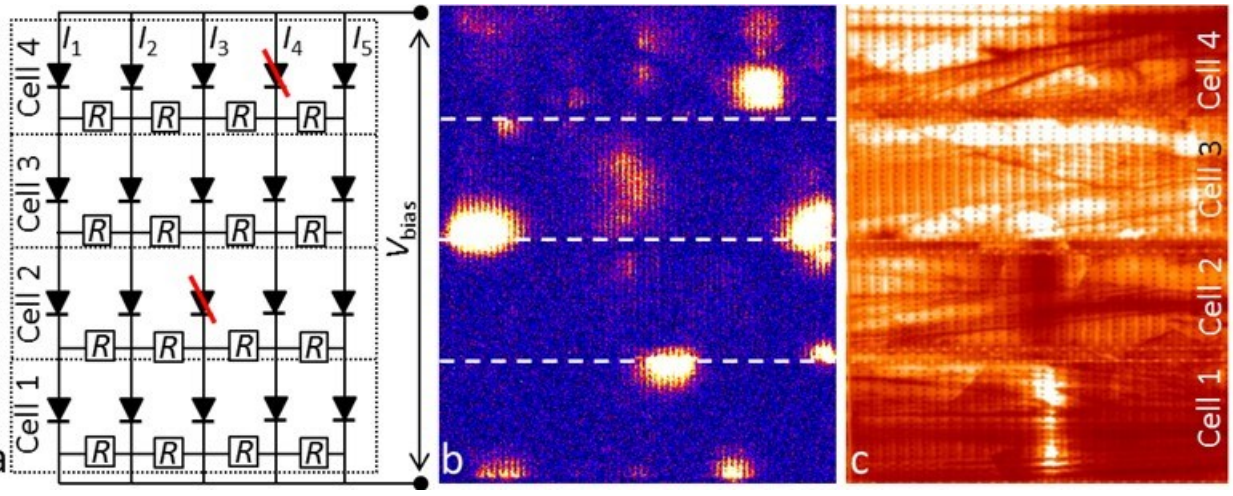


**Figure 6-5.** Figure a shows a schematic depiction of an equivalent circuit for the 4-cell mini-module. Figures b and c show DLIT (b) and PL (c) images of the same 4 $cm^2$ mini-module. The dotted lines indicate the isoscribes.

Comparison of the DLIT and PL images shows that many hotspots in the DLIT image have no (or very small) corresponding dark areas in the PL image, suggesting that these hotspot are not (significant) shunts. On the other hand, the large dark areas in the PL image do not result in clear hotspots in the DLIT image. Considering the aforementioned problems with the interpretation of DLIT module measurements, PL imaging appears to be a better suited method for imaging shunts in the LPC-Si point contact modules.

## 6.3 Conclusions

LPC-Si point contact mini-modules of different sizes were demonstrated, using either “separate crack catchers and isoscribes” or using “the crack catchers as isoscribe”. LBIC measurements of the module with separate crack catchers and isoscribes indicated that the (~90 µm wide) isoscribe causes a dead area width of only 11-22 µm, while the (~50 µm wide) crack catcher causes a (bias light dependent) dead area width

of ~200 µm. The small dead area for the isoscribe can be explained by the diffuse reflector in the isoscribe, scattering the light into the cell area. The large dead area for the crack catcher can be explained by the small-grained (low quality) c-Si next to the crack catcher. The poorly contacted area between the crack catcher and isoscribe caused additional dead area by cutting off part of the cell.

Together these dead area losses due to the crack catcher can explain the ~4 mA/cm$^2$ lower $J_{SC}$ for the mini-modules cells that had crack catchers through the cell area. This loss was compensated by a higher *FF*, which can partly be explained by a higher $V_{MPP}$ for the cells in these modules that did not have crack catcher in the cell area.

Despite the 1 cm$^2$ reference cells being completely shunted, the mini-modules were not shunted. This low sensitivity to shunts of the point contact modules can be explained by the high resistance perpendicular to the fingers, confining the effect of the shunt to a small part of the cell. It was argued that DLIT measurements can be misleading for the modules and PL imaging is better suited to characterize the effect of shunts in LPC-Si point contact modules. The highest efficiency was obtained for a 4 cm$^2$ mini-module with an $\eta$ of 9.2 % (without ARF), despite many local shunts.

# 7 Comparison of Cell and Doping Type

In this chapter the results from the previous chapters will be used to compare the textured, p- and n-type FrontERA and point contact cells. This comparison is summarized in Table 7-1.

The point contact cells had a lower $f_{DA}$ due to the absorber contact than the FrontERA cells (see Table 7-1), which roughly translates to a ~1 mA/cm$^2$ $J_{SC}$ advantage compared to p-type FrontERA cells and a ~2 mA/cm$^2$ $J_{SC}$ advantage compared to n-type FrontERA cells (assuming a $J_{SC}$ of ~30 mA/cm$^2$). The lower $f_{DA}$ for the p-type cells due to collection through the inversion layer represents a ~1 mA/cm$^2$ gain for the p-type FrontERA cells, but only a ~0.3 mA/cm$^2$ gain for the p-type point contact cells. This $J_{SC}$ advantage due to the lower $f_{DA}$ for the point contact cells, was counteracted by higher parasitic absorption and light trapping losses for the point contact cells, especially for the p-type point contacts cells. However, several relatively straightforward methods were proposed to reduce these losses, so they should not be considered fundamental disadvantages of the point contact device. A $J_{SC}$ loss of 2 mA/cm$^2$ represents a relative efficiency loss of ~7 % (assuming a $J_{SC}$ of ~30 mA/cm$^2$).

The absorber contact resistance was very low (<0.1 Ωcm$^2$) for the p-type FrontERA cells and high for the n-type FrontERA cells ([60], section 3.3.2), while the opposite was observed for the point contact cells (section 5.4). The lateral resistance in the absorber was 2-4 times higher for the p-type cells due to a 2-4 times lower mobility of the majority carriers (for the same doping concentration). Based on the literature [28], [99], [115] and p-type emitter/TCO $\rho_c$ wafer test structures (not included in the thesis, but published in [110]), the emitter/TCO $\rho_c$ is potentially lower for the p-type cells (~0.1 Ωcm$^2$) than for the n-type cells (~0.2-0.5 Ωcm$^2$). However, this could so far not be confirmed by point contact cell $R_s$ analysis. An $R_s$ increase of 1 Ωcm$^2$, represents a relative efficiency loss of ~ 7 % (assuming a *FF* of ~80 %)

Based on literature data [21], FrontERA experiments (chapter 3) and quasi cell experiment (e.g. appendix A.4-A.5), the $V_{OC}$ is typically ~30-50 mV lower for p-type cells than for n-type cells, which represents a relative efficiency loss of ~5-8 % (assuming a $V_{OC}$ of ~630 mV)

The n-type FrontERA cells are highly sensitive to shunting by LPC-Si cracks, which resulted in a very low cell yield (~1 %, section 3.3.4). The point contact cells are less sensitive to shunting by the LPC-Si cracks, but they are affected by shunting at the absorber point contacts and isoscribes (see overview of shunting causes in appendix A.6). Though the point contact modules are just as likely to have shunts as the point contact cells, their *J-V* parameters are relatively unaffected by these shunts.

Based on this comparison, summarized in Table 7-1, the highest performance would be expected from the

n-type point contact cells, followed by the p-type FrontERA cells. That the highest efficiency in this thesis was nonetheless obtained with the n-type FrontERA cell can mostly be attributed to a high material quality for the FrontERA experiments and a large quantity of FrontERA cells to compensate for the low yield (the $\eta$ = 12.1 % was the only shunt free cell out of 142 cells).

From a practical point of view: the FrontERA cells allow for measurements from both sides (bifacial) and the design has more cells on the sample (which compensates for the low yield), but the FrontERA cells also have a poor cell edge definition, resulting in measurements difficulties. Also, the point contact device is a proven, industry compatible, mini-module concept

**Table 7-1**. Comparison of textured p- and n-type FrontERA and point contact cells. The colors roughly correspond to advantage (+), neutral (o) and disadvantage (-).

| | **Cell type** | | **FrontERA** | | **Point Contacts** | |
|---|---|---|---|---|---|---|
| | **Doping type** | | **p** | **n** | **p** | **n** |
| **Performance** | Dead area absorber contact ($f_{DA}$) | | ~7 % | ~11 % | ~2 % | ~3 % |
| | Light trapping loss (mA/cm$^2$) | | ~0.2 | | ~1 | |
| | Parasitic absorption (mA/cm$^2$) | | ~2.2 | | ~4 | ~3 |
| | Absorber resistance (Ωcm$^2$) | contact | < 0.1 | > 1 | 0.2-1 | 0-0.2 |
| | | lateral | 0.1-0.5 | 0.04-0.14 | 0.3-0.9 | 0.06-0.26 |
| | Emitter/TCO resistivity (Ωcm$^2$) | | 0.1? | 0.2-0.5 | 0.1? | 0.2-0.5 |
| | $V_{OC}$ (mV) | | 550-620 | 600-650 | 550-620 | 600-650 |
| | Shunting | | o | - | o (cell), + (module) | |
| **Practical** | Bifacial | | + | | - | |
| | # cells & test structures on sample | | 9 (0.6 cm$^2$) cells + 1 TLM + Hall | | 4 (1 cm$^2$) cells + 12 TLM | |
| | Cell edge definition | | - | | + | |
| | Mini-module concept | | - | | + | |
| | Industry compatibility | | - | | + | |

# 8 Summary

## Comparison of the PECVD and PVD Deposited Interlayers and Si Precursors

In chapter 3 the e-beam evaporated precursors and sputtered (PVD) ONO interlayers, were compared to PECVD precursors and NO(ON) interlayers. It was shown that the PECVD material can result in similar solar cells efficiencies as the established PVD/e-beam material. LBIC measurements indicated that cells with a PVD ONO interlayer stack showed a strongly reduced collection near to the grain boundaries, contrary to cells with a PECVD NO(ON) interlayer stack, for which the collection was not visibly affected by the grain boundaries. In chapter 5 the NON(ON) interlayer stack also resulted in the lowest direct reflection loss (~4 mA/cm$^2$ w/o ARF and ~1.5 mA/cm$^2$ with ARF) due to a high refractive index of the $SiN_x$ layer. Using PECVD material, new LPC-Si efficiency and $V_{OC}$ records for p-type (11.8 %, 618 mV) and n-type (12.1 %, 649 mV) FrontERA cells were obtained, showing the high quality of the PECVD material.

## Cracks and Crack Catcher Scribes on Borofloat33 Substrates

So far, the PECVD material could only be deposited on 3.3 mm BOROFLOAT33 (Boro33) substrates and this resulted in cracks in the LPC-Si absorber. For the FrontERA cells, these cracks resulted in interrupted grid fingers, thereby reducing the $J_{SC}$ and *FF*, and increasing shunting. “Crack catcher” laser scribes were implemented in an attempt to prevent cracks though the cell area, but this was only partially successful due to side-cracks coming out of the crack catchers. It was shown that especially n-type FrontERA cells are easily shunted by cracks crossing the stacked bus bars, resulting in a very low yield. The point contact cells are less sensitive to LPC-Si cracks, though they can still cause shunts and cut off small parts of the cell. For the point contact modules, the crack catchers were integrated into the cell design as isolation scribe between the cells. LBIC measurements indicate that the crack catchers result in a dead area with a width of ~200 µm (~4 % $J_{SC}$ loss), which can be explained by a low material quality of the small grained material next to the crack catchers.

## Dead Area due to the Absorber Contacts

LBIC measurements were used to determine the dead area fraction due to the absorber contact ($f_{DA}$) for n-type ($f_{DA}$ ≈ 11 %) and p-type ($f_{DA}$ ≈ 7 %) FrontERA cells and for n-type ($f_{DA}$ ≈ 3 %) and p-type ($f_{DA}$ ≈ 2 %) point contact cells. The lower $f_{DA}$ for p-type cells could be explained by conduction of minority carriers through a frontside charge inversion layer that was induced in the c-Si(p) by positive fixed charges in the $SiO_xN_y$ based interlayer stack.

The $f_{DA}$ for the point contact cells is strongly related to the etching of the TCO and the emitter in the

absorber point contact openings. In order to prevent shunting in n-type point contact cells, the purple etch solution ($KMnO_4$ + HF) that was used to etch the emitter was replaced by poly-Si etch ($HNO_3$ + HF). Though this succeeded in preventing shunts, it also increased the $f_{DA}$ to 5-8 %. In order to reduce this $f_{DA}$ a new emitter etch process was implemented, consisting of a short etch and reflow to remove the high-etch-rate layers and protect them from further etching, followed by a longer etch and reflow to remove and isolate the low-etch-rate layers. This process resulted in a high yield and low $f_{DA}$ of 3 %. Optimization of the point contact spacing indicated that, for ~$10^{17}$ $cm^{-3}$ doped n-type cells, the spacing should be doubled, thereby reducing the $f_{DA}$ further to ~1.5 %.

### Light Trapping and Parasitic Absorption in Textured LPC-Si Cells

Comparison of the light trapping properties of FrontERA and point contact cells showed that the best light trapping (lowest light trapping loss ($LT_{loss}$) was obtained for a textured FrontERA cell ($LT_{loss}$ ≈ 0.2 mA/$cm^2$), followed by textured point contact cells ($LT_{loss}$ ≈ 0.7-1.4 mA/$cm^2$), a planar point contact cell ($LT_{loss}$ ≈ 2 mA/$cm^2$) and a planar FrontERA cell ($LT_{loss}$ ≈ 5.5 mA/$cm^2$). About 40-50 % of the $LT_{loss}$ for the point contact cells was due to transmission through the metal cut scribes and the other 50-60 % was due to $R_{esc}$. It was argued that this higher $R_{esc}$ could be explained by the attached white reflector (P150W/Ag) for the point contact cells, compared to the detached white reflector (paper) for the FrontERA cells. This difference allows more light to reach the white reflector for the point contact cells, which then scatters part of the light out of the cell.

Comparison of the *IQE* measurements of planar and textured FrontERA cells indicated that texturing the c-Si absorber strongly reduces the relative $A_{par}$ by trapping most of the light within the absorber layer. Analysis of textured FrontERA and point contact cells indicated an $A_{par}$ loss of 4.1 mA/$cm^2$ for the p-type point contact cells, 3.1 mA/$cm^2$ for the n-type point contact cells and 2.2 mA/$cm^2$ for the FrontERA cell. It was argued that the higher $A_{par}$ of the point contact cells is partly due to the higher absorptance of the P150W/metal reflector (8-15 %) compared to the white paper reflector (~3 %) used for the FrontERA cells, and partly because the P150W is attached to the TCO, allowing more light to reach the reflector. Using ray tracing simulation, the $A_{par}$ losses were estimated at 1 mA/$cm^2$ in the ITO (FrontERA), 0.7 mA/$cm^2$ in the AZO (point contact cells), 0.2 mA/$cm^2$ in the detached white paper reflector, 3 mA/$cm^2$ in the P150W/Ag/Al (p-type) reflector, 1.9 mA/$cm^2$ in the P150/Ag (n-type) reflector and 0.4-0.7 mA/$cm^2$ in both the Boro33 glass and ARF. It was proposed that the $A_{par}$ losses in the glass and ARF could be reduced by thinning and texturing the glass by sandblasting and HF etching, as was done by CSG Solar [16]. For the point contact cells, it was proposed that the light trapping and parasitic absorption losses could be reduced by (a)

removing the $TiO_2$ particles from the P150W or (b) by depositing an Ag layer on the TCO before applying the P150W. Modelling results indicated that the optimum absorber thickness for textured LPC-Si cells is ~6 µm, for the typical material quality determined in this thesis ($L_{eff}$ = 12-20 µm).

### Absorber Doping Dependence of Point Contact Cells on PECVD Material

On p- and n-type (FrontERA) cells with PECVD NO(ON) interlayer stacks, it was found that by increasing the absorber doping from ~3-4·$10^{16}$ to ~7-9·$10^{16}$ $cm^{-3}$, the $V_{OC}$ increased by 10-20 mV, the $J_{SC}$ was unaffected and the $R_s$ decreased, resulting in a net $\eta$ gain of about 1 % absolute.

For the point contact cells, the corrected TLM measurements indicated that the absorber contact resistance depends strongly on the c-Si sheet resistance (independent of doping type). The ~100 Ω/□ sheet resistance of the ~9·$10^{16}$ $cm^{-3}$ doped n-type LPC-Si cells resulted in contact and lateral resistance contributions to the cell $R_s$ of < 0.1 Ω$cm^2$. The ~1300 Ω/□ sheet resistance of the ~2·$10^{16}$ $cm^{-3}$ doped p-type LPC-Si cells resulted in contact and lateral resistance contributions to the cell $R_s$ of ~0.9 Ω$cm^2$ each. The potential relative power gain for increasing the absorber doping from 2·$10^{16}$ to $10^{17}$ $cm^{-3}$, using the optimum spacing for each doping level, was estimated at 5.5 % for p-type samples and 2.5 % for n-type samples.

For textured point contact cells, it was found that increasing the absorber doping resulted in a large *FF* loss and it was argued that this was due to increased recombination at the isoscribe. This recombination could be prevented by implementing a passivated isoscribe process, consisting of a 1$^{st}$ isoscribe before hydrogen passivation (e.g. the crack catcher) and a 2$^{nd}$ isoscribe, within the first isoscribe, after TCO deposition.

### Emitter-TCO and Point Contact Cell Resistance

It was attempted to reduce the emitter/TCO resistivity ($\rho_c$) by replacing the a-Si by nc-Si and the TMB doping gas by $B_2H_6$. Using quasi cells and test structures it was found that replacing a-Si by nc-Si resulted in very low $\rho_c$ of 0.05 Ω$cm^2$, but also a 80 mV $V_{OC}$ loss. This $V_{OC}$ loss could be prevented by adding a ~6 nm doped a-Si layer between the a-Si(i) and nc-Si layers, but not without increasing the $\rho_c$. From $R_s$ analysis of textured point contact cells It was found that the $\rho_c$ on the textured LPC-Si cells is approximately 0.51 ± 0.13 Ω$cm^2$ for the a-Si(i/p)/nc-Si(p)(TMB)/ITO/AZO stack and 0.31 ± 0.28 Ω$cm^2$ for the a-Si(i/p)($B_2H_6$)/ITO/AZO stack. For ~9·$10^{16}$ $cm^{-3}$ doped n-type cells, an $R_s$ of ~0.8 Ω$cm^2$ was obtained with the a-Si/nc-Si (TMB) emitter and ~0.6 Ω$cm^2$ should be obtainable with the a-Si ($B_2H_6$) emitter.

## Best Cell Results

The highest efficiency cells obtained in this thesis are listed in Table 8-1, the 11.8 % n-type FrontERA cell, 11.5 % n-type point contact cell and 13.2 % IBC-SHJ cells were added as reference (grey), but were not obtained as part of this thesis. As mentioned before, the PECVD material resulted in increased FrontERA efficiency. For the point contact cells, the increased absorber doping, the implementation of absorber texturing and the a-Si/nc-Si(p)(TMB) emitter resulted in a 12.0 % efficient solar cell, despite a high recombination loss. This high recombination is the main reason why the efficiency did not exceed that of the FrontERA cells. The 9.2 % point contact module efficiency was obtained despite crack catcher scribes through the cell area and many local (material related) shunts, showing the inherent insensitivity of the point contact module to shunts.

**Table 8-1.** Highest Efficiency LPC-Si Cells.

| Cell type | Inlayer type | p/n-type | Ref. | $N$ ($cm^{-3}$) | KOH text | $J_{SC}$ ($mA/cm^2$) | $V_{OC}$ (mV) | $FF$ (%) | $\eta$ (%) |
|---|---|---|---|---|---|---|---|---|---|
| **FrontERA 0.6 $cm^2$ cells** | **PVD: ONO** | **p** | **-** | **$10^{17}$** | **No** | 25.8 | 598 | 73 | 11.3 |
| | | **n** | **[7]** | **$4 \cdot 10^{16}$** | **No** | 27.8 | 632 | 67 | 11.8 |
| | **PECVD: NO(ON)** | **p** | [89] | **$6 \cdot 10^{16}$** | **Yes** | 29.4 | 618 | 65 | 11.8 |
| | | **n** | [89] | **$9 \cdot 10^{16}$** | **Yes** | 27.3 | 649 | 68 | 12.1 |
| **Point contact - 1 $cm^2$ cells** | **PECVD: NON(ON)** | **n** | **[27]** | **$2 \cdot 10^{16}$** | **No** | 28.2 | 619 | 66 | 11.5 |
| | | **n** | - | **$8 \cdot 10^{16}$** | **Yes** | 26.6 | 645 | 70 | 12.0 |
| **- 4 $cm^2$ module** | **PC1:ONO** | **n** | **-** | **$1.5 \cdot 10^{17}$** | **Yes** | 20.8 | 603 | 73 | 9.2 |
| **IBC-SHJ** | **PC1:ONO (improved)** | **n** | [114] | **$2 \cdot 10^{16}$** | **Yes** | 31.3 | 626 | 67 | 13.2 |
| | | | | **$10^{17}$** | **Yes** | 27.5 | 643 | 75 | 13.2 |

# A Additional Results

## A.1 Inversion Layer Diodes

In section 4.2 bias light dependent *EQE* and LBIC measurements were used to argue that for p-type LPC-SI cells, minority carriers are collection though the frontside inversion layer as is shown schematically in Figure A-1a. However, it was not explained how the current can flow through the diode inside and the diode outside the cell area in opposite directions. In this section an explanation from ref. [81] was adapted to our cell and measurements in order to explain qualitatively how this is possible. Figure A-1b shows calculated *J-V* curves of the diode inside and the diode outside the cell (using the diode model), for local illumination outside the cell area by the LBIC laser or *EQE* spot, without bias light illumination. In this case the diode inside the cell area is in the dark, while the diode outside the cell area is illuminated. As the current (*I*) through the diodes is opposite and equal, the current densities inside ($J_{in}$) and outside ($J_{out}$) the cell area are given by:

$$J_{\mathrm{in}} \cdot A_{\mathrm{in}} = I = -J_{\mathrm{out}} \cdot A_{\mathrm{out}}\,, \qquad (37)$$

where $A_{in/out}$ is the effective area of the diode inside/outside the cell area. The voltage difference between the diodes is given by $\Delta V = IR$. The arrows in Figure A-1 show hypothetical examples of the *V* and *J* (operating points) for $A_{in} = 3A_{out}$, with and without resistance loss ($\Delta V$). It can be seen that if $A_{in} >> A_{out}$, a large fraction of the $J_{SC}$ outside the cell area can be transmitted by the diodes ($J_{out}/J_{SC}$), especially without resistance loss ($\Delta V$).

For a very small current *I* (e.g. no bias light), $\Delta V$ is very small and the resulting transmission by the diodes ($J_{out}/J_{SC}$) is large. For increasing distance between the diodes, *R* increases, increasing $\Delta V$, reducing $J_{out}/J_{SC}$. For collection from below the absorber contact, $A_o$ is much smaller than $A_i$, as the absorber contact area is much smaller than the emitter contact area, increasing $J_{out}/J_{SC}$.

For uniform bias light illumination, the diode inside the cell area is no longer in the dark, but the large area *EQE* curves in Figure 4-9 (section 4.2) show that there is nonetheless a significant collection outside the cell area. In ref. [81] it is also observed that, even for their cells with uniform illumination and equal diode areas, there is a significant current collection through the FFE. It was speculated that this is because the current generated below the emitter is divided between the emitter diode (back side) and the inversion/FFE diode (front side). Therefore, the $J_{SC}$ of the inversion diode inside cell area, is much smaller than the $J_{SC}$ of the inversion diode outside the cell area, allowing for current collection through the inversion layer.

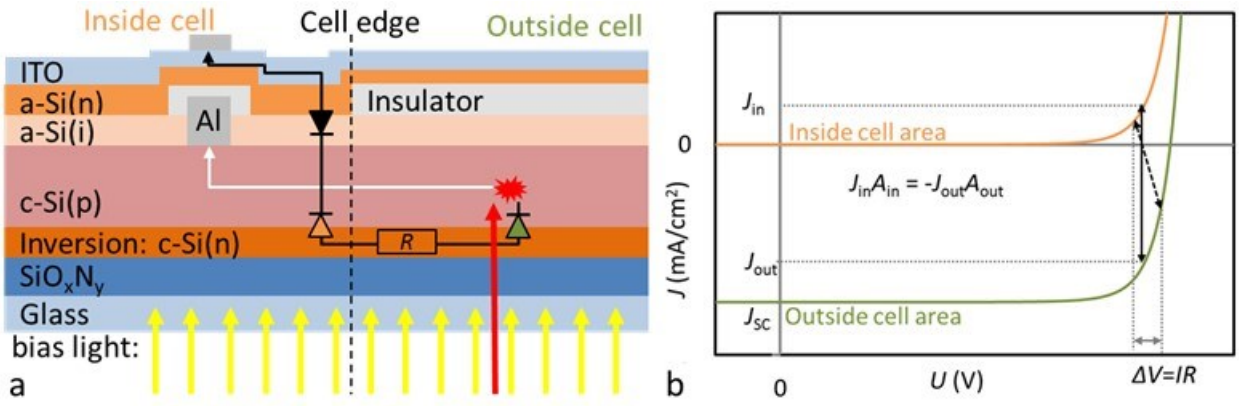


**Figure A-1.** Figure a schematically shows the collection through the inversion layer from outside the p-type FrontERA cell area. Figure b shows calculated (hypothetical) *J-V* curves, representing the diodes at the inversion layer, outside (green, illuminated) and inside (orange, dark) the cell area, for local illumination outside the cell area, without bias light illumination. The total current through the diodes (*I*), given by the product of the current density (*J*) and the diode area (*A*), is equal and opposite. The voltage difference (*ΔV*) between the diodes is determined by the product of *I* and the resistance (*R*) of the inversion layer. The black arrows show hypothetical examples of the *V* and *J* (operating points) for $A_{in} = 3A_{out}$, with and without resistance loss (*ΔV*).

## A.2 Lateral Resistance Models

This section presents the derivation, calculation and verification (through simulation) of the analytical resistance models. In section A.2.1 the resistance in the metal fingers is calculated, which is used in the $R_s$ analysis of the point contact cells in section 5.5. In section A.2.2 a new rectangular model for calculating the resistance toward a point contact is compared to an older circular model and 3D electrical simulations in Quokka. This rectangular model was published in ref. [110] and was used for the spacing optimization in section 5.4.

### A.2.1 Metal Finger Resistance

Figure A-3a schematically shows two Ag (TCO contact) fingers and one Ag (c-Si contact) finger with current moving in opposite directions. The figure includes the relevant geometrical parameters needed for calculating the resistance: the finger width ($w_f$), the width of the unit cell ($w_{uc}$) from which the current is collected and the length of the finger ($l_f$), which is also the length of the unit cell. The equation for calculating the resistance in the metal fingers can be derived in the following way (e.g. [116]):

$$dR = \frac{\rho_m}{w_f t_m} dx \,, \tag{38}$$

$$i = J_M w_{uc} x \,, \tag{39}$$

$$P_{R,f} = \int i^2 dR = \frac{\rho_m}{w_f t_m} (J_M w_{uc})^2 \int_0^{l_f} x^2 dx = \frac{\rho_m}{w_f t_m} (J_M w_{uc})^2 \frac{l_f^3}{3} \,, \tag{40}$$

$$R_{\mathrm{s,f}} = 2\frac{P_{\mathrm{R,f}}}{I^2} w_{\mathrm{uc}} l_{\mathrm{f}} = \frac{w_{\mathrm{uc}}\rho_{\mathrm{m}}}{w_{\mathrm{f}} t_{\mathrm{m}}} \frac{l_{\mathrm{f}}^2}{3}, \tag{41}$$

Where $\rho_m$ is the resistivity of the metal, $t_m$ is the thickness of the metal, $J_M$ is the current density at the maximum power point without resistance losses in A/cm$^2$, $x$ is the direction parallel to the grid finger and $R_{s,f}$ is the combined contribution of both Ag/c-Si and Ag/TCO grid fingers (i.e. factor 2) to the series resistance of the cell (Ωcm$^2$).

Figure A-2 shows $R_{s,f}$ as a function of the metal thickness ($t_m$) (fig. a) and the finger length ($l_f$) (fig. b) for both Ag ($\rho_m$ = 1.59·10$^{-8}$ Ωm) and Al ($\rho_m$ = 2.65·10$^{-8}$ Ωm). The grey dots shows the $R_{s,f}$ for the current cell design for p-type (20/100 nm Ag/Al, ~0.11 Ωcm$^2$) and n-type cells (100 nm Ag, ~0.09 Ωcm$^2$). This rather low contribution to the cell resistance is mainly due to the relatively small finger length (i.e. cell length, Figure A-2b) and the high conductivity of the (sputtered) Ag. A thicker metal layer could result in a small efficiency gain, but at some point (>150-250 nm) it becomes more difficult to open the metal layer with the laser, resulting in shunts.

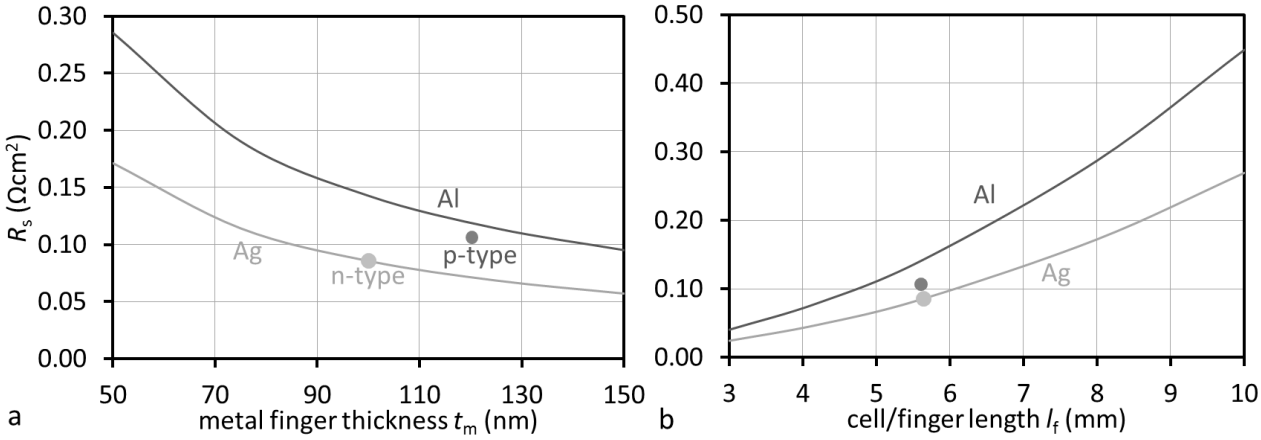


**Figure A-2.** $R_{s,f}$ as a function of $t_m$ (a) and $l_f$ ( b) for both Ag ($\rho_m$ = 1.59·10$^{-8}$ Ωm) and Al ($\rho_m$ = 2.65·10$^{-8}$ Ωm). The grey dots show the current resistance in the metal fingers for the p- and n-type cells.

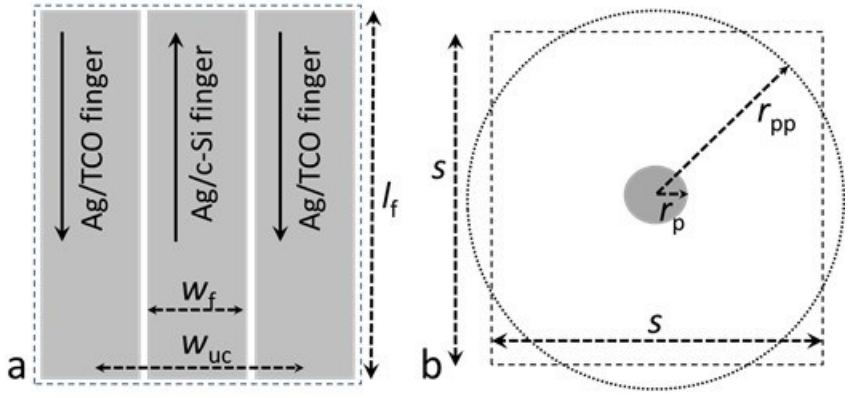


**Figure A-3.** Schematic drawings of the unit cells used for calculating the resistance in grid fingers (a) and in a layer toward a point contact (b). The geometric units used in the resistance models are included in the figure.

### A.2.2 Lateral Resistance in Point Contacted Layers

Figure A-3b shows the unit cell and relevant geometrical parameters for calculating the lateral resistance toward a point contact using the circular model from ref. [117], by Basore. This circular model was made for a square unit cell and redistributes the area of this unit cell into a circle with the same area, as shown in the figure. The equations for calculating the resistance in a layer toward a point contact can be derived in the following way:

$$dR = \frac{\rho_{\mathrm{layer}}}{2\pi r \cdot d_{\mathrm{layer}}} dr = \frac{R_{\mathrm{layer}}}{2\pi r} dr \,, \tag{42}$$

$$i = J_{\mathrm{M}} \pi \left(r_{\mathrm{pp}}^2 - r^2\right), \tag{43}$$

$$P_{\mathrm{R,l}} = \int i^2 dR = J_{\mathrm{M}}^2 \frac{\pi}{2} R_{\mathrm{layer}} \int_{r_{\mathrm{p}}}^{r_{\mathrm{pp}}} \frac{\left(r_{\mathrm{pp}}^2 - r^2\right)^2}{r} dr \; = \\ J_{\mathrm{M}}^2 \frac{\pi}{2} R_{\mathrm{layer}} \frac{r_{\mathrm{pp}}^4}{\left(r_{\mathrm{pp}}^2 - r_{\mathrm{p}}^2\right)^2} \left[ \ln\left(\frac{r_{\mathrm{pp}}}{r_{\mathrm{p}}}\right) - \frac{3}{4} + \left(\frac{r_{\mathrm{p}}}{r_{\mathrm{pp}}}\right)^2 - \frac{1}{4}\left(\frac{r_{\mathrm{p}}}{r_{\mathrm{pp}}}\right)^4 \right], \tag{44}$$

$$R_{\mathrm{s,l}} = \frac{P_{\mathrm{R,l}}}{I^2} s^2 \,, \tag{45}$$

$$r_{\mathrm{pp}} = \frac{s}{\sqrt{\pi}} \,, \tag{46}$$

Where $R_{\mathrm{layer}}$ is the sheet resistance of the layer, $d_{\mathrm{layer}}$ is the thickness of the layer, $r_{\mathrm{p}}$ is the radius of the point contact, $r_{\mathrm{pp}}$ is the radius of the unit cell, $s$ is the distance between adjacent point contacts and $R_{\mathrm{s,l}}$ is the contribution of the lateral resistance to the series resistance of the cell ($\Omega\mathrm{cm}^2$). The model doesn't exactly apply to rectangular geometry of the point contact cells in this thesis, which is the reason why a new model was developed and simulations in Quokka were made. Here, the circular model will be compared to the rectangular model by equating the area of the circle to the area of the rectangular unit cell.

The rectangular model was developed (by summer student C. Matarazzo) to calculate the resistance contribution due to the lateral resistance in both the c-Si absorber layer and the TCO for a rectangular geometry with point contacts. As it is assumed that the current flows radially toward the central point contact, polar coordinates are used to calculate the resistance. Figure A-4a shows the unit cells for the circular and rectangular models, where the yellow dots represent the point contacts. Using symmetry, the resistance only has to be calculated for the triangular areas *a* and *b*, in order to obtain the resistance for the entire cell. Figure A-4b shows the input parameters for the models: $\Delta x$ and $\Delta y$ (half the distances between the point contact cells in the x and the y direction), $r_{\mathrm{p}}$ (the radius of the point contact), the polar coordinates ($r$ and $\Theta_{\mathrm{a/b}}$) and derived parameters ($r_{\mathrm{ppa}}$, $\mathrm{d}\Theta$, $\Theta_{\mathrm{Ma/b}}$) used in the model equations.

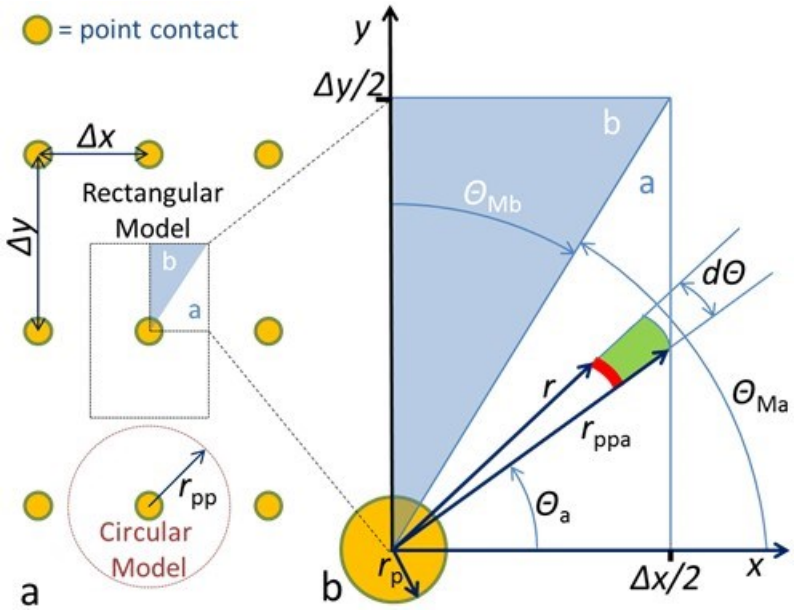


**Figure A-4.** Fig. a shows unit cells for the circular model and rectangular models, where the yellow dots represent the point contacts. Fig. b shows the input parameters for the models $\Delta x$, $\Delta y$ and $r_p$, as well as the polar coordinates and derived parameters used in eq. (47)-(51).

The rectangular model consists of the following equations to determine the $R_s$ contribution due to lateral transport toward the point contacts ($R_{s,l}$):

$$dR = \rho \frac{dr}{dA} = \frac{\rho}{d} \frac{dr}{r d\Theta_{a,b}} = R_{layer} \frac{dr}{r \cdot d\Theta_{a,b}}, \tag{47}$$

$$i = J_M d\Theta_{a,b} \frac{r_{ppa,b}^2 - r^2}{2}, \tag{48}$$

$$P_{R,a,b} = \int i^2 dR = R_{layer} \frac{J_M^2}{4} \int_0^{\Theta_{Ma,b}} \int_{r_p}^{r_{ppa,b}(\Theta)} \frac{\left(r_{ppa,b}^2(\Theta_{a,b}) - r^2\right)^2}{r} d\Theta_{a,b} dr, \tag{49}$$

$$r_{ppa}(\Theta_a) = {\Delta x}/{2\cos\Theta_a} \text{ and } \Theta_{Ma} = \tan^{-1}\frac{\Delta y}{\Delta x}, \quad \text{for triangle a,} \tag{50}$$

$$r_{ppb}(\Theta_b) = {\Delta y}/{\cos\Theta_b} \text{ and } \Theta_{Mb} = \tan^{-1}\frac{\Delta x}{\Delta y}, \quad \text{for triangle b,} \tag{51}$$

$$R_{s,l} = \frac{P_{R,l}}{I_M^2} \frac{\Delta x \Delta y}{4} = \frac{4\left(P_{R,a} + P_{R,b}\right)}{J_M^2 \Delta x \Delta y}, \tag{52}$$

where the geometric parameters $r_{ppa}$, $\Theta_a$, $\Theta_{Ma}$ and $\Theta_{Mb}$ are shown in Figure A-4b and $i$ is the current generated in the green region and flowing through the red region. From the equations it can be seen that $R_s$ doesn't depend on $J_M$. It can also be seen that $R_s$ depends linearly on $R_{layer}$, and $R_{s,l} = 0$ for $R_{layer} = 0$. This means that $R_s$ can be calculated (or simulated) for any $R_{layer}$ and scaled linearly to the $R_s$ for any other $R_{layer}$.

**Quokka Simulations**

Quokka numerically solves the charge carrier transport in a silicon device using quasi-neutrality and conductive boundaries. The emitter and contact resistances were set to extremely low values, leaving only the resistance in the c-Si absorber. For the comparison, the point contact radius $r_p$ was set to 30 µm (between the 17 µm c-Si/Ag and 45 µm TCO/Ag point contacts) and the sheet resistance $R_{layer}$ was set to 500 Ω/□. From many simulations, the uncertainty in the Quokka simulation is estimated at approximately ±10 %. This could not be further improved by using a finer mesh. The uncertainty is also larger for small resistance values due to the inaccuracy of determining the resistance from the *J-V* curves. Quokka uses five different methods for determining $R_s$ from the *J-V* curves [118]. The values here reported are the median of these 5 methods after removing obvious outliers. The main disadvantage of 3D electrical simulation is that it is time intensive, requiring long calculation times, consistency checking and mesh (re)optimization. The main disadvantage of analytical modelling is that it makes fundamental assumptions and simplifications which can result in systematic inaccuracies.

**Comparison**

Figure A-5a shows $R_s$ vs. $\Delta x$ (keeping $\Delta y$ fixed at 600 µm), for the circular and rectangular models and for the Quokka simulation. These results were used to calculate the relative difference of both models to the Quokka simulations and this is plotted in Figure A-5b. It can be seen that for aspect ratios deviating from 1 (secondary horizontal axis), the circular model underestimates $R_{s,l}$, while the new model overestimates $R_{s,l}$. For an aspect ratio of 1, the rectangular model does appear to produce more accurate results than the circular model. For the circular model, the underestimation can be explained by the conversion of the rectangular unit cell to a circle (of the same area), thereby reducing the average distance to the contact and perhaps also reducing current crowding. Current crowding refers to the fact that the resistive power loss (eq. (49)) depends on the square of the local current density (*i*) and therefore, local high current densities contribute disproportionally to the power loss. Current spreading refers to the fact that the current will spread out to avoid current crowding. For the rectangular model, the overestimation can be explained because it assumes that the current will flow in a straight line to the point contact, while in reality it will take a detour to minimize current crowding. This is confirmed by the simulated current flow shown in Figure A-6. The figure shows how the current generated at x = 700 µm, initially flows in the x-direction before flowing more radially to the point contact from x ≈ 200-300 µm, thereby minimizing the current density next to the contact. The better result for the rectangular model for an aspect ratio of 1, can be explained because for an aspect ratio of 1 the current does flow approximately radially toward the

point contact. This makes the rectangular model an accurate description of the current flow, while the circular model still underestimates $R_s$ by redistributing the square unit cell into a circle. In section 5.4 the rectangular model was used for parameter variations (mainly with aspect ratio 1), which would be too time-intensive for 3D simulation. The standard c-Si/Ag and TCO/Ag point contact geometries have aspect ratios of 0.5 and 0.25 respectively and were therefore simulated in Quokka.

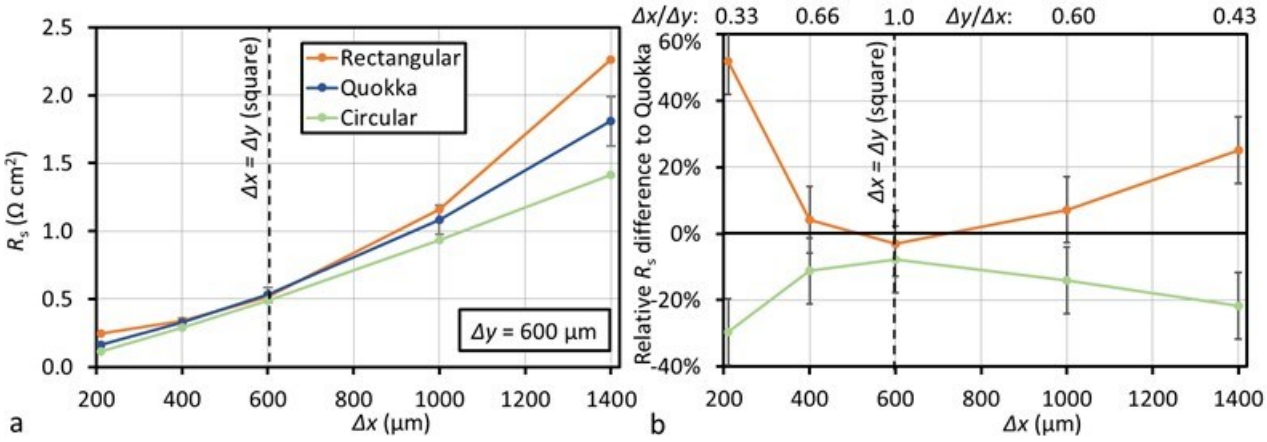


**Figure A-5.** Comparison of Quokka simulations with circular and rectangular models (eq. (52)) as function of $\Delta x$, for a fixed $\Delta y$ = 300 µm, plotted as $R_s$ (a) and as relative $R_s$ difference for the models compared to the Quokka $R_s$ ($(R_{model}-R_{Quokka})/R_{Quokka}$) vs. $\Delta x$ (b). The aspect ratio ($\Delta x/\Delta y$ or $\Delta y/\Delta x$) is shown above fig. b.

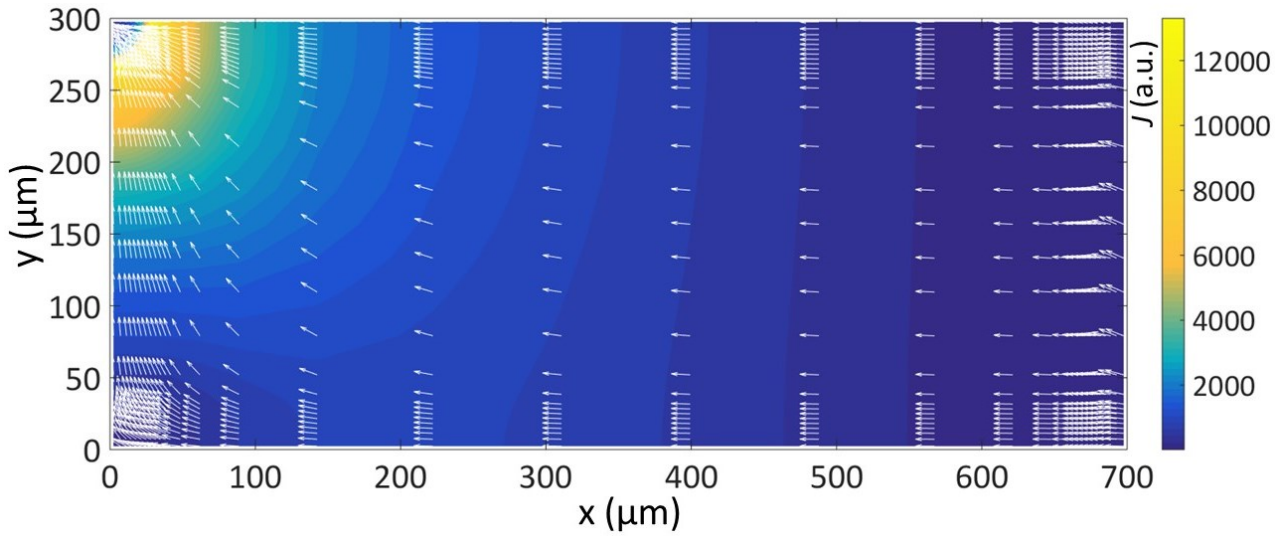


**Figure A-6.** Simulated current (in color) and flow direction (arrows) using Quokka for $X_M$ = 700 µm, $X_M$ = 300 µm, $r_p$ = 30 µm and $R_{layer}$ = 500 Ω/□. The arrow density varies due to the finer mesh near the point contact.

## A.3 Majority Carrier Mobility and Resistance Uniformity

This section presents and discusses the measured LPC-Si mobility and resistance uniformity.

### A.3.1 Hall Mobility in LPC-Si

Hall mobilities and carrier densities were measured for p- and n-type LPC-Si samples with different absorber doping concentrations. The measurements were made in the dark and at room temperature, using square (~0.25 $cm^2$) van der Pauw structures with contacts in the corners. Figure A-7a shows the hole mobilities for p-type LPC-Si, compared to 40, 60, 80 and 100 % of the hole mobility of mono-crystalline c-Si(p) [38]. The blue dots include PVD/e-beam samples on Corning glass (section 3.3.2, Figure 3-6) and it also includes PECVD samples on Boro33 glass using an older laser crystallization process (10 mm/s, section 3.3.2, Figure 3-7). The red dots represent Boro33 samples using the optimized process (3 mm/s, section 3.3.3). It can be seen that all p-type LPC-Si samples have a much lower $\mu$ than mono-Si. For the blue dots, $\mu$ even decreases for lower $N$ instead of increasing. The Boro33/PEVCD samples with the 3 mm/s crystallization process appear to have a somewhat higher mobility. Figure A-7b shows the electron mobility for n-type samples with and without hydrogen plasma passivation (HPP) (partly published in ref. [86]). It can be seen that the measured $\mu$ without HPP is slightly lower than the measured $\mu$ with HPP and reaches a minimum for approximately $N = 5 \cdot 10^{15}$ $cm^{-3}$.

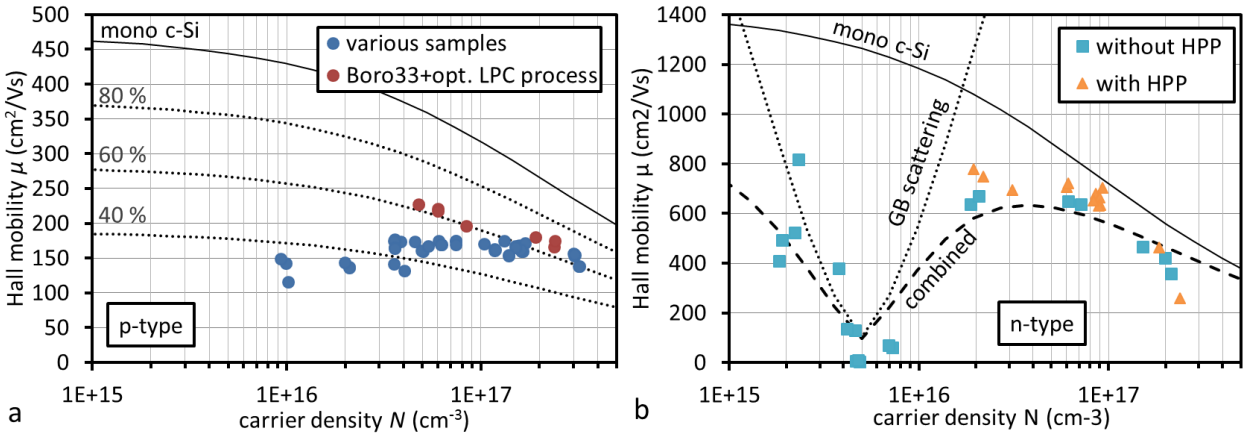


**Figure A-7.** P-type (a) and n-type (b) majority carrier mobilities $\mu$ vs. carrier density $N$, both measured by Hall effect measurements. Fig. a includes 40, 60, 80, 100 % of the mono c-Si $\mu$ as reference (grey lines). The blue dots represent samples fabricated on various materials with various LPC processes, while the red dots consist only of Boro33/PECVD samples fabricated using the 3 mm/s LPC process [48]. Fig. b shows Hall effect measurements on samples with and without hydrogen plasma passivation (HPP). These values were fitted using a grain boundary (GB) scattering model from ref. [86], showing how GB scattering can qualitatively explain the observed Hall mobility vs $N$ data.

Such a minimum in the $\mu$ vs $N$ dependence was also found for 1 µm thick poly-silicon films in ref. [86], though there the minimum was found around $2 \cdot 10^{18}$ $cm^{-3}$. This behaviour was explained by carrier scattering of the field generated by carriers trapped at the grain boundaries: for low $N$ the traps are empty and $\mu$ is unaffected; as $N$ increases, $\mu$ decreases until the traps are completely filled. As $N$ increases further, the charge difference between the traps and the rest of the material decreases, resulting in an increasing

$\mu$. The $\mu$ minimum in ref [86] could be successfully modelled with grain boundary (GB) scattering for a measured (TEM) grain size of 20 nm, and a fitted trapping state density at the GB interfaces of 3-4·$10^{12}$ $cm^{-2}$. In the discussion it was stated that the model is only quantitatively valid up to 60 nm grain size, but beyond this grain size the qualitative features are still valid. Therefore, the GB scattering fit shown in Figure A-7b (for a grain size of 300 nm) should only be considered as a qualitative indication that the observed dependency of $\mu$ on *N* is likely due to grain boundary scattering or similar potential barriers by trapped carriers.

An argument against grain boundary scattering is that for many Hall measurement samples the grains size was similar to the sample size. We therefore speculate that the reduced mobility is due to a different carrier trapping effect observed for mc-Si wafers in ref. [119], where it results in artificially increased lifetimes in the QSSPC measurements. Such artificially increased lifetimes were also observed for QSSPC measurements on SPC-Si [120] and LPC-Si (not shown), indicating that LPC-Si also has many of these trapping centres. Carriers trapped in these trapping centres should also form potential barriers, affecting the mobility by scattering the carriers.

### A.3.2 Resistance Uniformity in LPC-Si

Figure A-8a shows the ratio of the horizontal and the vertical resistance of all the Hall effect measurements from Figure A-7. Trendlines are added for both the p- and n-type samples, showing that the asymmetry appears to be decreasing for increasing *N*. However, the $R^2$ value is only about 30 %, indicating that only about 30 % of the variance can be explained by the dependence on *N*. No clear pattern was found correlating the higher/lower resistance to the crystallization direction or visible grain boundaries.

For all the PECVD LPC-Si samples made at HZB, the sheet resistance $R_{layer}$ was measured at three different positions on the sample. Figure A-8b shows the relative deviation of $R_{layer}$ (standard deviation / average) plotted against the average $R_{layer}$ of those three measurements for each sample. Again the non-uniformity (relative deviation) appears to decrease for increasing *N* (decreasing $R_{layer}$), though the $R^2$ is only about 10 %, which might be related to the larger distances between the measurements.

It can be concluded that the LPC-Si resistance is very non-uniform and that this is partly related to the measured *N*. Considering the mild scattering of the measured mobility in Figure A-7, it seems more likely that the resistance non-uniformity is due to the absorber doping than due to mobility non-uniformity.

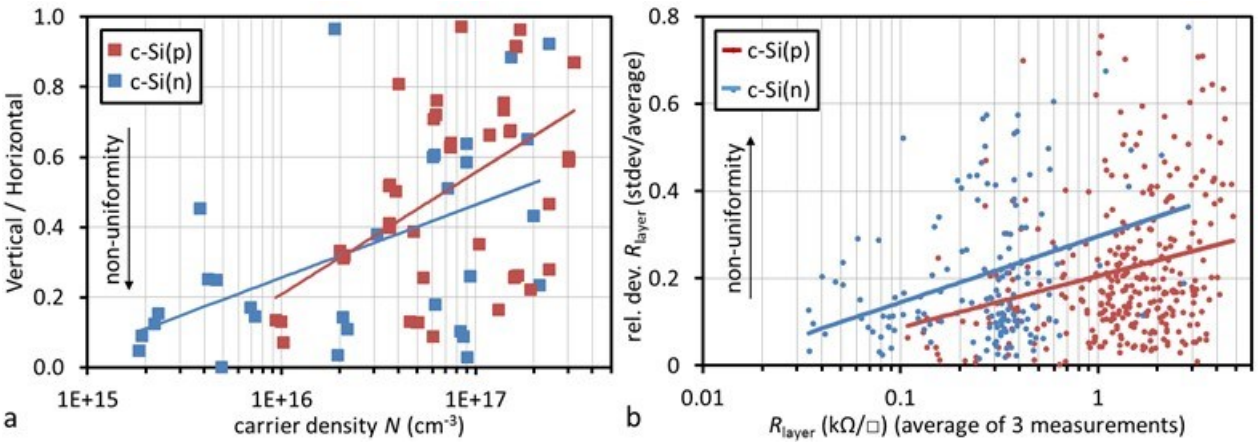


**Figure A-8**. Figure a shows the ratio of the horizontal and the vertical resistance of all the Hall effect measurements from Figure A-7. The lines are logarithmic trendlines for the p- (red) and n-type (blue) samples. Figure b shows the relative deviation of $R_{layer}$ (standard deviation / average) plotted against the average $R_{layer}$ of those three measurements for each sample

## A.4 *IQE*, $V_{OC}$ and *pFF* Analysis of Quasi Cells

In this section bifacial *IQE* measurements of quasi cells are used to estimate the *L* and *S* for these cells. Subsequently, it is determined to what extend these *L* and *S* values can predict the measured $V_{OC}$ and *pFF*, allowing us to draw some conclusions about recombination in LPC-Si. The first part of this *IQE* analysis was published in ref. [86].

Sub- and superstrate *IQE* was measured for low (2-3·$10^{16}$ $cm^{-3}$) and highly (1-2·$10^{17}$ $cm^{-3}$) doped, p- and n-type quasi cells with NO(ON) interlayer stacks, with and without HPP. The substrate *IQE* measurements were corrected for parasitic absorption in the emitter and TCO and the superstrate *IQE* was corrected for absorption in the glass. The inverse *IQE* was plotted against the absorption length ($\alpha^{-1}$) and this data was fitted with a line through $IQE^{-1} = 1$ at $\alpha^{-1} = 0$, to obtain a first estimate of the diffusion length [39]. Examples of these fits are shown in Figure A-9a and b for the highly doped n- and p-type samples, with and without HPP. Subsequently, all these sub- and superstrate *IQE* measurements were fitted with the collection efficiency equations as explained in section 2.7. This is shown in Figure A-9c-f, for the highly doped n- and p-type samples, with and without HPP. For the sample with *L* = 3.8 µm, it can be seen that changing *S* from 0 to 100000 cm/s has almost no effect on the substrate $\eta_c$, but clearly improves the superstrate $\eta_c$ fit. In general, it is possible to increase *L* and *S* in such a way that the substrate $\eta_c$ remains unchanged, but the superstrate $\eta_c$ decreases (until both are completely *S*-limited), and vice versa, thereby obtaining a good fit for both sub- and superstrate measurement for specific combination of *L* and *S*.

For the n-type samples, good fits are obtained by assuming that the diffusion length from the $IQE^{-1}$ fit equals *L*. This was somewhat unexpected as it is generally assumed that the $IQE^{-1}$ fit equals $L_{eff}$. Perhaps

this difference is due can be explained by the fact that the $IQE^{-1}$ plot was only fitted for very low $\alpha^{-1}$ and therefore dominated by the bulk recombination. Also, the bulk diffusion lengths for these samples are low compared to the layer thicknesses, meaning that the substrate recombination is mostly dominated by bulk recombination, especially for the $L$ = 3.8 µm sample. The (highly doped) p-type samples appear to be more $S$ limited.

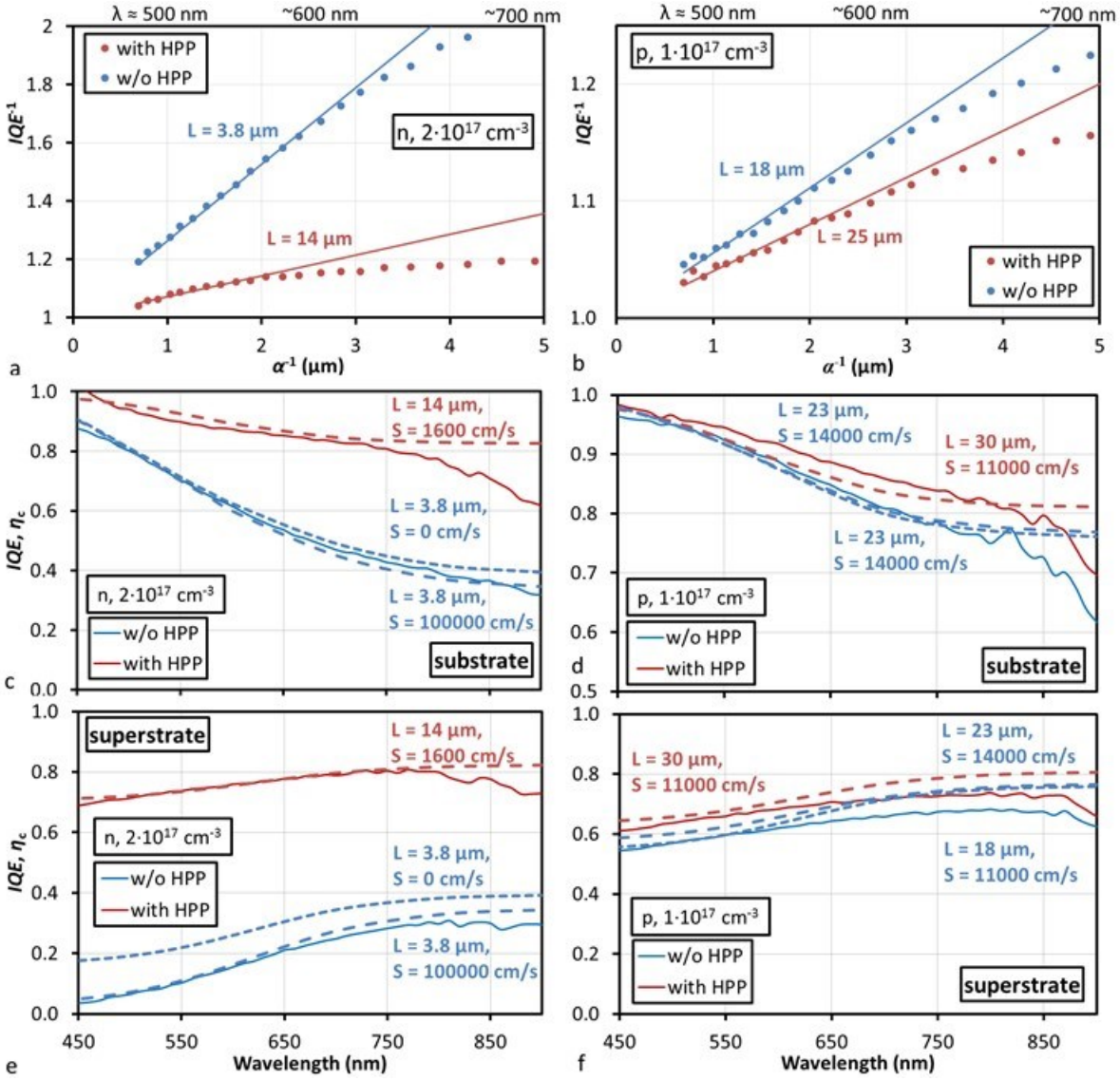


**Figure A-9.** Figure a and b show the inverse (substrate) *IQE* (dots) vs. the absorption length $\alpha^{-1}$ and the fitted diffusion length $L$ for the highly doped n-type (a) and p-type (b) quasi cells with (red) and without HPP (blue). Fig. c-f show the substrate (c and d) and superstrate (e and f) *IQE* (solid) and fitted $\eta_c$ (dashed), for the same n-type (c and d) and p-type (d and f) cells. The fitted values are included in the figures.

Table A-1 shows the fitted $L$ & $S$ parameters and measured $J_{SC}$ (*EQE*). The limiting $L$ and/or $S$ values are underscored. It should be noted that these limiting values have a much smaller uncertainty than the non-limiting value, which has a relatively small impact on the calculated $\eta_c$. The fitting results were published

in ref. [86], using the measured mobility values. Here, the mono-Si mobilities were used, as in the rest of the thesis. This was done because it is unclear if the minority mobility is affected in the same way by the effect that is reducing the measured majority carrier mobility (see appendix A.3.1). Using lower mobilities, based on the measured majority carrier mobility, resulted in lower *S* and/or higher *L* values, but doesn't significantly change the extent to which the curves could be fitted.

**Table A-1.** Fitted & Calculated Parameters

| doping | | HPP | *L* | *L* | *S* | $J_{SC}$ (mA/cm²) | | $V_{OC}$ (V) | | *pFF* | |
|---|---|---|---|---|---|---|---|---|---|---|---|
| Type | *N* (cm⁻³) | | (*IQE*⁻¹) | (µm) | (cm/s) | sub | sup | sub | sup | sub | sup |
| n | $2{\cdot}10^{16}$ | No | 4.8 | **4.8** | >10⁵ | 14.8 | 4.6 | 0.518 | 0.478 | 75% | 72% |
| | | Yes | 25 | 25 | **5500** | 20.5 | 16.8 | 0.578 | 0.574 | 82% | 81% |
| | $2{\cdot}10^{17}$ | No | 3.8 | **3.8** | >10⁵ | 13.9 | 3.8 | 0.580 | 0.532 | 76% | 73% |
| | | Yes | 14 | **14** | **1600** | 20.8 | 16.9 | 0.644 | 0.640 | 83% | 82% |
| P | $3{\cdot}10^{16}$ | No | 8 | **8** | 1000 | 18.1 | 14.6 | 0.530 | 0.524 | 77% | 76% |
| | | Yes | 21 | **21** | **4000** | 22.1 | 19.7 | 0.576 | 0.572 | 81% | 81% |
| | $1{\cdot}10^{17}$ | No | 18 | 23 | **14000** | 20.2 | 14.7 | 0.598 | 0.590 | 82% | 81% |
| | | Yes | 25 | 30 | **11000** | 21.4 | 16.1 | 0.608 | 0.600 | 82% | 82% |

Subsequently, these *L* and *S* values together with the *N*, $J_{SC}$ and $\mu$ values, were used in the double diode model from ref. [121] to calculate the $V_{OC}$ and *pFF*:

$$J = J_{SC} - J_{01}\left(e^{\frac{V}{V_T}} - 1\right) - J_{02}\left(e^{\frac{V}{2V_T}} - 1\right), \tag{53}$$

$$J_{01} = \frac{qDn_i^2}{N}\frac{1}{LK} \tag{54}$$

$$K = \frac{\cosh\left(d/L\right) + SL/D\,\sinh\left(d/L\right)}{\sinh\left(d/L\right) + SL/D\,\cosh\left(d/L\right)} \tag{55}$$

$$J_{02} = \frac{q\pi Dn_i V_T}{F_{max}}\frac{1}{L^2}, \tag{56}$$

$$with\ F_{max} = \sqrt{2NqV_{bi}/\varepsilon_s}, \tag{57}$$

where $J_{01}$ is the saturation current density due to recombination in the bulk (more accurate: quasi-neutral region) and at the interlayer interface, $J_{02}$ is the saturation current density due to recombination in the space charge region (SCR), $F_{max}$ is the maximum field strength in the SCR for an abrupt junction, $\varepsilon_s$ is the absolute dielectric constant of Si and $V_{bi}$ is the built-in potential (~0.8 V). In the middle of the SCR, the electron and hole densities are equal, which strongly increases the recombination at this position. For c-Si wafer cells, *L* is sufficiently large that SCR recombination is negligible [112], but for LPC-Si cells, *L* is much lower. This model assumes an abrupt junction where the recombination is completely domination by *L*.

The presence of the heterojunction in the junction region means that the $J_{02}$ (SCR) recombination can be much higher if the heterojunction is not well passivated by the a-Si(i) layer.

Using eq. (53) the *J-V* curves and corresponding $V_{OC}$ and *pFF* values were calculated with and without $J_{02}$, i.e. with and without space charge recombination. Subsequently, these values were plotted against the measured substrate (Suns-$V_{OC}$) $V_{OC}$ and *pFF* values and superstrate (Solar Simulator) $V_{OC}$ values in Figure A-10. The $V_{OC}$ and *pFF* calculated with $J_{02}$ are also included in Table A-1.

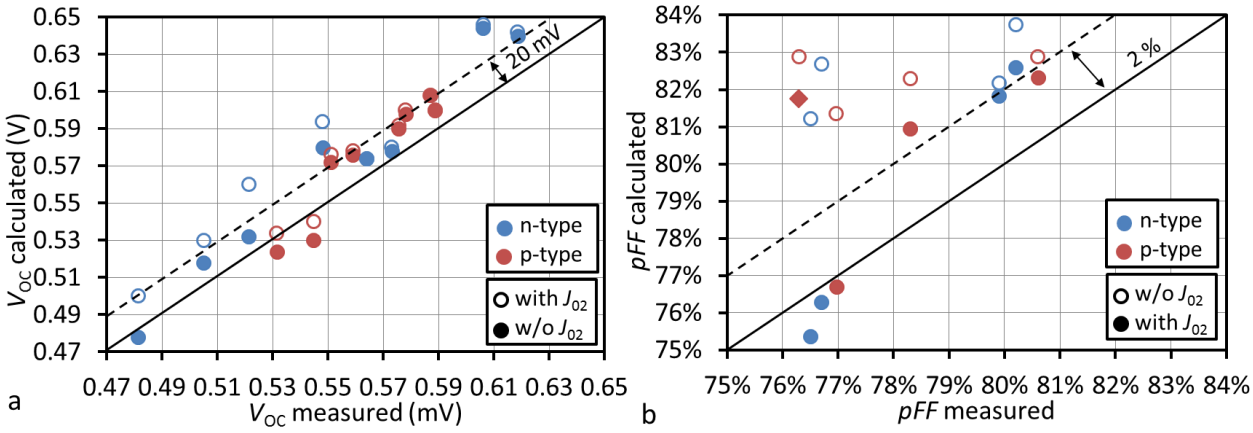


**Figure A-10.** Calculated vs measured $V_{OC}$ (a) and *pFF* (b) values for n- (blue) and p-type (red) quasi cell with (filled) and without (open) using $J_{02}$ for the calculation. The solid lines indicate when the calculated and measured values are identical. The *pFF* of the highly doped p-type cell is indicated by the diamond shaped symbol.

It can be seen that without $J_{02}$ (open symbols) the calculated $V_{OC}$ is about 20 mV higher than the measured $V_{OC}$ and the calculated *pFF* is almost unaffected by the measured *pFF*. With $J_{02}$ (solid symbols) the calculated $V_{OC}$ fits the measured $V_{OC}$ and *pFF* much better, especially for the low $V_{OC}$ and *pFF*. This indicates that SCR recombination is a significant recombination effect in LPC-Si cells, reducing the $V_{OC}$ for low *L* samples and the *pFF* for all LPC-Si samples.

The highly doped p-type cell without HPP has a much lower *pFF* (diamond symbol) than predicted by the model. This can be explained by a $\Delta n$ dependence of $S_{eff}$ as predicted for highly doped p-type samples in section 4.2.4.

For the cells with higher $V_{OC}$ and *pFF* values, the measured values are about 20 mV and 2 % lower than the calculated values. Using the measured mobility values increases the difference between the calculated and measured values (by ~10-20 mV), so this cannot explain the difference. A decreasing lifetime for increasing $\Delta n$ could explain the lower measured than predicted $V_{OC}$, but would also result in a higher *pFF*, which contradicts the lower than predicted measured *pFF* results. A more likely explanation is that the $V_{OC}$

and *pFF* are affected by recombination at the heterojunction emitter interface, which would increase the SCR recombination without affecting the *IQE* (or *L*).

## A.5 a-Si(i) Surface Passivation

This section will investigate the impact of c-Si surface passivation on textured LPC-Si.

### A.5.1 a-Si(i) layer and RCA cleaning

Figure A-11a and b show the $V_{OC}$ and *pFF* of n- and p-type quasi cells from experiment 2 (see section 5.2.6) with and without a-Si(i):H layer. All cells had a 10 nm a-Si(p/n):H emitter and 200 °C LOS1 ITO. For the n-type cells, the a-Si(i):H layer causes a $V_{OC}$ gain of approximately 40 mV (~7 % relative). For the p-type cells, the a-Si(i):H layer did not result in a significant $V_{OC}$ gain. The *pFF* shows a similar behaviour, with a relative gain of 9 % for the n-type cells and no gain for the p-type cells.

Figure A-11c and d show the $V_{OC}$ and *pFF* of n and p-type quasi cells from experiment 3 (see section 5.2.6) with and without RCA cleaning. All cells had an 5 nm a-Si(p/n):H + 30/20 nm nc-Si(p/n):H emitter and 200 °C LOS1 ITO. The RCA clean appears to have a similar effect as the a-Si(i):H layer: a ~60 mV $V_{OC}$ gain and ~10 % *pFF* gain (median values) for the n-type cells and no gain for the p-type cells.

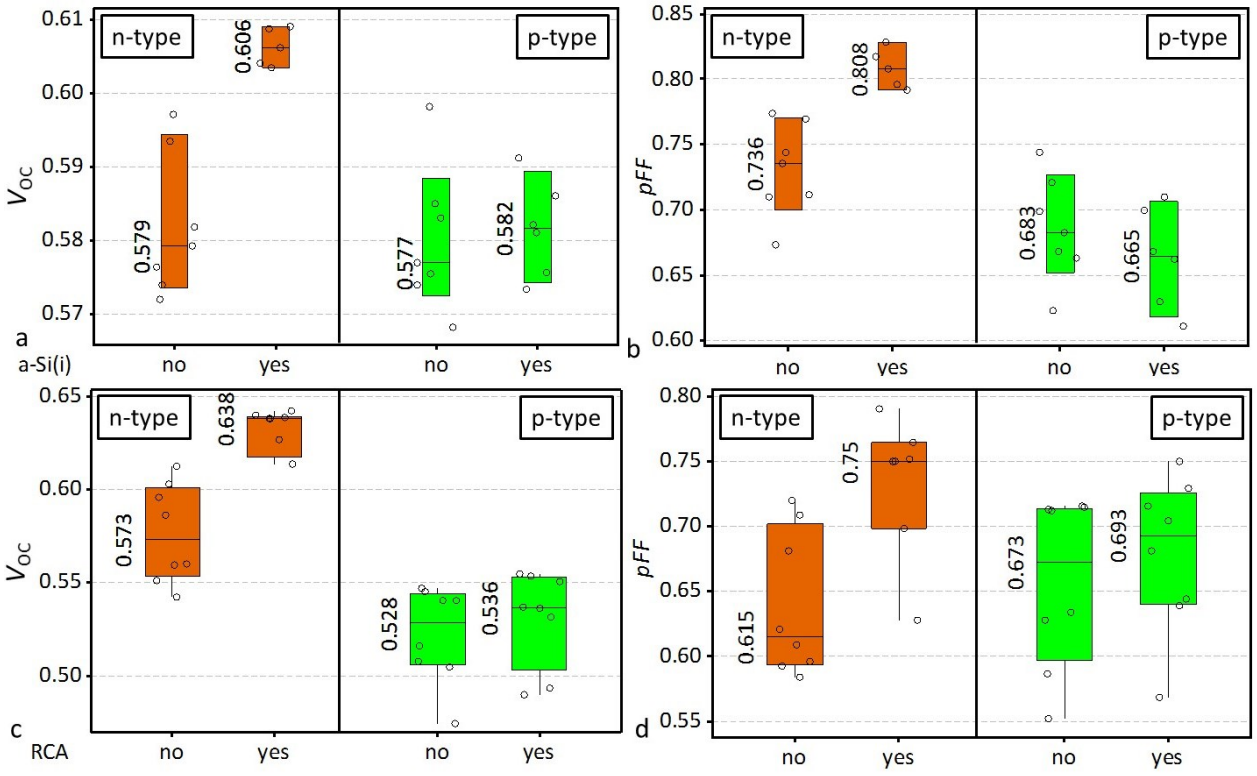


**Figure A-11.** $V_{OC}$ (a and c) and *pFF* (b and d) for p- and n-type quasi cells with and without a-Si(i):H layer (a and b) and with and without RCA cleaning (c and d). Each point represents a quasi cell.

These results appear to indicate that the p-type cell hetero-junction is less sensitive to interface defects, **or** that the standard cleaning and/or a-Si(i) layer do not passivate the surface of p-type LPC-Si cell and therefore leaving them out does not cause a loss. This difference for p-type compared to n-type cells, might be related to the small a-Si/c-Si conduction band offset (0.15 eV) compared to the valence band offset (0.44 eV).

### A.5.2 Prevention of Epitaxial Growth

For good surface passivation it is important that the a-Si(i) grows amorphously and not epitaxially [103]. A very important factor influencing epitaxial growth is the growth rate, as a slow growth rate gives the Si atoms more time to diffuse over the growing surface and find a position matching the underlying c-Si crystal structure, thereby growing epitaxially (e.g. [122]). In order to prevent epitaxial growth, quasi cells were fabricated in experiment 2, for which the 1$^{st}$ nm of the a-Si(i) layer (see Table 5-2, section 5.2.2) was deposited with double the power (60 W), assuming that this would roughly double the deposition rate. The experiment was repeated in quasi cell experiments 3 and 5, where for the latter experiment the power and thickness of the high power a-Si(i) layer was increased to 120-180W and 1-2 nm. For exp. 5 emitter/TCO $\rho_c$ test structures were also fabricated. The first experiment was performed with the 12 nm a-Si(p) (TMB) emitter, and exp. 3 and 5 used a 6 nm a-Si(p) + 30 nm nc-Si(p) (TMB) emitter. The $V_{OC}$, *pFF*, $V_{OC}$·*pFF* and $\rho_c$ of these experiments are shown in Figure A-12

The $V_{OC}$ and *pFF* appear to be increasing by about 20 mV and 2 % by using the high power a-Si(i) layer and the $V_{OC}$·*pFF* increase is approximately identical for all experiments (~20 mV). Similar $V_{OC}$ gains were observed on p-type quasi cells (not shown). It appears to be irrelevant whether the fast a-Si(i) layer is 1 or 2 nm thick and whether the power is 2, 4 or 6 times the normal power. These gains approximately equals the unidentified $V_{OC}$ and *pFF* losses observed in appendix A.4 that were speculated to be due to emitter interface recombination.

It can be seen that the high power a-Si(i) layer results in strongly increased $\rho_c$. This same $\rho_c$ trend was observed on planar wafers and on a-Si(p) ($B_2H_6$) emitters (not shown). Further experiments should determine the $\rho_c$ for the 2x power (60 W) a-Si(i) layer. By increasing the power in smaller steps it might be possible to find an optimum where the $V_{OC}$·*pFF* is increased, but the $\rho_c$ is not (significantly) increased.

The deposition rates for the 1-2 nm thick, 2-6x power layers were estimated with a linear dependence on the power. For increasing power, the deposition rate will become limited by process gas rather than power. Consequently it is very likely that the high power a-Si(i) layers were slightly thinner than the reference a-Si(i) layers. Therefore it is very unlikely that the increased resistance can be explained by an

increased a-Si(i) thickness. Instead, the increasing resistance seems to indicate that some difference in the material properties of the a-Si(i) layer is causing the increased resistance. Possibly the increasing $\rho_c$ is due to the intended decrease in epitaxial growth.

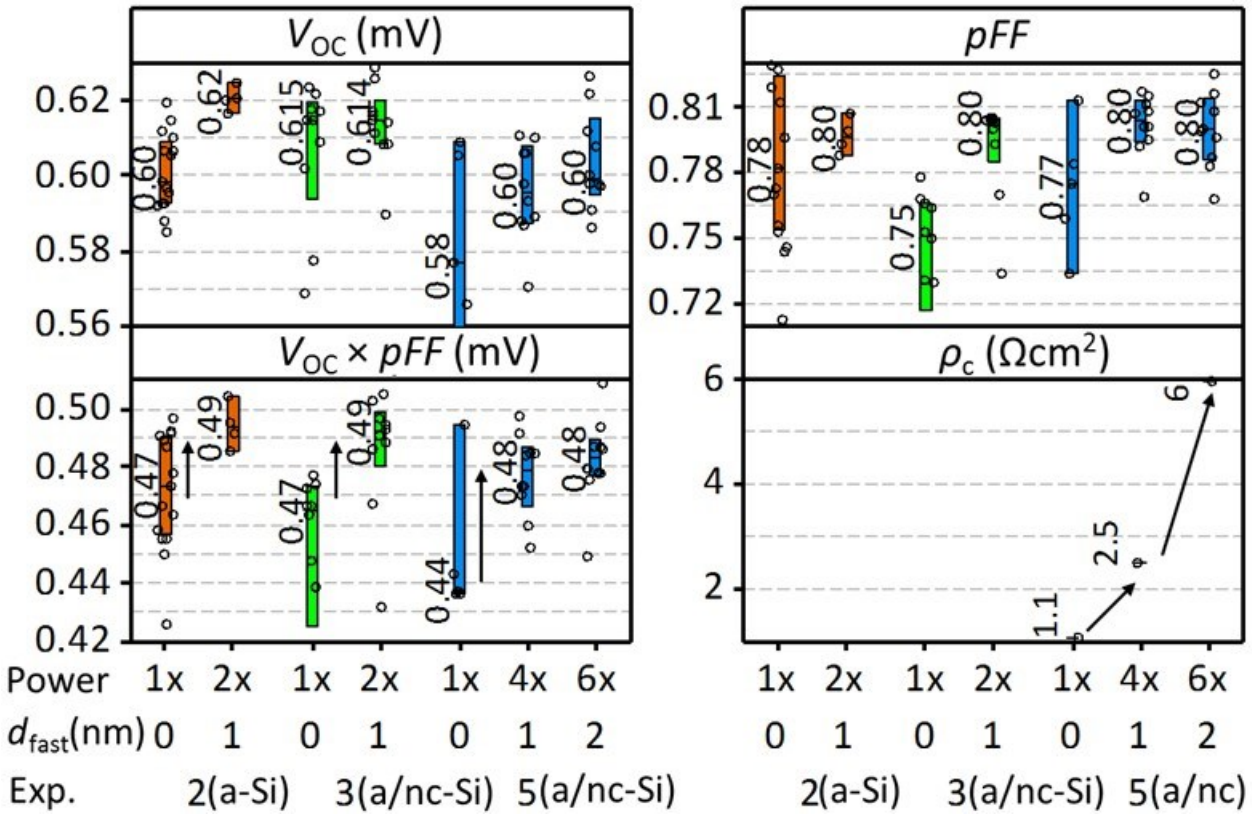


**Figure A-12.** $V_{OC}$, *pFF* and $\rho_c$ results for 3 n-type quasi cell experiments using a 1-2 nm thick initial a-Si(i) layer with 2-6x the normal power. The first experiment used an a-Si(p)(TMB) emitter, while the subsequent experiments used an a-Si(p)/nc-Si(p) (TMB) emitter.

In ref. [123] it is shown, through TEM imaging and modelling, that high efficiency tunnel oxide heterojunction cells can have sufficient pin holes in the $SiO_2$ layer to explain the low resistance of tunnel oxide cells, without affecting the passivation of these cells. It was also shown that a larger pin holes density does reduce the passivation. Hypothetically, something similar could be happening for the a-Si(i) heterojunction cells, but with epitaxial growth regions instead of pin holes.

The 1 nm, 4x power (120 W) a-Si(i) layer was used in both the 12.0 % efficiency point contact LPC-Si cell (section 5.7, experiment 5) and the 13.2 % efficiency HIT IBC LPC-Si cells [115].

## A.6 Shunting in LPC-Si Point Contact Cells

Though the most important reason for shunting in the point contact cells appears to be incomplete etching of the absorber point contact opening, there are also many possible shunts and shunt locations in the point contact device:

- At the c-Si/Ag (absorber) point contacts:
    - due to incomplete etching of the TCO or the emitter
        - due to inhomogeneous or too short etching (section 5.3)
        - perhaps due to inhomogeneous/incomplete opening of the P150W by the inkjet process (Figure A-13).
    - due to misalignment of the laser fired contact, contacting the metal to the TCO below the P150W
- At the isolation scribe,
    - due to incomplete scribing, i.e. some c-Si or TCO remaining in the scribe. This is usually due to cracks or bubbles in the glass, scattering the laser beam. (e.g. Figure 5-17b)
    - perhaps due to a shunt between the c-Si absorber and the TCO
- At cracks in the c-Si, (Figure A-13)
    - perhaps due to cracks through absorber point contact: P150W fills the crack and is too thick for complete removal by the KOH ink. Consequently the TCO and emitter in the crack are not removed, which might results in a shunt after reflow or laser fired contact.
    - perhaps due to an extremely thin emitter within the crack, resulting in a shunt between the TCO and the absorber
- Due to incomplete coverage by the P150W,
    - the P150W is always visibly thinner near the isolation scribe. If the isolation scribe is very deep, the paint flows into the isolation scribe after spin coating to the extent that the TCO is no longer covered (Figure A-13). The laser scribe can become this deep due to a combination of laser damage and too long HF etching. The unprotected TCO and emitter is etched away, but the metal contacts the c-Si, causing a shunt at the TCO/Ag fingers.
    - At (large) pinholes in the P150W which are not closed by the reflow (likely related to dust particles and large $TiO_2$ agglomerates).
- At the metal cut
    - due to incomplete metal removal (too low laser energy or too thick metal (> ~200 nm))
    - perhaps due to too high energy, evaporating the P150W (Figure A-13) and perhaps causing a shunt between the metal and the TCO.

Clearly, there are many possible causes for shunts in the point contact cells and it seems likely that even this list is incomplete. This results in many cells and even series being shunted to a certain degree, often due to multiple different shunts. Thermography can show the approximate location of the shunt, allowing

for differentiation between the isolation scribes and the inner region, but is too inaccurate for differentiation between e.g. the absorber point contact and the metal cut. However, even without knowing the exact cause, it is possible to observe how certain emitters and TCO's appear to result in more or more serious shunts than other emitters and TCO's and develop hypothesis about the causes.

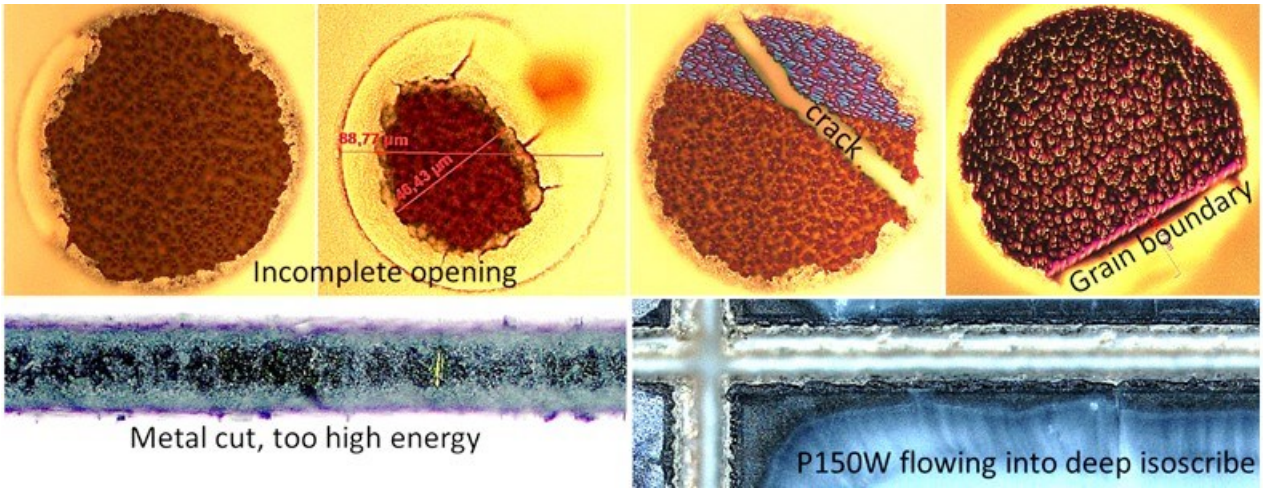


**Figure A-13.** Examples of possible shunt causes: incomplete opening of the absorber contact openings due to ink problem, crack or grain boundary, damage of the TCO due to too high metal cut energy and P150W flowing into the isoscribe, leaving the c-Si next to the isoscribe unprotected.

## A.7 Frontside vs Backside Texturing

In section 4.1.6 it was found that backside pyramid texturing results in better light trapping than Lambertian light trapping. This is somewhat better than the light trapping found for frontside and double side pyramid texturing found by ray tracing in ref. [75]. In order to understand this, ray tracing simulation were performed for a thin silicon wafer with planar and/or pyramid textured interfaces. Figure A-14 shows the simulated $\eta_{LT}$ (using the PV Lighthouse ray tracer) and calculated $A_{Si}$ (for the indicated $f_{esc}$), for a 10 µm c-Si absorber with a 75 nm $SiN_x$ antireflection layer at the front (no glass) and a 100 nm $SiO_2$ + detached mirror reflector at the back. For two planar interfaces the light is reflected back by the detached reflector and some light is reflected back at the front, resulting in a total absorption in the c-Si absorber that can be fitted by 2.2 passes through a 10 µm c-Si absorber. Texturing the frontside of the wafer increases $\eta_{LT}$ (light blue), but not as much as texturing the backside (purple). It can be seen that texturing the frontside of a backside textured solar cell, actually reduces light trapping. This can be explained by the textured interface providing an escape cones for each facet of the pyramid.

This simple simulation shows that backside texturing provides much more effective light trapping than backside texturing. This can be considered an advantage for illumination through the glass. Most SHJ wafer cells are only frontside textured, but they do not need very good light trapping because of their absorber

thickness. Frontside texturing does usually result in higher $J_{SC}$, as it strongly reduces reflection. The ARF, which does not significantly affect light trapping because it doesn't affect the c-Si interface, might offer a means of combining the excellent light trapping of backside-only textured c-Si with the good light trapping of front-side texturing.

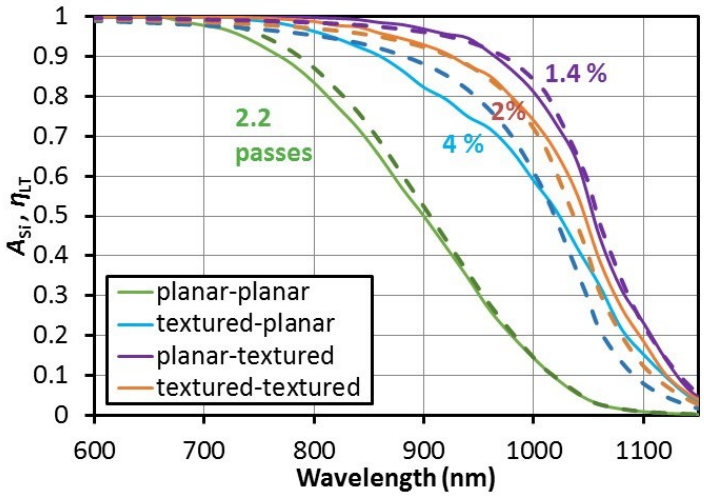


**Figure A-14.** The simulated $\eta_{LT}$ (using the PV Lighthouse ray tracer) and calculated $A_{Si}$ and corresponding $f_{esc}$ for a 10 µm c-Si absorber with a 75 nm $SiN_x$ antireflection layer at the front (no glass) and a 100 nm $SiO_2$ + detached mirror reflector at the back, for planar and pyramid textured interfaces

## A.8 Light Soaking

Light soaking experiments were performed (by summer student Carmine Pellegrino) for 72 hours (at 50 °C) on various point contact cells from different experiments. The $R_s$ and $J_{SC}$ deviation before/after light soaking is shown in Figure A-15. The $R_s$ deviation in fig. a shows that for most of the n-type samples the $R_s$ increases after light soaking, while for the p-type samples it remains unaltered.

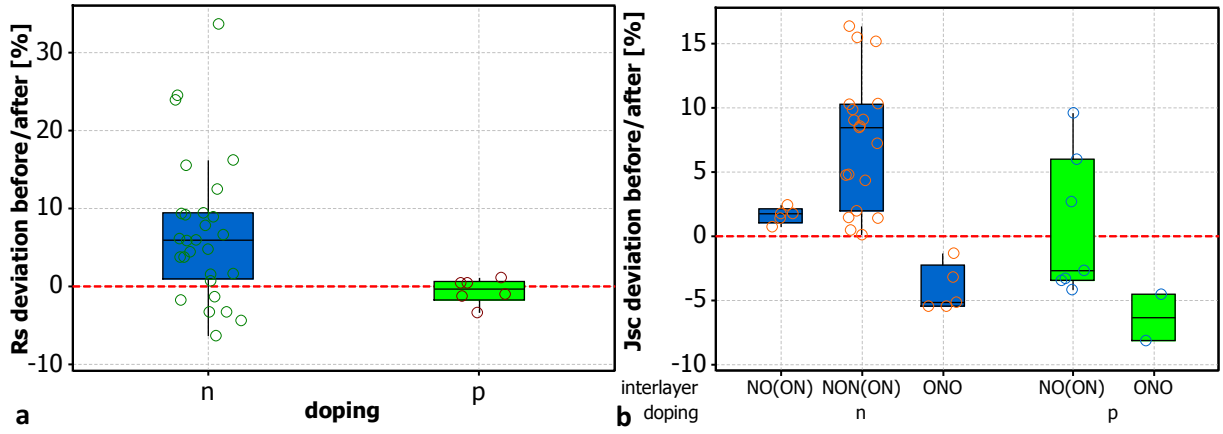


**Figure A-15.** Relative $R_s$ (a) and $J_{SC}$ (b) deviation before/after 72h light soaking for n and p-type point contact cells, with different interlayer stacks.

The $J_{SC}$ deviation in fig. b shows that the $J_{SC}$ of the SiON based interlayers, especially the NON(ON) interlayer stack, is increasing after light soaking. The same $J_{SC}$ gain was observed for quasi cells (not shown). The *IQE* measurements before and after light soaking could be fitted by a *S*-limited $\eta_c$, as for all point contact cells with SiON based interlayers (section 5.8.1), i.e. it was found that the $J_{SC}$ gain can be fitted very well with a decrease of *S* (not shown).

The $J_{SC}$ of the cells with ONO interlayers appears to be decreasing, but, for some unknown reason, the corresponding *EQE* measurements did not decrease. Comparison of the p- and n-type samples indicates that there is also a JSC loss after LID for the p-type samples, separate from the gain for the NON(ON) and loss for the ONO interlayers.

## A.9 Laser Diffused Homojunction Emitters

Several years ago, the first experiments were made at HZB with laser diffused homojunction emitters on p-type LPC-Si, using spin coated P508 as dopant source and the line-shaped LIMO cw laser (also used for LPC) to diffuse the dopants into the absorber [124]. During this thesis work (together with Mehmet Karaman, a PhD student from Turkey [125]) a new, laser diffused homojunction emitter experiment was performed, using 8.5 µm thick, ~$4 \cdot 10^{16}$ $cm^{-3}$ doped p-type and ~$10^{17}$ $cm^{-3}$ doped n-type cells with NON(ON) interlayers, testing the influence of hydrogen passivation and emitter depth. This was partially a repetition of the previous experiments, with the addition of using n-type samples and analyzing the $J_{SC}$.

For the dopant source, P508 (n-type emitters) or B153 (p-type emitters) was spin coated on the samples, and annealed at 200°C for 5 min to form a phosphor/boro silicate glass layer. In [124] two promising laser processes were identified: 1 mm/s with 11.7 A and 5 mm/s with 15 A, and these were also used in this new experiment. Figure A-16 shows the P (a) and B (b) dopant concentration profiles for both processes, measured by SIMS. It can be seen that the 1 mm/s laser process results in a relatively shallow emitter with a depth of approximately 300 ± 100 nm, while the 5 mm/s process results in a deep emitter with a depth more than 1 µm. The new measurement shows approximately the same profile. For the n-type samples in figure b, there is also the difference between the deep and shallow emitter, but at a different order of magnitude: the shallow emitter has a depth of only ~100 nm and the “deep” emitter has a depth of ~150 nm.

Hydrogen plasma passivation (HPP) was performed at 400°C for 30 min. Kapton dots were used to define the cell area and the emitter outside the cell area was etched away with poly-Si etch for 30-180 s, depending on the emitter depth. A Suns-$V_{OC}$ measurements were made before and after metallization of the absorber contact with a 200 nm Al layer and subsequent annealing at 200°C. Figure A-17 shows the

$V_{OC}$ values of these p- and n-type quasi cells, with deep or shallow emitter, with and without HPP, before and after metallization.

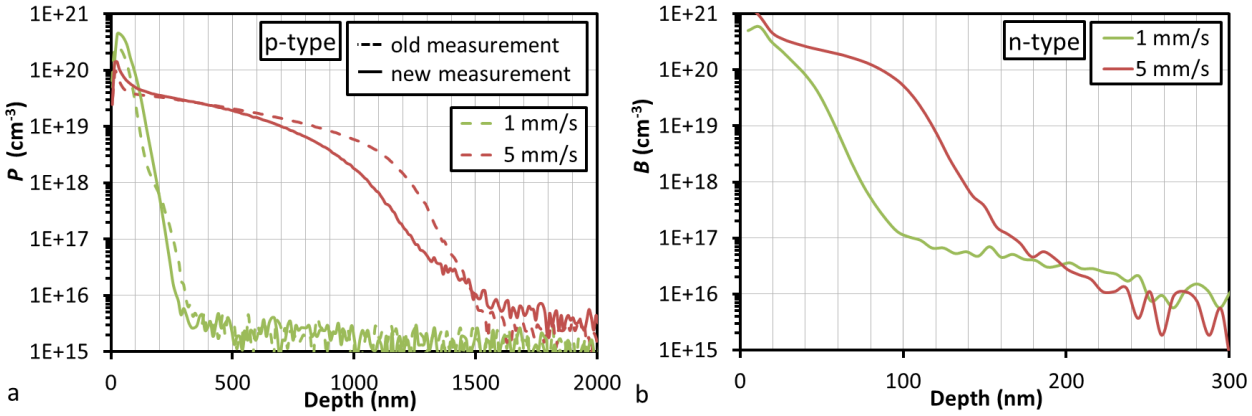


**Figure A-16.** *P* (a) and *B* (b) concentration depth profiles, measured by SIMS for the old experiment (SIMS was calibrated, dashed lines) and the new experiment (SIMS was not calibrated, solid lines).

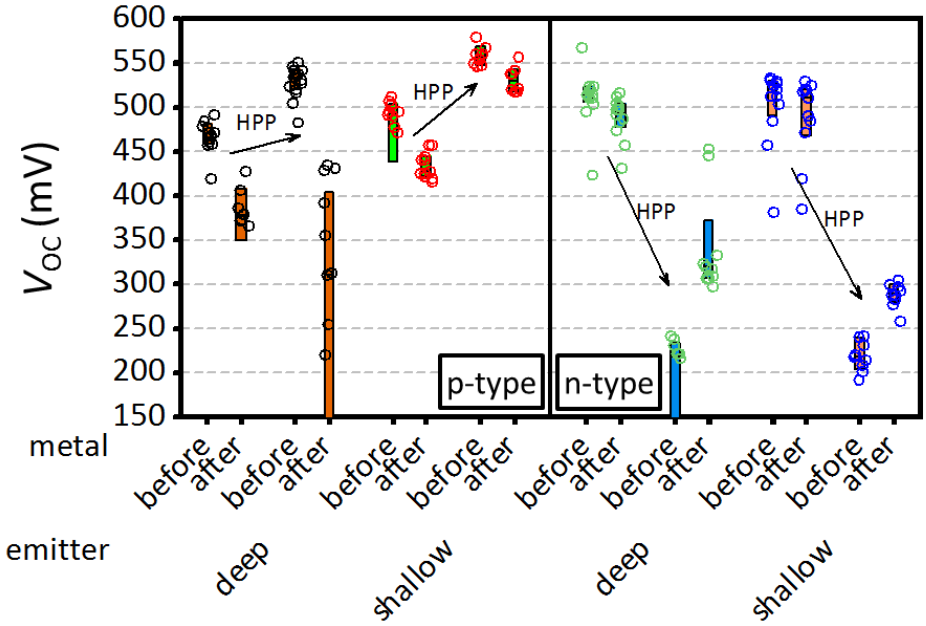


**Figure A-17.** The (Suns-)$V_{OC}$ values for p-type (left) and n-type (right) quasi cells, with deep or shallow emitter, with and without HPP, before and after metallization.

For p-type samples the shallow emitter results in higher $V_{OC}$ and HPP results in a $V_{OC}$ gain of about 60 mV. For the n-type samples, the emitter depth makes no significant difference on the $V_{OC}$ and HPP results in a $V_{OC}$ loss of about 200-300 mV. For the p-type cells, especially those with a deep emitter, the metallization results in a large $V_{OC}$ loss, while for the n-type cells, especially those with a shallow emitter, the metallization has no effect.

The $V_{OC}$ reduction due to metallization can be explained by non-homogeneous etching causing shunts: the LBIC measurements in Figure A-18 show strong collection in the metal gap outside the cell area, indicating the emitter was not removed there. The solution will probably be to etch the samples even longer. As the emitter consists of c-Si, etching below the Kapton should not be a problem, even after long etching times.

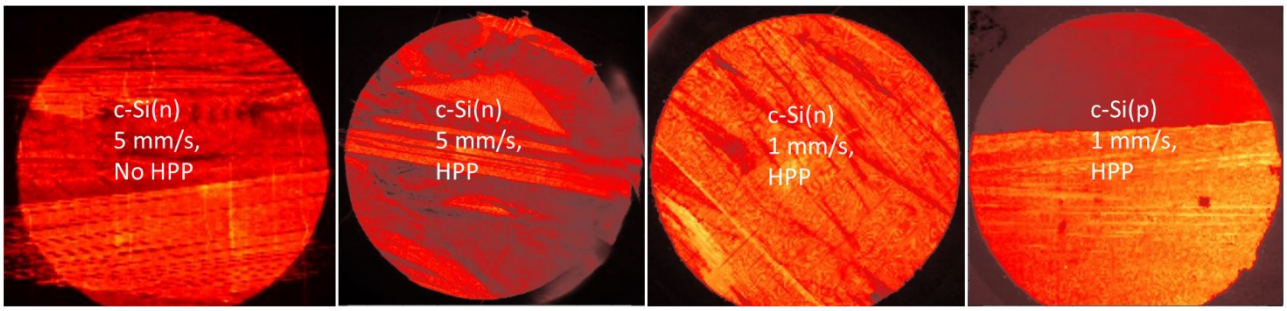


**Figure A-18.** LBIC measurements of quasi cells with laser process and HPP indicated in the figure.

Figure A-19a-d shows substrate and superstrate *EQE* measurements of the best p-type and n-type metallized quasi-cells, with deep (red) or shallow (green) emitter, with (solid) and without (dashed) HPP. For both p- and n-type samples, the deep emitter results in a lower substrate *EQE* (fig. a and b) for the lower wavelength range than the shallow emitter. For the p-type sample, the long wavelength superstrate *EQE* (fig. c) is also lower for the deep emitter. Both effects can be explained by parasitic absorption in the emitter. For the n-type emitter, the short wavelength superstrate *EQE* (fig. d) is reduced by the deep emitter, indicating an increased recombination.

The HPP results in a lower (short wavelength) substrate *EQE* for both doping types. This can be explained by increased emitter recombination. The HPP also results in a strong increase of the superstrate *EQE* and (long wavelength) substrate *EQE*, indicating that the HPP is passivating the absorber as expected.

**Conclusions**

It was observed that the same laser process resulted in much shallower emitters for the n-type than for the p-type samples. The diffusion coefficients of B and P in Si are very similar e.g. [126], so this probably cannot explain the difference. Perhaps the higher doping and corresponding (~10x) higher conductivity of the n-type samples can explain the difference. These shallower emitters were incompatible with the subsequent HPP process, resulting in a ~200 mV $V_{OC}$ loss. The *EQE* measurements showed that hydrogen passivation strongly reduces recombination in the LPC-Si absorber, but also damages the homo-emitter, reducing collection from the emitter.

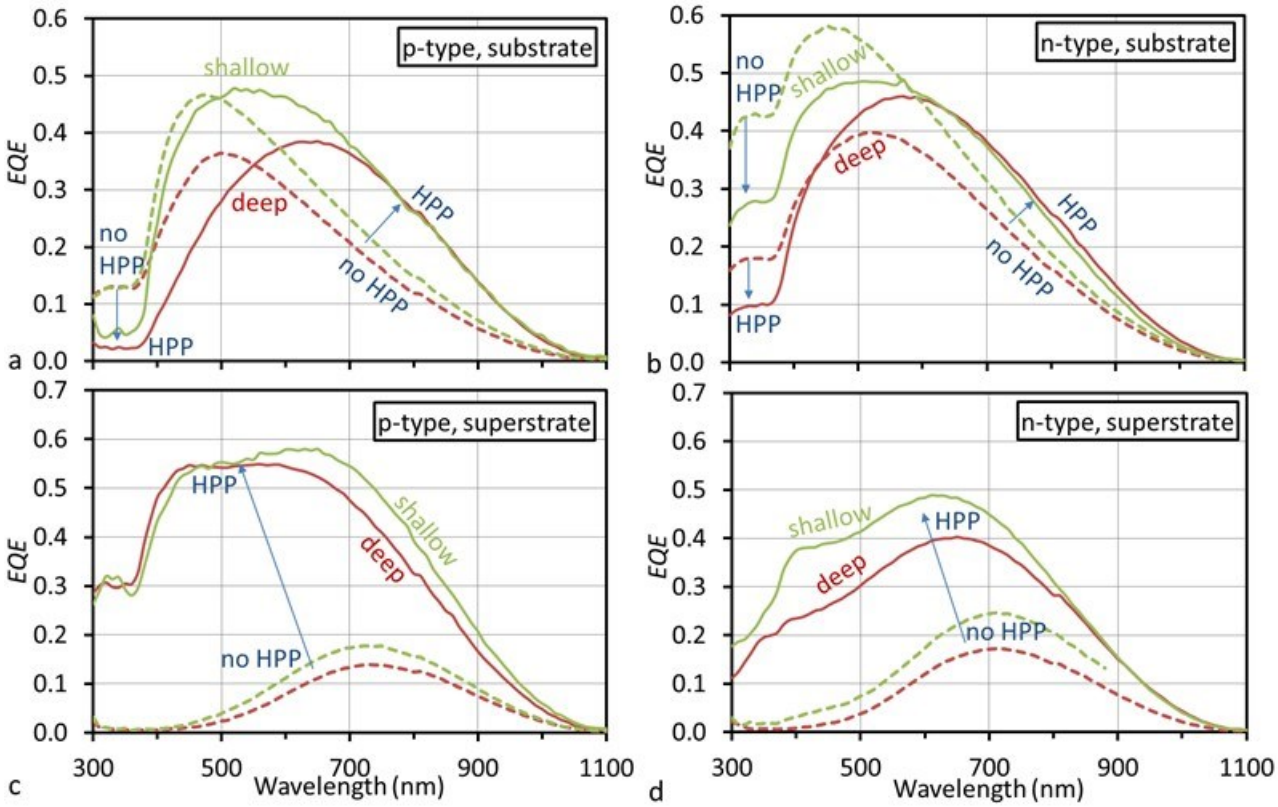


**Figure A-19.** Substrate (a and b) and superstrate (c and d) *EQE* measurements of the best p- (a and c) and n-type (b and d) metallized quasi-cells, with deep (red) or shallow (green) emitter, with (solid) and without (dashed) hydrogen plasma passivation (HPP).

For homo-emitter cells, HPP cannot be performed before emitter formation, as the high temperature emitter diffusion process will cause hydrogen effusion. Due to non-uniform etching it will also be extremely difficult to remove the HPP damage by etching without etching away the entire emitter at some positions. Instead it will probably be better to use the hydrogen passivation technique used for homo-emitter wafers: depositing an $SiN_x$:H layer and annealing the sample, driving the hydrogen into the silicon [127]. This has the added advantage that the positive fixed charge $SiN_x$ layer can passivate the (n-type) emitter. For n-type cells, the p-type emitter will have to be passivated by $Al_2O_3$.

By screen printing the dopant sources [128] and doping the interlayers, it might be possible to combine the backside emitter and local BSF diffusion (for the absorber point contacts) with a front surface field (FSF) diffusion and a phosphorus defect gettering process in a single laser diffusion process. The screen printing can be aligned to the reference crosses, such that they are aligned with the subsequent absorber point contact openings. The homo-emitter (without TCO) would also allow for an HF dip before metallization. Together with the $p^+$ or $n^+$ laser doping, this would very likely avoid the need for laser fired contacts. Such a process would be much cheaper and potentially easier than the heterojunction process and might even result in higher efficiencies. A possible problem with the homo-emitter is that texturing

might be a problem. Assuming a shallow, passivated emitter, parasitic absorption losses will likely be less than the parasitic absorption losses in the TCO.

## A.10 LPC-Si production on a Glass Float Line

During the beginning of this thesis, working at Masdar PV, the idea was developed to fabricate LPC-Si on a glass float line and a patent was filed [129]. The idea is to deposit the interlayers and Si precursor on the glass float at 1100-800°C, using atmospheric pressure CVD (APCVD) and trichlorsilane (TCS) as process gas [130]. At these high temperatures, the APCVD can achieve very high deposition rates (> 1 µm/min). TCS is produced during an early phase in the Siemens process for making polysilicon, making it a relatively cheap source of silicon. APCVD is presumably also relatively cheap as it operates at atmospheric pressure. Most of the process line and heat for the process is basically for free, as it is already needed to make the glass substrate. Therefore, this process should result in very inexpensive LPC-Si. The cells and modules should probably be processed on a different line. Aside from the low precursor costs, other advantages of this method likely include:

- the glass properties can more easily be optimized to fit the LPC-Si
- the laser crystallization process can also take place on the glass float (at 700-1000 °C)
- it might be easier to texture the glass on the float line

The following challenges were identified:

- The “minimum” size of a glass float line, will make it hard to set-up a pilot line.
- The glass float probably has to move at a certain velocity
- It might be tricky to prevent (metal) contamination

Together with the homo-emitter process suggested in appendix A.9, this could result in an extremely low cost, very low capex LPC-Si solar module process.

# B List of Publications

## Peer reviewed Journal articles

### As first author

1. [67] T. Frijnts, S. Kühnapfel, S. Ring, O. Gabriel, S. Calnan, J. Haschke, B. Stannowski, B. Rech, R. Schlatmann, "Analysis of photo-current potentials and losses in thin film crystalline silicon solar cells", *Sol. Energy Mater. Sol. Cells*, vol. 143, pp. 457–466, Dec. 2015
    - Section 4.1: I wrote the paper, made the cells, did the measurements, analysed the data, and developed/implemented the methods.
2. [69] T. Frijnts, N. Preissler, S. Gall, S. Neubert, B. Rech, R. Schlatmann, "Influence of the Frontside Charge Inversion Layer on the Minority Carrier Collection in Backside Contacted Liquid Phase Crystallized Silicon on Glass Solar Cells", *Sol. RRL*, vol. 1, no. 9, p. 1700100, Sep. 2017.
    - Preprint version in section 4.2: I wrote the paper, did the measurements, analysed the data and developed/implemented most of the methods (not: extended SRH model and AFORS-HET simulation of interface, EQE (600 nm) vs. bias light measurement)

### As co-author

3. [52] O. Gabriel, T. Frijnts, S. Calnan, S. Ring, S. Kirner, A. Opitz, I. Rothert, H. Rhein, M. Zelt, K. Bhatti, J.-H. Zollondz, A. Heidelberg, J. Haschke, D. Amkreutz, S. Gall, F. Friedrich, B. Stannowski, B. Rech, R. Schlatmann, "PECVD Intermediate and Absorber Layers Applied in Liquid-Phase Crystallized Silicon Solar Cells on Glass Substrates," IEEE J. Photovolt., vol. 4, no. 6, pp. 1343–1348, Nov. 2014.
    - Contribution: many discussions and ideas regarding material development, fabrication and characterization of FrontERA cells on PECVD material (section 3.3.1)
4. [21] J. Haschke, D. Amkreutz, T. Frijnts, S. Kühnapfel, T. Hänel, and B. Rech, "Influence of Barrier and Doping Type on the Open-Circuit Voltage of Liquid Phase-Crystallized Silicon Thin-Film Solar Cells on Glass," *IEEE J. Photovolt.*, vol. PP, no. 99, pp. 1–5, 2015.
    - Contribution: fabricated p-type FrontERA doping series (section 3.3.2). Proposed and made the LBIC measurement (section 3.3.3)
5. [86] O. Gabriel, T. Frijnts, N. Preissler, D. Amkreutz, S. Calnan, S. Ring, B. Stannowski, B. Rech, R. Schlatmann, "Crystalline silicon on glass—interface passivation and absorber material quality," *Prog. Photovolt. Res. Appl.*, vol. 24, no. 12, pp. 1499–1512, Nov. 2015.

- Contribution: Hall mobility measurements (appendix A.3.1) and *IQE* analysis of the cells to determine *L* & *S* (appendix A.4).

6. [131] S. Kirner, M. Hartig, L. Mazzarella, L. Korte, T. Frijnts, H. Scherg-Kurmes, S. Ring, B. Stannowski, B. Rech, R. Schlatmann, "The Influence of ITO Dopant Density on J-V Characteristics of Silicon Heterojunction Solar Cells: Experiments and Simulations," *Energy Procedia*, vol. 77, pp. 725–732, Aug. 2015.
    - Contribution: discussion regarding the interpretation of the results.
7. [28] P. Sonntag, J. Haschke, S. Kühnapfel, T. Frijnts, D. Amkreutz, and B. Rech, "Interdigitated back-contact heterojunction solar cell concept for liquid phase crystallized thin-film silicon on glass," *Prog. Photovolt. Res. Appl.*, vol. 24, no. 5, pp. 716–724, Mai 2016.
    - Contribution: proposed and made LBIC measurement, helped with analysis.
8. [65] P. Sonntag M. Bokalič, M. Filipič, T. Frijnts, D. Amkreutz, M. Topič, B. Rech, "Analysis of Local Minority Carrier Diffusion Lengths in Liquid-Phase Crystallized Silicon Thin-Film Solar Cells," *IEEE J. Photovolt.*, vol. PP, no. 99, pp. 1–5, 2016. (also: presentation and conference proceeding 43th IEEE PVSC)
    - Contribution: helped develop part of the analysis method ($L_{eff}$ from LBIC scan)

## Conference contributions

1. [61] T. Frijnts, O. Gabriel, J. Haschke, S. Ring, S. Calnan, H. Rhein, D. Amkreutz, B. Stannowski, J.-H. Zollondz, S. Gall, A. Heidelberg, B. Rech, R. Schlatmann, "Single-side-contacted HIT Cells from Liquid Phase Crystallized Silicon on Glass using PECVD Precursors," presented at the EUPVSEC, Amsterdam, 2014 (poster presentation)
    - Contribution: made abstract and poster. E-beam vs PECVD comparison (section 3.3.1)
2. T. Frijnts, N. Preissler, S. Gall, B. Rech, R. Schlatmann, "Minority Carrier Collection Through the Front Side Inversion Layer in Liquid Phase Crystallized Silicon", presented at the EMRS spring meeting, Lille, 2015 (oral presentation)
    - Contribution: made the abstract and presentation and presented the research. I did the measurements, analysed the data and developed/implemented most of the methods.
    - Was later with some additions turned into a paper (see above) (Section 4.2)
3. T. Frijnts, S. Kühnapfel, H. Rhein, S. Gall, C. Schultz, B. Rech, R. Schlatmann, „Laser Processing of Solar Cells on Laser Crystalized Silicon", Lasertech 2016, Berlin (invited presentation).

- Contribution: made and presented the presentation (overview of the various laser processes)

4. [110] T. Frijnts, S. Gall , H. Rhein, P. Sonntag, L. Mazzarella, S. Kirner, C. Matarazzo, B. Rech, R. Schlatmann, “Backside Contacted Solar Cells with HTJ Emitters and Laser Fired Absorber Contacts for Crystalline Silicon on Glass,” in *Proceedings of the 43th IEEE PVSC*, Portland, 2016. (poster presentation)
    - Contribution: made the proceeding paper and poster, made the cells and test structures, did the measurements and analysed the data.
    - Contains rectangular resistance model from Appendix A.2.2
    - Contains most of the emitter/TCO $\rho_c$ measurements and an early version of the cell $R_s$ analysis (section 5.5)

# Acknowledgement

I would like to thank everybody who have made this thesis possible:

- Prof. Dr. Bernd Rech for his supervision and guidance.
- Prof. Dr. Rutger Schlatmann for giving me the opportunity to be part of PVcomB and continue my thesis after Masdar PV withdrew from production (and the financing of my thesis). Also many thanks for the repeated proofreading of my thesis.
- Prof. Dr. Arno Smets for being co-examiner and Prof. Dr. Bernd Szyszka for being chairman of the thesis evaluation committee.
- Dr. Bernd Stannowski for being my supervisor during the first part of my thesis work and for telling me to put the reflector comparison in some context of the other $J_{SC}$ losses.
- Dr. Stefan Gall for being my supervisor during the second part of the thesis and for his many insights, ideas, support and detailed feed-back.
- Dr. Hendrik Zollondz and Dr. Andreas Heidelberg from Masdar PV for making this thesis work possible, for their support during the first part of the thesis and for convincing Masdar PV to attempt commercializing the LPC-Si technology.
- The “PECVD Deposition for LPC-Si” team: Dr. Onno Gabriel, Dr. Bernd Stannowski, Dr. Sven Ring, Dr. Sonya Calnan, Dr. Hendrik Zollondz, Dr. Andreas Heidelberg, Andreas Opitz, Holger Rhein, Matthias Zelt, Khalid Bhatti, Inga Rothert, Dr. Simon Kirner, Natalie Preissler, Prof. Dr. Rutger Schlatmann and many others at PVcomB.
- My LPC-Si colleagues Paul Sonntag, Natalie Preissler, Dr. Sven Kühnapfel, Dr. Jan Haschke and Dr. Daniel Amkreutz for the many helpful discussions and their help with many experiments.
- Dr. Jan Haschke for developing (and instructing me in) the FrontERA process.
- Natalie Preissler for implementing the extended SRH model and AFORS-HET interlayer simulation.
- Dr. Moshe Weizman, Holger Rhein, Dr. Stefan Gall and Mathias Nittel for developing the point contact device and process up to the point where I took over and for instructing me.
- Dr. Sven Kühnapfel for our joint FrontERA and point contact experiments and for continuing the point contact development after I started writing my thesis.
- Dr. Sebastian Neubert for the *EQE* vs. bias light measurements.
- Costantino Matarazzo for developing the rectangular point contact resistance model.
- Dr. Michael Vetter from Masdar PV for the many helpful discussions.

- The students that helped with my experiments and analysis: Ivona Kafedjiska, Moritz Künzler, Carmine Pellegrino, Zoltan Müller-Karpe.
- Prof. Dr. Heinrich Christoph Neitzert for the cooperation on the proton degradation experiments and for sending over such great students.
- Mehmet Karaman for our joint experiments with laser diffused homojunction emitters.
- Dr. Luana Mazzarella, Dr. Simon Kirner, Matthias Zelt, Erhard "Conny" Conrad, Dr. Anna Morales and Andreas Opitz for their help with the emitter depositions (and development).
- Manuel Hartig, Iris Dorbrant, Martin Muske and many others for their help with many depositions.
- Tobi(as) Hänel and Karo(lina) Mack for their help and for keeping the analysis equipment at PVcomB in such excellent shape.
- The many other people at HZB that are keeping everything working smoothly.
- Stefan Körner for the helpful discussions and measurement data on different TCO's.
- Carola Klimm for the SEM cross-section measurements.
- Dr. Jonathon Dore for the helpful discussions and our joint FrontERA experiment.
- The people at PV Lighthouse, and especially Dr. Keith McIntosh, for their wonderful, amazing website, without which a significant part of this thesis would have been **much** more difficult to realize.
- Dr. Bart Pieters for Sourcefield (including a Matlab routine just for me) and the helpful discussions on point contact resistance.
- Dr. Paul Basore for discussions on PC2D
- Dr. Ron Sinton for discussions on my adapted model for deriving $L_{eff}$ from $V_{OC}$.
- This work was supported in part by the German Federal Ministry of Education and Research (BMBF), by the German Federal Ministry of Environment (BMU), and the state government of Berlin (SENBWF) in the framework of the program "Spitzenforschung und Innovation in den Neuen Landern" under Grant 03IS2151 and the "DEMO14" project under Grant 0325237
- This work was partly financed by the European Commision under Project CHEETAH (Grant no. 609788).
- The organizers and workshop leaders of the PhD retreats.
- All the people I forgot to mention.
- The many people at HZB that were not just colleagues, but friends.

- Last but not least: my wife Katharina and my daughters Anna and Fleur for their support and patience, especially during the first year when I was travelling back and forth between Arnstadt and Berlin and during the last half year when I was usually home late.

# Bibliography


[1] "NOAA National Centers for Environmental Information, State of the Climate: Global Analysis for September 2016, published online October 2016." [Online]. Available: https://www.ncdc.noaa.gov/sotc/global/201609. [Accessed: 17-Nov-2016].

[2] "Global Temperatures - Climate Action Tracker." [Online]. Available: http://climateactiontracker.org/global.html. [Accessed: 22-Oct-2016].

[3] D. B. Needleman, J. R. Poindexter, R. C. Kurchin, I. Marius Peters, G. Wilson, and T. Buonassisi, "Economically sustainable scaling of photovoltaics to meet climate targets," *Energy Env. Sci*, vol. 9, no. 6, pp. 2122–2129, 2016.

[4] "Key world energy statistics," IEA, 2016.

[5] "IEA PVPS report - A Snapshot of Global PV - 1992-2014."

[6] B. Stannowski *et al.*, "Achievements and challenges in thin film silicon module production," *Sol. Energy Mater. Sol. Cells*, vol. 119, pp. 196–203, Dec. 2013.

[7] M. D. Archer and M. A. Green, *Clean Electricity from Photovoltaics, p. 192*. World Scientific, 2014.

[8] S. Philipps and W. Warmuth, "©Fraunhofer ISE: Photovoltaics Report, updated: 20 October 2016."

[9] C. W. Lan *et al.*, "The emergence of high-performance multi-crystalline silicon in photovoltaics," *J. Cryst. Growth*.

[10] H. C. Sio, S. P. Phang, H. T. Nguyen, D. Yan, T. Trupke, and D. Macdonald, "Comparison of Recombination Activity of Grain Boundaries in Various Multicrystalline Silicon Materials," *Conf. Proc. 31st EU PVSEC*, 2015.

[11] W. Deng *et al.*, "Development of High-efficiency Industrial p-type Multi-crystalline PERC Solar Cells with Efficiency Greater Than 21%," *Energy Procedia*, vol. 92, pp. 721–729, Aug. 2016.

[12] M. A. Green *et al.*, "Crystalline silicon on glass (CSG) thin-film solar cell modules," *Sol. Energy*, vol. 77, no. 6, pp. 857–863, Dec. 2004.

[13] P. A. Basore, "Pilot production of thin-film crystalline silicon on glass modules," in *Photovoltaic Specialists Conference, 2002. Conference Record of the Twenty-Ninth IEEE*, 2002, pp. 49–52.

[14] S. Varlamov *et al.*, "Polycrystalline silicon on glass thin-film solar cells: A transition from solid-phase to liquid-phase crystallised silicon," *Sol. Energy Mater. Sol. Cells*, vol. 119, pp. 246–255, Dec. 2013.

[15] T. Matsuyama *et al.*, "High-quality polycrystalline silicon thin film prepared by a solid phase crystallization method," *J. Non-Cryst. Solids*, vol. 198, pp. 940–944, May 1996.

[16] M. Keevers, T.L. Young, U. Schubert, and M.A. Green, "10% Efficient CSG minimodules," in *Proceedings of the 22nd EUPVSEC*, 2007, p. 1783.

[17] Z. Shi, "Recrystallisation of Semiconductor Material," WO0122500 (A1), 29-Mar-2001.

[18] F. Falk and G. Andrä, "Laser crystallization — a way to produce crystalline silicon films on glass or on polymer substrates," *J. Cryst. Growth*, vol. 287, no. 2, pp. 397–401, Jan. 2006.

[19] D. Amkreutz, J. Müller, M. Schmidt, T. Hänel, and T. F. Schulze, "Electron-beam crystallized large grained silicon solar cell on glass substrate," *Prog. Photovolt. Res. Appl.*, vol. 19, no. 8, pp. 937–945, Dec. 2011.

[20] J. Dore, D. Ong, S. Varlamov, R. Egan, and M. A. Green, "Progress in Laser-Crystallized Thin-Film Polycrystalline Silicon Solar Cells: Intermediate Layers, Light Trapping, and Metallization," *IEEE J. Photovolt.*, vol. 4, no. 1, pp. 33–39, Jan. 2014.

[21] J. Haschke, D. Amkreutz, T. Frijnts, S. Kuhnapfel, T. Hanel, and B. Rech, "Influence of Barrier and Doping Type on the Open-Circuit Voltage of Liquid Phase-Crystallized Silicon Thin-Film Solar Cells on Glass," *IEEE J. Photovolt.*, vol. 5, no. 4, pp. 1–5, Jul. 2015.

[22] D. Amkreutz, J. Haschke, S. Kuhnapfel, P. Sonntag, and B. Rech, “Silicon Thin-Film Solar Cells on Glass With Open-Circuit Voltages Above 620 mV Formed by Liquid-Phase Crystallization,” *IEEE J. Photovolt.*, vol. 4, no. 6, pp. 1496–1501, Nov. 2014.
[23] S. Steffens *et al.*, “Impact of dislocations and dangling bond defects on the electrical performance of crystalline silicon thin films,” *Appl. Phys. Lett.*, vol. 105, no. 2, p. 022108, Jul. 2014.
[24] S. Kühnapfel *et al.*, “Lifetime analysis of laser crystallized silicon films on glass,” *J. Appl. Phys.*, vol. 118, no. 5, p. 055304, Aug. 2015.
[25] J. Haschke, D. Amkreutz, L. Korte, F. Ruske, and B. Rech, “Towards wafer quality crystalline silicon thin-film solar cells on glass,” *Sol. Energy Mater. Sol. Cells*, vol. 128, pp. 190–197, Sep. 2014.
[26] M. A. Green, K. Emery, Y. Hishikawa, W. Warta, and E. D. Dunlop, “Solar cell efficiency tables (version 48),” *Prog. Photovolt. Res. Appl.*, vol. 24, no. 7, pp. 905–913, Jul. 2016.
[27] “World’s Highest Conversion Efficiency of 26.33% Achieved in a Crystalline Silicon Solar Cell,” *NEDO/Kaneka*, 14-Sep-2016.
[28] P. Sonntag, J. Haschke, S. Kühnapfel, T. Frijnts, D. Amkreutz, and B. Rech, “Interdigitated back-contact heterojunction solar cell concept for liquid phase crystallized thin-film silicon on glass,” *Prog. Photovolt. Res. Appl.*, vol. 24, no. 5, pp. 716–724, May 2016.
[29] M. Weizman *et al.*, “Efficiency and stability enhancement of laser-crystallized polycrystalline silicon thin-film solar cells by laser firing of the absorber contacts,” *Sol. Energy Mater. Sol. Cells*, vol. 120, Part B, pp. 521–525, Jan. 2014.
[30] M. Weizman *et al.*, “Rear-side All-by-Laser Point-contact Scheme for liquid-phase-crystallized silicon on glass solar cells,” *Sol. Energy Mater. Sol. Cells*, vol. 137, pp. 280–286, Jun. 2015.
[31] V. Preidel, D. Amkreutz, J. Haschke, M. Wollgarten, B. Rech, and C. Becker, “Balance of optical, structural, and electrical properties of textured liquid phase crystallized Si solar cells,” *J. Appl. Phys.*, vol. 117, no. 22, p. 225306, Jun. 2015.
[32] C. Ulbrich, A. Gerber, K. Hermans, A. Lambertz, and U. Rau, “Analysis of short circuit current gains by an anti-reflective textured cover on silicon thin film solar cells: Short circuit current gains by a texture coating on silicon thin film solar cells,” *Prog. Photovolt. Res. Appl.*, vol. 21, no. 8, pp. 1672–1681, Dec. 2013.
[33] R. A. Sinton and A. Cuevas, “A quasi-steady-state open-circuit voltage method for solar cell characterisation,” presented at the 16th EUPVSEC, 2000.
[34] J. Haschke, “Einseitig kontaktierte amorph/kristalline Silizium Heterosolarzellen,” TU Berlin, Berlin, 2014.
[35] O. Breitenstein and H. Straube, “Lock-in thermography investigation of solar modules,” *Proc 26th Eur PVSEC*, pp. 1451–1453, 2011.
[36] D. Abou-Ras, T. Kirchartz, and U. Rau, *Advanced Characterization Techniques for Thin Film Solar Cells*. John Wiley & Sons, 2016.
[37] M. Green, *Solar Cells - Operating Principles, Technology and System Applications*. Prentice-Hall, 1992.
[38] G. Masetti, M. Severi, and S. Solmi, “Modeling of carrier mobility against carrier concentration in arsenic-, phosphorus-, and boron-doped silicon,” *IEEE Trans. Electron Devices*, vol. 30, no. 7, pp. 764–769, Jul. 1983.
[39] P. A. Basore, “Extended spectral analysis of internal quantum efficiency,” in *Conference Record of the 23rd IEEE PV-SC*, 1993, pp. 147–152.
[40] S. M. Sze, *Physics of semiconductor devices*, 3rd ed. Hoboken, N.J: Wiley-Interscience, 2007.
[41] A. B. Sproul, “Dimensionless solution of the equation describing the effect of surface recombination on carrier decay in semiconductors,” *J. Appl. Phys.*, vol. 76, no. 5, p. 2851, 1994.
[42] “EAGLE XG ® Slim Glass - Product information and material properties.” [Online]. Available: https://www.corning.com/media/worldwide/cdt/documents/EAGLE%20XG%20%C2%AE%20Slim%20Glass.pdf. [Accessed: 22-Nov-2016].

[43] J. Dore, R. Evans, B. D. Eggleston, S. Varlamov, and M. A. Green, “Intermediate Layers for Thin-Film Polycrystalline Silicon Solar Cells on Glass Formed by Diode Laser Crystallization,” *MRS Online Proc. Libr. Arch.*, vol. 1426, pp. 63–68, Jan. 2012.
[44] “Schott Borofloat33 - product description & Material properties.” [Online]. Available: http://psec.uchicago.edu/glass/borofloat_33_e.pdf. [Accessed: 22-Nov-2016].
[45] J. Dore *et al.*, “Thin-film polycrystalline silicon solar cells formed by diode laser crystallisation: Thin-film polycrystalline silicon solar cells,” *Prog. Photovolt. Res. Appl.*, vol. 21, no. 6, pp. 1377–1383, Sep. 2013.
[46] J. Haschke, L. Jogschies, D. Amkreutz, L. Korte, and B. Rech, “Polycrystalline silicon heterojunction thin-film solar cells on glass exhibiting 582mV open-circuit voltage,” *Sol. Energy Mater. Sol. Cells*, vol. 115, pp. 7–10, Aug. 2013.
[47] D. Amkreutz, J. Haschke, T. Häring, F. Ruske, and B. Rech, “Conversion efficiency and process stability improvement of electron beam crystallized thin film silicon solar cells on glass,” *Sol. Energy Mater. Sol. Cells*, vol. 123, pp. 13–16, Apr. 2014.
[48] S. Kühnapfel *et al.*, “Preferential {100} grain orientation in 10 micrometer-thick laser crystallized multicrystalline silicon on glass,” *Thin Solid Films*, vol. 576, pp. 68–74, Feb. 2015.
[49] T. Pliewischkies *et al.*, “Thermal stresses and cracking behavior during laser crystallization of silicon on glass for thin film solar cells,” *Phys. Status Solidi A*, 2014.
[50] B. Schwartz and H. Robbins, “Chemical etching of silicon IV. Etching technology,” *J. Electrochem. Soc.*, vol. 123, no. 12, pp. 1903–1909, 1976.
[51] H. Angermann *et al.*, “Wet-chemical passivation of atomically flat and structured silicon substrates for solar cell application,” *Appl. Surf. Sci.*, vol. 254, no. 12, pp. 3615–3625, Apr. 2008.
[52] O. Gabriel *et al.*, “PECVD Intermediate and Absorber Layers Applied in Liquid-Phase Crystallized Silicon Solar Cells on Glass Substrates,” *IEEE J. Photovolt.*, vol. 4, no. 6, pp. 1343–1348, Nov. 2014.
[53] J. D. Hylton, A. R. Burgers, and W. C. Sinke, “Alkaline Etching for Reflectance Reduction in Multicrystalline Silicon Solar Cells,” *J. Electrochem. Soc.*, vol. 151, no. 6, pp. G408–G427, Jan. 2004.
[54] M. Tanaka *et al.*, “Development of New a-Si/c-Si Heterojunction Solar Cells: ACJ-HIT (Artificially Constructed Junction-Heterojunction with Intrinsic Thin-Layer),” *Jpn. J. Appl. Phys.*, vol. 31, no. Part 1, No. 11, pp. 3518–3522, Nov. 1992.
[55] M. Ghannam, G. Shehadah, Y. Abdulraheem, and J. Poortmans, “On the possible role of the interfacial inversion layer in the improvement of the performance of hydrogenated amorphous silicon/crystalline silicon heterojunction solar cells [HIT],” *Sol. Energy Mater. Sol. Cells*, vol. 132, pp. 320–328, Jan. 2015.
[56] M. Mews, “Interfaces in amorphous/crystalline silicon heterojunction solar cells,” TU Berlin, 2016.
[57] “Photoresist AZ 4533 Photoresists MicroChemicals GmbH.” [Online]. Available: http://www.microchemicals.com/products/photoresists/az_4533.html. [Accessed: 11-Jan-2017].
[58] H. Plagwitz, M. Nerding, N. Ott, H. P. Strunk, and R. Brendel, “Low-temperature formation of local Al contacts to a-Si:H-passivated Si wafers,” *Prog. Photovolt. Res. Appl.*, vol. 12, no. 1, pp. 47–54, 2004.
[59] L. A. Clevenger, R. W. Mann, R. A. Roy, K. L. Saenger, C. Cabral Jr, and J. Piccirillo, “Study of C49-TiSi2 and C54-TiSi2 formation on doped polycrystalline silicon using in situ resistance measurements during annealing,” *J. Appl. Phys.*, vol. 76, no. 12, pp. 7874–7881, 1994.
[60] J. Haschke, D. Amkreutz, L. Korte, F. Ruske, and B. Rech, “Towards wafer quality crystalline silicon thin-film solar cells on glass,” *Sol. Energy Mater. Sol. Cells*, vol. 128, pp. 190–197, Sep. 2014.
[61] T. Frijnts *et al.*, “Single-side-contacted HIT Cells from Liquid Phase Crystallized Silicon on Glass using PECVD Precursors,” presented at the EUPVSEC, Amsterdam, 2014.
[62] S. Duttagupta, F. Ma, B. Hoex, T. Mueller, and A. G. Aberle, “Optimised Antireflection Coatings using Silicon Nitride on Textured Silicon Surfaces based on Measurements and Multidimensional Modelling,” *Energy Procedia*, vol. 15, pp. 78–83, Jan. 2012.

[63] H. Plagwitz, “Surface passivation of crystalline silicon solar cells by amorphous silicon films,” Gottfried Wilhelm Leibniz University Hannover, Hannover, 2007.
[64] J. Haschke, D. Amkreutz, and B. Rech, “Liquid phase crystallized silicon on glass: Technology, material quality and back contacted heterojunction solar cells,” *Jpn. J. Appl. Phys.*, vol. 55, no. 4S, p. 04EA04, Apr. 2016.
[65] P. Sonntag *et al.*, “Analysis of Local Minority Carrier Diffusion Lengths in Liquid-Phase Crystallized Silicon Thin-Film Solar Cells,” *IEEE J. Photovolt.*, vol. PP, no. 99, pp. 1–5, 2016.
[66] J. Dore, “Intermediate Layers for Laser-Crystallised Thin-Film Silicon Solar Cells on Glass,” University of New South Wales, 2014.
[67] T. Frijnts *et al.*, “Analysis of photo-current potentials and losses in thin film crystalline silicon solar cells,” *Sol. Energy Mater. Sol. Cells*, vol. 143, pp. 457–466, Dec. 2015.
[68] G. M. Smirnov and J. E. Mahan, “Distributed series resistance in photovoltaic devices; intensity and loading effects,” *Solid-State Electron.*, vol. 23, no. 10, pp. 1055–1058, 1980.
[69] T. Frijnts, N. Preissler, S. Gall, S. Neubert, B. Rech, and R. Schlatmann, “Influence of the Frontside Charge Inversion Layer on the Minority Carrier Collection in Backside Contacted Liquid Phase Crystallized Silicon on Glass Solar Cells,” *Sol. RRL*, vol. 1, no. 9, p. 1700100, Sep. 2017.
[70] S. Calnan *et al.*, “Influence of Chemical Composition and Structure in Silicon Dielectric Materials on Passivation of Thin Crystalline Silicon on Glass,” *ACS Appl. Mater. Interfaces*, vol. 7, no. 34, pp. 19282–19294, Sep. 2015.
[71] K. R. McIntosh and S. C. Baker-Finch, “OPAL 2: Rapid optical simulation of silicon solar cells,” in *2012 38th IEEE Photovoltaic Specialists Conference (PVSC)*, 2012, pp. 000265–000271.
[72] E. Yablonovitch, “Statistical ray optics,” *JOSA*, vol. 72, no. 7, pp. 899–907, 1982.
[73] “Wafer ray tracer.” [Online]. Available: http://www.pvlighthouse.com.au/calculators/wafer%20ray%20tracer/wafer%20ray%20tracer.html. [Accessed: 13-Mar-2015].
[74] E. Yablonovitch and G. D. Cody, “Intensity enhancement in textured optical sheets for solar cells,” *IEEE Trans. Electron Devices*, vol. 29, no. 2, pp. 300–305, Feb. 1982.
[75] P. Campbell and M. A. Green, “Light trapping properties of pyramidally textured surfaces,” *J. Appl. Phys.*, vol. 62, no. 1, p. 243, 1987.
[76] D. Eisenhauer, K. Jäger, G. Köppel, B. Rech, and C. Becker, “Optical Properties of Smooth Anti-reflective Three-dimensional Textures for Silicon Thin-film Solar Cells,” *Energy Procedia*, vol. 102, pp. 27–35, Dec. 2016.
[77] T. J. Coutts, D. L. Young, and X. Li, “Characterization of Transparent Conducting Oxides,” *MRS Bull.*, vol. 25, no. 8, pp. 58–65, Aug. 2000.
[78] N. Preissler *et al.*, “Interface passivation of liquid-phase crystallized silicon on glass studied with high-frequency capacitance–voltage measurements,” *Phys. Status Solidi A*, vol. 213, no. 7, pp. 1697–1704, Feb. 2016.
[79] H. Mäckel and R. Lüdemann, “Detailed study of the composition of hydrogenated SiNx layers for high-quality silicon surface passivation,” *J. Appl. Phys.*, vol. 92, no. 5, pp. 2602–2609, Aug. 2002.
[80] S. Dauwe, J. Schmidt, A. Metz, and R. Hezel, “Fixed charge density in silicon nitride films on crystalline silicon surfaces under illumination,” in *Conference Record of the 29th IEEE PVSC*, 2002, pp. 162–165.
[81] I. Cesar *et al.*, “Mercury: A Back Junction Back Contact Front Floating Emitter Cell with Novel Design for High Efficiency and Simplified Processing,” *Energy Procedia*, vol. 55, pp. 633–642, 2014.
[82] A. R. Burgers *et al.*, “FFE IBC cells: Impact of Busbars on Cell Performance with Circuit Modelling,” *Energy Procedia*, vol. 77, pp. 21–28, Aug. 2015.
[83] S. W. Glunz, A. B. Sproul, W. Warta, and W. Wettling, “Injection-level-dependent recombination velocities at the Si-SiO2 interface for various dopant concentrations,” *J. Appl. Phys.*, vol. 75, no. 3, pp. 1611–1615, Feb. 1994.

[84] D. Amkreutz *et al.*, “Liquid-Phase Crystallized Silicon Solar Cells on Glass: Increasing the Open-Circuit Voltage by Optimized Interlayers for n- and p-Type Absorbers,” *IEEE J. Photovolt.*, vol. PP, no. 99, pp. 1–5, 2015.

[85] J. Schmidt, A. Merkle, B. Hoex, M. C. M. van de Sanden, W. M. M. Kessels, and R. Brendel, “Atomic-layer-deposited aluminum oxide for the surface passivation of high-efficiency silicon solar cells,” in *Conference Record of the 33rd IEEE PVSC*, 2008, pp. 1–5.

[86] O. Gabriel *et al.*, “Crystalline silicon on glass—interface passivation and absorber material quality,” *Prog. Photovolt. Res. Appl.*, vol. 24, no. 12, pp. 1499–1512, Nov. 2015.

[87] R. Varache, C. Leendertz, M. E. Gueunier-Farret, J. Haschke, D. Muñoz, and L. Korte, “Investigation of selective junctions using a newly developed tunnel current model for solar cell applications,” *Sol. Energy Mater. Sol. Cells*, vol. 141, pp. 14–23, Oct. 2015.

[88] A. G. Aberle, S. Glunz, and W. Warta, “Impact of illumination level and oxide parameters on Shockley–Read–Hall recombination at the Si-SiO2 interface,” *J. Appl. Phys.*, vol. 71, no. 9, p. 4422, 1992.

[89] J. Schmidt and A. G. Aberle, “Carrier recombination at silicon–silicon nitride interfaces fabricated by plasma-enhanced chemical vapor deposition,” *Sol. Cells*, vol. 2, p. 11, 1999.

[90] B. W. H. van de Loo, B. Macco, J. Melskens, M. Verheijen, and W. M. M. Kessels, “Atomic-Layer Deposited Passivation Schemes for c-Si Solar Cells,” presented at the 43th IEEE PVSC, 2016.

[91] S. Dauwe, “Low-Temperature Surface Passivation of Crystalline Silicon and its Application to the Rear Side of Solar Cells,” Uni Hannover, 2004.

[92] R. Hezel and K. Jäger, “Properties of inversion layers for MIS/IL solar cells studied on low-temperature-processed MNOS transistors,” *Solid-State Electron.*, vol. 26, no. 10, pp. 993–997, Oct. 1983.

[93] A. Fell, “A Free and Fast Three-Dimensional/Two-Dimensional Solar Cell Simulator Featuring Conductive Boundary and Quasi-Neutrality Approximations,” *IEEE Trans. Electron Devices*, vol. 60, no. 2, pp. 733–738, Feb. 2013.

[94] R. B. Girisch, R. P. Mertens, and R. F. De Keersmaecker, “Determination of Si-SiO 2 interface recombination parameters using a gate-controlled point-junction diode under illumination,” *IEEE Trans. Electron Devices*, vol. 35, no. 2, pp. 203–222, 1988.

[95] D. Macdonald and A. Cuevas, “Reduced fill factors in multicrystalline silicon solar cells due to injection-level dependent bulk recombination lifetimes,” *Prog. Photovolt. Res. Appl.*, vol. 8, no. 4, pp. 363–375, Jul. 2000.

[96] S. Wenham, M. Green, and M. Taouk, “Buried Contact, Interconnected Thin Film and Bulk Photovoltaic Cells,” WO9312543 (A1), 24-Jun-1993.

[97] P. A. Basore, “Large-area deposition for crystalline silicon on glass modules,” in *Proceedings of 3rd World Conference onPhotovoltaic Energy Conversion, 2003*, 2003, vol. 1, pp. 935-938 Vol.1.

[98] K. Ji, H. Syn, J. Choi, H.-M. Lee, and D. Kim, “The Emitter Having Microcrystalline Surface in Silicon Heterojunction Interdigitated Back Contact Solar Cells,” *Jpn. J. Appl. Phys.*, vol. 51, no. 10S, p. 10NA05, Oct. 2012.

[99] S.-Y. Lee *et al.*, “Analysis of a-Si:H/TCO contact resistance for the Si heterojunction back-contact solar cell,” *Sol. Energy Mater. Sol. Cells*, vol. 120, pp. 412–416, Jan. 2014.

[100] S. Kirner, L. Mazzarella, L. Korte, B. Stannowski, B. Rech, and R. Schlatmann, “Silicon Heterojunction Solar Cells With Nanocrystalline Silicon Oxide Emitter: Insights Into Charge Carrier Transport,” *IEEE J. Photovolt.*, vol. 5, no. 6, pp. 1601–1605, Nov. 2015.

[101] M. Pomaska, W. Beyer, E. Neumann, F. Finger, and K. Ding, “Impact of microcrystalline silicon carbide growth using hot-wire chemical vapor deposition on crystalline silicon surface passivation,” *Thin Solid Films*, vol. 595, Part B, pp. 217–220, Nov. 2015.

[102] P. Roca i Cabarrocas, N. Layadi, T. Heitz, B. Drévillon, and I. Solomon, “Substrate selectivity in the formation of microcrystalline silicon: Mechanisms and technological consequences,” *Appl. Phys. Lett.*, vol. 66, no. 26, pp. 3609–3611, Jun. 1995.
[103] L. Mazzarella *et al.*, “Nanocrystalline silicon emitter optimization for Si-HJ solar cells: substrate selectivity and CO2 plasma treatment effect,” *submitted*, 2016.
[104] L. Mazzarella *et al.*, “Comparison of TMB and B2H6 as Precursors for Emitter Doping in High Efficiency Silicon Hetero Junction Solar Cells,” *Energy Procedia*, vol. 60, pp. 123–128, 2014.
[105] S. Olibet *et al.*, “Textured silicon heterojunction solar cells with over 700mV open-circuit voltage studied by transmission electron microscopy,” in *23 EUPVSEC*, 2008.
[106] D. K. Schroder, *Semiconductor material and device characterization*, 3rd ed. IEEE Press, John Wiley & Sons, Inc., 2006.
[107] K. Kotsovos and K. Misiakos, “Three-Dimensional Simulation of Base Carrier Transport Effects in Back Side Point Contact Silicon Solar Cells,” *Lead. Edge Res. Sol. Energy*, p. 1, 2007.
[108] S. Haas, S. Krumscheid, A. Bauer, A. Lambertz, and U. Rau, “Novel series connection concept for thin film solar modules,” *Prog. Photovolt. Res. Appl.*, p. n/a-n/a, Mar. 2012.
[109] B. E. Pieters and U. Rau, “A new 2D model for the electrical potential in a cell stripe in thin-film solar modules including local defects: Model for cells in thin-film modules including local defects,” *Prog. Photovolt. Res. Appl.*, vol. 23, no. 3, pp. 331–339, Mar. 2015.
[110] T. Frijnts *et al.*, “Backside Contacted Solar Cells with HTJ Emitters and Laser Fired Absorber Contacts for Crystalline Silicon on Glass,” in *Proceedings of the 43th IEEE PVSC*, Portland, 2016.
[111] M. Filipič, Z. C. Holman, F. Smole, S. De Wolf, C. Ballif, and M. Topič, “Analysis of lateral transport through the inversion layer in amorphous silicon/crystalline silicon heterojunction solar cells,” *J. Appl. Phys.*, vol. 114, no. 7, p. 074504, 2013.
[112] K. R. McIntosh, “Lumps, Humps and Bumps: Three detrimental effects in the current–voltage curve of a silicon solar cell,” UNSW, 2001.
[113] T. Tiedje, E. Yablonovitch, G. D. Cody, and B. G. Brooks, “Limiting efficiency of silicon solar cells,” *IEEE Trans. Electron Devices*, vol. 31, no. 5, pp. 711–716, May 1984.
[114] O. Breitenstein, R. Gupta, and J. Schneider, “Surface potential mapping on crystalline silicon on glass solar modules,” *J. Appl. Phys.*, vol. 102, no. 2, p. 024511, Jul. 2007.
[115] P. Sonntag *et al.*, “Silicon Solar Cells on Glass with Power Conversion Efficiency above 13 % and thickness below 15 µm,” *Accept. Sci. Rep.*, 2017.
[116] A. Mette, “New Concepts for Front Side Metallization of Industrial Silicon Solar Cells,” Freiburg, 2007.
[117] P. A. Basore, “Crystalline silicon on glass device optimization,” in *Conference Record of the Thirty-first IEEE Photovoltaic Specialists Conference, 2005.*, 2005, pp. 967–970.
[118] D. Pysch, A. Mette, and S. W. Glunz, “A review and comparison of different methods to determine the series resistance of solar cells,” *Sol. Energy Mater. Sol. Cells*, vol. 91, no. 18, pp. 1698–1706, Nov. 2007.
[119] D. Macdonald and A. Cuevas, “Trapping of minority carriers in multicrystalline silicon,” *Appl. Phys. Lett.*, vol. 74, no. 12, pp. 1710–1712, Mar. 1999.
[120] C. Leendertz, A.-M. Teodoreanu, L. Korte, and B. Rech, “The influence of space charge regions on effective charge carrier lifetime in thin films and resulting opportunities for materials characterization,” *J. Appl. Phys.*, vol. 113, no. 4, p. 044510, Jan. 2013.
[121] K. Taretto, U. Rau, and J. H. Werner, “Method to extract diffusion length from solar cell parameters—Application to polycrystalline silicon,” *J. Appl. Phys.*, vol. 93, no. 9, pp. 5447–5455, May 2003.
[122] B. Demaurex *et al.*, “Low-temperature plasma-deposited silicon epitaxial films: Growth and properties,” *J. Appl. Phys.*, vol. 116, no. 5, p. 053519, Aug. 2014.
[123] D. Tetzlaff *et al.*, “Evolution of oxide disruptions: The (W) hole story about poly-Si/c-Si passivating contacts,” in *Photovoltaic Specialists Conference (PVSC), 2016 IEEE 43rd*, 2016, pp. 0221–0224.

[124] J. Schneider, “Emitterbildung für flüssigphasenkristallisierte Silizium Dünnschichtsolarzellen auf Glas Substrat mittels Diodenlaser Dotierung,” Master thesis, TU Berlin, 2014.
[125] M. Karaman, “Polycrystalline Silicon Thin Film Processing on Glass Substrates for Photovoltaic Applications,” PhD thesis, Middle East Technical University, Ankara, 2016.
[126] S. Selberherr, *Analysis and Simulation of Semiconductor Devices*. 1984: Springer.
[127] P. Hamer, B. Hallam, S. Wenham, and M. Abbott, “Manipulation of Hydrogen Charge States for Passivation of P-Type Wafers in Photovoltaics,” *IEEE J. Photovolt.*, vol. 4, no. 5, pp. 1252–1260, Sep. 2014.
[128] G. Scardera *et al.*, “All-screen-printed Dopant Paste Interdigitated Back Contact Solar Cell,” *Energy Procedia*, vol. 77, pp. 271–278, Aug. 2015.
[129] T. Frijnts, H. Zollondz, and A. Heidelberg, “Method for Applying Semiconductor Material, Semiconductor Module, and Substrate Production System,” WO/2015/169331, 13-Nov-2015.
[130] Rachow, T., Ledinsky, M., Janz, S., Reber, S., and Fejfar, A., “μc-Si Solar Cells by Direct Deposition with APCVD,” in *Proceedings of the 27th EUPVSEC*, 2012.
[131] S. Kirner *et al.*, “The Influence of ITO Dopant Density on J-V Characteristics of Silicon Heterojunction Solar Cells: Experiments and Simulations,” *Energy Procedia*, vol. 77, pp. 725–732, Aug. 2015.